LIDAR MEASUREMENTS OF POLLUTION ABOVE THE CANADIAN OIL SANDS

MONIKA AGGARWAL

A DISSERTATION SUBMITTED TO THE FACULTY OF GRADUATE STUDIES
IN PARTIAL FULFILLMENT OF THE REQUIREMENTS FOR THE DEGREE OF
DOCTOR OF PHILOSOPHY

GRADUATE PROGRAM IN PHYSICS AND ASTRONOMY
YORK UNIVERSITY
TORONTO, ONTARIO

January 2018

Abstract

A lidar for measurements of aerosol and ozone was developed at York University and deployed on an aircraft to assess the impact of emissions from the Alberta oil sands extraction industry. The downward viewing lidar system was operated from a Twin Otter aircraft to investigate the vertical distribution of aerosol and ozone above the oil sands region north of Fort McMurray, Alberta.

An aerosol correction technique was developed and applied to the ozone retrieval in regions where significant pollution from the oil sands industry was observed. This correction technique made use of an additional aerosol measurement (the particle size distribution) that was used in Mie scattering calculations. It was found that the aerosol correction is significant and the maximum amount of correction in the ozone value was calculated to be up to 15 ppbv in regions where there were strong gradients in the aerosol backscatter profile (e.g. at the top of the surface boundary layer).

Ozone mixing ratios in background (unpolluted) air within the lower troposphere typically range between 25 and 45 ppbv during the summer above Alberta. Sources of anthropogenic pollution are the primary cause of enhanced ozone mixing ratios near the ground. The processes related to oil and gas extraction are

known sources of volatile organic compounds (VOCs) and nitrogen oxides (NO_x) (Simpson et al., 2010), and the photochemistry between NO_x and VOC emissions in daylight generates ozone.

Lidar measurements were collected upwind, downwind and directly above the oil sands mining industry to assess whether ozone is generated from the industrial emissions. Ozone mixing ratios were determined in regions affected by industrial pollution and in some cases up to 150 km downwind of the industry. The pollution from the oil sands contained a substantial amount of aerosol that was distributed throughout the depth of the surface boundary layer to heights of up to 1.1 km above ground. The amount of ozone measured in polluted air was between 10 and 35 ppbv. Ozone mixing ratios in pollution were often less than the values in background unpolluted air. In addition, ozone mixing ratios greater than the background were not observed up to 150 km downwind of the industry. The reduction in ozone in polluted air near the industry could be explained as being due to chemical reactions involving nitrogen oxide emissions that reduce ozone through NO_x titration. The increased levels of NO emissions directly over the industry provide an explanation for the observed low ozone mixing ratios in the vicinity of the oil sands and within the polluted air. There were no measured enhancements in ozone that are usually found in polluted air. Ozone mixing ratios greater than 80 ppbv (much higher than the background) are usually expected in conditions comparable to a warm summer day in an urban area (Yap et al., 1988; Geddes et al., 2009). The atmospheric conditions were such that the temperature was below what is usually associated with sufficient

VOC concentration to produce substantial amounts of ozone. Also, the stagnant conditions that are usually associated with urban pollution events did not occur over the oil sands region during the field campaign.

On one of the flights, the lidar detected a separated layer of aerosol above the surface boundary layer and this was associated with enhanced ozone mixing ratios up to 70 ppbv. Air trajectory calculations revealed that the separated aerosol layer had passed over an area of forest fires. Measurements of the linear depolarization ratio were obtained with a ground based lidar and this helped in separating the sources of pollution between industry and forest fires. The depolarization ratio was 5 – 6% in forest fire smoke and 7 – 10% in the industrial pollution.

Dedication

I would like to dedicate this work to my family: my loving father and mother, and to my wonderful brother.

Acknowledgments

My sincere thank you goes to my supervisor Dr. James Whiteway, for the continuous support, guidance, and for the unique opportunity that I was given to work on the oil sands project. I am fortunate to have a supervisor who assisted and motivated me at all times of research and at conferences. It has been a great pleasure working under the supervision of an intelligent, cooperative, and a patient advisor.

I would like to thank the rest of my supervisory committee: Dr. Thomas McElroy and Dr. Michael Daly for their valuable comments, suggestions and for all of the questions which motivated me to broaden my research knowledge. My sincere appreciation to Dr. Robert McLaren for providing direction with the in situ measurements.

I would like to express my gratitude to members of Dr. Whiteway's research group; especially Mr. Lawrence Gray and Dr. Jeffrey Seabrook, for their hard work and assistance in making the oil sands field campaign in 2013 a success. I would also like to thank Mr. George Nikolakakos for his assistance in collecting lidar measurements in Toronto.

I would like to thank my colleagues at Environment and Climate Change Canada for their wonderful collaboration and for giving me the opportunity to join

their team in helpful discussions about the oil sands project. In particular, I am grateful to Dr. Kevin Strawbridge, Dr. Peter Liu, and Dr. Jason O'Brien, who have provided additional measurements that were very useful for this project.

I would also like to thank Mr. Cordy Tymstra from the Fort McMurray wildfire branch, under the Environment and Sustainable Resource Development of Alberta for providing records of forest fires locations.

A special thank you goes to my dear family and friends. The work that was done for my Ph.D thesis wouldn't have been possible without the help and support of my family. My father, Vaishno, my mother, Suman, and my brother, Gaurav, provided endless love and care throughout my graduate career. I would also like to thank my best friend and my love, Subir Sutradhar, for believing in me and cheering me on with his best wishes. Last but not least, I thank my wonderful friends at York University, Hermina Beica and Urmela Selventhiran for all of the good times we had during our research breaks and for providing encouragement throughout the hard years of work.

Finally, I would like to thank Environment and Climate Change Canada (ECCC), the Natural Science and Engineering Research Council (NSERC) of Canada, FedDev Ontario (through Communitech Corp.), and the Canadian Foundation for Innovation (CFI) for financial support that was provided to conduct this research.

Table of Contents

Abstract . . . . . **ii**

Dedication . . . . . **v**

Acknowledgments . . . . . **vi**

Table of Contents . . . . . **viii**

List of Tables . . . . . **xi**

List of Figures . . . . . **xii**

1 Introduction **1**

2 Measurement Technique **10**

2.1 Differential Absorption Lidar System 10

2.2 Field Experiment 27

2.3 In Situ Instrumentation 29

2.3.1 Measurement of Particle Size 29

2.3.2 Measurement of Ozone 31

2.3.3 Measurement of Nitrogen Species 32

2.4 Ground Based Lidar System 33

3 Analysis **35**

3.1 Lidar Equation 35

3.2 The Differential Absorption Lidar Equation 44

3.3 Differential Absorption Lidar Correction Techniques 52

3.3.1 Correction for Aerosol in the Lidar O_3 Retrieval 52

3.3.1.1 Aerosol Optical Properties Derived from Size Distribution Measurements 53
3.3.1.2 Aerosol Extinction Derived from the 532 nm Lidar Backscatter Signal 57
3.3.1.3 Aerosol Height Profile from Combined Lidar and In Situ Measurements 60
3.3.1.4 Aerosol Correction in the Ozone Retrieval. 63

3.3.2 Interference from Atmospheric Gases 66

3.3.2.1 Correction for SO_2 Differential Absorption 68
3.3.2.2 Correction for NO_2 Differential Absorption 70

3.4 Non-linearity in Photon Counting Detection 71

3.5 Signal Induced Noise in the Lidar Measurement 73

3.6 Temperature Dependence of O_3 Absorption Cross-section 77

3.7 Hybrid Single Particle Integrated Trajectory (HYSPLIT) Model . . 78

3.8 Relative Uncertainty in Lidar Measurements 79

3.8.1 Error Analysis for the Differential Absorption Lidar Method 81

3.8.2 Error Analysis in Aerosol Correction Method 82

3.8.2.1 Uncertainty from the Particle Equivalent Area Radius and Lidar Ratio 82
3.8.2.2 Uncertainty from the Aerosol Extinction Coefficient 86
3.8.2.3 Uncertainty from the Particle Refractive Index . . 88

3.9 Validation of Ozone Lidar Measurements 89

4 Lidar Measurements above Toronto 92

4.1 Introduction 92

4.2 Observations 93

4.2.1 In Situ Measurements in Toronto 97

4.3 Discussion 99

5 Airborne Lidar Measurements over the Alberta Oil Sands Region 101

5.1 Observations 105

5.1.1 Industrial Pollution 105

5.1.1.1 Explanation of Low O_3 in the Oil Sands Industry . 109

5.1.1.2 Measurements Above the Oil Sands Industry . . . 111

5.1.1.3 Measurements Downwind of the Oil Sands Industry 132

5.1.1.4 Comparison between Lidar and In Situ Measurements 148

5.1.1.5 Transport Distance of Air in the Oil Sands Region. 150

5.1.1.6 Ground Based Air Monitoring Stations 154

5.1.2 Forest Fire Smoke 157

5.1.2.1 More Evidence of Forest Fire Smoke 163

5.2 Discussion 165

5.2.1 Industrial Pollution 165

5.2.2 Forest Fire Smoke 171

6 Conclusion 174

Appendix 1: Retrieval of Aerosol Extinction Coefficient 177

Bibliography 183

List of Tables

Table 2.1: Stokes wavelengths and the corresponding O_3 absorption cross-sections at 300 K 16

Table 2.2: Lidar system specifications 26

Table 3.1: Input parameters used in the Mie calculations for the oil sands aerosol correction 60

Table 3.2: O_3 and SO_2 differential absorption cross-sections and the corresponding correction sensitivity due to the interference of SO_2 in the O_3 retrieval 69

Table 3.3: O_3 and NO_2 differential absorption cross-sections and the corresponding correction sensitivity due to the interference of NO_2 in the O_3 retrieval 70

Table 3.4: Temperature dependent O_3 absorption cross-sections between 260 and 300 K at the lidar measurement wavelengths 77

Table 5.1: Input parameters used in the Mie calculations for forest fire aerosol correction 161

List of Figures

Figure 1.1: Location of the Athabasca oil sands in Alberta 4

Figure 2.1: Lidar system schematic diagram used during the oil sands field campaign 13

Figure 2.2: Energy level diagram of stimulated Raman scattering 14

Figure 2.3: O_3 absorption cross-section as a function of wavelength in the UV Hartley band 16

Figure 2.4: Expanded view of the alignment mirrors in the lidar system 17

Figure 2.5: The lidar field stop 18

Figure 2.6: The wavelength separation box for the lidar UV measurements .. 20

Figure 2.7: The lidar system detectors 21

Figure 2.8: The lidar system installed in an aircraft rack 23

Figure 2.9: The lidar system receiver fitted into an aircraft rack 24

Figure 2.10: The lidar system installed in Twin Otter aircraft 25

Figure 2.11: Screenshot of the in-flight visualization tool 28

Figure 2.12: The location of Environment and Climate Change Canada's ground based lidar system 34

Figure 3.1: Raw lidar signal and the derived aerosol extinction coefficient at a wavelength of 532 nm 42

Figure 3.2: Lidar measurement at a wavelength of 532 nm with the background signal subtraction 43

Figure 3.3: Raw lidar signal at the wavelength of 266 and 276 nm 45

Figure 3.4: Lidar backscatter signals and the derived O_3 mixing ratio 51

Figure 3.5: In situ particle size distribution measurement taken within the surface boundary layer and over the oil sands industry 54

Figure 3.6: A comparison between the aerosol extinction coefficient from the ground-based lidar system and that derived from Fernald's method 59

Figure 3.7: The calculated aerosol backscatter and extinction coefficients at the measurement UV wavelengths 62

Figure 3.8: O_3 retrieval with and without the aerosol correction 64

Figure 3.9: The amount of aerosol correction by using the six ON/OFF wavelength pair combinations 66

Figure 3.10: The absorption cross-sections of O_3, SO_2, and NO_2 molecules in the UV Hartley band 68

Figure 3.11: Non-linearity correction in the photon counting lidar measurement at a wavelength of 276 nm 72

Figure 3.12: Lidar signal at wavelengths of 266, 299, and 532 nm plotted as a function of range 74

Figure 3.13: The lidar signal with and without the signal induced noise correction 75

Figure 3.14: The effect of the signal induced noise correction in the O_3 retrieval 76

Figure 3.15: The effective radius and lidar ratio derived from the particle size distribution measurements across the oil sands industry 84

Figure 3.16: The derived O_3 profile by applying the aerosol correction for three different size distribution measurements 85

Figure 3.17: The derived O_3 profile by using three different aerosol extinction coefficients at a reference altitude in Fernald's technique 87

Figure 3.18: Air trajectory calculations for comparison of lidar O_3 and in situ O_3 measurements on August 23, 2013 90

Figure 3.19: A comparison between the in situ O_3 and the lidar derived O_3 for the measurements taken in unpolluted and polluted air 91

Figure 4.1: Contour plot of the aerosol backscatter ratio and the O_3 mixing ratio in July 2010 94

Figure 4.2: The aerosol extinction coefficient on July 6, 2010 and the temperature height profile from radiosonde measurements 95

Figure 4.3: Air trajectories initiated between July 6 and July 8, 2010 at 6:00 PM local time, Toronto 96

Figure 4.4: The location of four air monitoring stations in Toronto 98

Figure 4.5: Ground level in situ O_3 measurements at the four sites in Toronto in July 2010 98

Figure 5.1: Flight track of the Twin Otter aircraft on August 22, 2013 102

Figure 5.2: The track for the first Twin Otter flight on August 23, 2013 103

Figure 5.3: The track for the second Twin Otter flight on August 23, 2013 103

Figure 5.4: Flight track of the Twin Otter aircraft on August 24, 2013 104

Figure 5.5: Flight track of the Twin Otter aircraft on August 26, 2013 104

Figure 5.6: The flight segment G-H on August 23, 2013 106

Figure 5.7: Contour plot of the aerosol extinction coefficient and the O_3 mixing ratio for the flight segment G-H on Aug. 23, 2013 107

Figure 5.8: A map showing a portion of the Convair's flight path over the oil sands industry on Aug. 23, 2013 109

Figure 5.9: In situ measurements of O_3, NO, and NO_2 taken from a portion of the Convair's flight on August 23, 2013 110

Figure 5.10: The flight segment A-B on August 22, 2013 111

Figure 5.11: Contour plot of the aerosol extinction coefficient and the O_3 mixing ratio for the flight segment A-B on Aug. 22, 2013 112

Figure 5.12: The flight segment E-F on August 22, 2013 113

Figure 5.13: Contour plot of the aerosol extinction coefficient and the O_3 mixing ratio for the flight segment E-F on Aug. 22, 2013 114

Figure 5.14: The flight segment C-D on August 23, 2013 115

Figure 5.15: Contour plot of the aerosol extinction coefficient and the O_3 mixing ratio for the flight segment C-D on Aug. 23, 2013 116

Figure 5.16: Comparison of lidar data with in situ measurements collected during a Convair ascent over a polluted region on Aug. 23, 2013 .. 118

Figure 5.17: The flight segment E-F on August 23, 2013 120

Figure 5.18: Contour plot of the aerosol extinction coefficient and the O_3 mixing ratio for the flight segment E-F on Aug. 23, 2013 121

Figure 5.19: Comparison of lidar data with in situ measurements collected during a Convair ascent over an area not affected by industrial pollution on Aug. 23, 2013 124

Figure 5.20: The flight segment J-K on August 23, 2013 125

Figure 5.21: Contour plot of the aerosol extinction coefficient and the O_3 mixing ratio for the flight segment J-K on Aug. 23, 2013 127

Figure 5.22: Comparison of lidar data with in situ measurements collected during a Convair ascent over an area affected by oil sands pollution on Aug. 23, 2013 129

Figure 5.23: The flight segment C-D for the second flight on August 23, 2013.. 130

Figure 5.24: Contour plot of the aerosol extinction coefficient and the O_3 mixing ratio for the flight segment C-D on Aug. 23, 2013 131

Figure 5.25: The flight segment M-N on August 22, 2013 133

Figure 5.26: Contour plot of the aerosol extinction coefficient and the O_3 mixing ratio for the flight segment M-N on Aug. 22, 2013 134

Figure 5.27: Comparison of lidar data with in situ measurements collected during a Convair ascent around the oil sands industry on Aug. 22, 2013 137

Figure 5.28: The flight segment I-J on August 22, 2013 138

Figure 5.29: Contour plot of the aerosol extinction coefficient and the O_3 mixing ratio for the flight segment I-J on Aug. 22, 2013 139

Figure 5.30: The flight segment G-H on August 22, 2013 140

Figure 5.31: Contour plot of the aerosol extinction coefficient and the O_3 mixing ratio for the flight segment G-H on Aug. 22, 2013 141

Figure 5.32: The flight segment H-I on August 23, 2013 142

Figure 5.33: Contour plot of the aerosol extinction coefficient and the O_3 mixing ratio for the flight segment H-I on Aug. 23, 2013 143

Figure 5.34: The flight segment J-K on August 26, 2013 144

Figure 5.35: Contour plot of the aerosol extinction coefficient and the O_3 mixing ratio for the flight segment J-K on Aug. 26, 2013 145

Figure 5.36: Comparison of lidar data with in situ measurements collected during a Convair ascent over an area affected by industrial pollution on Aug. 26, 2013 147

Figure 5.37: A histogram comparison between in situ and lidar derived O_3 for the measurements collected in unpolluted and polluted air 149

Figure 5.38: The aerosol extinction coefficient and the O_3 mixing ratio as a function of the length of time the air had passed over the industry to reach the measurement point along all five flight tracks..... 152

Figure 5.39: Backward air trajectories used to calculate the transport distance of air 153

Figure 5.40: Location of a few selected air monitoring stations in the Athabasca oil sands region 154

Figure 5.41: Ground level O_3 measurements from six air monitoring stations in the Athabasca oil sands region 155

Figure 5.42: Ground level NO and NO_2 measurements from an Air Monitoring Station (AMS 13) on Aug. 23, 2013..... 156

Figure 5.43: The flight segment A-B on August 24, 2013 157

Figure 5.44: Contour plot of the aerosol extinction coefficient and the O_3 mixing ratio for the flight segment A-B on Aug. 24, 2013 158

Figure 5.45: The location of forest fires relative to the flight segment A-B, C-D on August 24, 2013 and Environment and Climate Change Canada's ground based lidar system 159

Figure 5.46: Contour plot of the aerosol extinction coefficient and the O_3 mixing ratio for the flight segment C-D on Aug. 24, 2013 162

Figure 5.47: Contour plot of the O_3 mixing ratio, aerosol extinction coefficient and depolarization ratio for forest fire smoke observed on Aug. 24, 2013 along a section of the flight segment A-B 165

1 Introduction

The Canadian oil sands are a natural source of crude bitumen and a valuable energy resource. The oil sands are primarily located in the north-eastern part of Alberta. There are three oil sands deposit regions in Alberta: Peace River, Athabasca and Cold Lake. The Athabasca oil sands are one of the largest deposits that consist of fine mineral clays and quartz sand mixed with water, viscous bitumen and trace amounts of heavy metals and minerals (Wightman et al., 1989). The composition of the Athabasca oil sands is about 75% solids, 5% water, 20% bitumen and 1% metals and minerals (Strausz, 1989).

Oil production in the Athabasca region started in 1967 by the Great Canadian oil sands company (currently known as Suncor Energy, Inc.). Syncrude Canada, Ltd. began operation in 1978, followed by Shell Canada in 2003. For the oil deposits located north of Fort McMurray, bitumen extraction is feasible by two methods: surface mining up to a depth of 75 m, and in situ for oil deposits greater than 75 m in depth. The oil-sand mixture excavated from surface mines is treated with hot water to separate the bitumen from the sands. Waste materials such as sand, clay, water, and residual bitumen are stored in tailings ponds. On the other hand, in situ oil extraction processes inject steam into a well which lowers the viscosity of bitumen and makes it

easier to pump out through a separate well. Both extraction processes cause air pollution by releasing nitrogen oxides and sulphur oxides (from high temperature combustion of oil, gasoline, and coal) and carbon dioxide (by heating bitumen and exhaust emissions from transport vehicles) directly into atmosphere.

Air pollutants can be categorised as either primary or secondary pollutants. Primary air pollutants are produced directly from processes related to human activities, such as the exhaust fumes from vehicles and power plants, and also from natural sources. A few examples of primary pollutants in the lower troposphere are sulphur oxides (SO_x), nitrogen oxides (NO_x), carbon monoxide (CO), volatile organic compounds (VOCs), aerosol or particulate matter (PM) and ammonia (NH_3). Secondary air pollutants are not directly emitted from natural and anthropogenic sources, but rather are formed in the troposphere when primary pollutants undergo chemical reactions. A few examples of secondary air pollutants are nitrogen dioxide (NO_2), ozone (O_3), secondary aerosol, and peroxyacetyl nitrate (PAN).

Airborne particulate matter, or aerosol, is a general term used to characterize solid and liquid particles that are suspended in air. They occur naturally and can be produced anthropogenically. Forest fire smoke, desert dust and sea salt are all natural forms of tropospheric aerosol, while secondary organic aerosol produced from photochemical reactions of biogenic VOCs, vehicular exhaust and industrial emissions are anthropogenic sources. Aerosol in the troposphere is an air pollutant because particles of diameter less than 10μm (PM_{10}) or 2.5μm ($PM_{2.5}$) can directly affect the health of humans and other living organisms. The presence of PM_{10} in the

lower troposphere, and even $PM_{2.5}$ can cause damage to the respiratory system (Wang et al., 2013), damage to cells of a living organism by supressing DNA repair (Metha et al., 2008) increase the chances of a brain stroke (Leiva G et al., 2013), and mortality (Elliott and Copes, 2011; Franklin et al., 2007). Exposure to large amounts of O_3 can result in damage to biological tissue in crops and other living organisms (Haagen-Smit, 1952), and decrease the rate of photosynthesis in plants (Morgan et al., 2003). Smog is the best example of enhanced O_3 concentrations present in urban areas.

The Fort McMurray oil sands are located in the north-eastern part of Alberta (Fig. 1.1) and are surrounded by boreal forests. There are no other industrial activities, only oil and gas development. Emissions from the facility stacks vent water vapour, carbon dioxide, natural gas and hydrocarbon vapours that accumulate during the processing of bitumen. Other pollution sources include mining operations, paved and unpaved roads within the mining area, and tailings ponds. The air pollutants released by the oil sands mining and upgrading facilities are nitrogen oxide (NO_x), nitrogen dioxide (NO_2), sulphur dioxide (SO_2), sulfate (SO_4), methane (CH_4), carbon dioxide (CO_2), carbon monoxide (CO), particulate matter ($PM_{2.5}$), volatile organic compounds (VOCs) and secondary organic aerosol (SOA) (Simpson et al., 2010; Davies, 2012; Howell et al., 2014; Liggio et al., 2016). In contrast to the gaseous air pollutants, high concentrations of mercury have been found in snow samples in the vicinity of the oil sands region (Kirk et al., 2014). Some of the natural sources of pollution that occur in the oil sands region are biogenic VOC emissions from trees and plants (Sharkey et al.,

2008) and CO, NO_x, and ozone (O_3) pollution from forest fires (Crutzen et al., 1979; Simpson et al., 2011).

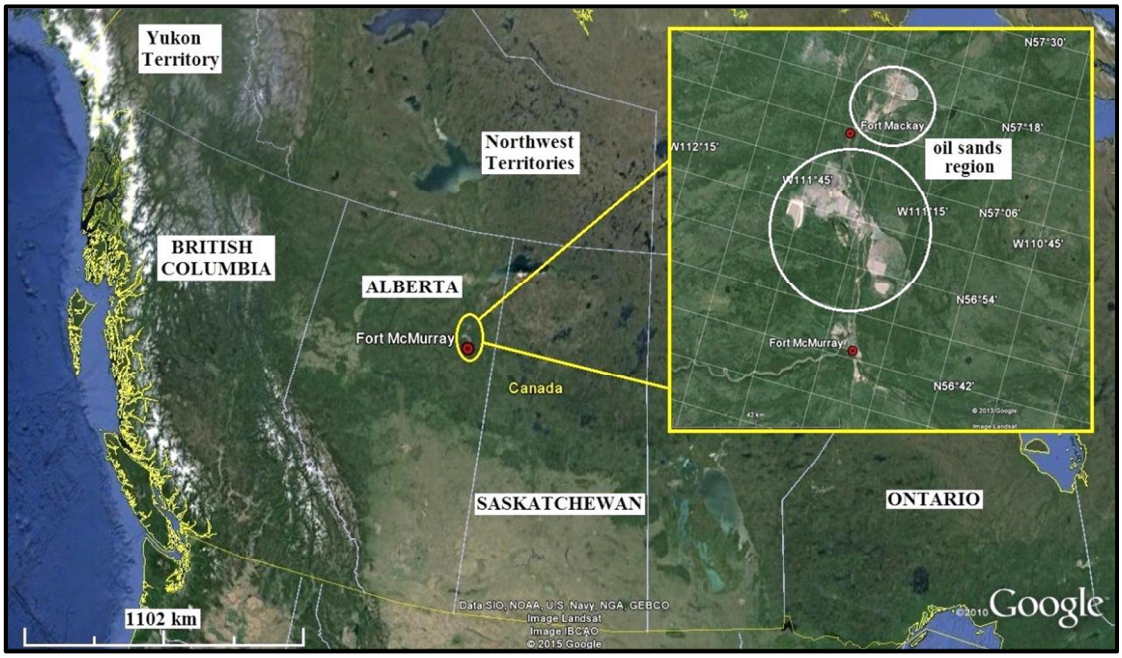

Figure 1.1: Location of the Athabasca oil sands in Alberta. Inset picture show the Fort McMurray oil sands region.

The air quality in the oil sands region is dependent upon the meteorological conditions, topography, deposition rates of pollutants, concentration of pollutants, and the chemical reactions that pollutants undergo within the lower troposphere. The air pollutant of interest in this study is ozone (O_3). Ozone in the stratosphere is very important as it shields life on earth from harmful UV radiation. However, in the troposphere near the ground, O_3 is a pollutant.

Natural and anthropogenic causes such as lightning, forest fires, exhaust from automobiles, and the combustion of coal and natural gas at high temperatures are

some sources that give rise to NO_2 molecules. The dissociation of NO_2 molecules by sunlight (*hv*) provides the essential atomic oxygen atoms that are required for the formation of O_3:

$$NO_2 + hv\ (\lambda \leq\ 400\ \text{nm}) \rightarrow NO + O \qquad \text{(C1)}$$

$$O + O_2 + M \rightarrow O_3 + M \qquad \text{(C2)}$$

Under normal conditions, a single NO molecule would react with O_3 to produce NO_2 and molecular oxygen:

$$NO + O_3 \rightarrow NO_2 + O_2 \qquad \text{(C3)}$$

Reactions (C1) to (C3) constantly continue under normal conditions (without the presence of VOCs) and there is no net production of O_3. However, biogenic VOCs (released from vegetation, plants, and trees) are always present in the atmosphere and anthropogenic activities related to fossil fuel combustion and solvent usage results in additional VOCs in the atmosphere.

When VOCs are present in the lower troposphere, they react with hydroxyl radicals (*OH*) to form reactive compounds. An example of a simple VOC is methane. An organic peroxy radical is one example of a reactive compound that is formed from the oxidation of VOC. Organic peroxy radicals are typically denoted as RO_2 in the chemical equations and they represent compounds in which a hydrogen atom from the VOC molecule is replaced by an O_2 molecule during the VOC oxidation process.

According to Crutzen (1979), the production of tropospheric ozone in the presence of VOCs occurs by the following steps:

$$NO_2 + h\nu\ (\lambda \leq 400\ \text{nm}) \rightarrow NO + O \quad \text{(C1)}$$

$$O + O_2 + M \rightarrow O_3 + M \quad \text{(C2)}$$

$$VOC + OH + O_2 \rightarrow RO_2 + H_2O \quad \text{(C4)}$$

$$RO_2 + NO \rightarrow NO_2 + RO \quad \text{(C5)}$$

$$\text{Net reaction: } VOC + OH + 2O_2 \rightarrow RO + O_3 + H_2O$$

The compound *RO* in reaction (C5) is called an organic oxy radical (the compound has lost an oxygen atom). Suppose that the VOC in reaction (C4) is methane (CH_4). The corresponding RO_2 compound in reaction (C4) would be CH_3O_2 (called methyl peroxy radical) and the *RO* compound in reaction (C5) would be CH_3O (called methoxy radical). The molecule, *M* in chemical reaction (C2) represents any inert molecule that removes energy and balances the equation. Unlike reaction (C3), NO_2 is produced in reaction (C5) without the loss of ozone. Therefore, in the presence of VOCs, reaction (C3) is insignificant and excess O_3 is formed.

The enhancement of O_3 in polluted regions is associated with calm wind conditions and warm temperatures (Chu, 1995; Camalier et al., 2007; Haman et al., 2014). High O_3 mixing ratios are typically observed under stagnant conditions and light winds (Chu, 1995; Permadi and Oanh, 2008; Kuang et al., 2011) and in the presence of a temperature inversion or shallow boundary layer heights that trap air near the surface (Haman et al., 2014). In addition, large amounts of O_3 can be

observed in the troposphere due to stratosphere-troposphere exchange. Stratospheric intrusions during the springtime in northern Alberta increase the background level of O_3 (up to 45 ppbv). In late August, the background level drops to 25-35 ppbv (Angle and Sandhu, 1986).

The emissions of large amounts of NO (from high temperature combustion of oil, gasoline, and coal) in the vicinity of a pollution source have the potential to reduce the concentration of O_3 by titration: $NO + O_3 \rightarrow NO_2 + O_2$ (Sillman, 1999; Monks, 2005). Close to the surface, O_3 can also be removed naturally by deposition onto forest canopies and plant surfaces.

The Joint Canada-Alberta Implementation Plan for Oil Sands Monitoring (JOSM) was organized by the Canadian government to monitor the impact of oil sands emissions on the quality of air, water, land, and wildlife in the oil sands region of Alberta (Abbatt et al., 2011). In support of the JOSM a lidar from York University was installed on a Twin Otter aircraft in order to complement the main research aircraft, which was the Convair-580 from the National Research Centre Flight Research Laboratory (Gordon et al., 2015; Shephard et al., 2015; Liggio et al., 2016). This Ph.D. research project involved the development and testing of the lidar instrument, flight planning, airborne measurements, data analysis, and interpreting the lidar measurements of air pollution. The measurements were collected in the vicinity of the Athabasca oil sands industry north of Fort McMurray, Alberta as shown in Fig. 1.1.

The field campaign consisted of five flights out of Fort McMurray during the period between August 22 and August 26, 2013 and the duration of each flight was approximately four hours. A Twin Otter aircraft at an altitude of 2.4 km to 3.1 km above sea level (ASL) served as a platform for the downward directed lidar system. The flights were planned using meteorological analysis so that the flight path intersected the trajectory of air that had passed over the oil sands. Lidar measurements were taken along the upwind to downwind transects across the oil sands region and the vertical distribution of aerosol and O_3 was investigated within the surface boundary layer. The principal goal of this Ph.D. was to assess the impact of oil sands emissions on regional air quality.

The distribution of aerosol along the flight path provided information on boundary layer height in regions upwind and downwind of the oil and gas extraction facilities. These measurements were used to correct for the interference of aerosol in the lidar O_3 retrieval. The height of the boundary layer and the mixing ratio of O_3 in the lower troposphere provided useful information for improving air quality forecasts, to better understand the long range transport of pollutants in the lower troposphere, and to improve the chemistry in modelling studies.

Instruments for in situ sampling were installed on another aircraft, the Convair-580, led by Environment and Climate Change Canada (ECCC) under JOSM. In situ measurements made by ECCC were used in this study for 1) the development of an aerosol correction technique, 2) validation of lidar derived O_3 values and 3) to discriminate different sources of air pollution within the oil sands region. Chapter 2

will provide a description of the lidar instrument that was used to collect measurements from the Twin Otter aircraft, and also the instruments for in situ sampling installed on the Convair-580 aircraft. Chapter 3 will present an overview of the analysis methods that were used in this study. These methods include the O_3 retrieval from lidar measurements, the correction techniques in the O_3 retrieval due to the interference of aerosol and other atmospheric gases, corrections due to non-linearity in the signal acquisition as well as the uncertainty analysis. The process of developing the lidar system also resulted in interesting case studies of air pollution over Toronto. The results of an air pollution study with a stationary lidar system operating at York University in the summer of 2010 are presented in chapter 4. Results from the measurements of air pollution over the Athabasca oil sands region in August 2013 are shown in chapter 5. Lastly, conclusions from this research are summarized in chapter 6.

2 Measurement Technique

Differential absorption lidar systems can be used to determine the concentration of gas-phase molecules in the atmosphere. One of the first differential absorption lidar systems was used by Schotland (1964) for atmospheric measurements of water vapour profiles. Ground-based differential absorption lidar systems were used in the late 1970s for measurements of O_3 in the stratosphere (Mégie et al., 1977) and later extended to aircraft platforms for measurements of O_3 abundance in the lower troposphere (Menzies and Shumate, 1978). The vertical distribution of air pollutants such as NO_2 (Fukuchi et al., 2003), NO (Menyuk et al., 1980), and SO_2 (Xiaoqin et al., 2005) can be measured with differential absorption lidar systems operating from an aircraft or from the ground. In this chapter, the development of a lidar system for ozone and aerosol measurements will be described. Environment and Climate Change Canada's instrumentation for which supplementary measurements were used in this thesis will also be presented.

2.1 Differential Absorption Lidar System

The differential absorption lidar system that was installed on the Twin Otter aircraft transmitted four ultraviolet wavelengths along the same path into the

atmosphere and measured the backscattered radiation at the four wavelengths simultaneously. The differential absorption technique uses a pair of measurement wavelengths for the derivation of O_3. The wavelengths are chosen so that one of the wavelengths in the pair is absorbed strongly by the O_3 molecule and the other wavelength is absorbed less by the O_3 molecule. The signals at each wavelength are attenuated differently and this is used to determine the amount of ozone.

A lidar system consists of a transmitter and a receiver. The transmitter emits pulses of laser light into the atmosphere and the backscatter radiation is collected by the receiver telescope, detected, and recorded as a function of time or range. The differential absorption lidar system was previously used for aircraft lidar measurements to study ozone depletion events in the Arctic (Seabrook et al., 2013) and was modified to study air pollution during the oil sands field campaign. An additional 532 nm wavelength channel for aerosol measurements was introduced into the system.

A schematic diagram of the lidar system that was used during the oil sands 2013 field campaign is shown in Fig. 2.1. A Q-switched frequency doubled and quadrupled Nd:YAG laser emitted pulses of light at wavelengths of 532 nm and 266 nm with a pulse repetition frequency of 20 Hz. The 532 nm wavelength light was directed into the atmosphere, while the laser wavelength at 266 nm was focused into a cell of CO_2 gas at a pressure of 140 PSI in order to generate additional wavelengths in the UV range using stimulated Raman scattering (Nakazato et al., 2007).

Vibrational Raman scattering is inelastic scattering. The absorption of incident light energy temporarily excites the molecule to a virtual state and as the molecule relaxes from the virtual state to a different vibrational state (Fig. 2.2), a photon of different energy than the incident light is released. This corresponds to a shift in frequency of the scattered light. When the scattered photon has lower energy (longer wavelength) than the incident photon it is called Stokes scattering. The energy difference between the incident and the first Stokes photon is equivalent to the energy difference between the ground state and a particular vibrational state of the molecule (Hellwarth, 1963).

The process of stimulated Raman scattering is illustrated in Fig. 2.2. The Stokes photon with energy E_1 (generated from spontaneous Raman scattering) remains in the medium (i.e the CO_2 cell in Fig. 2.1) and more Stokes-I photons are generated as the incident photon (E_0) interacts with the molecule. The intensity of Stokes-I photons is amplified and they are used as incident photons for further Raman scattering to generate additional Stokes photons at the longer wavelengths.

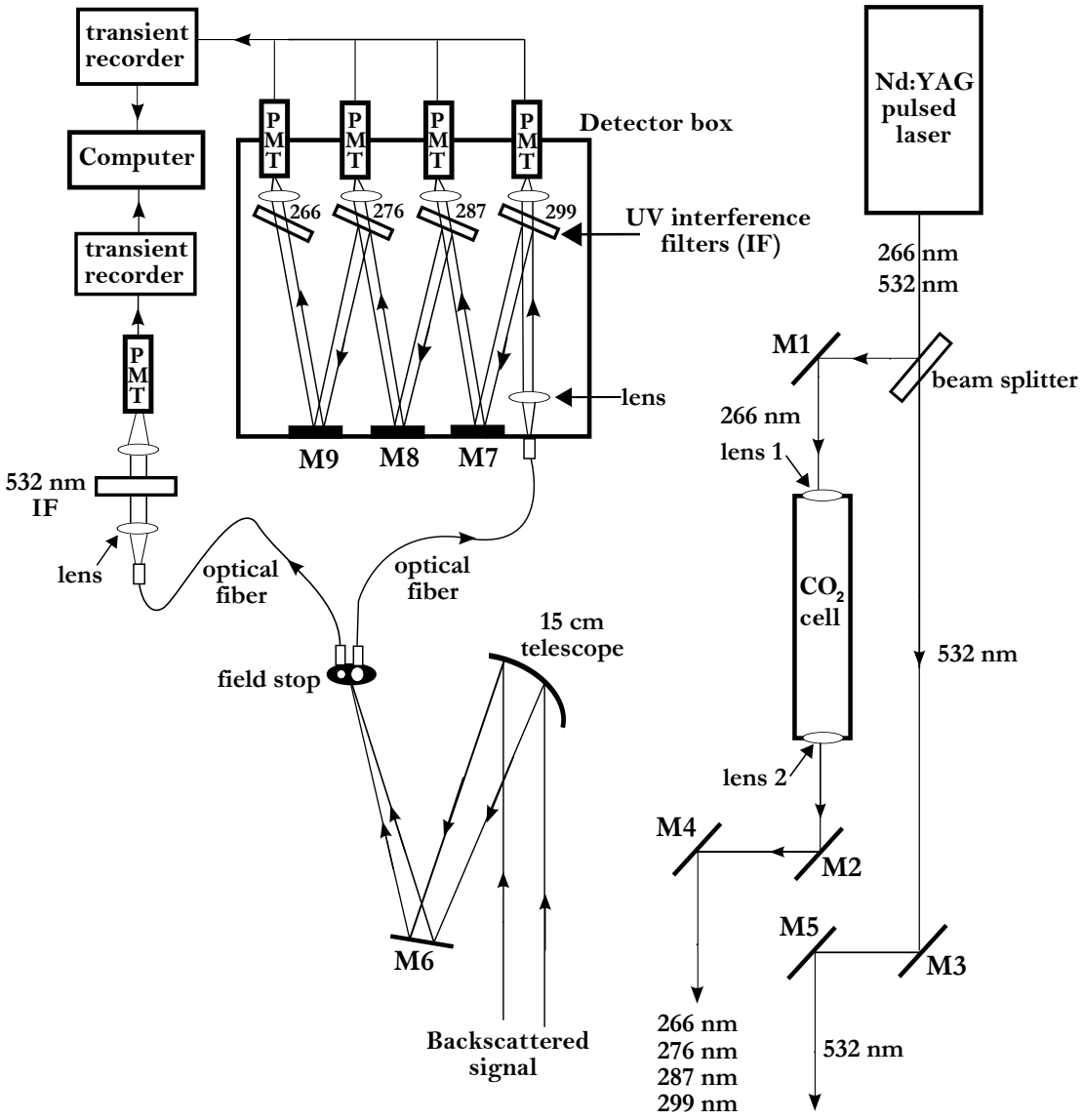

Figure 2.1: Differential absorption lidar system schematic used for measurement collection during the oil sands field campaign.

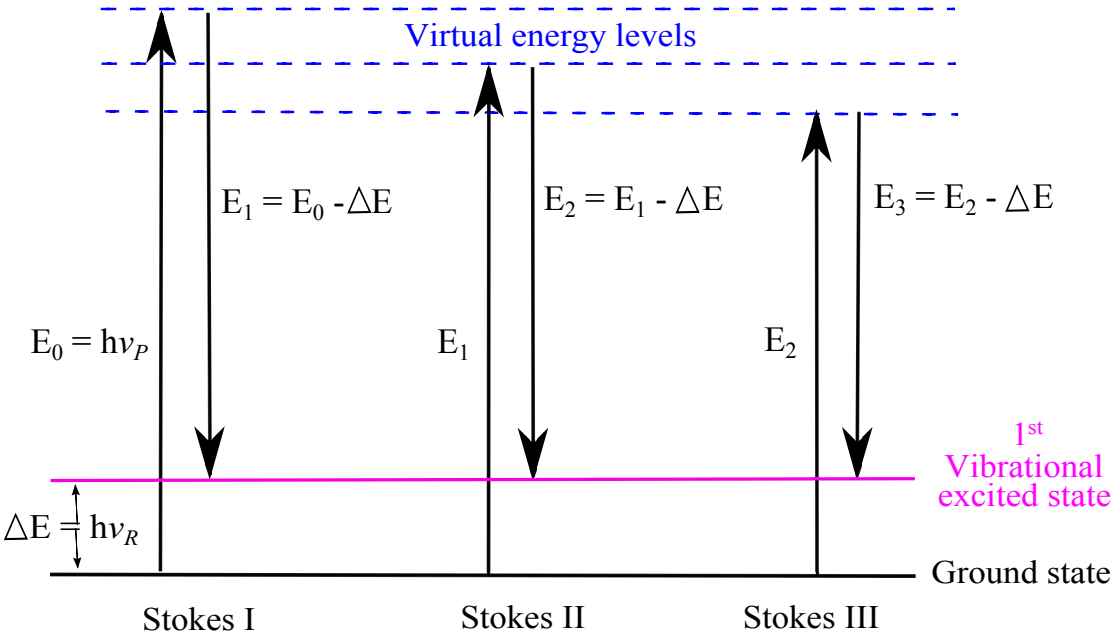

Figure 2.2: Energy level diagram of stimulated Raman scattering from a molecule (ν_R is the Raman shift frequency) by using an incident laser beam of frequency ν_P.

Carbon dioxide is a Raman active gas that has four vibrational modes. The symmetric stretching mode of a CO_2 molecule produces a Raman shift in frequency. The wavenumber for the first exited vibrational state of a CO_2 molecule depends on the C-O bond strength and the mass of carbon and oxygen atoms. For the symmetric stretching of the C-O bond, the wavenumber for the first excited vibrational state of a CO_2 molecule is 1388 cm^{-1} (Kuhn and Forsterling, 2000). Other examples of Raman active gases are CH_4, H_2 and N_2 and each gas will result in the generation of different UV wavelengths by stimulated Raman scattering.

The CO_2 Raman active medium used in the experiment results in three Stokes wavelengths produced from stimulated Raman scattering of the pulsed Nd:YAG laser

at a wavelength of 266 nm. The first, second and third generated Stokes wavelengths are 276.2 nm, 287.2 nm, and 299.1 nm respectively.

The compact and simple design of the lidar transmitter was made possible by using a single Raman cell with CO_2 gas. Other lidar measurement studies of ozone (Ancellet et al., 1989; Sunesson et al., 1994) deploy more than one Raman cell that is filled separately with Hydrogen (H_2) and Deuterium (D_2) gas. Both H_2 and D_2 are flammable gases and pose a challenge for collecting measurements of O_3 from an aircraft. Using CO_2 gas as a Raman active medium is highly beneficial for aircraft based projects because its non-flammable property makes it safe for use on aircraft and only a single cell is required to generate the multiple wavelengths that were necessary for this project.

The generated Stokes wavelengths fall within the UV Hartley band of the absorption spectrum for ozone. This absorption spectrum ranges between 200 and 300 nm and with a maximum absorption at a wavelength of 255 nm as shown in Fig. 2.3. The generated Stokes wavelengths by stimulated Raman scattering of laser light at a wavelength of 266 nm off of a CO_2 molecule are also indicated in Fig. 2.3. Figure 2.3 illustrates that the laser wavelength at 266 nm is strongly absorbed by the O_3 molecule and the generated wavelength at 299 nm is absorbed the least by the O_3 molecule. Table 2.1 lists the values of the absorption cross-section of the O_3 molecule at the generated Stokes wavelengths.

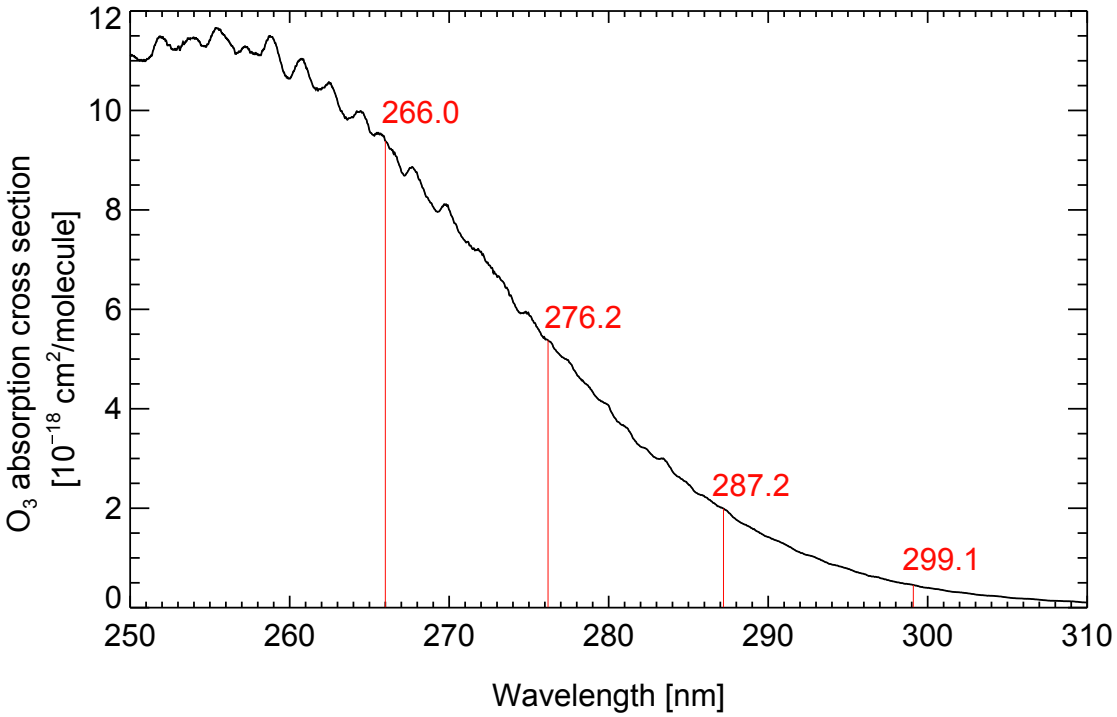

Figure 2.3: Ozone absorption cross-section as a function of wavelength in the UV Hartley band at a temperature of 300 K [HITRAN 2012 database]. The ozone absorption cross-section for the 4th harmonic of the Nd:YAG laser and the generated wavelengths that were used in this study are also indicated.

Table 2.1: Generation of the first three Stokes wavelengths by stimulated Raman scattering in CO_2 cell by using the Nd:YAG 266 nm wavelength and the corresponding ozone absorption cross-sections at a temperature of 300 K.

Stokes number	Stokes wavelength (nm)	O_3 absorption cross-section (cm^2/molecule)
I	276.2	5.38×10^{-18}
II	287.2	1.99×10^{-18}
III	299.1	0.46×10^{-18}

The wavelengths 266, 276.2, 287.2, and 299.1 nm were directed into the atmosphere along the nadir from the Twin Otter aircraft that was flying at an altitude between 2.4 and 3.1 km above sea level (ASL). The laser wavelength at 532 nm was directed independently into the atmosphere along the nadir. Two separate mirrors were used to transmit the signal at a wavelength of 532 nm and in the UV wavelength range into the atmosphere, as shown in Fig. 2.4. For this project, the measurements in the UV range were used to derive the O_3 mixing ratio and the measurements at a wavelength of 532 nm were used to detect the backscatter from aerosol.

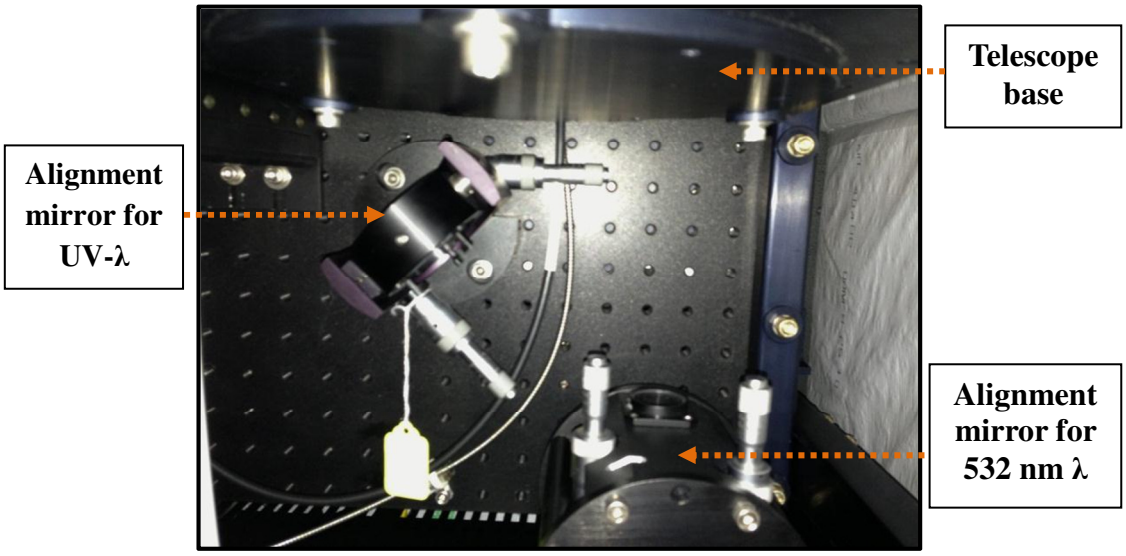

Figure 2.4: The expanded view of the alignment mirrors in Fig. 2.9 used for the transmission of 532 nm and the UV wavelengths into the atmosphere.

The lidar system receiver is also shown in Fig. 2.1. A 15 cm diameter off axis parabolic mirror was used to collect the light backscattered from molecules and aerosol particles. A field stop was placed at the focus to define a separate field of

view for the UV and 532 nm backscatter. The field stop was composed of two different sized pinholes drilled in a circular stainless steel sheet to form two separate receiver fields of view, positioned at the focal plane (approximately 500 mm from the mirror). The 0.5 mm diameter pinhole defined a field of view of 1 mrad for the 532 nm measurements and a 1 mm diameter pinhole (field of view of 2 mrad) for the UV measurements. The pinholes were placed over top of optical fibers as shown in Fig. 2.5.

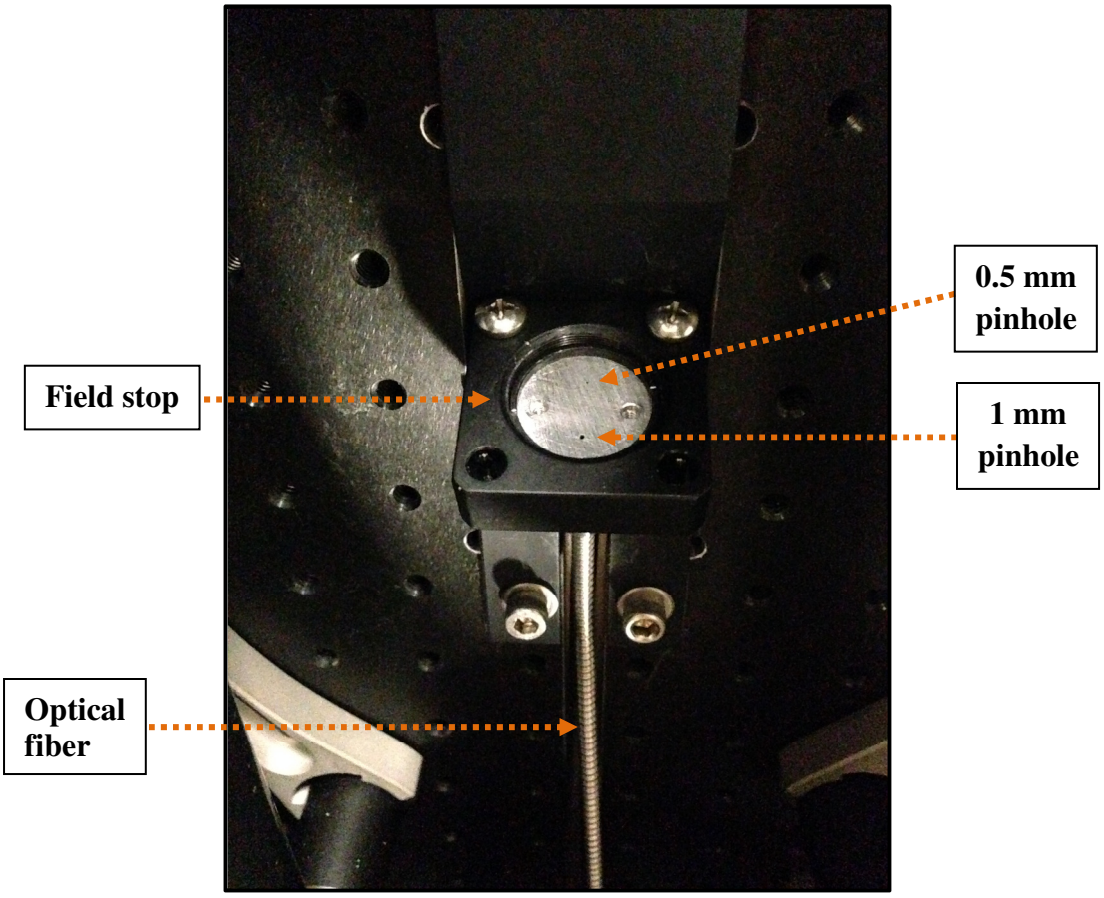

Figure 2.5: The expanded view of the lidar field stop as shown in Fig. 2.9. The second optical fiber is hidden behind the first one. The 0.5 mm pinhole is slightly too faint to be seen.

The smaller size pinhole for the measurements at a wavelength of 532 nm was used to reduce the signal from background light. Two separate 1.5 mm diameter optical fibers were positioned behind the pinholes, about 500 mm from the mirror. The 532 nm backscatter was aligned to the optical fiber corresponding to the 0.5 mm pinhole, while the UV backscatter was aligned to the fiber corresponding to the 1.0 mm pinhole.

The four UV wavelengths (266, 276.2, 287.2, and 299.1 nm) were separated in the receiver using the transmittance and reflectance from interference filters having a bandwidth of 1 nm and tilted at an angle of 7.5 degrees. The interference filters were placed in decreasing wavelength order (as shown in Fig. 2.6), such that the signal at a wavelength of 299 nm was detected first in order to avoid any losses (as it has the smallest transmitted energy and O_3 absorption), and the signal at a wavelength of 266 nm was detected last as in Fig. 2.6.

The wavelength separation box allowed up to four wavelengths to be detected. The four UV measurement wavelengths were all detected by using the detector box and the signal at a wavelength of 532 nm was detected separately. A separate interference filter and photomultiplier tube (PMT) mounted beside the UV wavelength separation box (shown in Fig. 2.7) was used to collect the backscatter signal at a wavelength of 532 nm.

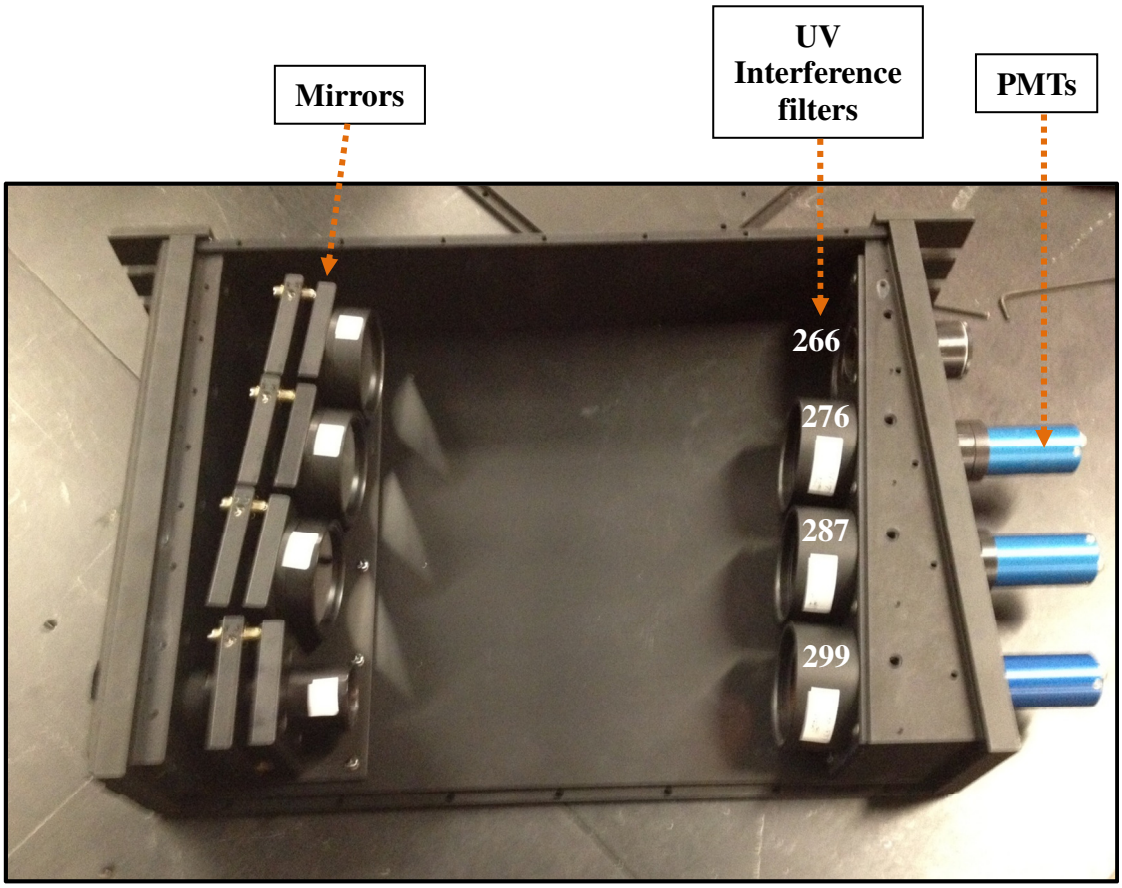

Figure 2.6: The wavelength separation box for the UV measurements. The UV wavelengths are indicated above each interference filter in the order that they were measured. The interference filter and PMT for the 266 nm measurement were not installed in this photograph.

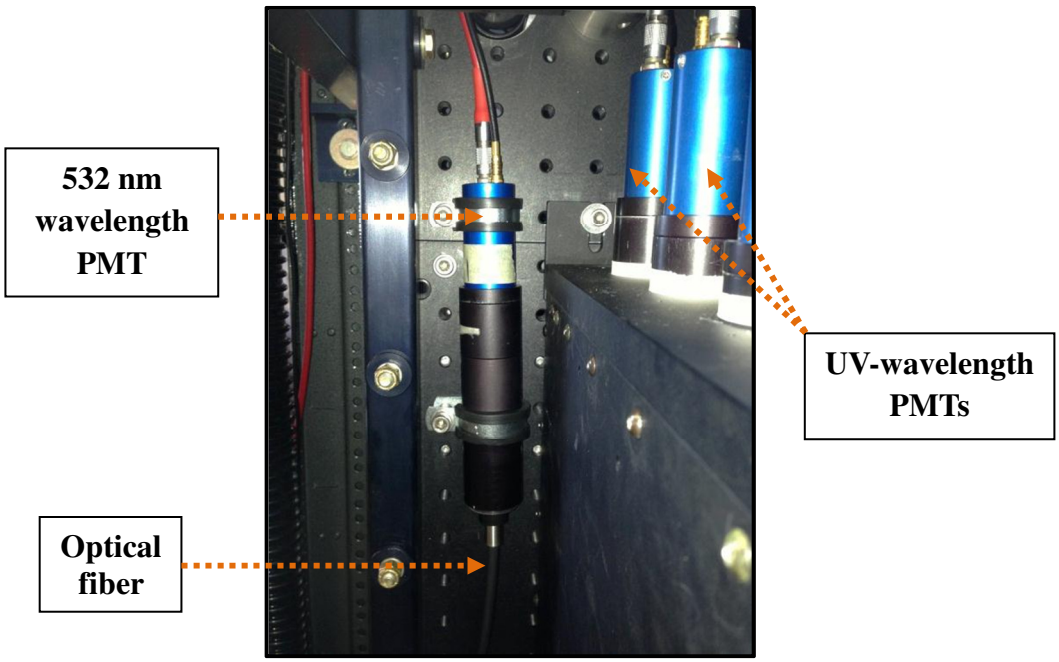

Figure 2.7: The expanded view of lidar system detectors as shown in Fig. 2.9.

Photomultiplier tubes were used to detect the backscattered light. A photomultiplier tube generates a pulse of current (converted to voltage) with each detected photon. The data acquisition electronics perform photon counting and also record the analog voltage with an analog to digital converter (ADC). The analog voltages are produced using a transimpedence amplifier and converted to a 12 bit binary number using an analog to digital converter. The combination of analog and photon counting detection was used because the lidar signal has a large dynamic range. The weak backscattered signal from distances greater than 1.8 km were recorded with photon counting and the strong backscattered signals in the near range were recorded using analog to digital conversion.

The data acquisition system consisted of transient recorders (LICEL model TR20-160) for recording the photon counting and analog signals from the PMT and a laptop (with Windows Operating System) for storing data. Four transient recorders were used for the measurements collected within the UV wavelength range and one transient recorder was used for the measurements collected at a wavelength of 532 nm. The Windows PC was equipped with software that was provided by the manufacturer (LICEL). The LICEL software has many important functions: it allows the user to adjust the transient recorder parameters (such as the amount of averaging over a user defined number of shots and the path for storing data) and it displays the acquired signal on the laptop screen.

The compact design of the differential absorption lidar system makes it suitable for installation in the aircraft. The lidar system was fitted into an aircraft rack as shown in Fig. 2.8 and Fig. 2.9. The aircraft rack includes mounts to damp external sources of vibrations. Heaters provide a controlled temperature environment for lidar operation and the covers on the aircraft rack are insulated to protect the lidar system from cold temperatures in the unpressurized aircraft. The lidar system was installed in the Twin Otter aircraft as shown in Fig. 2.10. An opening at the bottom of the aircraft allowed for the downward viewing measurements.

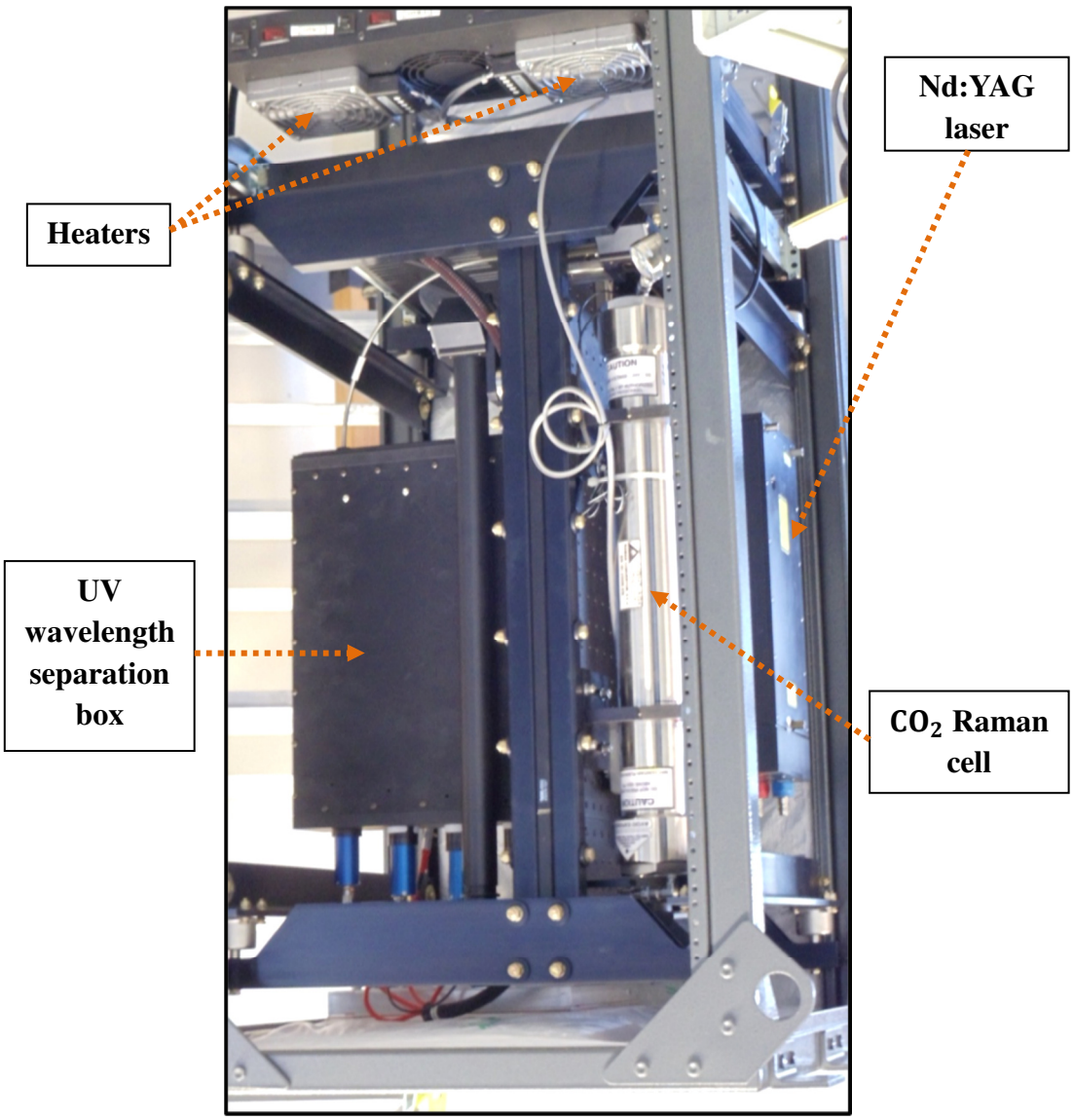

Figure 2.8: The lidar system installed in an aircraft rack. The aircraft rack is 0.635 meters in length, 0.56 meters wide, and 1.30 meters in height.

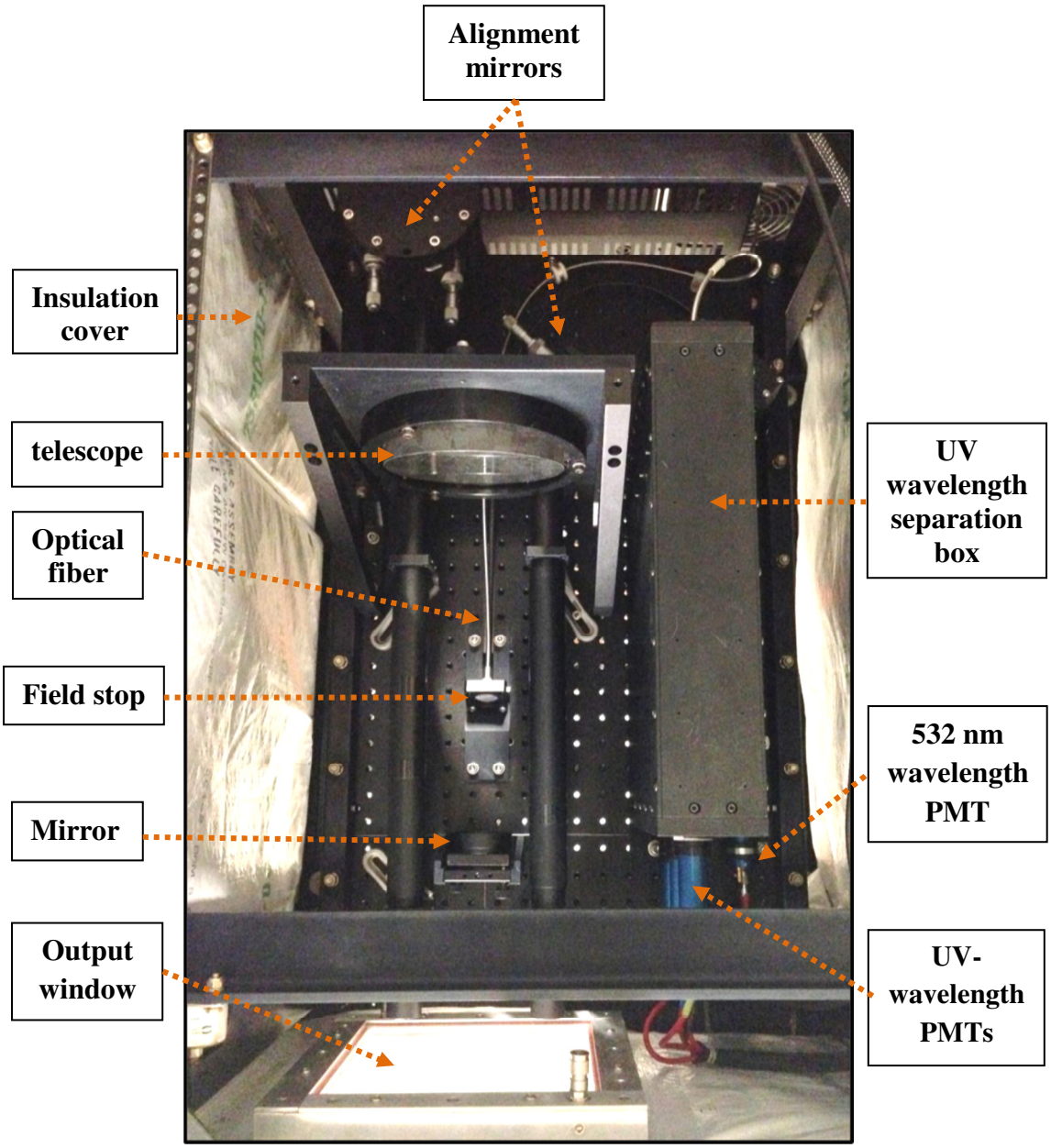

Figure 2.9: The lidar system receiver fitted into an aircraft rack.

Figure 2.10: The lidar system installed in Twin Otter aircraft.

During the Alberta field campaign, the raw data were recorded with a range gate of 3.75 m for the 532 nm signal and 7.5 m for the UV signals with hardware averaging over 200 laser shots (or 10 seconds). Table 2.2 summarizes important parameters for the differential absorption lidar system that was used during the oil sands field campaign in 2013.

Table 2.2: Specification table for the differential absorption lidar system and aircraft used during the oil sands field campaign.

Component	Specification	
Laser	Nd:YAG (CFR-800)	
Wavelength transmitted	**266 nm (Nd:YAG)** **276, 287, and 299 nm (Raman)**	**532 nm (Nd:YAG)**
Average power	0.3 W	0.07 W
Laser energy	70 mJ/pulse for 266 nm laser ouput	400 mJ/pulse for 532 nm laser output
	20 mJ/pulse for transmitted 266, 276, 287, and 299 nm	5 mJ/pulse for transmitted 532 nm
Pulse duration	10 ns	10 ns
Pulse repetition frequency	20 Hz	20 Hz
Raman Cell	CO_2 gas	
Length	0.5 m	
Diameter	0.06 m	
Pressure	140 PSI	
Material	Stainless steel	
Focal length of lenses	0.25 m	
Telescope	Off axis parabolic mirror	
Diameter	15 cm	
Focal length	50 cm	
Field stop	1 mm pinhole for UV	0.5 mm pinhole for visible
Field of view	2 mrad for UV	1 mrad for visible
Dimensions		
Output window	20 cm x 20 cm	
Aircraft rack	0.635 m x 0.56 m x 1.30 m	
Aircraft	Twin Otter	
Flight duration	4 hours	
Ceiling due to lidar system requirements	10,000 ft (or 3.1 km) above sea level	
Speed	300 km/h	

2.2 Field Experiment

The biggest advantage in studying air pollution in the oil sands region from an aircraft is the ability to travel long distances and to sample regions where there is no access from the ground. Collecting measurements from an aircraft provides the flexibility of making changes to the flight path based on current environmental conditions. The altitude of the Twin Otter aircraft during the oil sands field campaign was usually 3 km ASL. The ceiling of 10,000 ft (or 3 km) ASL was because the lidar electronics are not rated for lower pressure and electrolytic capacitors will fail at low pressure.

A software package for analyzing simultaneous real-time measurements of aerosol and O_3 height profiles on the Twin Otter aircraft was developed as part of this project. The program provided a contour plot of the backscattered signal from aerosol scattering and the O_3 mixing ratio as measurements were being collected and the program automatically updates the results as new measurements are recorded. The unique visualization program presented simultaneous line plots of aerosol backscatter and O_3 mixing ratio at the location the cursor was placed over the contour plot for profile-by-profile analysis on the aircraft. The program also contained tabs that would alternate between raw and processed data. The in-flight visualization tool was useful for preliminary data analysis and allowed real time decisions on the flight track based on current measurements. A screenshot of the visualization tool's display on one of the Twin Otter flights is shown in Fig. 2.11.

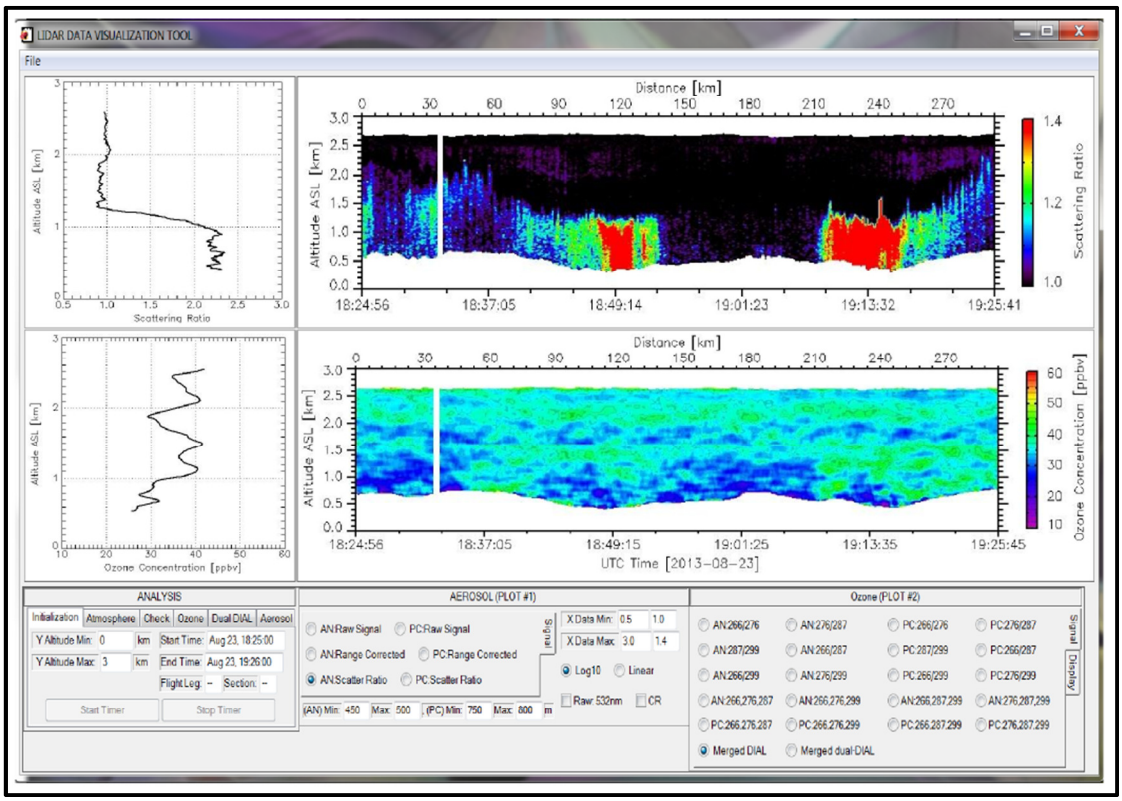

Figure 2.11: A screenshot of the visualization tool display for analyzing simultaneous real-time measurements of aerosol and ozone in flight.

An inertial measurement unit was installed in the Twin Otter aircraft that provided the latitude and longitude coordinates as well as the altitude, roll, pitch, yaw, and heading of the aircraft. For the measurements shown in this dissertation, the pitch and roll data from the inertial measurement unit were used to correct the height in the lidar data on a profile-by-profile basis.

Forward air trajectories (using the HYSPLIT model (Draxler and Hess, 1998)) from the oil sands location were computed twice a day (the night before and early morning, prior to the flight) to analyze the direction of wind. The direction of wind in the oil sands region aided with planning the flight tracks. The flight tracks were

designed to collect measurements along a line (either oriented parallel or perpendicular to the direction of wind) that includes regions upwind and downwind from the oil sands pollution sources. In some cases, the flight tracks extended more than 100 km downwind to sample the polluted air mass. The longitude and latitude coordinates of the flight track were provided to the pilots and this information was used to navigate the aircraft.

2.3 In Situ Instrumentation

This section will describe instruments for particle size, O_3, NO_2 and NO measurements that were installed on the Convair-580 aircraft that was operated for ECCC as part of the Joint Oil Sands Monitoring Program. More information on ECCC's aircraft campaign can be found in Gordon et al. (2015) and Liggio et al. (2016). The Convair-580 aircraft collected measurements within and above the boundary layer in the Athabasca oil sands region. These in situ measurements were used in the analysis of lidar measurements and for the validation of lidar derived O_3 values.

2.3.1 Measurement of Particle Size

Particle size distribution measurements were made with an Ultra-High Sensitivity Aerosol Spectrometer (UHSAS) and a Forward Scattering Spectrometer Probe (FSSP, model 300). Particles with diameters between 0.06 and 1 μm were

sampled with the UHSAS instrument and larger particles ranging in diameter from 0.3 to 20 μm were measured with the FSSP-300 instrument.

The FSSP-300 was mounted on the wing of the Convair-580 aircraft, whereas the UHSAS was rack mounted in the fuselage. Air samples for the UHSAS instrument were drawn in with a shrouded diffuser inlet. The UHSAS instrument uses a laser beam (at a wavelength of 1054 nm) to illuminate a sample of air. Single particles in the air sample will scatter light in all directions and only the light scattered perpendicular to the particle flow (between an angle of 33° and 147°) is collected by two different photodiodes. An avalanche photodiode is used for collecting the scattered light from particles in the smaller size range and a PIN photodiode is used for collecting the light scattered from particles in the larger size range. The intensity of scattered light is used to determine the size of the particle (Droplet Measurement Technologies Inc., 2013).

The FSSP-300 instrument was mounted on the wing of the Convair-580 aircraft and unlike the UHSAS instrument; the particles were sampled in the free airstream without the use of an inlet. Single particles pass through a laser beam and only the light scattered in the forward direction (between an angle of 4° and 12°) is collected onto a beam splitter. The scattered light is divided into two by a beam splitter and detected by individual photodetectors. One photodetector is masked with a 0.25 mm wide slit aperture, while the other photodetector is unmasked. The signal from the masked photodetector is compared to the unmasked detector for particle sizing. The particle size is computed only if the signal from the masked photodetector is greater

than or equal to the signal from unmasked detector. Particles are assumed to be spherical and a refractive index of 1.58 is used in the particle size calculation (Baumgardner et al., 1992). The particle size is derived from the measured intensity of the scattered light in the forward direction. The angular distribution of scattered light by the particle is predicted by Mie scattering theory. The amount of light scattered by the particle is proportional to its size. For larger particles, more light will be scattered in the forward direction relative to the backward direction.

2.3.2 Measurement of Ozone

Ozone measurements were collected on the Convair-580 aircraft with a Thermo Scientific 49*i* analyzer. The unit contains a low pressure mercury lamp that provides UV light at a wavelength of 254 nm. Ambient air is drawn into the instrument (by a rear-facing inlet located at the top of the Convair-580) and the air sample is divided into two channels. In one of the channels, the air sample flows through an ozone scrubber cell (which removes O_3 molecules from the sample) and the other cell contains the sample of air. The scrubbed air alternates between the cells every five seconds. Ultraviolet light propagates through both cells simultaneously and photodiode detectors placed at the opposite end measure the intensity of light through each cell. The light detected from the cell scrubbed of O_3 provides the initial intensity value (I_0). The light detected from the cell containing the sample of air will be attenuated by O_3 molecules and the intensity will be I. Ozone concentrations, N, can be found by using the Beer-Lambert law for the intensities of light measured by the photodiode:

$$I = I_0 exp(-kLN)$$

Where k is the molecular absorption coefficient of O_3 (k = 308 cm^{-1} at a temperature and pressure of 0°C and 101.3 kPa respectively) and L is the length of the cell, 0.38 m (Thermo Fisher Scientific Inc., 2007).

2.3.3 Measurement of Nitrogen Species

In situ measurements of NO and NO_2 were collected on the Convair-580 aircraft with a Thermo Scientific 42*i* analyzer. Ambient air is drawn into the instrument by a rear-facing inlet located at the top of the Convair-580. The air sample is split into two streams by a solenoid value. One stream of air is used to determine the NO concentration and the other air stream is used to determine the concentration of NO_x. In order to determine the concentration of NO_x in an air sample, the air stream passes through a heated NO_2 to NO converter. The NO_2 to NO converter contains an element (Molybdenum) that converts NO_2 to NO and the air stream now consists of total amount of NO_x. Both air streams alternatively flow to the reaction chamber.

In a separate inlet, dry air is drawn into the Thermo Scientific 42*i* analyzer and flows through an ozonator. The ozonator generates O_3 molecules that are required for the measurement of NO and NO_x species. The ozone rich air then flows to the reaction chamber.

In the reaction chamber, O_3 molecules react with NO molecules present in each air stream to produce electronically excited NO_2 molecules. As the excited NO_2 molecules decay to their ground state, infrared light is emitted ($NO + O_3 \rightarrow NO_2 + O_2$

+ hν) and detected by a photomultiplier tube. The intensity of infrared light emission is proportional to the NO concentration in one air stream and NO_x concentration in the other air stream. The concentration of NO_2 is then calculated as: $NO_2 = NO_x - NO$ (Thermo Fisher Scientific Inc., 2007).

2.4 Ground Based Lidar System

A ground based lidar system operated by Environment and Climate Change Canada collected lidar measurements at wavelengths of 1064 nm and 532 nm (with a pulse energy of 150 mJ and a pulse repetition frequency of 10 Hz). The lidar system was housed in a trailer, located at 57.14 °N and 111.6 °W, as shown in Fig. 2.12 (close to Ft. McKay) and operated on a daily basis during the two week campaign period in August 2013. The ground based lidar system provided vertical profiles of backscatter up to 15 km above ground.

The parallel and perpendicular components of linear polarization in the backscatter at a wavelength of 532 nm were detected to obtain the depolarization ratio and this will be discussed in section 5.1.2.1. The depolarization ratio is a useful tool for discriminating particles of different shapes. It is defined as the ratio of the perpendicular to the parallel component (relative to the transmitted polarization) of the backscattered radiation. For example, hexagonal ice crystals can cause a depolarization ratio greater than 0.5 whereas spherical water droplets result in a small (almost zero) depolarization ratio. In this dissertation, the linear depolarization ratio in

regions of aerosol backscatter will be used to discriminate among the different pollution sources in the vicinity of the oil sands region.

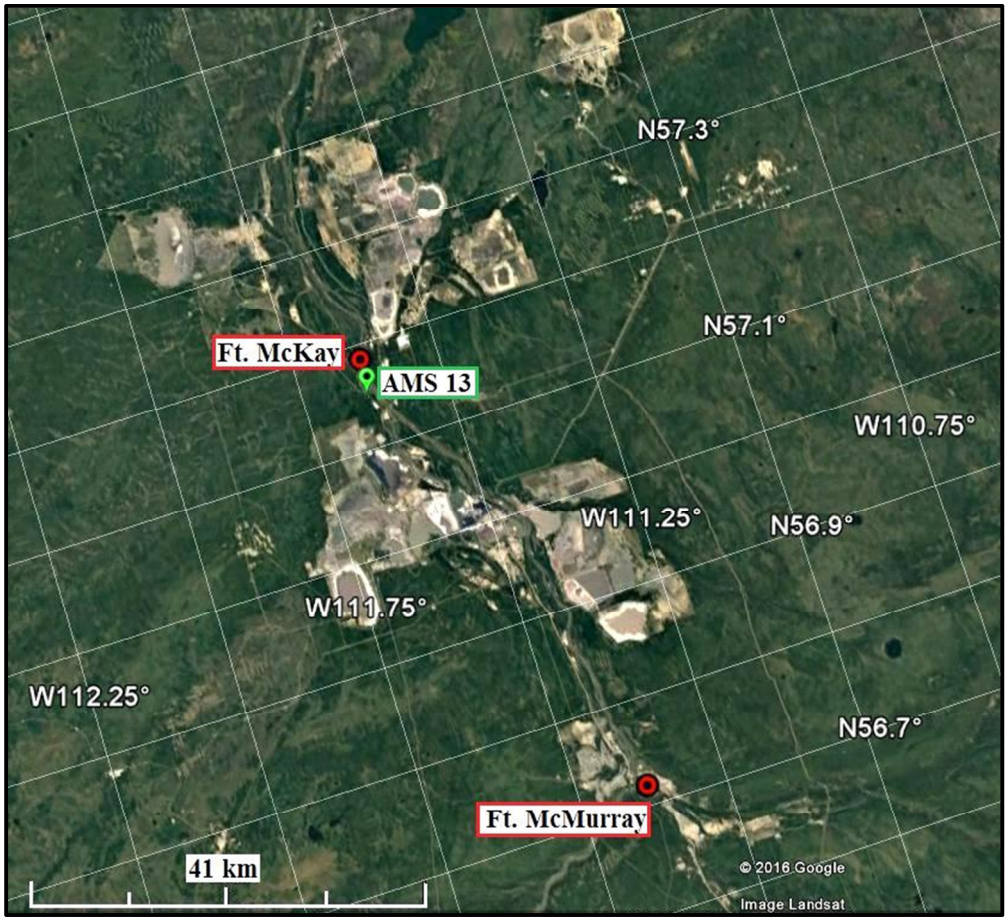

Figure 2.12: Map of the Fort McMurray oil sands region. The location of the ground based lidar is indicated as AMS 13.

3 Analysis

Lidar measurements at wavelengths of 266, 276, 287, 299, and 532 nm were obtained over the altitude range from the Twin Otter aircraft position to the ground. Measurements in the UV wavelength range were used to derive the O_3 mixing ratio and measurements at a wavelength of 532 nm were used to retrieve aerosol optical properties and to correct for the interference of aerosol in the lidar O_3 retrieval. In this chapter, the analysis method for O_3 retrieval will be described, as well as a correction for the interference of aerosol and other atmospheric gases. Additional corrections that were applied to the lidar measurements to account for detection non-linearity will be described as well as the uncertainty analysis.

3.1 Lidar Equation

For single scattering and elastic processes within the UV wavelength range, the backscattered lidar signal, $P_\lambda(z)$ (in number of photons), as a function of range, z, is described as

$$P_\lambda(z) = Q\, P_0 \left(\frac{A}{z^2}\right) \Delta z\ \beta(\lambda, z)\ exp\left[-2\int_0^z \left(\sigma_\lambda\, N(z') + \alpha(\lambda, z')\right) dz'\right] \qquad (1)$$

In equation (1), the number of photons in a laser pulse (transmitted into the atmosphere) is represented by P_0. The optical throughput and detector efficiency is represented by Q. The lidar range z is defined as $z = ct/2$ and it is the distance that the photons travel (at the speed of light, c) during the time, t, after the laser pulse was emitted. The solid angle of the lidar receiver as viewed from range z is A/z^2, where A represents the area of the receiver telescope. The range bin Δz is defined as $\Delta z = c\Delta t/2$ where Δt is the sampling interval. Typically, the constants Q, P_0, A, and Δz are combined into a single constant, C_λ, to express the lidar equation in a simple way.

The backscatter coefficient, $\beta(\lambda, z)$, is the fraction of photons in the laser light pulse that are scattered back to the receiver per unit length through the atmosphere and per unit solid angle. Physically, one can think of the backscatter coefficient as the efficiency of particles to scatter light in the backwards direction. The backscatter coefficient is dependent upon the size, type, and number of scattering particles in the atmosphere. It is equal to the product of particle number density, N_p (in units of particles/m^3), and the differential scattering cross-section for backward scattering at a specific wavelength, $d\sigma(\lambda,\pi)/d\Omega$ (in units of m^2 per sr per particle):

$$\beta(\lambda, z) = \sum_j N_{p,j}(z) \frac{d\sigma_j(\lambda, \pi)}{d\Omega} \tag{2}$$

The summation in equation (2) is computed over all types of scattering species, j, in the atmosphere encountered by a pulse of laser light. This includes scattering from various molecules and aerosol particles.

The final term in the lidar equation is the exponential term. The exponential term in equation (1) represents the round trip transmittance of the laser pulse between the ground and range z and it originates from the Beer-Lambert law: as the laser pulse (with incident intensity, I_0) propagates through a certain distance in the atmosphere (dz), the transmitted intensity of the laser light (I_λ) becomes weaker due to scattering and absorption by particles and molecules in the atmosphere. The amount of light attenuated depends on the properties of the atmospheric medium (particle number density, N_p, and the scattering cross-section of particles in the medium, $\sigma(\lambda)$). The Beer-Lambert Law is a differential equation that relates the attenuation of light to the characteristics of the medium:

$$\frac{dI_\lambda}{I_\lambda} = -\sigma(\lambda)\, N_p(z)\, dz \tag{3}$$

The product $\sigma(\lambda)N_p(z)$ in equation (3) is referred to as the extinction coefficient: $\alpha(\lambda, z) = \sigma(\lambda)N_p(z)$. The solution to the differential equation in (3) is

$$I_\lambda(z) = I_\lambda(0) exp\left[-\int_0^z \alpha(\lambda, z)\, dz\right] \tag{4}$$

The extinction coefficient, $\alpha(\lambda, z)$, in equation (1) represents the fractional decrease in the laser pulse intensity per unit length in the atmosphere due to scattering. The extinction coefficient is proportional to the particle number density, to the square of the equivalent area radius of the particle, R_a^2, and to the particle extinction efficiency, Q_{ext}:

$$\alpha(\lambda, z) = N_P(z)\, \pi\, {R_a}^2\, Q_{ext}(m, R_a, \lambda) \quad (5)$$

Equation (5) uses the equivalent area radius of the particle to calculate the extinction coefficient. Equation (5) is an approximation to equation (17). The extinction efficiency for a single particle with radius equal to the equivalent area radius and a refractive index, m, at the measurement wavelength, λ, is $Q_{ext}(m, R_a, \lambda)$ in equation (5). It will be shown in section 3.3.1.3 that this approximation provides a simple way to calculate the number density of aerosol as a function of height.

The laser pulse energy is not only lost from the beam to scattering processes but also to absorption by other gaseous molecules in the atmosphere that have absorption bands in the UV measurement wavelength range. For this experiment, the molecule under investigation is O_3 with an absorption cross-section of σ_λ. Temperature-dependent O_3 absorption cross-sections were obtained from the HITRAN 2012 database (Rothman et al., 2013). The number density of O_3 molecules in the atmosphere is represented by $N(z)$ in equation (1) and the product, $\sigma_\lambda\, N(z)$, represents the fractional decrease in the laser pulse intensity per unit length due to the absorption by O_3.

The backscatter and extinction coefficients contain information on atmospheric properties. A challenge in the analysis of the lidar signal is that there are two unknown parameters ($\beta(\lambda,z)$ and $\alpha(\lambda,z)$) in one equation. This can be solved by assuming a simple relationship between the backscatter and the extinction coefficient by using a quantity called the lidar ratio, S:

$$S = \frac{\alpha(\lambda, z)}{\beta(\lambda, z)} \tag{6}$$

The importance of the lidar ratio will be explained in section 3.3.1.2.

Both the backscatter and extinction coefficients can be separated into molecular and aerosol components:

$$\beta(\lambda, z) = \beta_{aerosol}(\lambda, z) + \beta_{molecule}(\lambda, z) \tag{7}$$

$$\alpha(\lambda, z) = \alpha_{aerosol}(\lambda, z) + \alpha_{molecule}(\lambda, z) \tag{8}$$

The molecular component of the backscatter and extinction coefficient was calculated from atmospheric measurements of temperature, *T*, and pressure, *P*, by using radiosonde (weather balloons) profiles launched in Edmonton, AB (approximately 450 km away from Ft. McMurray):

$$\beta_{molecular}(\lambda, z) = \frac{P(z)}{k_B\, T(z)} \cdot \frac{d\sigma_{air}(\lambda, \pi)}{d\Omega} \tag{9}$$

$$\alpha_{molecular}(\lambda, z) = \frac{8\pi}{3} \cdot \beta_{molecular}(\lambda, z) \tag{10}$$

The molecular backscatter coefficient (equation (9)) is expressed as a product of the Rayleigh differential backscatter cross-section for air, $d\sigma_{air}(\lambda,\pi)/d\Omega$, and the density of air. The parameter k_B in equation (9) is Boltzmann's constant. Radiosonde measurements were obtained from the University of Wyoming, Department of

Atmospheric Sciences website: (http://weather.uwyo.edu/upperair/-sounding .html). The atmospheric density measurements nearest in time to the lidar operation time were used to calculate the molecular component of the backscatter and extinction coefficients.

At a wavelength of 532 nm, the value for the O_3 absorption cross-section is 2.9×10^{-21} cm^2/molecule (Bogumil et al., 2003). This value is 10^3 times smaller than the absorption cross-sections at the UV wavelengths. For single and elastic scattering at a wavelength of 532 nm, the product $\sigma_{532nm}\, N(z)$ has an insignificant contribution to the attenuation of the lidar signal and can be neglected in equation (1). Equation (1) can be reduced to express the lidar signal as a function of range at a wavelength of 532 nm:

$$P_{532}(z) = \frac{C_{532}}{z^2}\, \beta(532, z)\, exp\left[-2\int_0^z \alpha(532, z')\, dz'\right] \tag{11}$$

An example of the lidar signal at a wavelength of 532nm (for a downward-directed lidar system) is shown in Fig. 3.1(a).

In this study, the extinction coefficient at a wavelength of 532 nm (*α(532,z)* in equation (11)) will be derived for the aerosol analysis. The retrieval of the aerosol extinction coefficient was achieved by the method of Fernald (Fernald, 1984) and is described in more detail in Appendix 1.

The aerosol extinction coefficient profile derived from the measurement in Fig. 3.1(a) is shown in Fig. 3.1(b). The aerosol extinction coefficient between 0.4 km and

1.4 km ASL in Fig. 3.1(b) is due to scattering from particles that are mixed up from the surface in the boundary layer. As solar radiation heats the surface of the earth, convective air motions generate thermal plumes that cause particles to mix vertically within the surface boundary layer. The thermal plumes rise until an inversion layer is encountered. An inversion layer is a region of the atmosphere where warmer air lies above cooler air and this prevents further mixing of particles higher into the troposphere. The top height of the boundary layer is determined by a sharp decrease in the concentration of particles (or by an increase in temperature). In Fig. 3.1(b), a decrease in the amount of scattering (from particles) is observed at 1.4 km ASL and this altitude represents the height of the top of the boundary layer. Above the boundary layer, the extinction coefficient values are small (< 0.01 km^{-1}) and there is minimal scattering from particles. The region above the boundary layer is called the free troposphere.

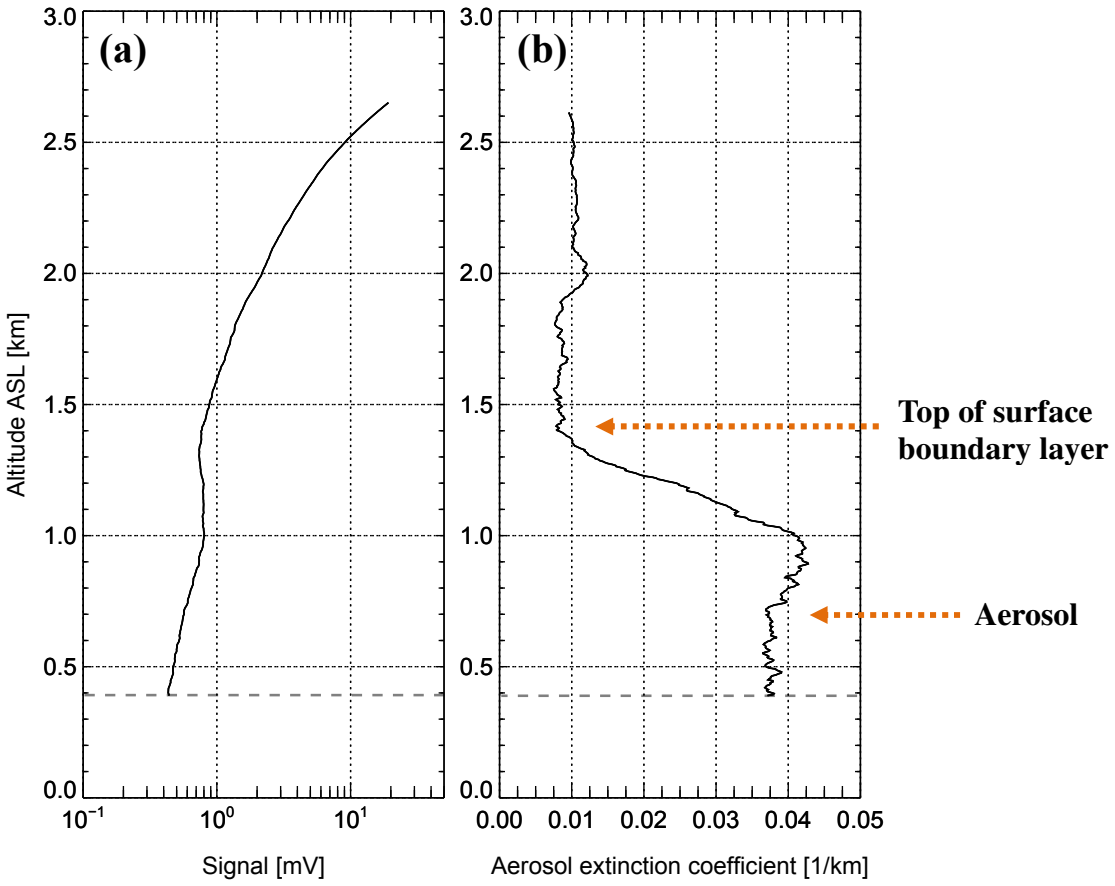

Figure 3.1: (a) Lidar measurement at a wavelength of 532 nm for a downward-directed system, and **(b)** the derived aerosol extinction coefficient at a wavelength of 532 nm. The dashed line represents the height of the ground. The measurements shown here were collected on August 23, 2013 as the Twin Otter flew directly above the Fort McMurray oil sands industry.

In order to reduce the measurement noise in the lidar backscatter signal before signal processing, the raw signal was averaged with vertical boxcar smoothing over 23 m and 45 m for measurements collected at the wavelength of 532 nm and within the UV wavelength range respectively. Complete overlap between the transmitted laser pulses and the field of view of the telescope occurred at a distance of 300 m (below the aircraft) and signals recorded closer to the aircraft were not used in the

analysis. The background skylight contribution was removed from the lidar signal by averaging the last 1.5 km of the profile (where there was no signal) and subtracting the average value from the entire profile. This is graphically shown in Fig. 3.2.

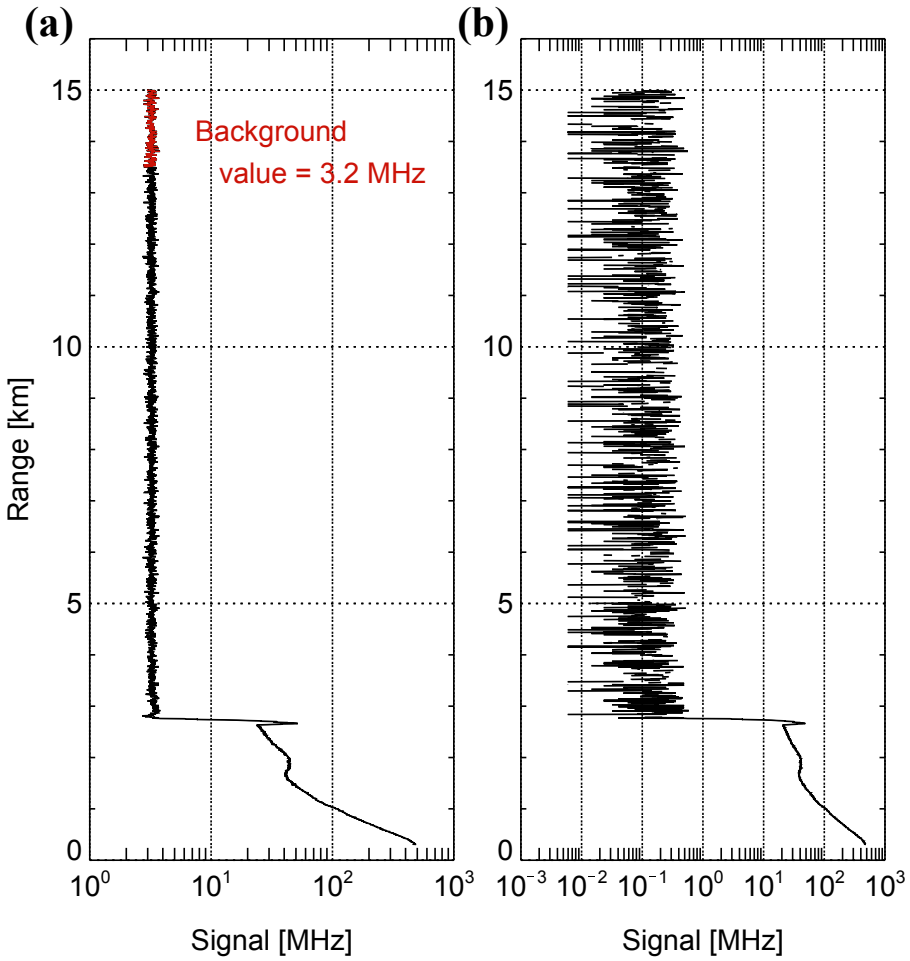

Figure 3.2: Lidar measurement at a wavelength of 532 nm as a function of range. **(a)** The raw signal profile showing the region for calculating the background contribution. **(b)** The signal profile with the background removed. The measurements shown here were collected on August 23, 2013 as the Twin Otter flew directly above the Fort McMurray oil sands industry.

3.2 The Differential Absorption Lidar Equation

The differential absorption lidar technique was used to determine the mixing ratio of O_3. When laser light pulses at two closely spaced UV wavelengths are transmitted into the atmosphere, the measured backscatter radiation will be different at the two wavelengths. The measurement wavelength that is strongly absorbed by the O_3 molecule will have a backscatter signal that decreases more rapidly with distance than the signal at a wavelength that is not as strongly absorbed. An example of this concept is shown in Fig. 3.3. In Fig. 3.3, the backscattered signal decreases more rapidly as a function of range at a wavelength of 266 nm as compared to the backscattered signal at a wavelength of 276 nm. This is because the absorption cross-section at a wavelength of 266 nm is greater than at a wavelength of 276 nm, as shown in Fig. 2.3.

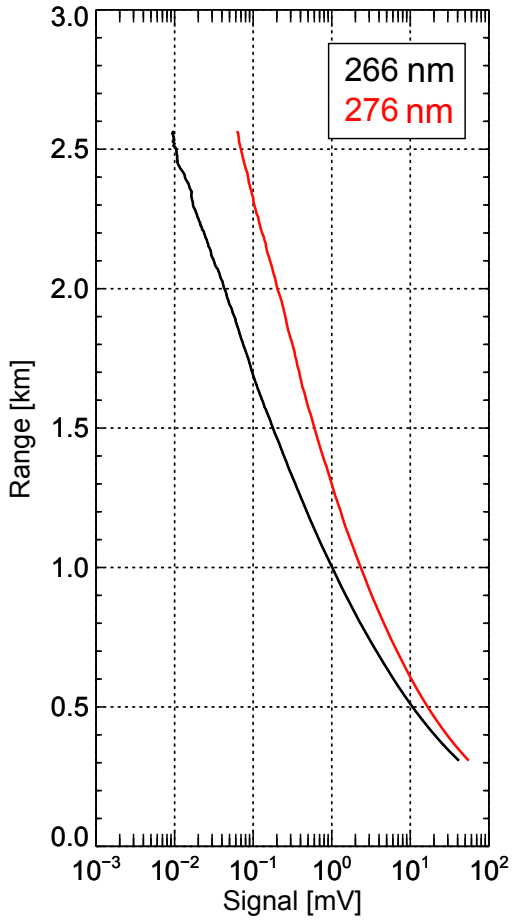

Figure 3.3: Raw lidar signal at a wavelength of 266 and 276 nm plotted as a function of range.

Equation (1) can be written out twice, one for the measurement wavelength that is strongly absorbed by the O_3 molecule (denoted as the ON wavelength, λ_{ON}) and the other measurement wavelength that is less absorbed by the O_3 molecule (called the OFF wavelength, λ_{OFF}). Taking the ratio of the ON signal to the OFF signal results in:

$$\frac{P_{\lambda_{ON}}(z)}{P_{\lambda_{OFF}}(z)} = \frac{\frac{C_{\lambda_{ON}}}{z^2}\,\beta(\lambda_{ON},z)\,exp\left[-2\int_0^z \alpha(\lambda_{ON},z')\,dz'\right]}{\frac{C_{\lambda_{OFF}}}{z^2}\,\beta(\lambda_{OFF},z)\,exp\left[-2\int_0^z \alpha(\lambda_{OFF},z')\,dz'\right]} \tag{12}$$

The range dependence in equation (12) cancels out. The extinction coefficient in equation (12) can be expressed as the sum of all loss processes that cause a reduction in the laser beam intensity. The losses include 1) absorption by atmospheric gaseous molecules within the measurement UV wavelength range and 2) scattering of laser light by aerosol and air molecules in the atmosphere. Thus, the extinction coefficient in equation (12) can be represented as the sum of all of these processes:

$$\alpha(\lambda, z) = \alpha'(\lambda, z) + \sigma_{O_3}(\lambda) N_{O_3}(z) + \sum \sigma_{gas}(\lambda)\, N_{gas}(z) \tag{13}$$

Molecules other than O_3 that absorb UV radiation within the wavelength range 266 – 299 nm are SO_2 and NO_2 (in the order of greatest to least absorption strength). The parameters expressed as the variables $\sigma_X(\lambda)$ and $N_X(z)$ in equation (13) represent the absorption cross-sections of X-molecules and their corresponding number density (molecules/m^3) in the atmosphere. The parameter $\alpha'(\lambda,z)$ represents the extinction of light from molecules and aerosol.

The extinction coefficient expressed in equation (13) was substituted into equation (12). The end goal is to isolate for the number density of ozone ($N_{O_3}(z)$) and this was accomplished by taking the natural logarithm of both sides in equation (12) and taking the derivative with respect to height as shown in equation (14). The ratio of the lidar constants in equation (12) (and the natural logarithm of this ratio) is a constant with range. The term involving the derivative with respect to range of the logarithm of the lidar constant ratio then drops out. This is an advantage of this

technique as one doesn't need to have an absolute calibration of the system in order to calculate the number density of O_3 in the atmosphere.

$$\begin{aligned} &\frac{d}{dz} ln\left(\frac{P_{\lambda_{ON}}(z)}{P_{\lambda_{OFF}}(z)}\right) - \frac{d}{dz}\ ln\left(\frac{\beta(\lambda_{ON},z)}{\beta(\lambda_{OFF},z)}\right) \\ &= -2\left(\left(\alpha'(\lambda_{ON},z) - \ \alpha'(\lambda_{OFF},z)\right)\right. \\ &+ \left(\sigma_{O_3}(\lambda_{ON})N_{O_3}(z) - \sigma_{O_3}(\lambda_{OFF})N_{O_3}(z)\right) \\ &\left.+ \left(\sum \sigma_{gas}(\lambda_{ON})\, N_{gas}(z) - \sum \sigma_{gas}(\lambda_{OFF})\, N_{gas}(z)\right)\right) \end{aligned} \tag{14}$$

By rearranging equation (14), the number density of O_3 as a function of range was isolated as follows:

$$N_{O_3}(z) = \ N_l(z) + \ N_b(z) - \ N_e(z) - \sum N_g(z) \tag{15}$$

$$N_l(z) = \ \frac{1}{2}\ \frac{-1}{\Delta\sigma_{O_3}}\ \frac{d}{dz}\left[ln\left(\frac{P(\lambda_{ON},z)}{P(\lambda_{OFF},z)}\right)\right] \tag{15a}$$

$$N_b(z) = \frac{1}{2}\ \frac{1}{\Delta\sigma_{O_3}}\ \frac{d}{dz}\left[ln\left(\frac{\beta(\lambda_{ON},z)}{\beta(\lambda_{OFF},z)}\right)\right] \tag{15b}$$

$$N_e(z) = \ \frac{\alpha'(\lambda_{ON},z) - \ \alpha'(\lambda_{OFF},z)}{\Delta\sigma_{O_3}} \tag{15c}$$

$$N_g(z) = \frac{(\sigma_{gas,ON} - \ \sigma_{gas,OFF})}{\Delta\sigma_{O_3}}\ N_{gas}(z), \qquad gas = SO_2\ and\ NO_2 \tag{15d}$$

$$\text{Where } \Delta\sigma_{O_3} = \ \left(\sigma_{O_3,ON} - \ \sigma_{O_3,OFF}\right)$$

In equation (15), the units of O_3 number density are in molecules of O_3 per m^3. In order to obtain O_3 mixing ratios in parts per billion by volume (ppbv), the number

density of O_3 was divided by the number density of air and scaled by a factor of $1x10^9$. The number density of gaseous molecules in the atmosphere such as, SO_2 and NO_2 are represented in equation (15) by $N_{gas}(z)$. These molecules have strong absorption cross-sections in the UV wavelength range (as shown in Fig. 3.9) and will be discussed in more detail in section 3.3.2.

The term $N_l(z)$ in equation (15) represents the O_3 number density calculated from the lidar return. The terms $N_b(z)$ and $N_e(z)$ in equation (15) are corrections for the wavelength dependence in the backscatter and extinction coefficients respectively. When insignificant amounts of aerosol are present in the atmosphere, term $N_b(z)$ is very small and the O_3 mixing ratio can be derived quite accurately by using $N_l(z)$ and applying an additional correction for the molecular component of differential extinction ($N_e(z)$ in equation (15)).

The terms $N_b(z)$ and $N_e(z)$ in equation (15) are correction terms and are applied for the retrieval of O_3 in regions of spatially distributed and inhomogeneous aerosol. Not only does the interference of aerosol need to be taken into account, but other gaseous molecules that are present in the atmosphere that have absorption bands in the same wavelength region as O_3 also need to be considered. For example, SO_2 and NO_2 molecules absorb UV radiation between the measurement wavelength range 266 and 299 nm. The term $N_g(z)$ in equation (15) is a correction term to reduce the interference of SO_2 and NO_2 absorption in the O_3 retrieval. The correction for $N_g(z)$ in equation (15) requires knowledge of SO_2 and NO_2 concentration in the atmosphere.

One of the biggest challenges in deriving the O_3 mixing ratio accurately with an elastic backscatter differential absorption lidar system is to correct for the interference of aerosol. The standard technique for correcting the interference of aerosol in the O_3 lidar retrieval requires an assumption to be made for the aerosol size distribution (Browell et al., 1985; Alvarez II et al., 1998). Increasing the number of assumptions can increase the uncertainty in the final O_3 derived value. In the next section, a correction method to minimize the uncertainty in the O_3 measurement due to the interference of aerosol will be discussed. The aerosol correction method presented in this dissertation is unique: the method is based on in situ measurements of aerosol size distribution collected in the vicinity of the Twin Otter flights (and on the same flight day). There was no need to make an assumption for the aerosol size distribution since these measurements were carried out on the Convair aircraft and the data was available from Environment and Climate Change Canada. To the author's best knowledge, the use of in situ measurements for the aerosol correction has not been carried out before and it is the first time in this dissertation that the aerosol correction method is applied to the measurements collected within the Alberta oil sands region.

The slope term (d/dz in equations (15a) and (15b)) was calculated by using a running least squares fit over 20 data points (each data point has a range resolution of 7.5 m). The signal from distances corresponding to the ground was cut off before applying the least squares fit, so that the ground signal would not be processed in the slope calculation. For the slope calculation approaching the profile boundary (close to

the aircraft altitude and close to the ground), the least squares fit was performed over a smaller number of data points.

A total of four wavelengths were used for the O_3 measurements: 266 nm, 276 nm, 287 nm, and 299 nm. The O_3 mixing ratio can be derived by considering six different ON/OFF wavelength pair combinations in equation (15). Profiles of O_3 mixing ratio were derived from the analog (AN) and photon counting (PC) measurements separately. Analog was used for distance less than 1.5 km and photon counting beyond a distance of 1.5 km below the aircraft to obtain the final profile. For the O_3 measurements presented in this dissertation, the analog measurements at wavelengths of 276 nm and 299 nm were used at distances within 1.5 km of the aircraft. Photon counting measurements at the wavelengths 266 nm and 299 nm were used at greater distances from the aircraft (near the ground).

Lidar measurements collected within cloudy regions contain large backscatter from clouds and the signals are strongly attenuated. These measurements have not been used for deriving the O_3 number density.

In order to reduce the uncertainty, temporal boxcar averaging was applied over 1.3 minutes (corresponding to a distance of about 7 km along the path of the aircraft) to the ozone contour plots in section 5.1.1. Figure 3.4(a) illustrates an example of backscatter signals recorded from below the aircraft at wavelengths of 266, 276, and 299 nm. Figure 3.4(b) to Fig. 3.4(d) show the analysis of the first three terms in equation (15). Figure 3.4(e) shows O_3 mixing ratio derived with the analog and photon counting lidar measurements. The derivation of the correction terms (due to

the interference from aerosol and atmospheric gases other than O_3) in equation (15) are described in more detail in the next sections. The uncertainty analysis in the lidar O_3 retrieval and the uncertainties associated with the aerosol correction terms are presented in detail in section 3.8.

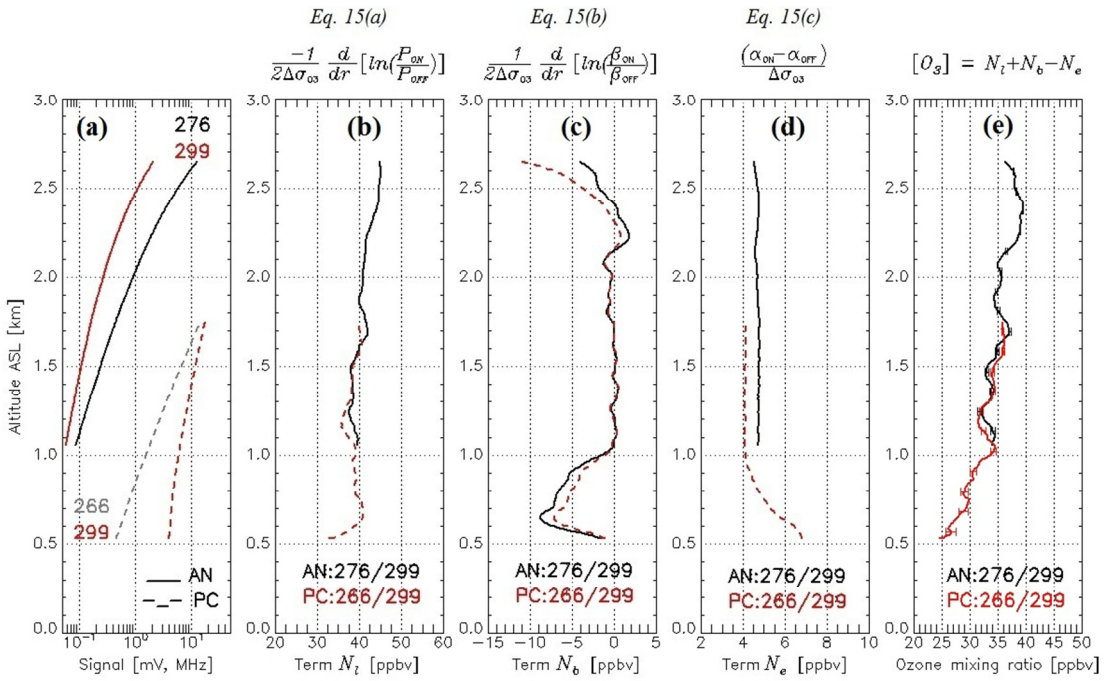

Figure 3.4: (a) Lidar backscatter signals for the analog (AN) and photon counting (PC) measurements collected on August 26, 2013. Terms in the differential absorption lidar equation associated with **(b)** the slope of the logarithm of the lidar signal ratio, **(c)** the slope of the logarithm of the ratio of total backscatter coefficients, and **(d)** the differential extinction. **(e)** The O_3 mixing ratio derived by using the AN:276/299 and PC:266/299 wavelength pairs. The measurements shown here were collected on August 26, 2016 as the Twin Otter flew downwind of the Fort McMurray oil sands industry.

3.3 Differential Absorption Lidar Correction Techniques

To accurately derive the O_3 mixing ratio from lidar measurements, the complete differential absorption lidar equation (Eq. (15)) must be considered where the backscatter and extinction coefficients are separated into their molecular and aerosol components at the ON and OFF measurement wavelengths. This section will discuss the development of an aerosol correction method and the interference of aerosol in the O_3 retrieval. For this project, the interference of aerosol in the O_3 retrieval was evaluated by making the smallest number of assumptions and by incorporating other aerosol measurements taken within the oil sands pollution with ECCC instruments on the Convair-580 aircraft. Corrections for aerosol extinction and backscatter coefficient at the UV measurement wavelengths in the differential absorption lidar equation were carried out and are described in the next few sections.

3.3.1 Correction for Aerosol in the Lidar O_3 Retrieval

The interference of aerosol in the O_3 retrieval is accounted for by the terms $N_b(z)$ and $N_e(z)$ in equation (15). When the amount of aerosol in the atmosphere is insignificant, term $N_b(z)$ is very small and only the molecular component of $N_e(z)$ needs to be calculated. Significant amounts of aerosol can result in significant biases in the O_3 derivation if the aerosol backscatter and extinction coefficients are not accounted for.

In this study, the aerosol backscatter and extinction coefficients at the UV measurement wavelengths were derived by making use of the lidar signal at a

wavelength of 532 nm and in situ measurements of aerosol from the Convair-580 aircraft. For the purposes of correcting the aerosol interference in the lidar O_3 measurements, it was assumed that the characteristics of the aerosol were consistent throughout the boundary layer, or separately above the boundary layer. The main steps in the process of correcting the interference of aerosol in the lidar O_3 retrieval are:

1) Calculate the equivalent area radius of particles and the particle number density from in situ size distribution measurements
2) Derive the aerosol component of the backscatter and extinction coefficients from the 532 nm lidar backscatter signal
3) Calculate the aerosol number density as a function of height by combining lidar and in situ measurements
4) Calculate the backscatter and extinction coefficients at the UV wavelengths as a function of height
5) Substitute the backscatter and extinction coefficients at the UV wavelengths into equation (15)

More details of each step are provided in the following sections.

3.3.1.1 Aerosol Optical Properties Derived from Size Distribution Measurements

The interference of aerosol in the O_3 retrieval was evaluated by using in situ measurements of particle size distribution, $N(r)$, for particles with radius in the range between r and $r+dr$. The particle size distribution measurements from the UHSAS and FSSP-300 were collected on the Convair-580 aircraft. The particle size

measurements from both instruments were combined (as shown in Fig. 3.5) to determine the equivalent area radius of the particles.

The equivalent area radius of the particles, R_a was determined by using the mean cross-sectional area of the particle size distribution:

$$R_a{}^2 = \frac{\int_0^\infty N(r)\, r^2\, dr}{N_0} \tag{16}$$

The parameter N_0 in equation (16) represents the total particle number density, $N_0 = \int_0^\infty N(r)dr$. The calculated value of the particle equivalent area radius for the size distribution measurements shown in Fig. 3.5 is 0.072 μm.

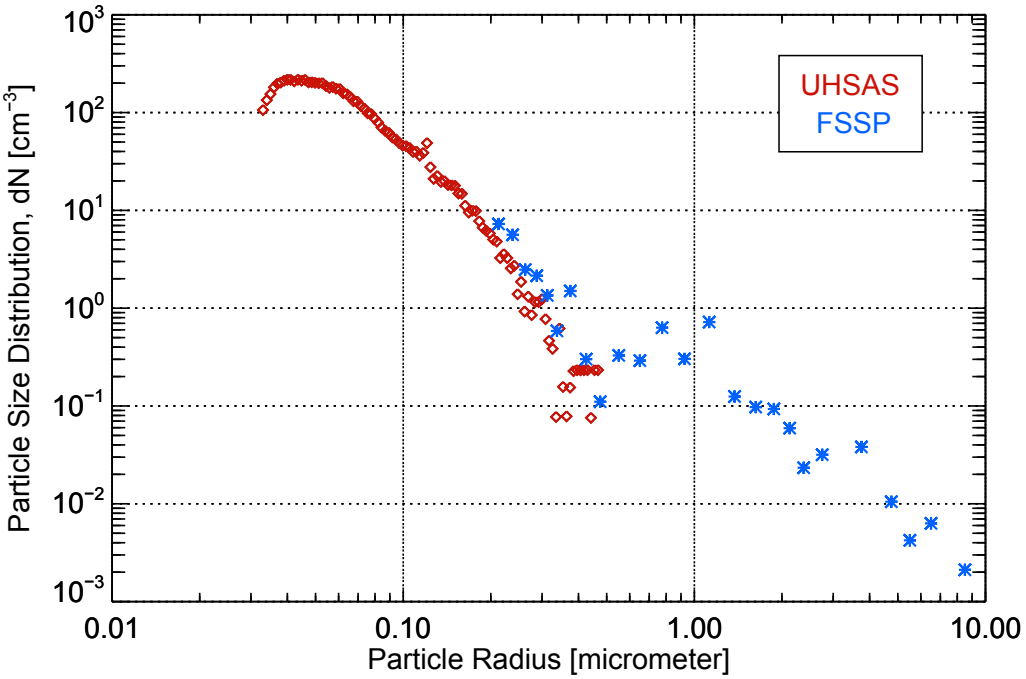

Figure 3.5: The particle size distribution measurements collected on August 23, 2013 as the Convair-580 aircraft flew directly above the Fort McMurray oil sands industry at an altitude of 785 m ASL (within the boundary layer). The data points plotted in red are particle size measurements from the UHSAS instrument and the data points in blue are from the FSSP-300 instrument.

The in situ particle size distribution measurements were also used to determine the aerosol extinction ($\alpha_{aerosol}$) and backscatter coefficient ($\beta_{aerosol}$) at a single altitude, given by equations (17) and (18).

$$\alpha_{aerosol}(\lambda_{532}) = \int_0^\infty \pi r^2 \, Q_{ext}(m, r, \lambda_{532}) \, N(r) \, dr \tag{17}$$

$$\beta_{aerosol}(\lambda_{532}) = \int_0^\infty \pi r^2 \, Q_{back}(m, r, \lambda_{532}) \, N(r) \, dr \tag{18}$$

The aerosol extinction and backscatter efficiencies (Q_{ext} and Q_{back}) in equations (17) and (18) were determined from the in situ measurements with calculations based on the theory of Mie scattering for spherical particles. A subroutine called BHMIE.pro (http://reef.atmos.colostate.-edu/~odell/at721/resources/codes/idl/) determines the scattering amplitudes and the efficiency for extinction and backscatter of a single homogenous spherical particle. The derivation of scattered electromagnetic radiation from spherical particles takes into consideration a spherical-coordinate reference system that is centered on a spherical particle of radius "*r*". The derivation also requires the scalar wave equation to be evaluated in spherical coordinates, which yields solutions that are associated with Legendre and Bessel functions. The interaction of an incident plane wave at the surface of the particle results in a discontinuity due to the differences in the refractive index of the particle and the surrounding medium. The boundary condition at the surface of the particle is considered in this subroutine. The solution for the scattered electromagnetic field

results in scattering amplitudes and the efficiency for extinction and backscatter (Bohren and Huffman, 1983). The subroutine requires a value of the complex refractive index of particles, *m*, at the measurement wavelength, λ, and the size parameter ($2\pi r/\lambda$) in order to compute extinction and backscatter efficiencies of the aerosol particles.

In the region directly above the oil sands (where the maximum aerosol loading occurred), the particle refractive index corresponding to the mineral Kaolinite was used. Kaolinite is a clay mineral composed of aluminum silicate. Studies done by Cloutis et al. (1995), Omotoso and Mikula (2004), and Mercier et al. (2008), have found kaolinite to be the prominent clay particle with size < 2 μm in the oil sands region. Kaolinite is a non-swelling clay mineral (Barshad, 1955). The strong hydrogen bond between the hydroxyl group and the oxygen atom on the surface of the silicate layers is the primary reason that the mineral does not absorb water (Schuttlefield et al., 2007). The refractive index of kaolinite at a wavelength of 532 nm is $1.57+0.006i$ (Arakawa et al., 1997) and was used in the Mie scattering calculations to estimate the backscatter and extinction efficiencies of the aerosol particles. Kaolinite does not absorb water and it will not expand upon contact with water. So any changes in the humidity level in the oil sands region will not affect the size of kaolinite particles. Table 3.1 outlines the input parameters that were used in the Mie scattering calculations.

3.3.1.2 Aerosol Extinction Derived from the 532 nm Lidar Backscatter Signal

Retrieval of the aerosol extinction coefficient height profile (used in calculating correction terms in equations (15b) and (15c)) from the lidar backscatter signal at the wavelength of 532 nm was achieved by the method of Fernald (Fernald, 1984). The algorithm based on the method of Fernald is shown in Appendix 1. The absorption by O_3 is not significant at this wavelength and the backscatter and extinction coefficients can be derived from the data independent from the O_3 measurement. Fernald's method requires three input values: the aerosol extinction coefficient at a reference height, the lidar ratio, and height profiles of the molecular extinction and backscatter coefficient.

A reference value of the aerosol extinction coefficient $\alpha_A(z)$ at a known height is required in Fernald's method. The aerosol extinction coefficient at a reference altitude was estimated by using the particle size distribution measurements taken above the surface boundary layer over the industry and integrating over all particle sizes, *r*, as shown in equation (17). It was found that above the boundary layer in the oil sands region, the aerosol extinction coefficient ranged between 0.002 km^{-1} and 0.014 km^{-1}. An average extinction coefficient of 0.008 km^{-1} was used in Fernald's method at a reference height of 1.7 km ASL. The difference in the calculated O_3 value by using 0.002 km^{-1} and 0.014 km^{-1} as the aerosol extinction coefficient at a reference height will be discussed in section 3.8.2.2.

The ratio of aerosol extinction to backscatter coefficients is defined as the aerosol lidar ratio. The method of Fernald assumes that the aerosol lidar ratio S_A does not vary with distance away from the lidar. This means that any change in the vertical distribution of aerosol in the atmosphere is directly related to the variation in aerosol concentration and not from the variation in particle size. The aerosol and molecular lidar ratio S_M are defined as constants:

$$S_A = \frac{\alpha_{aerosol}(\lambda_{532}, z)}{\beta_{aerosol}(\lambda_{532}, z)}, \qquad S_M = \frac{\alpha_{molecular}(z)}{\beta_{molecular}(z)} = \frac{8\pi}{3} \tag{19}$$

In situ particle size measurements taken directly over the oil sands region (within the boundary layer and at an altitude of 785 m ASL, as shown in Fig. 3.5) were used to estimate a value of lidar ratio due to the scattering particles. The aerosol lidar ratio was determined by substituting equations (17) and (18) into equation (19). The aerosol lidar ratio (within the boundary layer and directly over the oil sands industry) at a wavelength of 532 nm was found to be 31 sr from Mie scattering calculations. For the aerosol correction in the O_3 retrieval, it was assumed that this lidar ratio is independent of height.

An example of the aerosol extinction coefficient as derived from the lidar measurements at a wavelength of 532 nm is shown in Fig. 3.6. The measurements in black (in Fig. 3.6) were taken from the York University lidar system during an overpass of the Twin Otter aircraft on August 23, 2013 above an air monitoring station (AMS 13) where the ECCC ground-based lidar was located. ECCC provided a data product in which the aerosol lidar ratio was assumed to be 25 sr was used to

generate the extinction coefficient profile (shown in red in Fig. 3.6) at AMS 13, whereas a lidar ratio of 31 sr was used to derive the extinction profile from the Twin Otter lidar measurements. Differences between the aerosol extinction coefficient profiles in Fig. 3.6 are due to the different values of lidar ratio used.

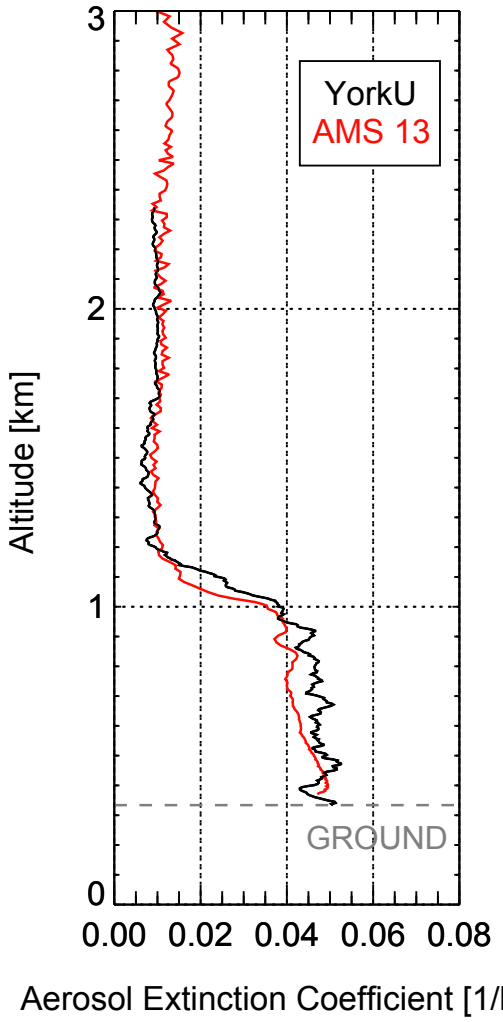

Figure 3.6: A comparison between the aerosol extinction coefficients as a function of altitude for measurements taken at a wavelength of 532 nm on August 23, 2013. The aerosol extinction coefficient from the ground-based lidar system (located at AMS 13 in Fig. 2.12) is shown in red and the aerosol extinction as derived from Fernald's method during an overpass of the Twin Otter aircraft at AMS 13 is shown in black.

Table 3.1: Input parameters used in Mie calculations for the aerosol correction. The equivalent area radius and lidar ratio of particles were derived from in situ size distribution measurements. The refractive index for kaolinite particles was taken from the literature (Arakawa et al., 1997).

Quantity	Oil sands aerosol
Equivalent area radius of the particle, R_a	0.072 μm
Aerosol lidar ratio, S_A (532 nm)	31 sr
Particle refractive index, m	$\lambda_{530nm} = 1.57 + 0.006i$ $\lambda_{260nm} = 1.68 + 0.041i$

3.3.1.3 Aerosol Height Profile from Combined Lidar and In Situ Measurements

The aerosol extinction coefficient derived by using the lidar measurements at a wavelength of 532 nm can be related to the aerosol number density by using the equivalent area radius of the particle. The number density of aerosol as a function of height was calculated by using equation (20):

$$N_{aerosol}(z) = \frac{\alpha_{aerosol}(\lambda_{532}, z)}{\pi {R_a}^2 \, Q_{ext}(m, R_a, \lambda_{532})} \tag{20}$$

There is an uncertainty associated with using the equivalent area radius approximation, but the lidar derived ozone concentration was always in agreement with the in situ measurements when comparisons could be made (e.g. Fig. 3.19).

Mie scattering calculations were used to estimate the backscatter and extinction efficiencies of aerosol at the UV wavelengths. By integrating over all particle sizes in

the distribution the aerosol components of extinction and backscatter coefficients at the UV measurement wavelengths and as a function of height were determined by equations (21) and (22):

$$\alpha_{aerosol}(\lambda_{UV}, z) = \frac{N_{aerosol}(z)}{N_0} \int_0^{\infty} \pi r^2 \, Q_{ext}(m, r, \lambda_{UV}) \, N(r) \, dr \qquad (21)$$

$$\beta_{aerosol}(\lambda_{UV}, z) = \frac{N_{aerosol}(z)}{N_0} \int_0^{\infty} \pi r^2 \, Q_{back}(m, r, \lambda_{UV}) \, N(r) \, dr \qquad (22)$$

The scaling factor $N_{aerosol}(z)/N_0$ was required to account for the variation in aerosol number density with height. It was assumed that the shape of the particle size distribution remained constant with height and any changes in the vertical distribution of aerosol in the atmosphere is directly related to the variation in aerosol concentration. $N_{aerosol}(z)$ was derived from the lidar measurements at a wavelength of 532 nm by using equation (20). N_0 in equations (21) and (22) is the total number density in the in situ measurements of size distribution.

Figure 3.7 shows an example of aerosol extinction and backscatter coefficients as a function of altitude measured at 532 nm and calculated for the UV measurement wavelengths.

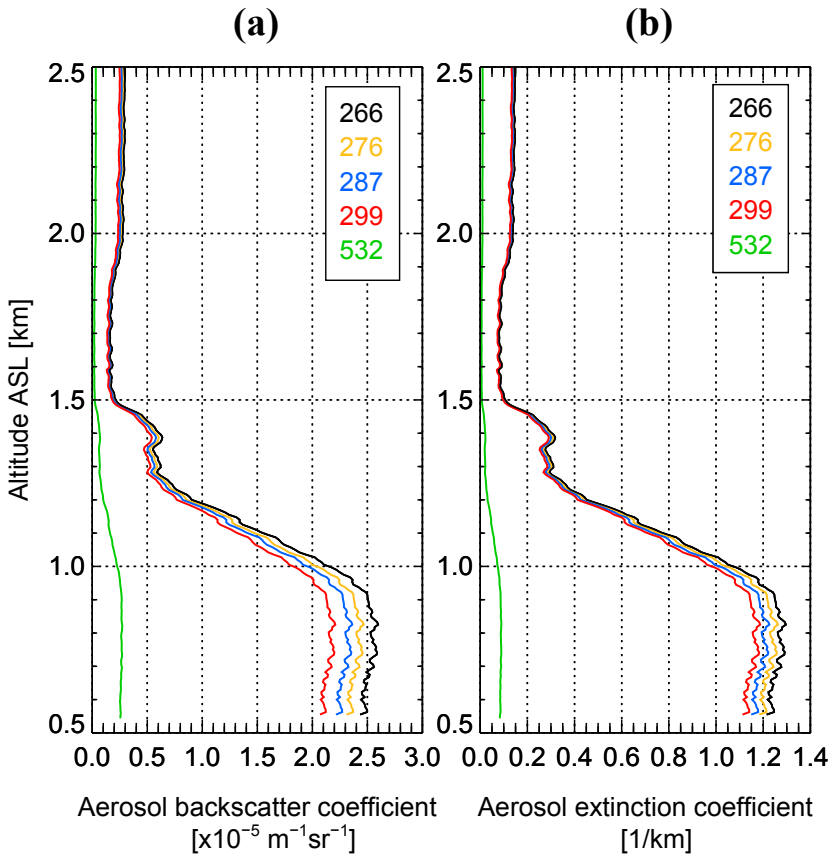

Figure 3.7: The calculated **(a)** aerosol backscatter and **(b)** extinction coefficients at the measurement UV wavelengths and measured at a wavelength of 532 nm as a function of altitude. The measurements shown here were collected on August 23, 2013 as the Twin Otter flew directly above the Fort McMurray oil sands industry where significant amounts of aerosol were mixed up to an altitude of 1.5 km ASL.

The efficiency of light scattered from small sized particles is much greater in the UV wavelength range as compared to the visible wavelength range. For this reason, the extinction (or backscatter) coefficient at a wavelength of 532 nm in Fig. 3.7 is much smaller than the extinction coefficient at the UV wavelengths.

The height profile of the aerosol backscatter coefficient in Fig. 3.7(a) is proportional to the aerosol extinction profile. Since the extinction coefficient is related

to the backscatter coefficient by the lidar ratio, the two profiles in Fig. 3.7(a) and (b) look very similar.

3.3.1.4 Aerosol Correction in the Ozone Retrieval

The aerosol component of backscatter and extinction coefficients at the UV wavelengths were substituted into equation (7) and (8) respectively. Equations (7) and (8) were then substituted into Eq. (15) to retrieve the O_3 number density.

In regions where there is an insignificant amount of aerosol or the gradient in the aerosol backscatter profile is small, the contribution of term $N_b(z)$ in equation (15) is very small. In such a case, only the molecular component of the differential extinction term ($N_e(z)$) has a significant contribution in the O_3 retrieval.

Figure 3.8 illustrates the analysis for the first three terms in equation (15) that was used to derive the O_3 mixing ratio by applying the aerosol correction for a case in which significant amounts of aerosol were encountered on August 23, 2013 directly over the oil sands industry (same case as Fig. 3.7). In Fig. 3.8(c), the differential backscatter term ($N_b(z)$) in the correction method had the greatest contribution to the O_3 retrieval in the presence of aerosol. It was observed that strong gradients in the aerosol backscatter profile can account for a change of up to 15 ppbv in the O_3 retrieval. Figure 3.8(d) shows that a correction of 4 ppbv in the O_3 retrieval is due to the differential molecular extinction and a correction of approximately 6 ppbv is due to the differential aerosol extinction. Figure 3.8(e) shows that the amount of correction in the O_3 retrieval due to significant amounts of aerosol is -15 ppbv at the

top of the boundary layer. The calculated aerosol corrections are small (a few ppbv) above the boundary layer and approximately -6 ppbv within the boundary layer.

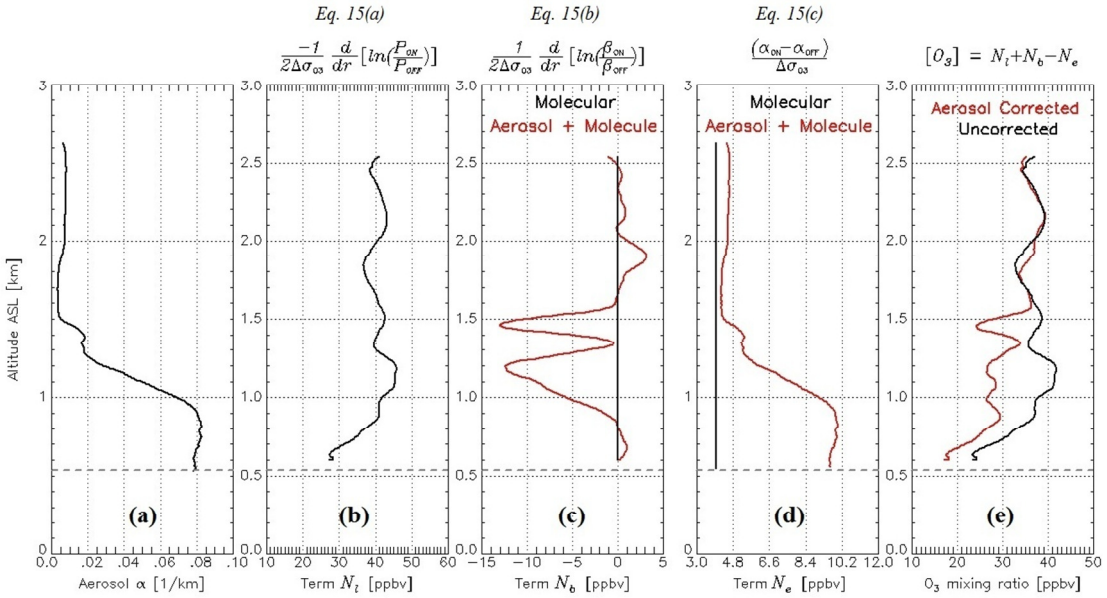

Figure 3.8: The O_3 retrieval for the 276/299 wavelength pair. **(a)** The aerosol extinction coefficient derived by using the lidar measurement at a wavelength of 532 nm. Analysis of the term **(b)** $N_l(z)$ (Eq. (15a), **(c)** $N_b(z)$ (Eq. (15b), **(d)** $N_e(z)$ (Eq. (15c), and **(e)** the addition of the first three terms in Eq. (15). The line plots in red represent the aerosol corrected term and the dashed line in all of the plots represents the height of the ground. The measurements shown here were collected on August 23, 2013 as the Twin Otter flew directly above the Fort McMurray oil sands industry where significant amounts of aerosol were mixed up to an altitude of 1.5 km ASL.

The amount of correction due to aerosol is different for the six different ON/OFF wavelength pair combinations in the differential absorption lidar equation. Figure 3.9 illustrates the total amount of correction in the O_3 retrieval due to aerosol (by considering only the aerosol components of $N_b(z)$ and $N_e(z)$ terms in Eq. (15)). All wavelength pairs in Fig. 3.9 show that the correction is largest where significant

gradients are present in the aerosol backscatter profile. The maximum amount of correction in the O_3 retrieval can be attributed to the 287/299 wavelength pair, whereas the 266/276 wavelength pair results in the smallest correction.

The magnitude of the aerosol correction to the retrieved O_3 mixing ratio is consistent with what has been reported from previous lidar O_3 studies that employ different methods for calculating the aerosol extinction and backscatter coefficients at UV wavelengths. The aerosol correction in previous lidar O_3 retrievals was small (<3 ppbv) in regions of low aerosol loading or in regions where the gradient in the backscatter profile is small (Sullivan et al., 2014), but corrections between 15 and 35 ppbv have been calculated due to the presence of large aerosol gradients at the top of the boundary layer (Browell et al., 1985; Alvarez II et al., 1998; Eisele and Trickl, 2005).

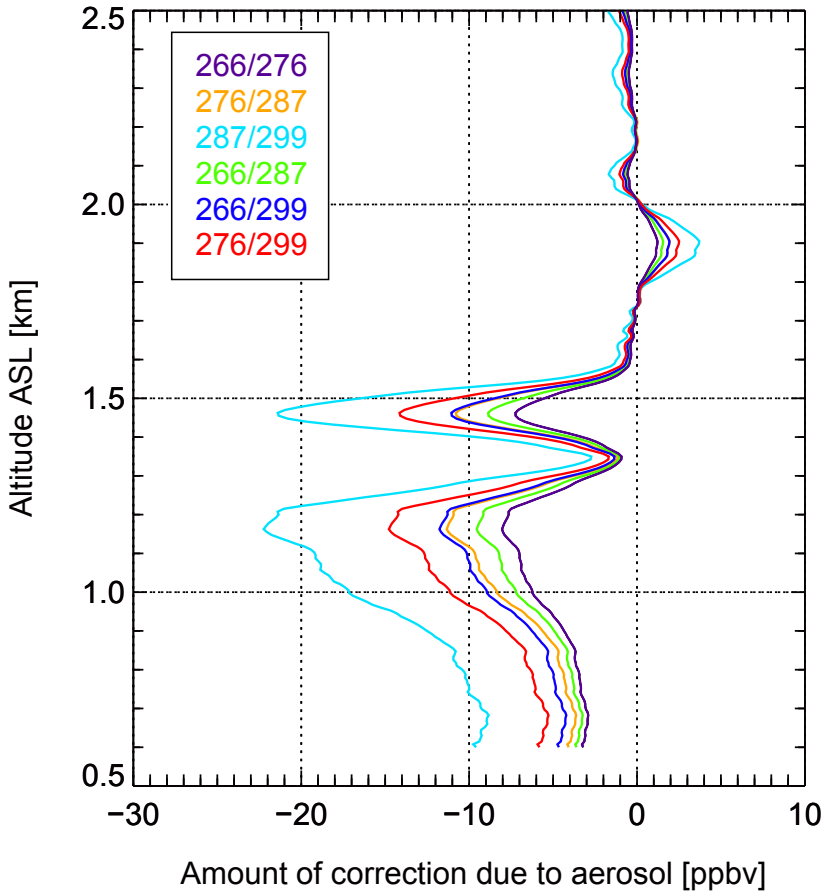

Figure 3.9: The amount of correction in the O_3 retrieval due to the presence of aerosol by using the six different ON/OFF wavelength pair combinations in the differential absorption lidar equation. The measurements shown here were collected on August 23, 2013 as the Twin Otter flew directly above the Fort McMurray oil sands industry where significant amounts of aerosol were mixed up to an altitude of 1.5 km ASL.

3.3.2 Interference from Atmospheric Gases

The correction term $N_g(z)$ in equation (15) represents the interference of other atmospheric gases such as SO_2 and NO_2 in the O_3 retrieval. The wavelengths used to derive the O_3 mixing ratio fall within the UV band where SO_2 and NO_2 molecules have substantial and varying absorption cross-sections as well. Large concentrations

of SO_2 and NO_2 were present within the oil sands region as bitumen contains an abundance of sulphur compounds and NO_2 mostly comes from the combustion of hydrocarbons. The contribution of these gases in the O_3 retrieval can be substantial, especially within the boundary layer where the concentration of the gases is high. The absorption cross-sections of O_3, SO_2, and NO_2 molecules as a function of wavelengths in the O_3 measurement region are shown in Fig. 3.10.

The interference of SO_2 and NO_2 in the O_3 retrieval was assessed by calculating the ratio of the differential absorption cross-section of SO_2 or NO_2 to the differential absorption cross-section of O_3 in equation (15c): $\frac{(\sigma_{gas,ON} - \sigma_{gas,OFF})}{\Delta\sigma_{O_3}}$. This is referred to as the correction sensitivity. The wavelength pairs that result in large values of the correction sensitivity have the greatest influence in the O_3 retrieval. The correction sensitivity when multiplied by the concentration of SO_2 or NO_2 determines the amount of change in the O_3 retrieval due to their presence in the atmosphere.

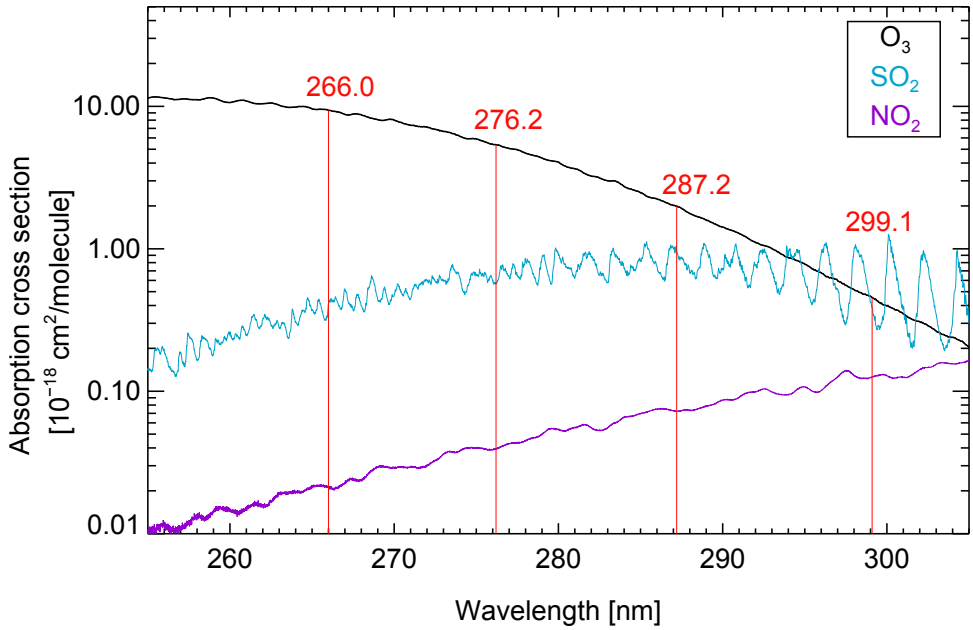

Figure 3.10: The absorption cross-sections of O_3, SO_2, and NO_2 molecules in the UV Hartley band at a temperature of 300 K, 298 K, and 294 K respectively [HITRAN 2012 database]. The vertical lines indicate the wavelengths emitted from the lidar system.

3.3.2.1 Correction for SO_2 Differential Absorption

Table 3.2 shows the value of the correction sensitivity for each wavelength pair that would need to be applied to the O_3 retrieval in order to account for SO_2 absorption in the lidar O_3 measurement. It was found that the wavelength pair 266/299 can result in a contribution of 0.2% of the SO_2 concentration to the retrieved O_3. The largest interference comes from using the 287/299 wavelength pair, at about 37% of the SO_2 concentration.

Table 3.2: Differential absorption cross-sections of O_3 and SO_2 (at a temperature of 300 K and 298 K respectively) for the different ON/OFF wavelength pairs and the corresponding correction sensitivity due to the interference of SO_2 in the O_3 retrieval.

Wavelength Pair $\left(\lambda_{ON}/\lambda_{OFF}\right)$	**Differential O_3 absorption cross-section, $\Delta\sigma_{O_3}$ ($\times 10^{-18}$ cm^2/molecule)**	**Differential SO_2 absorption cross-section, $\Delta\sigma_{SO_2}$ ($\times 10^{-18}$ cm^2/molecule)**	**Correction sensitivity** $\frac{\Delta\sigma_{SO_2}}{\Delta\sigma_{O_3}}$
266/276	+4.00	-0.17	-0.042
276/287	+3.39	-0.39	-0.115
287/299	+1.54	+0.58	+0.377
266/287	+7.39	-0.56	-0.076
266/299	+8.93	+0.02	+0.002
276/299	+4.92	+0.19	+0.039

In situ SO_2 measurements were taken on the Convair-580 aircraft and mixing ratios of SO_2 typically range between 30 and 150 ppbv within the boundary layer. In this dissertation the 266/299 wavelength pair was used to retrieve O_3 mixing ratios within the boundary layer and a SO_2 concentration of 150 ppbv would result in a 0.3 ppbv change in the O_3 value. Corrections for SO_2 were not substantial and were not applied to the O_3 retrieval since the actual concentration of SO_2 along the Twin Otter flight path was not known. The wavelength pair with the smallest sensitivity to SO_2 (266/299) was used to derive the O_3 mixing ratio within the boundary layer.

3.3.2.2 Correction for NO_2 Differential Absorption

Table 3.3 shows the value of the correction sensitivity for each wavelength pair that would need to be applied to the O_3 retrieval in order to account for NO_2 absorption in the lidar measurement.

Table 3.3: Differential absorption cross-sections of O_3 and NO_2 (at a temperature of 300 K and 294 K respectively) for the different ON/OFF wavelength pairs and the corresponding correction sensitivity due to the interference of NO_2 in the O_3 retrieval.

Wavelength Pair $\left(\lambda_{ON}/\lambda_{OFF}\right)$	**Differential O_3 absorption cross-section, $\Delta\sigma_{O_3}$ ($\times 10^{-18}$ cm^2/molecule)**	**Differential NO_2 absorption cross-section, $\Delta\sigma_{NO_2}$ ($\times 10^{-18}$ cm^2/molecule)**	**Correction sensitivity** $\frac{\Delta\sigma_{NO_2}}{\Delta\sigma_{O_3}}$
266/276	+4.00	-0.018	-0.0045
276/287	+3.39	-0.033	-0.0097
287/299	+1.54	-0.053	-0.034
266/287	+7.39	-0.052	-0.007
266/299	+8.93	-0.105	-0.012
276/299	+4.92	-0.086	-0.017

It was calculated that the largest interference of 3.4% of the NO_2 concentration in the O_3 retrieval comes from the 287/299 wavelength pair and 1.2% of the NO_2 concentration if using the 266/299 pair. In situ NO_2 measurements were taken on the Convair-580 aircraft and mixing ratios of NO_2 typically range between 5 and 30 ppbv within the boundary layer. A 30 ppbv mixing ratio of NO_2 would result in a 0.36 ppbv change in the O_3 value for the 266/299 wavelength pair.

Corrections for NO_2 were not applied to the O_3 retrieval since the actual concentration of NO_2 along the Twin Otter flight path was not known. The 266/299 wavelength pair has the smallest sensitivity to NO_2 and this wavelength pair was used to derive the O_3 mixing ratio within the boundary layer.

3.4 Non-linearity in Photon Counting Detection

For weak signals, PMTs are the most efficient detectors for measurements collected in the visible and UV wavelength range. The photon count rate is proportional to the incident optical power. At high count rates (greater than 10 MHz), the photon counting signal is nonlinear due to overlapping pulses from the detector. The detection system is unable to count separate individual pulses accurately within a certain time period commonly referred to as dead time t_d (Donovan et al., 1993). A dead time correction was applied to the raw photon counting data by calculating the true count rate N_T, in terms of the measured count rate N_m, as shown in equation (23) (Evans, 1955).

$$N_T = \frac{N_m}{1 - N_m \times t_d} \tag{23}$$

The true count rate was found by using a value of a dead time for which the ratio of N_T to the recorded analog signal is a constant up to a count rate of 100 MHz. Five separate PMTs were used to collect measurements at wavelengths of 266 nm, 276 nm, 287 nm, 299 nm, and 532 nm and the dead time correction applied to each

photon counting measurement wavelength was typically on the order of 4.5 ns, 5.0 ns, 5.5 ns, 7.5 ns, and 5.0 ns respectively. The optimal dead time correction at each wavelength was determined from lidar measurements acquired along one leg of the Twin Otter flight on August 22, 2013 and these dead time corrections were applied to the measurements collected on all subsequent flights. The value of dead time correction at each wavelength was consistent throughout the campaign for each PMT. Figure 3.11 shows an example of the non-linearity correction in the photon counting measurement at a wavelength of 276 nm, and the corrected signal by using a dead time correction of 5.0 ns.

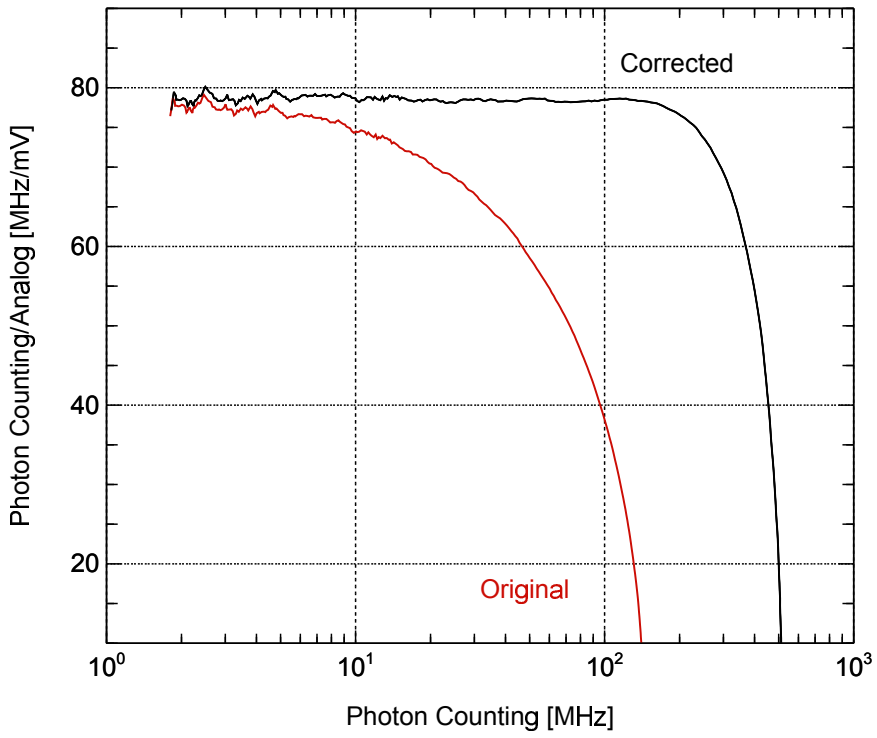

Figure 3.11: Ratio of photon counting and analog signals as a function of corrected count rate. The uncorrected signal is nonlinear at all signal levels, but the corrected signal is linear up to 100 MHz.

After the photon counting non-linearity correction is applied a good agreement is seen between the O_3 profiles derived separately from the analog and photon counting measurements.

3.5 Signal Induced Noise in the Lidar Measurement

Improper pulse counting is not the only source of nonlinearity that arises by using a PMT detector. Strong UV signals in the near range can introduce a residual decaying signal in the far range, most commonly referred to as the signal induced noise (SIN) or signal induced background. The cause of signal induced noise is likely UV fluorescence from the PMT (Zhao, 1999) and this occurs only in the UV wavelength range.

Figure 3.12 illustrates an example of a lidar signal at wavelengths of 266, 299, and 532 nm plotted as a function of range. It can be seen in Fig. 3.12 that the lidar signal at a wavelength of 266 nm (black line) decreases as a function of range past the ground return. This part of the lidar signal is not the true signal as there would be no real optical signal in this range. The decrease in the signal past the ground return is due to noise that was induced as a result of the PMTs being exposed to UV light pulses. The signal induced noise in Fig. 3.12 is not significant at the wavelengths of 299 and 532 nm as the signal past the ground return stays constant as a function of range. Hence, the fluorescence induced in the PMT by backscattered UV radiation only affected the measurements made at shorter UV wavelengths and the signal

induced noise correction was applied only to the lidar measurement collected at wavelengths of 266, 276, and 287 nm.

This residual signal had an amplitude that was proportional to the relatively large signal amplitude at near range. It can be modeled by an exponential function (Sunesson et al., 1994) and for the measurements collected with a downward directed lidar system, the residual signal was corrected by fitting a 3 km region of the signal past the ground return to a single exponential decaying function:

$$P(z) = C\,\exp(-D \times z) \tag{24}$$

Where C and D are fit parameters and z is the lidar range.

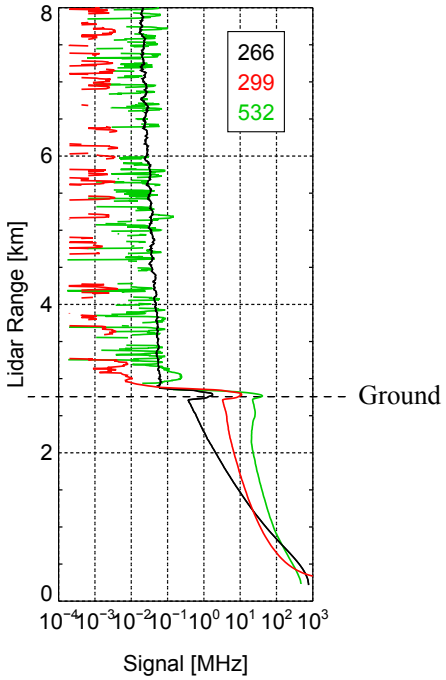

Figure 3.12: Lidar signal at wavelengths of 266, 299, and 532 nm plotted as a function of range. Note that the vertical axis is inverted with respect to previous line plots. The measurements shown here were collected on August 26, 2013 as the Twin Otter flew above the Fort McMurray oil sands industry.

An example of the exponential fit plotted on a logarithmic scale is shown in Fig. 3.13(a). The exponential fit was then subtracted from the lidar backscatter signal and it is shown in Fig. 3.13(b).

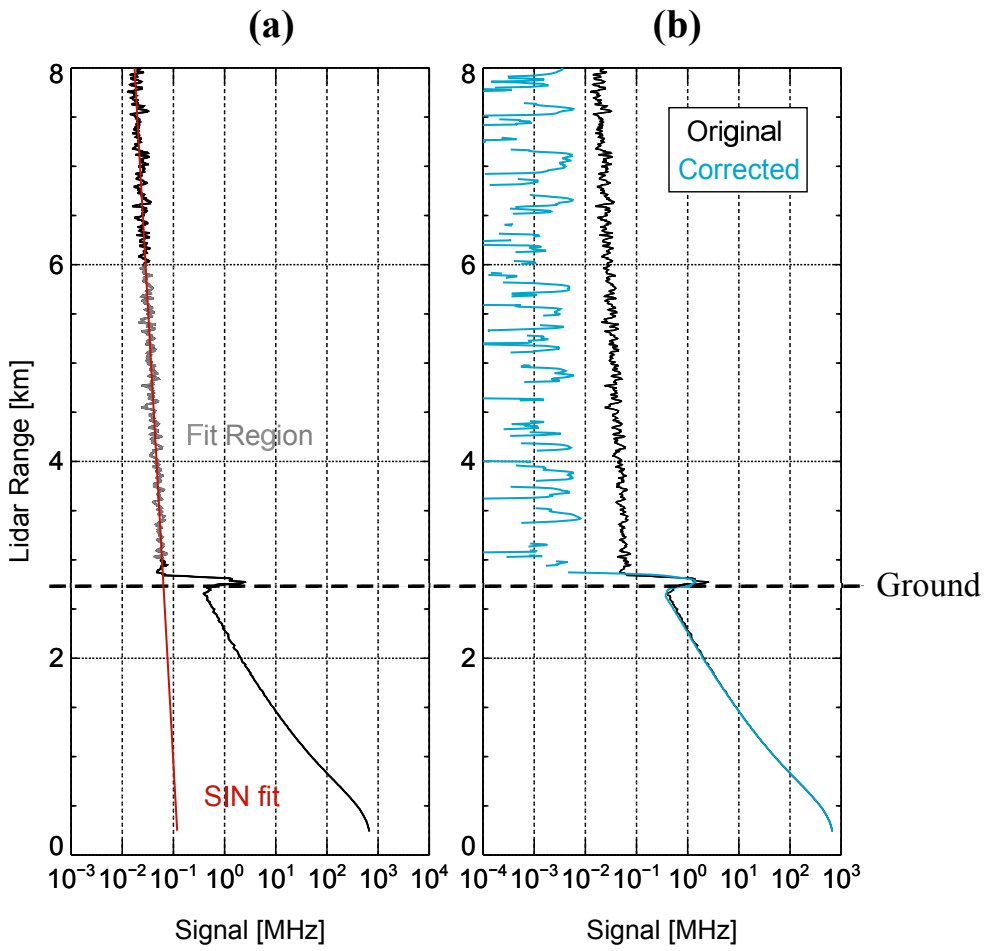

Figure 3.13: (a) Lidar signal plotted as a function of range (in black). The signal past the ground return was used for the SIN correction and the corresponding SIN fit to the measurement is shown in red. **(b)** The lidar signal with and without the SIN correction. The measurements shown here were collected on August 26, 2013 as the Twin Otter flew above the Fort McMurray oil sands industry (same case as Fig. 3.12).

For measurements collected with the downward directed lidar system, it is crucial to correct the signal induced noise in order to reduce the uncertainty in the derived O_3 mixing ratio in regions closer to the ground, (where the SIN correction is largest relative to the backscatter signal). Without applying the SIN correction to the lidar measurements, it was found that an uncertainty of up to 10 ppbv occurs in the O_3 mixing ratio close to the ground, as shown in Fig. 3.14.

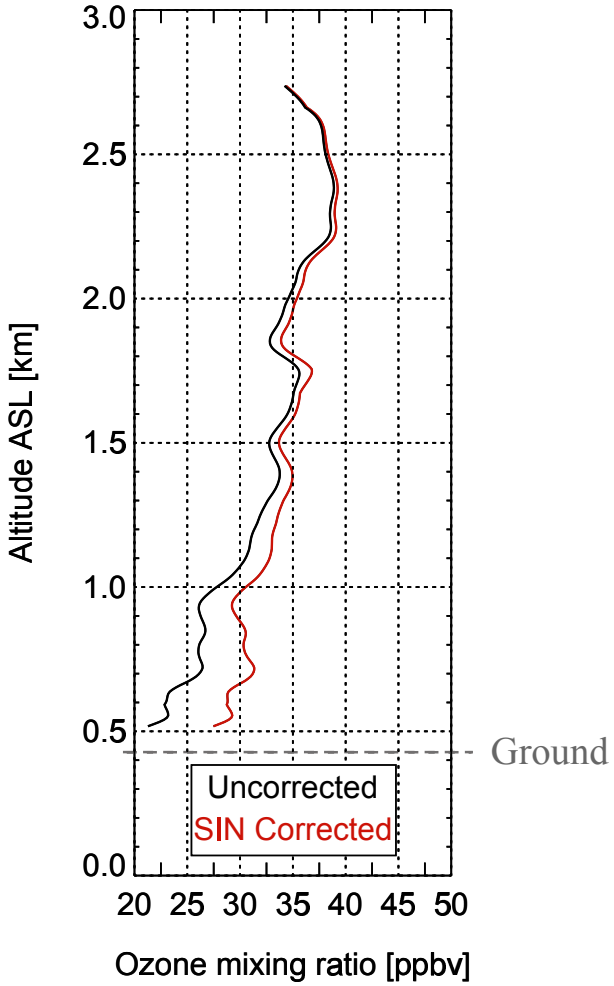

Figure 3.14: The effect of the SIN correction in the lidar O_3 retrieval. The measurements shown here were collected on August 26, 2013 as the Twin Otter flew above the Fort McMurray oil sands industry.

3.6 Temperature Dependence of O_3 Absorption Cross-section

The absorption cross-section of O_3 is temperature dependent. For lidar measurements collected within the 3 km region of the lower troposphere, the temperature changes from 293 K (close to the surface) to 268 K (at approximately 3 km). Table 3.4 shows the absorption cross-section of O_3 at a few different temperatures and at the UV measurement wavelengths.

Table 3.4: Absorption cross-sections of O_3 for temperatures between 260 and 300 K at the UV measurement wavelengths [HITRAN 2012 database].

Wavelength (nm)	**O_3 absorption cross-sections ($\times 10^{-18}$ cm^2/molecule)**		
	T = 260 K	**T = 280 K**	**T = 300 K**
266.0	9.40	9.39	9.38
276.2	5.366	5.375	5.376
287.2	1.95	1.97	1.99
299.1	0.43	0.44	0.46

The 276/299 wavelength pair was used to derive the O_3 mixing ratio at higher altitudes (above the surface boundary layer) and by using Table 3.4 the differential absorption cross-section of O_3 for the wavelength pair 276/299 changes from 4.92×10^{-18} cm^2/molecule at 300 K to 4.94×10^{-18} cm^2/molecule at 260 K. This change is not significant and it accounts for an uncertainty of up to 0.4% of the ozone

concentration. Since O_3 mixing ratios above the surface boundary layer are approximately 35 ppbv, the amount of correction translates to 0.1 ppbv.

The 266/299 wavelength pair was used to derive the O_3 mixing ratio within the surface boundary layer. The differential absorption cross-section of O_3 for the wavelength pair 266/299 (in Table 3.4) changes from 8.92×10^{-18} cm^2/molecule at 300 K to 8.97×10^{-18} cm^2/molecule at 260 K and this change accounts for an uncertainty of up to 0.6% of the ozone concentration. For an O_3 mixing ratio of 15 ppbv (typically observed within the boundary layer and in the pollution from the oil sands industry), the amount of correction translates to 0.09 ppbv.

Since significant changes in the calculated O_3 by using the absorption cross-section at temperatures of 260 and 280 K as compared to 300 K were not observed, the O_3 absorption cross-section at a constant temperature of 300 K was used to derive the O_3 mixing ratio from the ground to an altitude of 3.0 km ASL.

3.7 Hybrid Single Particle Integrated Trajectory (HYSPLIT) Model

The HYSPLIT model (Draxler and Hess, 1998) was used to predict the trajectory of the emissions released from the oil sands in both the forward and backward directions. Forward air trajectories from the oil sands locations were used for campaign flight planning, so that each flight path intersected the trajectory of air that had passed over the oil sands. In this dissertation, backward air trajectory

calculations (along isentropic surfaces) were executed to reconstruct the past motion of air parcels.

The HYSPLIT model was accessed through the NOAA ARL READY Website (http://www.arl.noaa.gov/HYSPLIT.php) and trajectories were computed by using the Global Data Assimilation System (GDAS) meteorological dataset. The resolution of the GDAS dataset is 1° latitude by 1° longitude on a global domain and contains the horizontal and meridional wind components, and temperature and humidity fields provided by National Center for Environmental Prediction (NCEP).

The accuracy of a trajectory calculation from the HYSPLIT model has been assessed by balloon flight tracks. For tropospheric altitudes, the uncertainty in a backward trajectory for a travel time of 48 hours is less than 20% of the travel distance (Baumann and Stohl, 1997). In this dissertation, air trajectories were used in the interpretation of lidar measurements and to support campaign flight planning. The largest travel time for a backward trajectory used in the analysis was 10 hours. The uncertainty in the air trajectory related to a travel time of 10 hours does not affect the final interpretation or conclusions derived from using these trajectories.

3.8 Relative Uncertainty in Lidar Measurements

For photon counting detection the uncertainty in the lidar measurement is a result of the statistical variation of detected photons. The number of detected photons follows a Poisson distribution. The standard deviation of a Poisson distribution is

equal to the square root of the mean value. This is the statistical (or random) noise in photon counting measurements. The signal-to-noise ratio (SNR) in the photo counting measurement is defined as (Heese et al., 2010):

$$SNR_{\lambda}(z) = \frac{P_{\lambda}(z)}{\sqrt{P_{\lambda}(z) + 2P_{BKG,\lambda}}} \tag{25}$$

Where $P_{\lambda}(z)$ represents the lidar measurement in counts and $P_{BKG,\lambda}$ represents the background signal. The SNR is the largest closer to the lidar system and is very small at distances further away. Thus, the SNR is range dependent.

The SNR for analog detection is determined by the current at the photocathode. For each detected photon there is an electron emitted from the photocathode of the PMT (prior to the chain of dynodes that amplify the current). The uncertainty in the analog detection is a result of the statistical variation in counting electrons, which is the square root of the number. The photocathode current at the measurement wavelength, $I_{k,\lambda}$, is equal to the current out of the PMT divided by the gain of the PMT. The SNR also depends on the bandwidth of the system, B, the noise figure of the PMT, F, and the charge of an electron, e, (Hamamatsu Photonics, 2007):

$$SNR_{\lambda}(z) = \frac{I_{k,\lambda}(z)}{\sqrt{2eFB\left[I_{k,\lambda}(z) + 2(I_{BKG,\lambda} + I_{d,\lambda})\right]}} \tag{26}$$

The background value of the photocathode current (at the measurement wavelength) in equation (26) is represented by $I_{BKG,\lambda}$ and $I_{d,\lambda}$ is the photocathode dark current. The term $(I_{BKG,\lambda} + I_{d,\lambda})$ is the standard deviation in the background analog signal.

3.8.1 Error Analysis for the Differential Absorption Lidar Method

In this section, the random uncertainty in the $N_l(z)$ term in equation (15) will be considered. This term represents the derivation of O_3 number density based on the lidar backscattered signals. Since the lidar measurement at the ON and OFF wavelength are made independently and are not correlated in any way, the propagation of uncertainty through the $N_l(z)$ term is done by adding the uncertainty in the lidar measurements (at the ON and OFF wavelengths) in quadrature (Papayannis et al., 1990):

$$\Delta N_l(z) = \frac{1}{2\,\Delta\sigma_{O_3}\,\Delta z\,\sqrt{N}}\sqrt{\frac{2}{SNR^2{}_{ON}(z)} + \frac{2}{SNR^2{}_{OFF}(z)}} \qquad (27)$$

The spatial resolution is represented by Δz and was equal to 200 m. The number of laser shots in a temporally averaged profile is represented by N in equation (27). An example of the derived O_3 profile with calculated error bars (by using Eq. (27)) is shown in Fig. 3.19.

3.8.2 Error Analysis in Aerosol Correction Method

The uncertainties associated with the calculated backscatter and extinction coefficients at the UV wavelength are mostly due to the natural variability in particle size distribution measurements. Since the aerosol lidar ratio, the aerosol extinction coefficient at a reference altitude and the equivalent area radius of the particle were derived from the size distribution measurement, the uncertainty associated with these quantities can be accounted for by analyzing the size distribution measurements collected over the oil sands industry, upwind and downwind of the industry at different times and at different days to observe how much the lidar ratio, aerosol extinction coefficient (at a reference height) and the equivalent area radius of the particle can change. The variation of particle equivalent area radius, lidar ratio, and the extinction coefficient (at a reference altitude) in the oil sands region was used to determine the maximum change in the derived O_3 concentration. Thus, the variation in the particle size distribution measurement across the industry determines the uncertainty in the O_3 value due to the interference of aerosol.

3.8.2.1 Uncertainty from the Particle Equivalent Area Radius and Lidar Ratio

The equivalent area radius of the particle was derived by using the mean cross-sectional area of the particle size distribution measurements in equation (16) and for the same particle size distribution, the aerosol lidar ratio was calculated by using equations (17)-(19). The equivalent area radius as a function of time was analysed from particle size distribution measurements collected on five Convair-580 flights in

regions upwind, downwind and over the industry. An example of the particle equivalent area radius is shown as a function of time for an east-west transect across the oil sands region in Fig. 3.15(a) and the corresponding lidar ratio derived from the particle size distribution measurements in Fig. 3.15(b). Figure 3.15 can be divided into three regions: upwind (region I), over the oil sands (region II) and downwind of the industry (region III). Upwind of the industry (from 17:28 to 17:30), the equivalent area radius of the particle varies between 0.06 and 0.07 μm and is not different downwind of the industry. Over the industry, the equivalent area radius of the particle varies between 0.06 and 0.08 μm and an average value of 0.07 μm is calculated. In Fig. 3.15(b), there is no significant change in the lidar ratio upwind and downwind of the industry and is an average of 35 sr. Over the industry, the lidar ratio varied between 20 and 50 sr.

The uncertainty in the O_3 value due to aerosol corrections can be assessed by using lidar measurements collected over the oil sands region (in an area where strong gradients are present in the aerosol backscatter profile) and by using particle size distribution measurements in which the particle equivalent area radius varied between 0.06 and 0.08 μm. It was shown in section 3.3.1 that the top of the boundary layer in the aerosol backscatter height profile results in the maximum amount of change in the O_3 value due to the interference from aerosol. For this reason, lidar measurements collected over the industry were used to assess the uncertainty in the O_3 value due to the variation in the equivalent area radius of the particles.

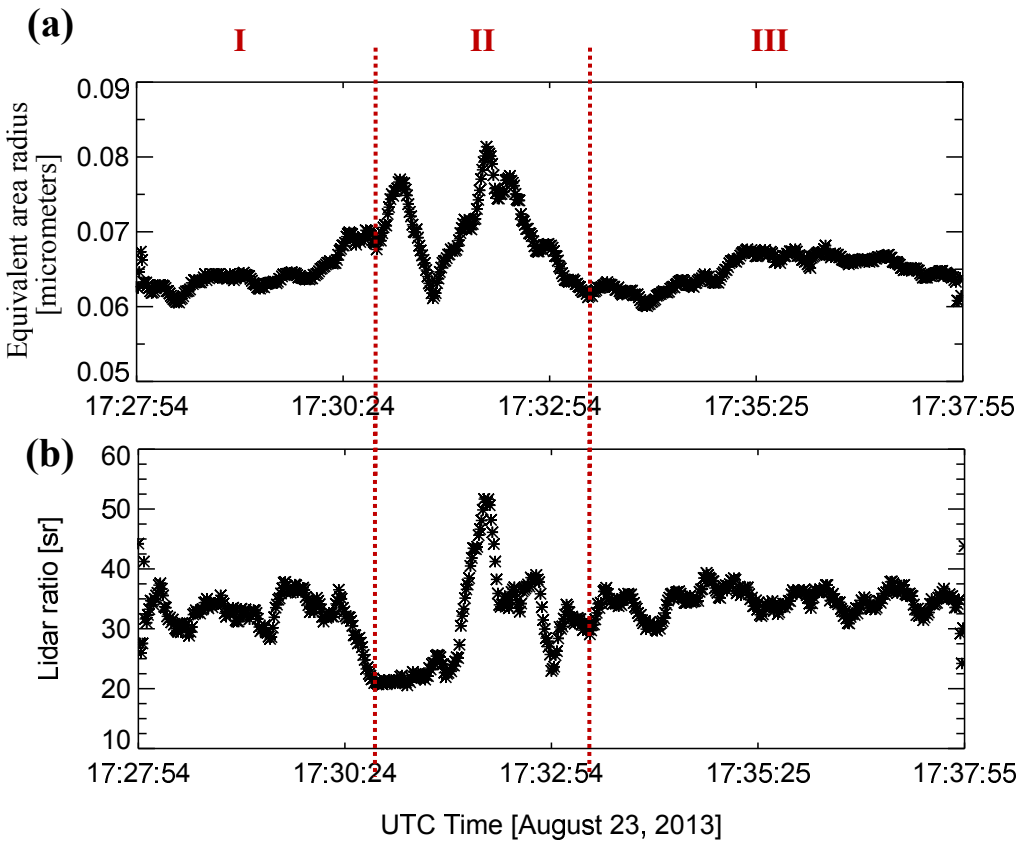

Figure 3.15: (a) The equivalent area radius of the particle and **(b)** lidar ratio derived from the particle size distribution measurements and plotted as a function of time for an east-west transect of the Convair-580 across the oil sands region on August 23, 2013. The location of the measurement is shown in Fig. 5.8. The dashed lines indicate three separate regions: I – upwind, II – over the oil sands, and III – downwind of the industry.

Figure 3.16(a) shows the aerosol extinction coefficient profile that was derived from the lidar measurements at a wavelength of 532 nm. A lidar ratio of 31 sr (which corresponds to an equivalent area radius of 0.07 μm) was used in Fernald's method to derive the extinction height profile in Fig. 3.16(a). Figure 3.16(b) shows the corresponding O_3 height profile with aerosol corrections applied by considering two additional particle size distribution measurements within the oil sands region. The

particle size distribution measurements resulted in an equivalent area radius of 0.06 and 0.08 μm and lidar ratios of 20 and 50 sr respectively. The O_3 mixing ratio in Fig. 3.16(b) derived with a particle equivalent area radii of 0.06 μm and 0.08 μm resulted in a bias of -5 ppbv and +3 ppbv respectively, within the boundary layer (for altitudes between 0.5 and 0.9 km). Small changes in the O_3 mixing ratio were observed above the surface boundary layer (where there are no strong gradients) between the equivalent area radii values of 0.06 and 0.08 μm.

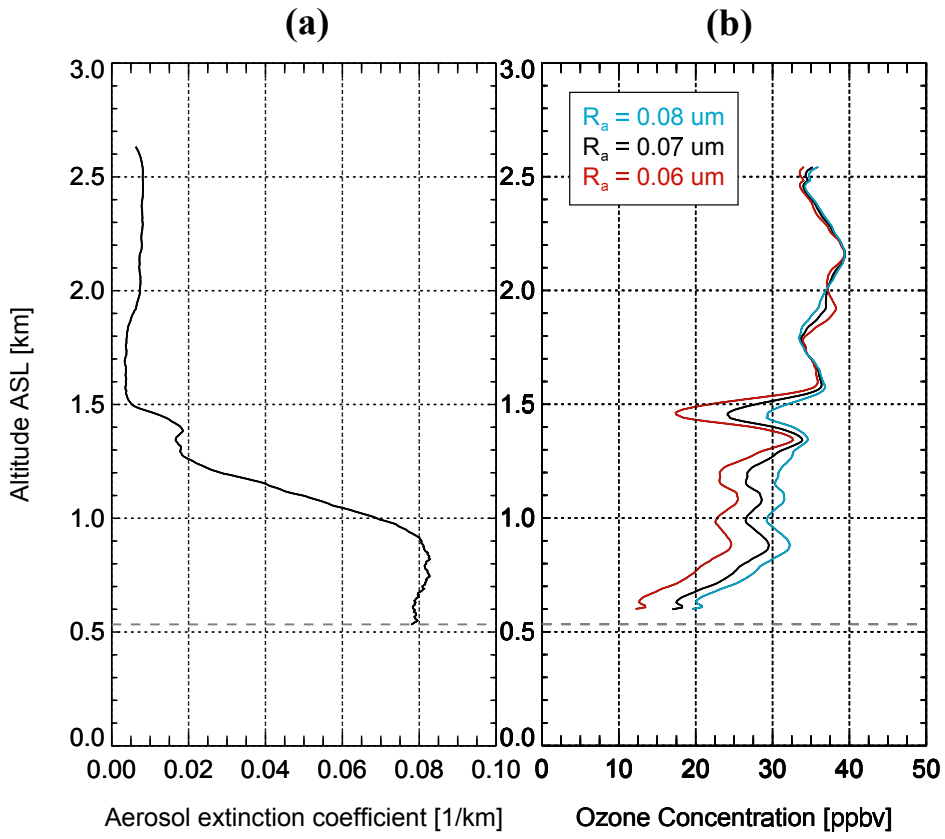

Figure 3.16: (a) The extinction coefficient derived from the lidar measurements. **(b)** The derived O_3 height profile from the lidar measurements by applying aerosol corrections for three different size distribution measurements. The dashed line close to an altitude of 0.5 km represents the height of the ground. The measurements shown here were collected on August 23, 2013 as the Twin Otter flew directly above the Fort McMurray oil sands industry.

3.8.2.2 Uncertainty from the Aerosol Extinction Coefficient

The aerosol extinction coefficient at a reference altitude for the lidar extinction retrieval was estimated from the in situ particle size distribution measurements (Eq. (17)) that were collected above the boundary layer between altitudes of 1.5 and 2.0 km ASL from the Convair-580 aircraft. For the measurement time period between August 22 and 26, 2013, the aerosol extinction coefficient varied between 0.002 km^{-1} and 0.014 km^{-1} at 1.7 km ASL in the Athabasca oil sands region. An average value of 0.008 km^{-1} was used as the reference aerosol extinction coefficient at an altitude of 1.7 km ASL for the extinction height profiles derived by using Fernald's method for the lidar measurements collected on all five Twin Otter flights.

Figure 3.17 illustrates the effect of changing the value of aerosol extinction coefficient at the reference height on the derived O_3 profile. The amount of bias in the O_3 retrieval is approximately ±2 ppbv at all heights from the ground to an altitude of 900 m ASL. The bias in the O_3 value is approximately ±1 ppbv above the surface boundary layer (beyond 1.5 km ASL in Fig. 3.17). Thus the uncertainty in the O_3 value by varying the reference aerosol extinction coefficient from 0.002 to 0.014 km^{-1} is about 2 ppbv within the boundary layer.

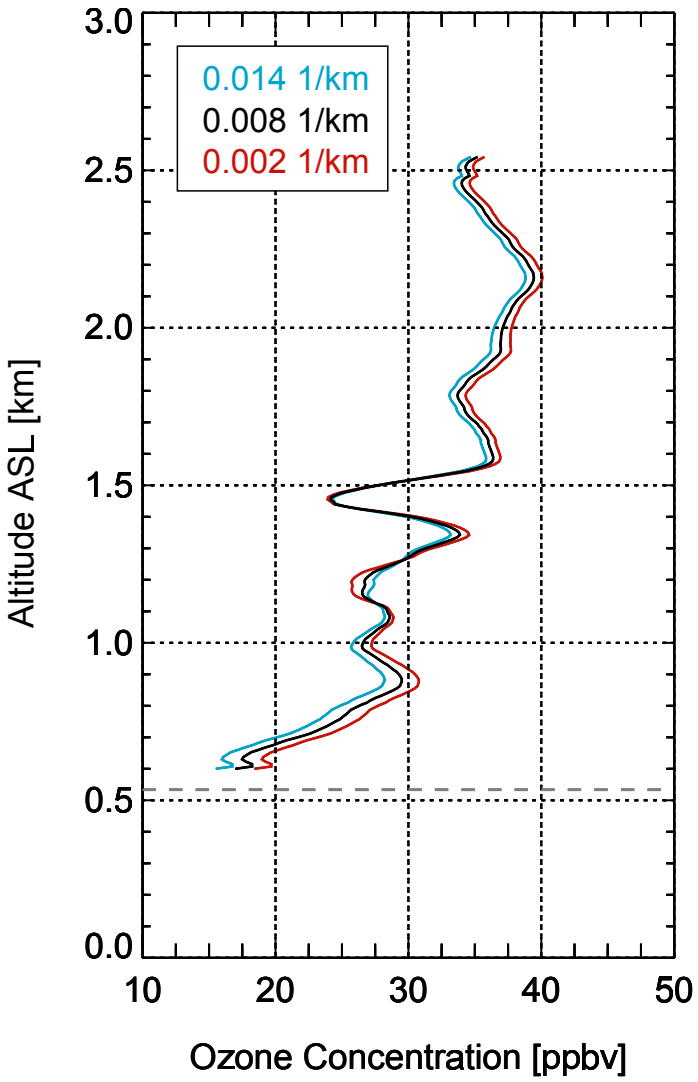

Figure 3.17: The derived O_3 mixing ratio from lidar measurements by using aerosol extinction coefficients of 0.002, 0.008, and 0.014 km^{-1} at a reference altitude of 1.7 km in Fernald's technique. The dashed line close an altitude of 0.5 km represents the height of the ground. The measurements shown here were collected on August 23, 2013 as the Twin Otter flew directly above the oil sands industry (same case as Fig. 3.16).

3.8.2.3 Uncertainty from the Particle Refractive Index

An assumption that was made for the aerosol correction presented in this dissertation was the value for the complex refractive index of particles. There is a systematic uncertainty in the O_3 retrieval from the assumption of the refractive index of particles used. In this study, the complex refractive index of compounds such as ammonium sulphate (Michel Flores et al., 2012), silicon dioxide (Gao et al., 2013), and toluene (Kozma et al., 2005) were used in Mie scattering calculations to assess the uncertainty in the O_3 value due to the interference of aerosol. In section 3.3.1 it was shown that using the refractive index of kaolinite accounted for a correction of up to 15 ppbv (at the top of the boundary layer) in the O_3 retrieval. The refractive index of the other compounds would change the correction by ± 4 ppbv. The uncertainty in the O_3 retrieval associated with using different refractive indices is within the envelope of potential bias to the variations in the aerosol size distribution as a function of position and time.

The overall uncertainty in the aerosol corrected O_3 profile was determined by adding up the individual uncertainties that are associated with the correction method. The uncertainties in the aerosol correction method originated from the variation in the particle size distribution and the extinction coefficient at a reference height. The total amount of change in the O_3 retrieval by using this aerosol correction technique was about ± 6 ppbv.

3.9 Validation of Ozone Lidar Measurements

The O_3 mixing ratio derived from lidar measurements (by applying the aerosol correction method presented in section 3.3.1) was compared with the in situ O_3 measurements that were collected by the Convair-580 aircraft. More information on the Twin Otter flight tracks is presented in chapter 5. In this section, two cases will be shown in which both the Twin Otter and Convair aircraft sampled the same region of air in terms of location and measurement time.

In situ measurements of O_3 were collected during two spiral ascents with the Convair aircraft on August 23, 2013. This provided a vertical distribution of O_3 for comparison with the lidar O_3 height profile. There were numerous times the Convair sampled the air in a spiral-ascending pattern and more cases will be shown in sections 5.1.1.2 and 5.1.1.3 of the comparison between the in situ O_3 measurements from the Convair spiral ascents and the lidar O_3 height profile.

For the comparison of measurements presented in this section, the locations where in situ O_3 measurements were collected during two spiral ascents are shown in Fig. 3.18 as A-in situ and B-in situ (indicated by a star-shape symbol). The Convair spiral ascent at point A-in situ in Fig. 3.18 was carried out in polluted air above the industry. The Twin Otter did not pass directly over this point; however the lidar measurements used for comparison were obtained 2.5 hours later at a location along the flight track where the back trajectory of the air passed over point A-in situ. The lidar and in situ measurements were in agreement within the limits of measurement

uncertainty in Fig. 3.19(a) and the O_3 mixing ratio was in the range 20 – 30 ppbv in the polluted air.

At point B-Lidar in Fig. 3.18, the Twin Otter aircraft collected measurements at a distance of 12 km away from the location of a Convair spiral ascent. At this point the air back trajectory did not pass over any pollution sources in the upwind direction and is referred to as unpolluted air. The measured lidar O_3 mixing ratio in Fig. 3.19(b) was in the range 30 – 40 ppbv from the ground to height 2.5 km in the unpolluted air.

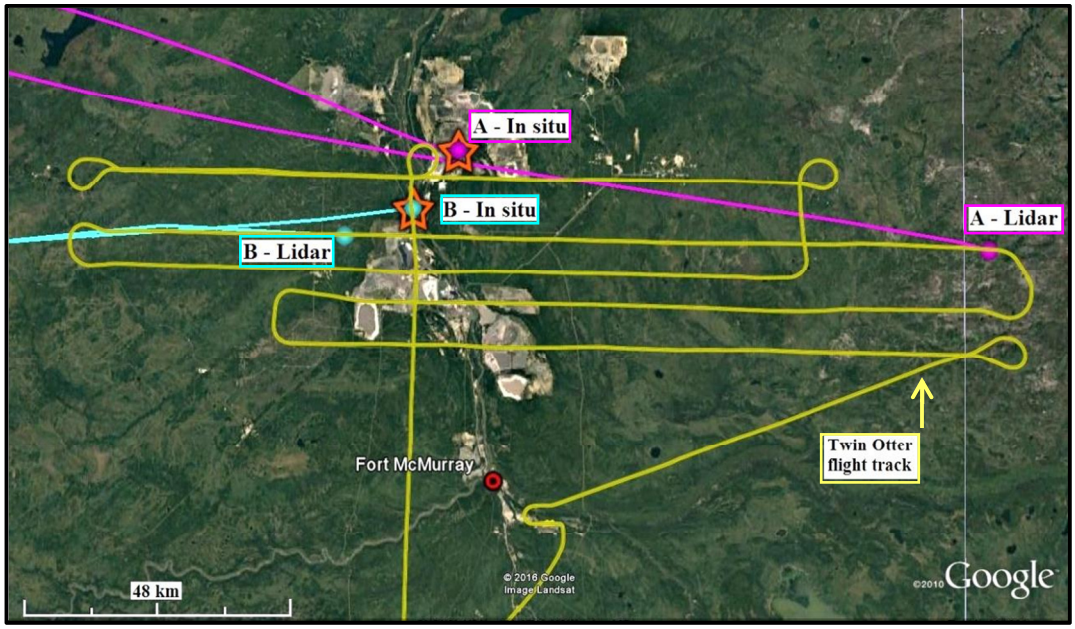

Figure 3.18: HYSPLIT back trajectories initiated from an altitude of 1 km ASL and around the same measurement time for comparison of lidar O_3 and in situ O_3 measurements on August 23, 2013. The in situ measurements were collected on a separate flight by Environment and Climate Change Canada and the location of the in situ measurement is represented by a star shape. The lidar measurements were taken from the Twin Otter aircraft (flight track shown in yellow). Backward trajectories coloured in blue and pink show the air coming from unpolluted and polluted areas respectively. Points labelled as A and B correspond to cases (a) and (b) in Fig. 3.19.

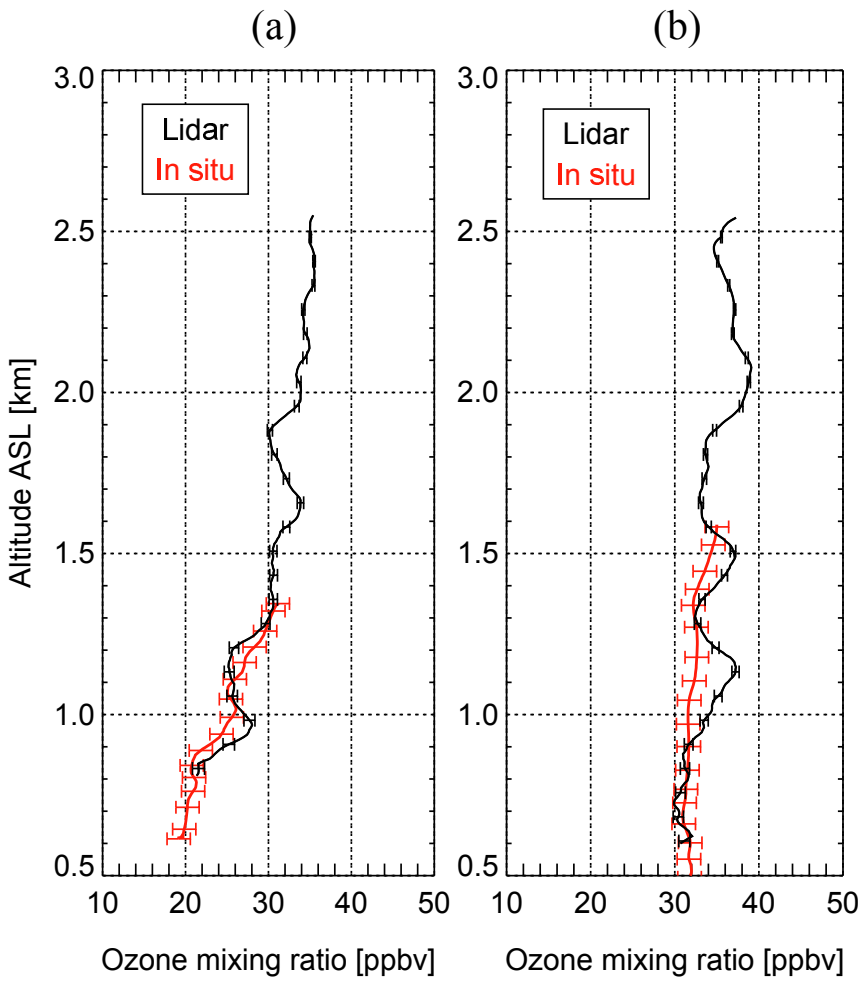

Figure 3.19: A comparison between the in situ O_3 and the lidar derived O_3 for the measurements taken in **(a)** polluted air and **(b)** unpolluted air. The location of the measurement is indicated in Fig. 3.18 as point A and B for cases (a) and (b) respectively.

The O_3 mixing ratios derived from the lidar measurements (by applying the aerosol correction method) are consistent with the in situ O_3 measurements collected within the oil sands region on the Convair aircraft.

4 Lidar Measurements above Toronto

4.1 Introduction

This chapter will present measurements of air pollution that were taken at York University, Toronto during the summer of 2010. The lidar system used for measurement collection during the period between May and August in 2010 is the same system as described in section 2.1, with the exception that the laser wavelength at 532 nm was not transmitted into the atmosphere and the lidar backscatter signal at a wavelength of 266 nm was not measured. The lidar wavelengths at 276.2, 287.2, and 299.1 nm were transmitted into the atmosphere for the Toronto air pollution study. The lidar system was operated from an atmospheric laboratory room on the fourth floor of the Petrie Science and Engineering Building in which an opened hatch allowed for upward viewing measurements.

Continuous measurements were collected with the stationary lidar system on weekdays from May to August in 2010. There were a few days in July of 2010 that were characterised by hot, humid, and stagnant conditions that are typically associated with poor air quality. These data are a good example of urban air pollution and serves

as a reference to compare with air pollution in the oil sands region. Measurements of pollution in the oil sands region will be shown in the next chapter.

4.2 Observations

There were four days in July 2010 that experienced hot and humid conditions. The Ministry of Environment and Climate Change issued a smog advisory and poor air quality rating on July 4-8, 2010. Lidar measurements collected over the four day period are shown in Fig. 4.1.

The aerosol backscatter ratio is the ratio of measured signal to expected signal if there was no aerosol. It represents the enhancement of the lidar signal due to aerosol scattering. An aerosol backscatter ratio of one represents scattering from molecules and any value greater than one indicates scattering from clouds and or aerosol. Figure 4.1(a) shows the attenuated aerosol backscatter ratio as derived from the lidar measurements at a wavelength of 299 nm and Fig. 4.1(b) shows the corresponding lidar derived O_3 mixing ratio. The depth of the surface boundary layer on July 5 to July 9 reached a maximum of 1.7 km in the afternoon. The top height of the surface boundary layer is approximated in Fig. 4.1(a) and is indicated by the dash line.

Three major pollution events were observed during July 6 – 8, which are characterized by O_3 mixing ratios greater than 80 ppbv in Fig. 4.1(b). Aerosols were mixed up to an altitude of approximately 1.7 km above ground during the pollution events. It was observed that the O_3 mixing ratio reached a maximum in the afternoon and persisted throughout the evening. These pollution events correspond to times

when the air quality index was rated as poor and smog advisory was issued in the Toronto region. The O_3 mixing ratio was observed to drop below 40 ppbv between an altitude of 1 km and 3 km above ground on July 5 and 7, 2010 in Fig. 4.1(b).

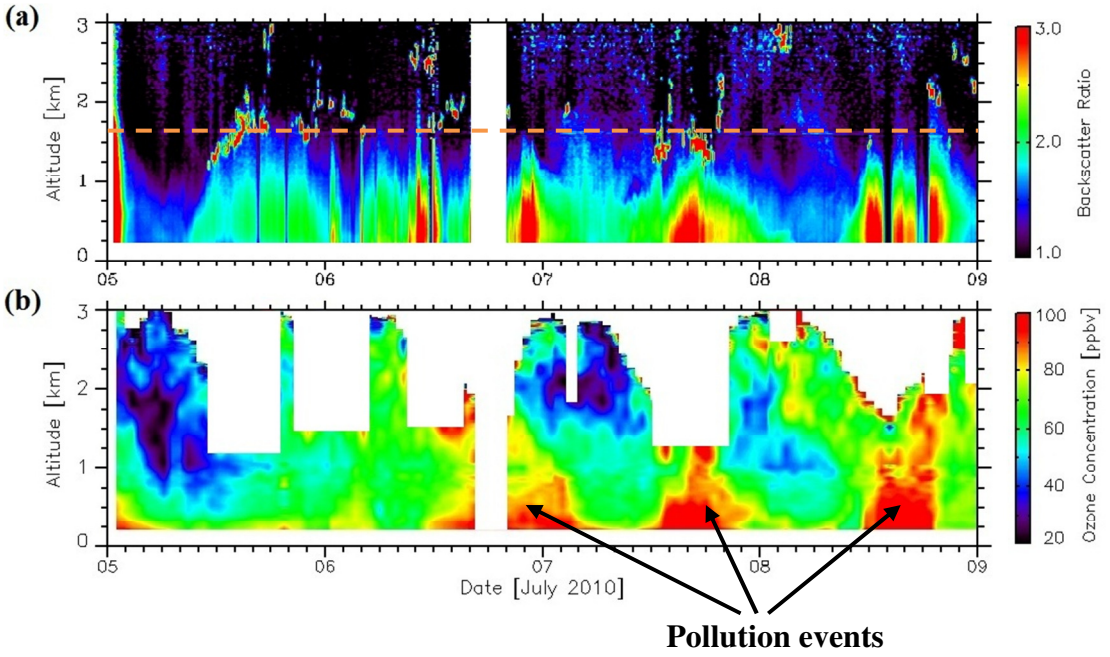

Figure 4.1: (a) The aerosol backscatter ratio derived from the lidar measurements at a wavelength of 299 nm. The dashed line represents the height of the surface boundary layer. **(b)** The O_3 mixing ratio derived from the lidar measurements over the four day period in July 2010. The white-out regions represent areas where the signal-to-noise ratio is small and where clouds were present. Altitude values are above ground level.

A section of the lidar aerosol measurements collected on July 6, 2010 from 22:00 to 23:30 local time is shown in Fig. 4.2(a). The aerosol extinction coefficient plotted as a function of altitude in Fig. 4.2(a) shows that aerosol is mixed throughout the boundary layer to a height of 1.75 km. The temperature profile obtained from a radiosonde launch at a weather station near Buffalo NY (100 kilometers to the

southwest of York University) on July 6, 2010 is plotted in Fig. 4.2(b). The presence of a temperature inversion is seen at a height of 1.75 km and corresponds to the top height of the surface boundary layer in Fig. 4.2(a).

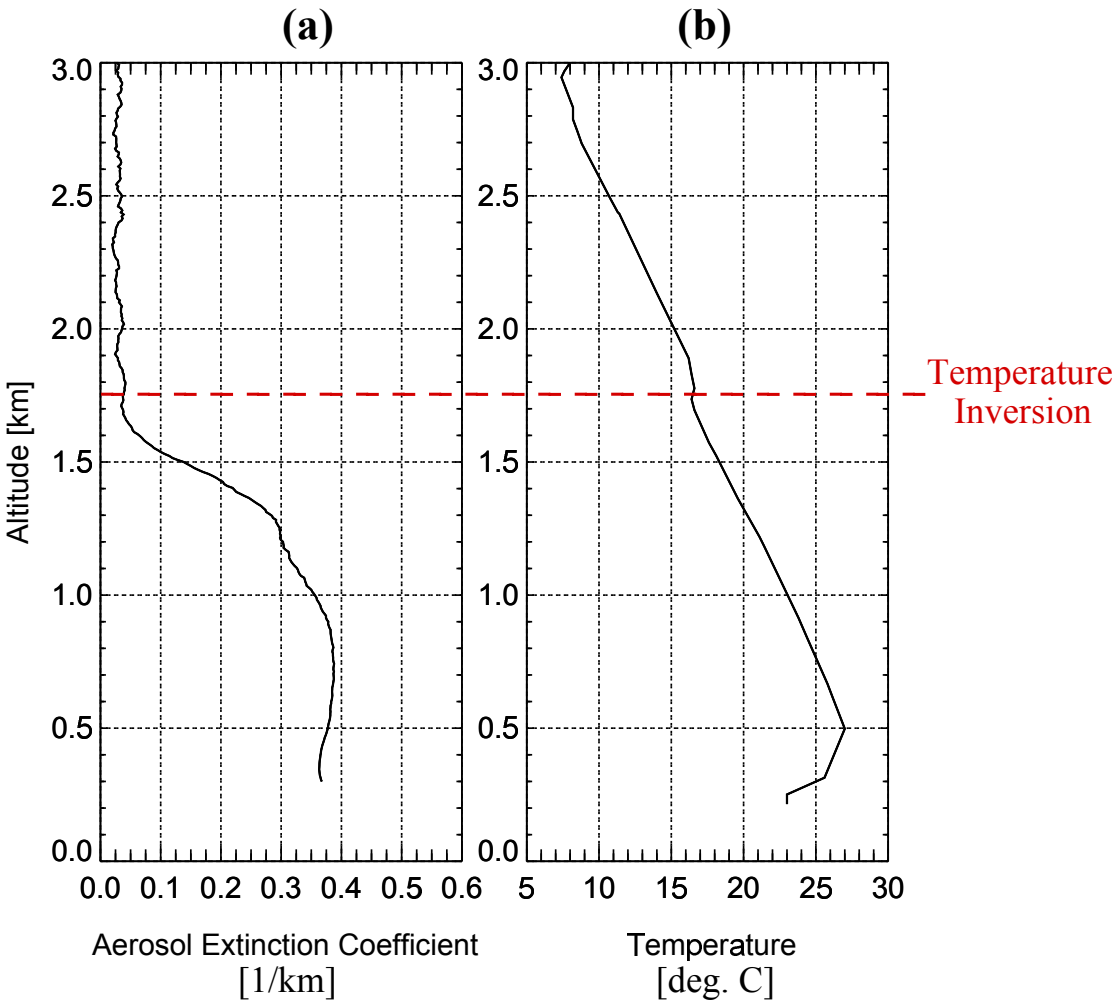

Figure 4.2: (a) The aerosol extinction coefficient derived from the lidar measurement at a wavelength of 299 nm on July 6, 2010. **(b)** A temperature profile from radiosonde measurements at Buffalo on July 6, 2010. A change in the temperature profile at 1.75 km indicates the height of the boundary layer. This is represented by the dash line.

Three backward air trajectories were initiated with the HYSPLIT model on the days that ozone pollution events were observed. In all of the cases, the trajectories revealed that the air came from the south west, as shown in Fig. 4.3.

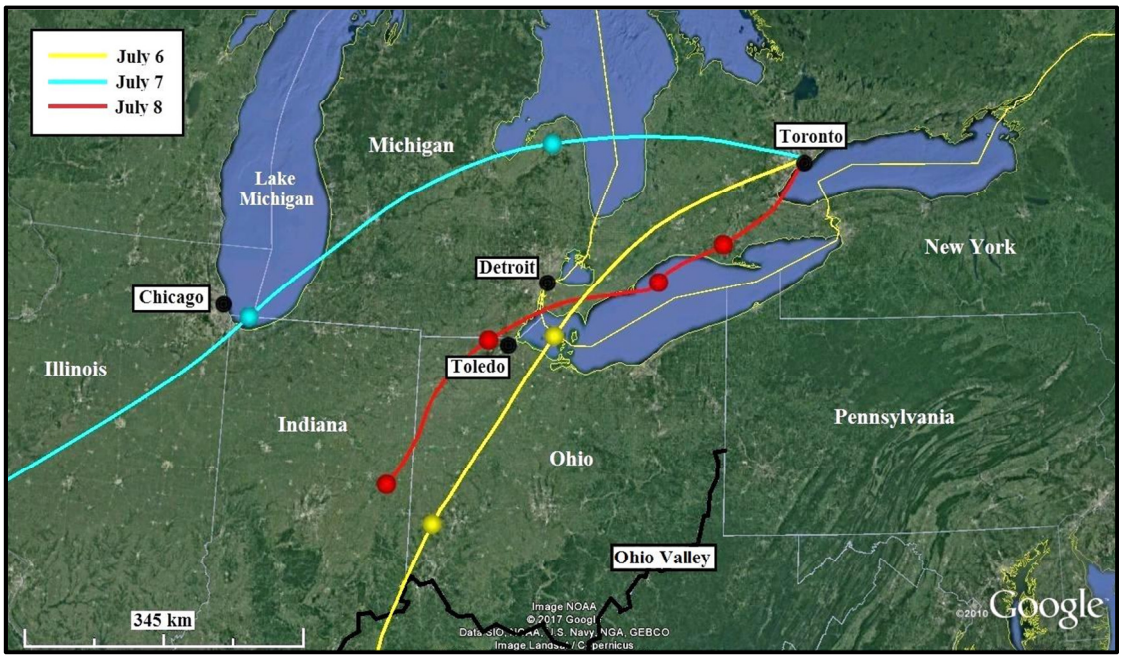

Figure 4.3: Backward trajectories initiated from an altitude of 700 m above ground on July 6 to July 8, 2010 at 6:00 PM local time from Toronto. Round marks along each trajectory represents a time interval of 12 hours. The Ohio Valley is located along the southern most border of Ohio and is represented by the black line.

The air trajectory on July 8th passed over the city of Hamilton which is located about 60 km to the southwest of Toronto. The sources of air pollution in Hamilton are mainly from the local industry and transportation. Hamilton contains many industrial plants that are used for manufacturing steel, petrochemical and paper products. Two major steel companies (Stelco and Dofasco) reside in the city of Hamilton and play a

major role in producing sixty percent of the country's steel products. Wallace et al. (2009) studied the air pollution in the Hamilton area using a mobile monitoring unit. They observed substantial amounts of SO_2 and NO_x pollution from Hamilton's local industry and traffic to exceed background levels.

Sources of industrial pollution to the southwest of the Great Lakes consist of oil and petroleum refineries in Toledo (Ohio) and steel mills and coal powered plants in Detroit (Michigan), Chicago (Illinois), and the Ohio Valley. The southern Lake Michigan shoreline houses many oil refineries, chemical plants and metal fabricating factories.

The air trajectories reveal that the pollutants released by the industry in Hamilton, Toledo, Ohio valley, Chicago, Detroit, and the southern Lake Michigan shoreline were transported to Toronto during the time that O_3 mixing ratios greater than 80 ppbv were observed.

4.2.1 In Situ Measurements in Toronto

The Ministry of the Environment and Climate Change has established air monitoring stations across Ontario that measure the concentrations of SO_2, NO_2, ground level O_3, and $PM_{2.5}$ to monitor the quality of air. Preliminary data are available to the public through their website (http://airqualityontario.com), although the data are not quality controlled. In situ measurements were collected at four sites in the Toronto area. The in situ sites (except the downtown Toronto site) were located at a radial distance of approximately 13.5 km from downtown Toronto and the measurement sites are shown in Fig. 4.4.

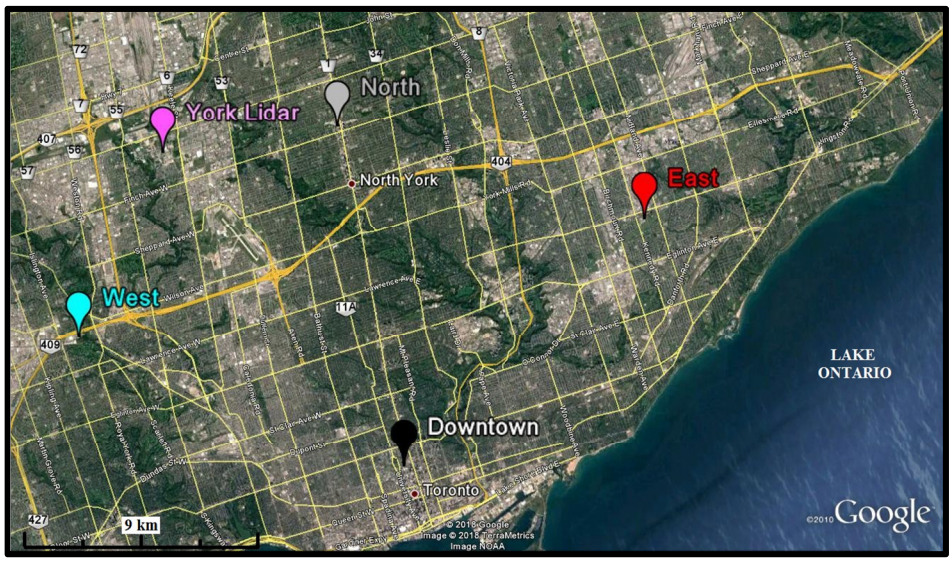

Figure 4.4: The location of four air monitoring stations in Toronto: downtown Toronto (black) and east (red), west (blue), and north (grey) of downtown Toronto. The location of the York University lidar (pink) is also shown as a reference.

In situ measurements of ground level O_3 collected during July 5 to 8, 2010 at the four sites are shown in Fig. 4.5. Ground level O_3 mixing ratios reached peak values between 80 and 100 ppbv during the afternoon on July 6 – 8.

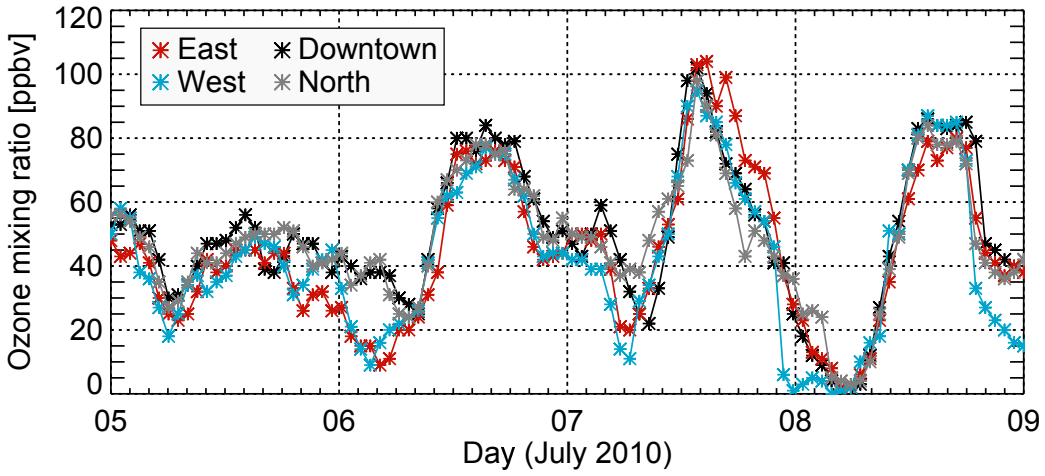

Figure 4.5: Ground level in situ O_3 measurements at four sites: downtown Toronto, east, north, and west of Toronto over the four day period in July 2010.

4.3 Discussion

Enhanced O_3 mixing ratios were observed in the air above Toronto during the afternoon to late evening on July 6 to July 8, 2010. Ozone mixing ratios of 100 ppbv were measured within the surface boundary layer and are much greater than the background value. Air monitoring stations located within the Toronto area show that ground level O_3 mixing ratios of up to 100 ppbv were measured during the same time period that the lidar observed enhanced O_3 values. The York University lidar system is capable of detecting high amounts of O_3 in Toronto's polluted air. The lidar measurements of O_3 are similar to those around Houston, Texas (Langford et al., 2010; Senff et al., 2010) and similar results of high O_3 mixing ratios were expected during the oil sands campaign.

The products of a complete combustion reaction are CO_2 and H_2O and incomplete combustion reactions produce additional pollutants such as NO, NO_2, CO, and hydrocarbons. Industrial emissions and automobile exhaust fumes emit such pollutants from incomplete combustion processes related to burning of fossil fuels or gasoline. The photochemical production of O_3 in the lower troposphere takes place by reactions of NO, NO_2, and VOCs in the presence of sunlight (Crutzen, 1979).

Air trajectory calculations revealed that the air came from the southwest during the time of smog advisories. Hence, the pollutants released by the industry in Hamilton, Toledo, the Ohio Valley, Chicago, and Detroit were transported to Toronto. In addition to the polluted south-westerly background air, the NO_x and VOC pollution emitted by vehicles in the rush hour time and the pollutants released from Toronto's

local industry were trapped near the surface due to a temperature inversion. Photochemical reactions in the presence of sunlight and under maximum surface temperature of 34°C led to an increase in ground-level O_3 that was observed in Toronto during the period between July 6 and July 8 in 2010. The development of photochemical smog is strongly influenced by the time of day, stagnant conditions, high ambient temperatures, and the source of NO, NO_2, and VOCs. Studies by Yap et al. (1988) and Geddes et al. (2009) also reported elevated O_3 mixing ratios in southern Ontario (during the summer months) to be highly correlated with south-westerly flow, high surface temperatures, and stagnant conditions.

5 Airborne Lidar Measurements over the Alberta Oil Sands Region

The results presented in this chapter are based on lidar measurements collected using a Twin Otter aircraft over the Alberta oil sands. The comparison with O_3 mixing ratio from ECCC's aircraft measurements and O_3 measurements collected from ground based air monitoring stations (maintained by Wood Buffalo Environmental Association) are also shown in this chapter. In this study, in situ measurements from the Convair-580 were collected on the same day as the Twin Otter aircraft, but the flight tracks were not identical. Long straight flight legs were used for the Twin Otter lidar measurements, while the Convair in situ measurements were more focused on specific pollution sources with climbing or descending spirals and boxes. This provided a vertical distribution of in situ O_3 measurements for comparison with the lidar O_3 height profile.

Meteorological data products that were available prior to flight planning were used to determine the direction of wind and aided in planning the flight tracks. The flights were designed to collect measurements along a line (either oriented parallel or perpendicular to the direction of wind) that includes regions upwind and downwind from the oil sands pollution sources. The Twin Otter flight tracks for the

measurements collected between August 22 and August 26, 2013 are shown in Figs. 5.1 to 5.5.

Lidar measurements collected upwind of the oil sands industry are representative of unpolluted air. Measurements collected downwind of the oil sands industry represent cases in which an air mass passed over a pollution source. Air trajectory calculations (from the HYSPLIT model) executed from the measurement point helped to determine whether or not the measured air passed over a pollution source.

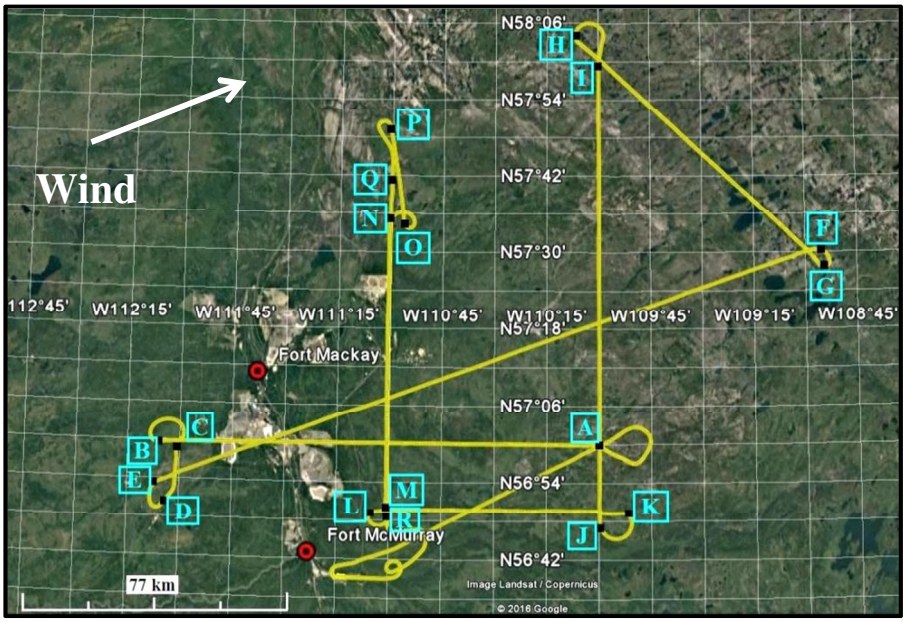

Figure 5.1: Flight track of the Twin Otter aircraft on August 22, 2013. The direction of wind at the start of the flight is represented by the arrow.

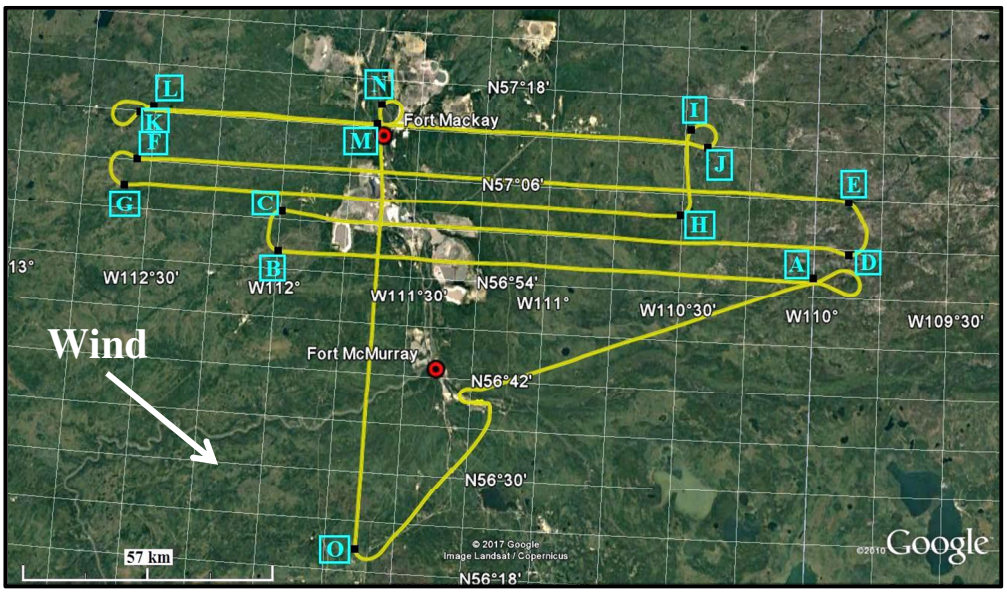

Figure 5.2: The track for the first Twin Otter flight on August 23, 2013. The direction of wind at the start of the flight is represented by the arrow.

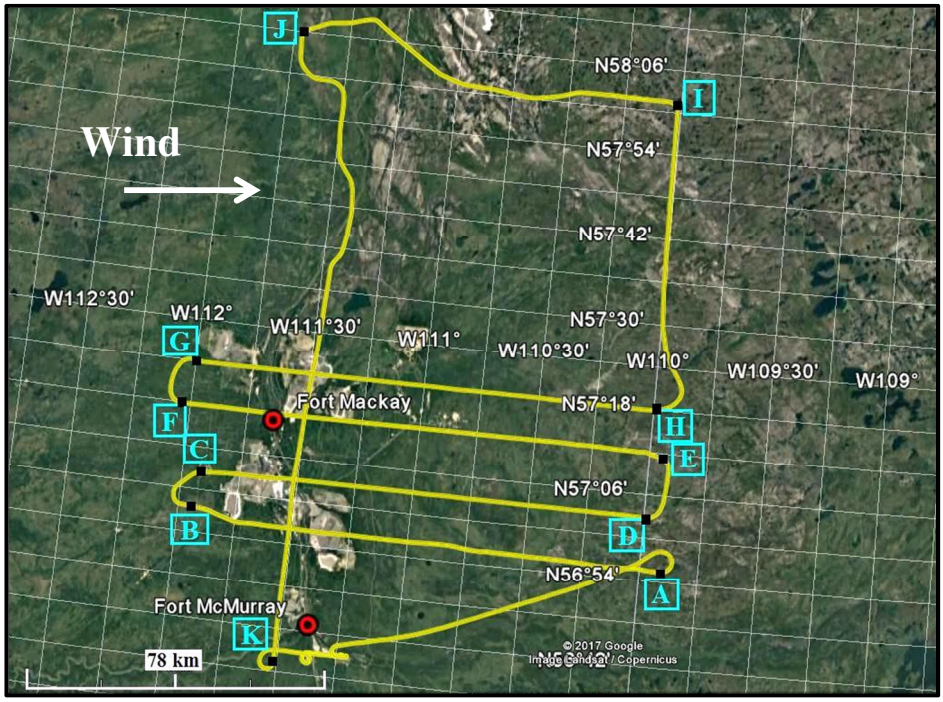

Figure 5.3: The track for the second Twin Otter flight on August 23, 2013. The direction of wind at the start of the flight is represented by the arrow.

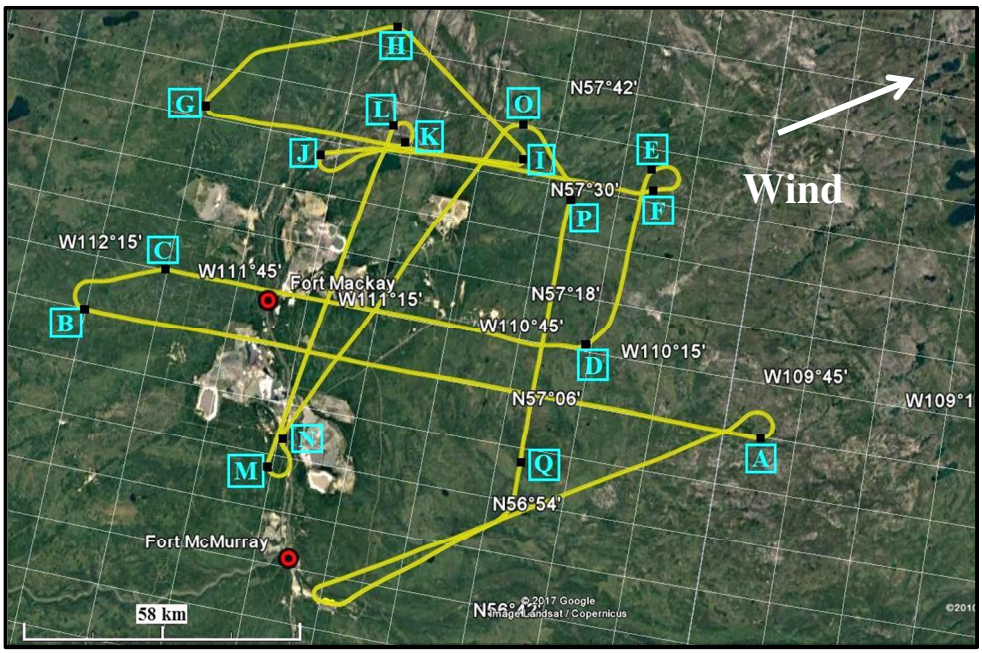

Figure 5.4: Flight track of the Twin Otter aircraft on August 24, 2013. The direction of wind at the start of the flight is represented by the arrow.

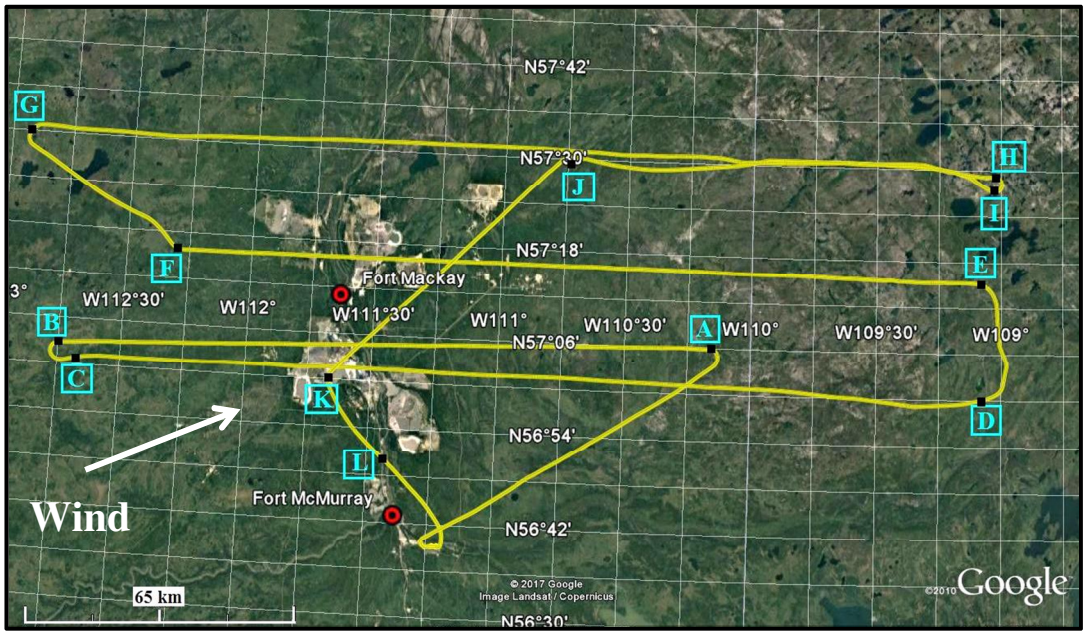

Figure 5.5: Flight track of the Twin Otter aircraft on August 26, 2013. The direction of wind at the start of the flight is represented by the arrow.

The flight tracks were designed to extend more than 100 km downwind (east and north) of the industry. Points labeled alphabetically on each flight track in Fig. 5.1 to Fig. 5.5 were used to represent the line segment for analysis and also provide information on start, end, and the direction of travel in alphabetical order.

5.1 Observations

5.1.1 Industrial Pollution

Lidar measurements of aerosol and O_3 that were taken along constant east-west and north-south transect across the industry as well as downwind of the industry are presented in this section.

A simple case of air pollution is presented here for one leg of the flight on 23 August 2013. The flight leg is shown in Fig. 5.6 and the Twin Otter aircraft traversed across the oil sands extraction industry from upwind (west, at point G) to downwind (east, at point H) at a height of 2.95 km ASL and at a constant latitude of N57°03'.

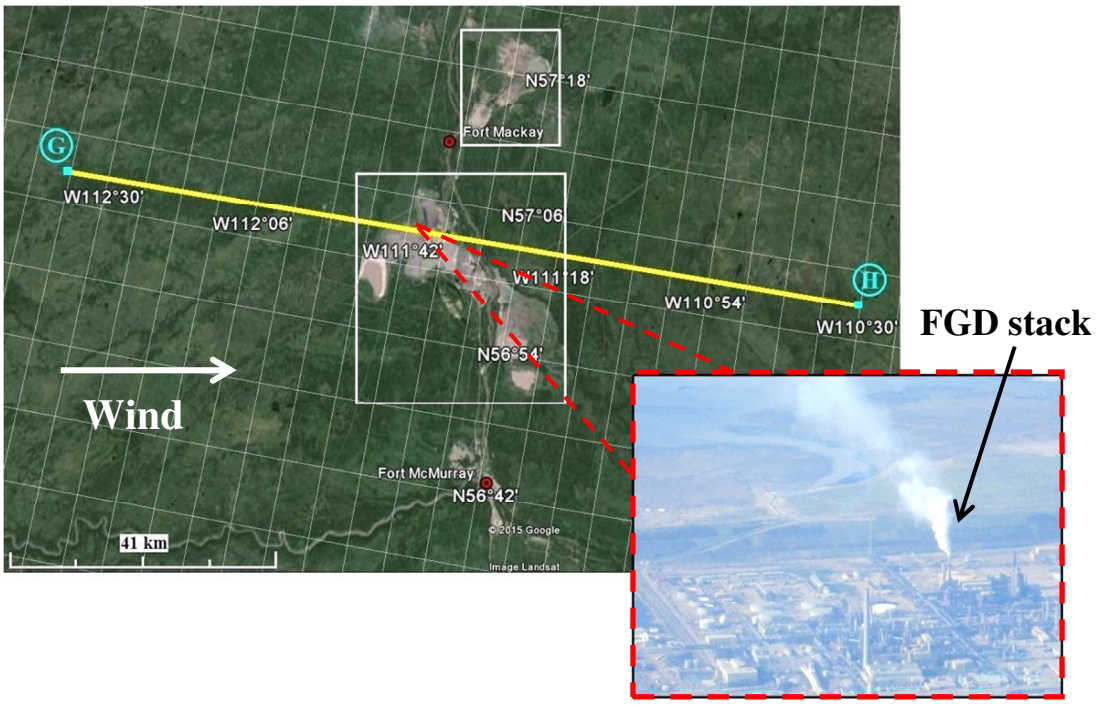

Figure 5.6: The flight segment G-H on August 23, 2013 displayed on GoogleEarth. Point G represents the starting position of the flight leg and point H the ending position. The oil sands industry was contained within the regions outlined in white. The average direction of the wind on August 23, 2013 at the measurement time is presented by the arrow. Inset photo shows the flue-gas desulphurization (FGD) stack that was intersected over the Syncrude Mildred Lake facility.

The aerosol extinction coefficient and the O_3 mixing ratio derived from the lidar measurements along this flight leg are shown in Fig. 5.7. Measurements collected upwind of the industry (closer to point G and distances up to 20 km from the start of the flight leg) in Fig. 5.7(a), show insignificant amounts of aerosol present in this region. In the oil sands region, aerosol typically occurs in the form of dust and other finer compounds such as secondary organic aerosol (Liggio et al., 2016).

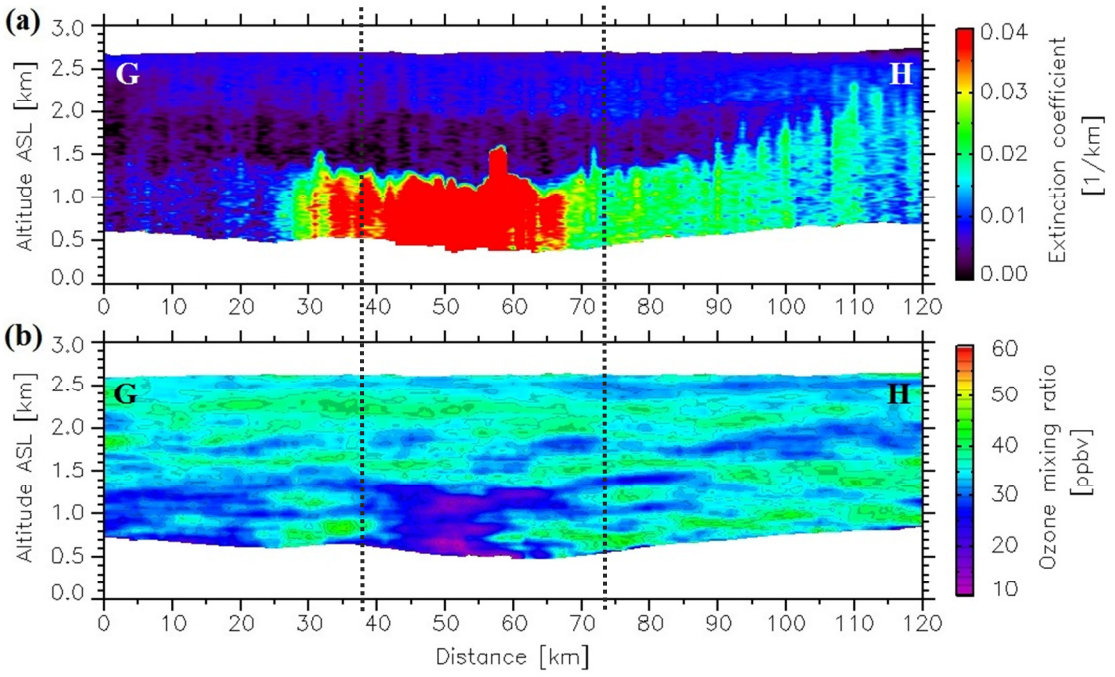

Figure 5.7: (a) The aerosol extinction coefficient derived from the lidar measurements at a wavelength of 532 nm and **(b)** the ozone mixing ratio derived from the lidar measurements for the flight segment G-H on August 23, 2013. The height is above sea level (ASL) and the distance is along the flight segment in Fig. 5.6. The measurements contained within the vertical dashed lines represent the part of the flight segment directly above the oil sands contained within the regions outlined in white in Fig. 5.6.

Figure 5.7(a) shows that significant amounts of aerosol were observed over the industry (the distance between 30 and 62 km along the flight leg); although, downwind of the industry (distance between 90 and 120 km along the flight leg) the aerosols dispersed out to heights of up to 2.5 km ASL (or 1.8 km above ground). The depth of the boundary layer over the industry was observed to be 1.5 km ASL (or 1 km above ground). Boundary layer heights typically range between 1.2 km and 1.5 km ASL in the late afternoon during summer in Alberta. For example, Howell et al. (2014) determined the height of the boundary layer to be 1.2 km ASL (or 800 m

above ground) from the lidar measurements collected near the Alberta oil sands facilities in July 2008. Portelli, (1977) studied mixing height measurements from 33 rawinsonde stations located across Canada and reported the maximum height at Fort Smith (NWT) and Edmonton (AB) stations (for the month of August) to be 1.54 km and 1.56 km above ground respectively. The height of the boundary layer as determined from the lidar measurement in this study agrees with the values reported in previous literature (Portelli, 1977; Howell et al., 2014).

Flue-gas desulphurization (FGD) stacks serve to remove sulphur dioxide (SO_2) emissions from the processes related to bitumen and heavy oil upgrading. The FGD stack from Syncrude Mildred Lake operators was intersected during the section of the flight leg over the oil sands industry as shown in Fig. 5.6. The FDG stack is 95 m in height, has a diameter of 6.1 m (National Pollutant Release Inventory, NRPI; http://www.ec.gc.ca/inrp-npri/. Date accessed: July 2016) and is situated at N57°03' and W111°39'. The FGD stack located at Synrcude Mildred Lake facility is characterized as a "wet stack" because the escape gases are saturated with water vapour. The condensation of water vapour in the exhaust flue gases from the stack is seen in the lidar aerosol measurements in Fig. 5.7(a), as the existence of a vertical feature between the distances of 55 to 60 km from the start of the flight leg.

The measured O_3 mixing ratio along this flight segment is shown in Fig. 5.7(b). As the pollution travelled downwind (distances greater than 70 km along the flight leg in Fig. 5.7(b)), it dispersed by mixing with the background air. The O_3 mixing ratio downwind of the industry is between 25 and 40 ppbv, and values higher than 45 ppbv

were not observed. Regions of increased amounts of aerosol and reduced O_3 mixing ratios between 15 and 34 ppbv were observed directly above the oil sands industry (between a distance of 45 and 65 km along the flight leg).

5.1.1.1 Explanation of Low O_3 in the Oil Sands Industry

Nitric oxide is one of the many pollutants emitted by oil sands operations and the production of NO in the lower troposphere can be attributed to high temperature combustion reaction with gasoline and oil (Ismail and Umukoro, 2016). In section 5.1.1 (Figs. 5.6 and 5.7), lower than background mixing ratios of O_3 from lidar measurements were observed and in this section, in situ measurements of NO, NO_2, and O_3 from the Convair aircraft were analyzed to investigate the source of low O_3.

A flight segment of the Convair aircraft on August 23, 2013 that travelled at a constant altitude (from west to east) while intersecting the oil sands industry is shown in Fig. 5.8.

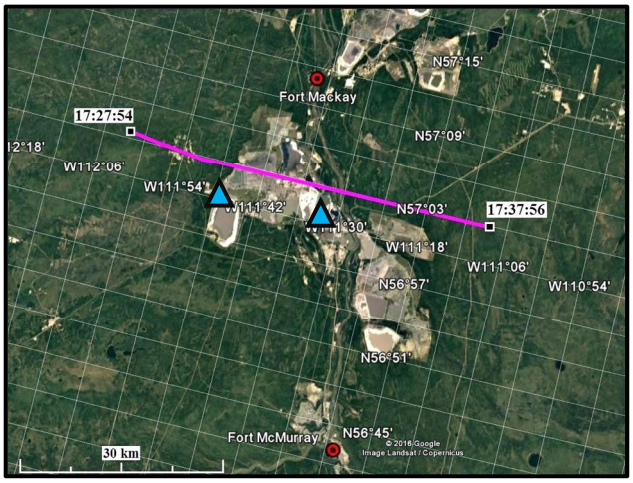

Figure 5.8: A section of the Convair flight on August 23, 2013 is shown in pink. In situ measurements were collected from west to east. The start and end times are indicated beside the end points of the flight section. The triangular marks indicate the intersection points of the oil sands industry along the Convair's flight path.

Figure 5.9 shows the in situ measurements of O_3, NO, and NO_2 mixing ratio taken along the section of the Convair's flight track at an altitude of 650 m ASL. In regions upwind and further downwind of the oil sands industry, relatively small amounts of NO were observed where NO mixing ratios were less than 2 ppbv. In such cases, the O_3 mixing ratio ranged between 25 and 30 ppbv. Directly over the oil sands industry (the region in Fig. 5.9 contained within the dashed lines), an increase in the mixing ratio of NO to 25 ppbv is observed and the O_3 mixing ratio decreased from 30 ppbv to 13 ppbv. The reduction in O_3 over the industry is consistent with NO titration: $NO + O_3 \rightarrow NO_2 + O_2$. In other words, every destroyed O_3 molecule corresponds to a new NO_2 molecule. In Fig. 5.9, the mixing ratio of NO_2+O_3 as a function of time is nearly constant across the flight segment and this demonstrates that NO titration can explain the reduced O_3 mixing ratios observed in pollution over the industry.

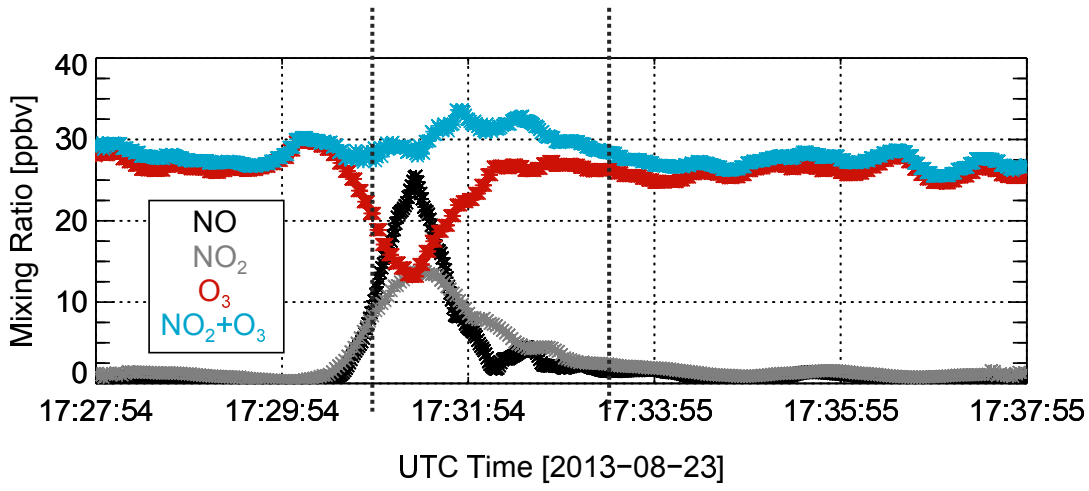

Figure 5.9: In situ measurements of O_3, NO, and NO_2 taken from a section of the Convair's flight on August 23, 2013 along the east-west direction over the oil sands industry and within the boundary layer. The measurements contained within the dashed lines represent the section of the Convair's flight directly over the oil sands industry.

5.1.1.2 Measurements Above the Oil Sands Industry

The oil sands industry was intersected more than once from the west to east and east to west directions (Figs. 5.1 – 5.5). A few examples of lidar measurements taken along W-E and N-S transects across the oil sands industry are shown below as well as the corresponding flight segment and air trajectory analysis.

The segment A-B for the flight on August 22, 2013 is shown in Fig. 5.10. The starting position of the flight segment occurs at point A and the ending position at point B. The corresponding lidar measurements collected along the flight segment A-B on August 22, 2013 are shown in Fig. 5.11.

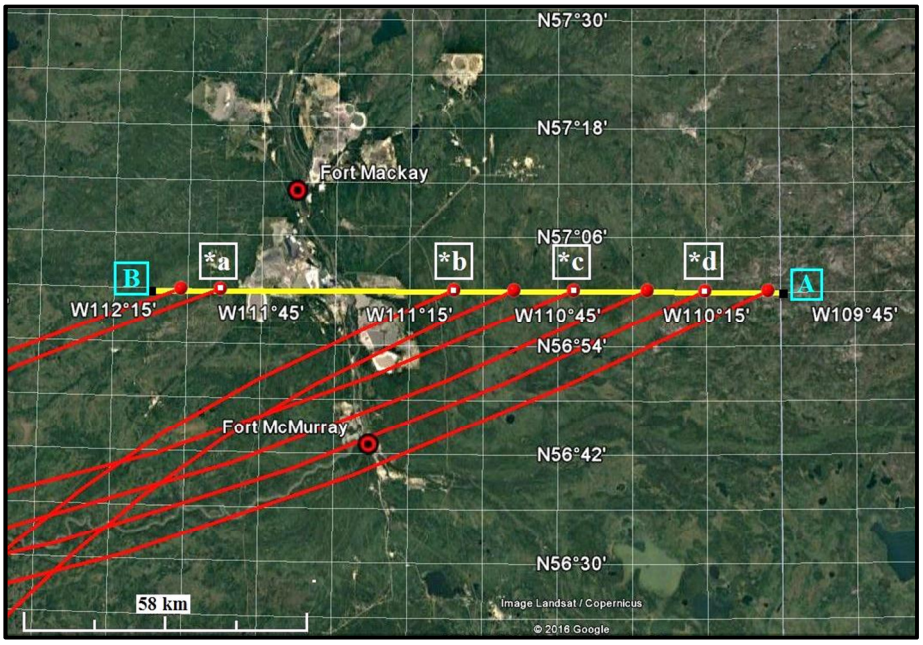

Figure 5.10: The flight segment A-B on August 22, 2013 is represented by the yellow line. Point A represents the starting position of the flight leg and point B, the ending position. Backward air trajectories initiated from an altitude of 850 m above sea level on August 22, 2013 at 18:30 UTC are shown in red and are indicated as points *a to *d along the flight segment.

Along this flight segment, the oil sands industry was intersected between a distance of 15 and 55 km in Fig. 5.11(a) and significant amounts of aerosol were observed in this region. The O_3 mixing ratio shown in Fig. 5.11(b) varies between 18 and 34 ppbv within the areas of industrial pollution.

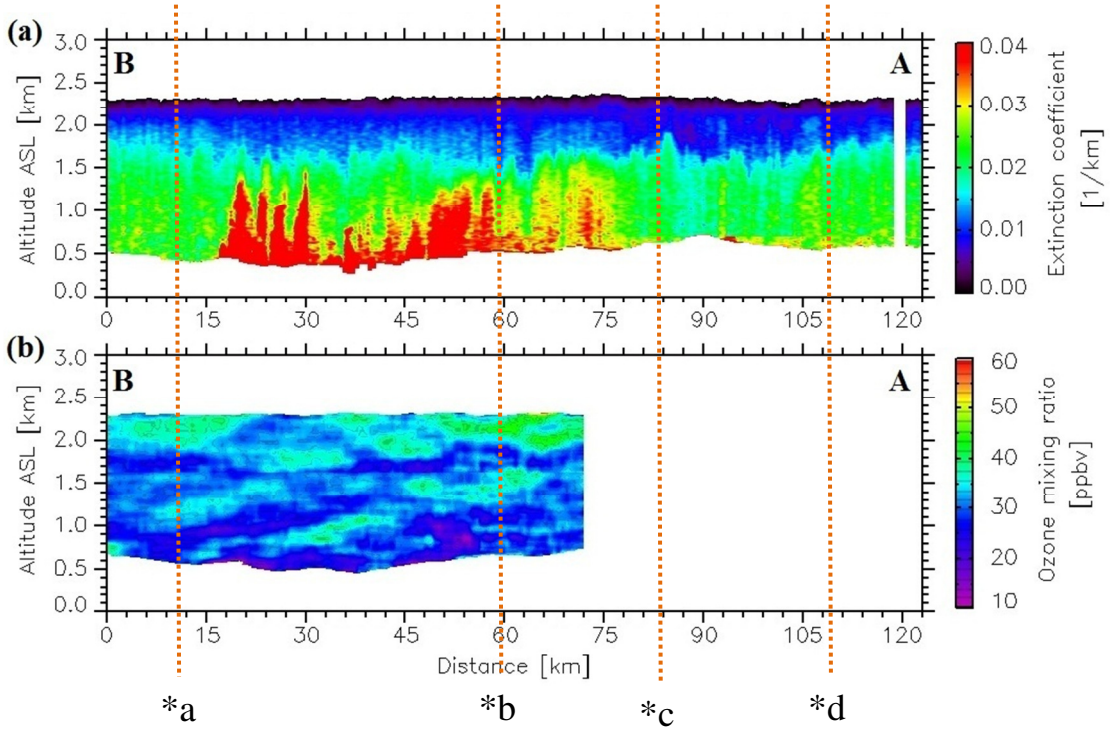

Figure 5.11: (a) The aerosol extinction coefficient measured at a wavelength of 532 nm and **(b)** the ozone mixing ratio derived from the lidar measurements for the flight segment A-B on August 22, 2013. Distance is along the flight segment in Fig. 5.10. Backward air trajectories were initiated along the measurement path and are represented by points *a to *d. These points are also marked along the flight segment in Fig. 5.10.

Lidar measurements were not collected at the UV wavelengths for distances greater than 75 km along the flight segment in Fig. 5.11(b). The lidar system was being aligned during this period. The blank section in Fig. 5.11(b) is due to a pause in

the UV measurements while alignment of the transmitter to the receiver was being optimized.

The segment E-F for the flight on August 22, 2013 is shown in Fig. 5.12. The oil sands industry was intersected at the start of the flight leg (closer to point E in Fig. 5.12) and measurements of aerosol backscatter and O_3 were collected up to a distance of approximately 160 km downwind of the oil sands industry. Lidar measurements taken along this flight segment are shown in Fig. 5.13.

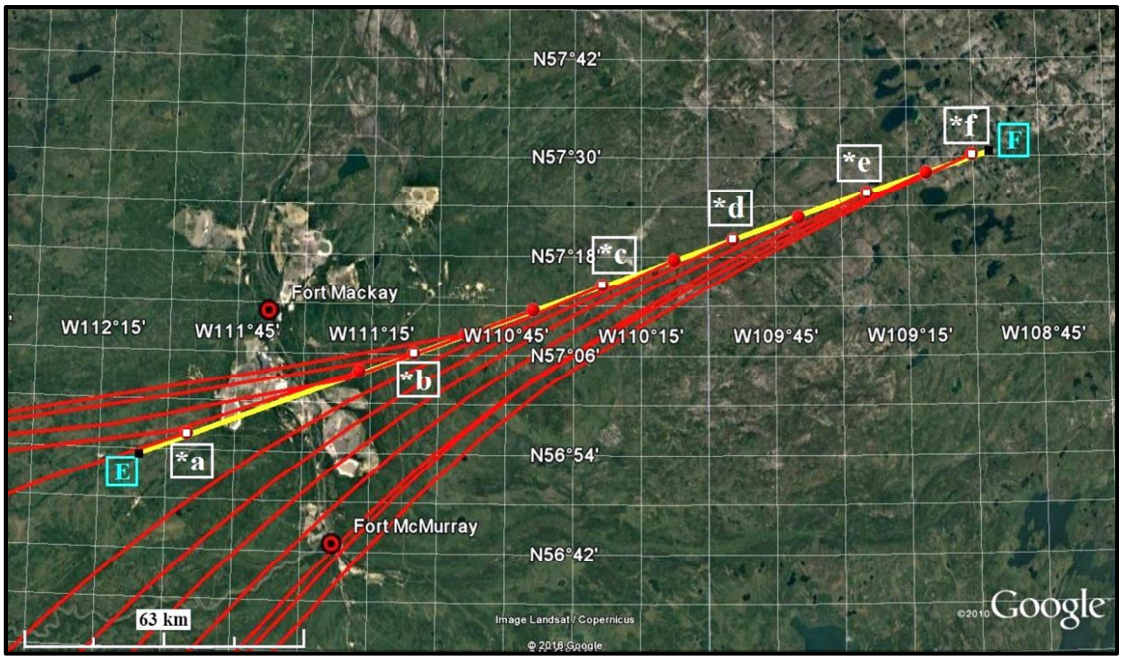

Figure 5.12: The flight segment E-F on August 22, 2013 is represented by the yellow line. Point E represents the starting position of the flight leg and point F, the ending position. Backward air trajectories initiated from an altitude of 1000 m above sea level on August 22, 2013 at 19:00 UTC are shown in red and are indicated as points *a to *f along the flight segment.

Distances between 20 and 55 km in Fig. 5.13 represent the intersection of the oil sands industry along the flight path. Significant amounts of aerosol were observed over the industry in which O_3 mixing ratios between 20 and 35 ppbv were observed in the pollution from the industry. Aerosol was present downwind of the industry between 60 and 90 km along the flight segment in Fig. 5.13(a) and this is not associated with enhanced O_3 mixing ratios.

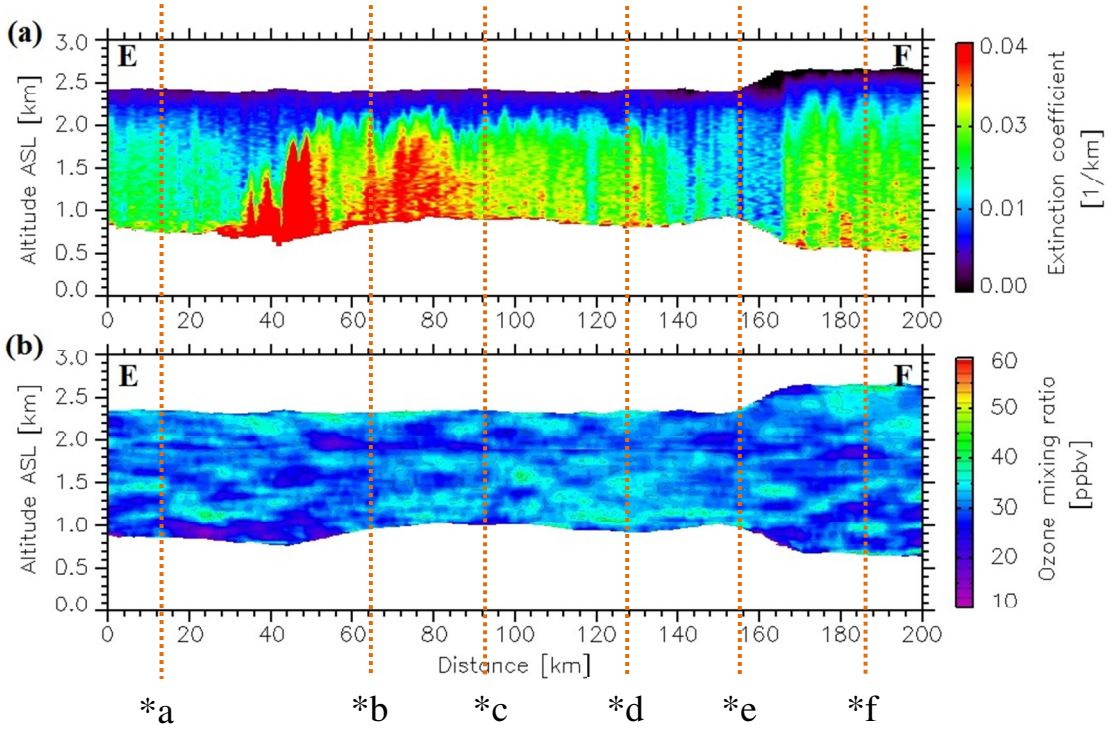

Figure 5.13: (a) The aerosol extinction coefficient measured at a wavelength of 532 nm and **(b)** the ozone mixing ratio derived from the lidar measurements for the flight segment E-F on August 22, 2013. Distance is along the flight segment in Fig. 5.12. Backward air trajectories were initiated along the measurement path and are represented by points *a to *f. These points are also marked along the flight segment in Fig. 5.12.

The flight segment C-D for the flight on August 23, 2013 is shown in Fig. 5.14. The oil sands industry was intersected closer to point C (the starting position of the flight leg) and measurements were collected up to a distance of approximately 80 km downwind of the oil sands industry. Lidar measurements taken along this flight leg are shown in Fig. 5.15. The results are similar to the previous cases: large values of aerosol extinction coefficients (from the start of the flight leg and up to a distance of 45 km in Fig. 5.15(a)) are associated with pollution from the industry in which the O_3 mixing ratio within the boundary layer and in the industrial pollution range between 16 and 32 ppbv.

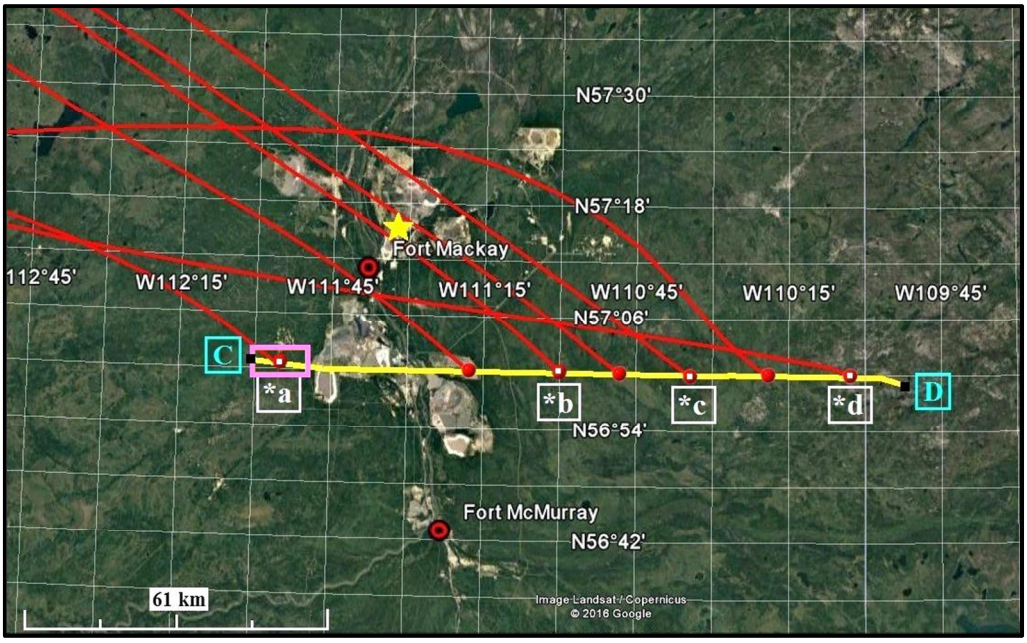

Figure 5.14: The flight segment C-D on August 23, 2013 is represented by the yellow line. Point C represents the starting position of the flight leg and point D, the ending position. Backward air trajectories initiated from an altitude of 800 m above sea level on August 23, 2013 at 18:00 UTC are shown in red and marked by the points *a to *d. The star shaped symbol represents the location of Convair's spiral ascent and the pink box along the flight segment C-D represents the location of lidar measurements for comparison with in situ.

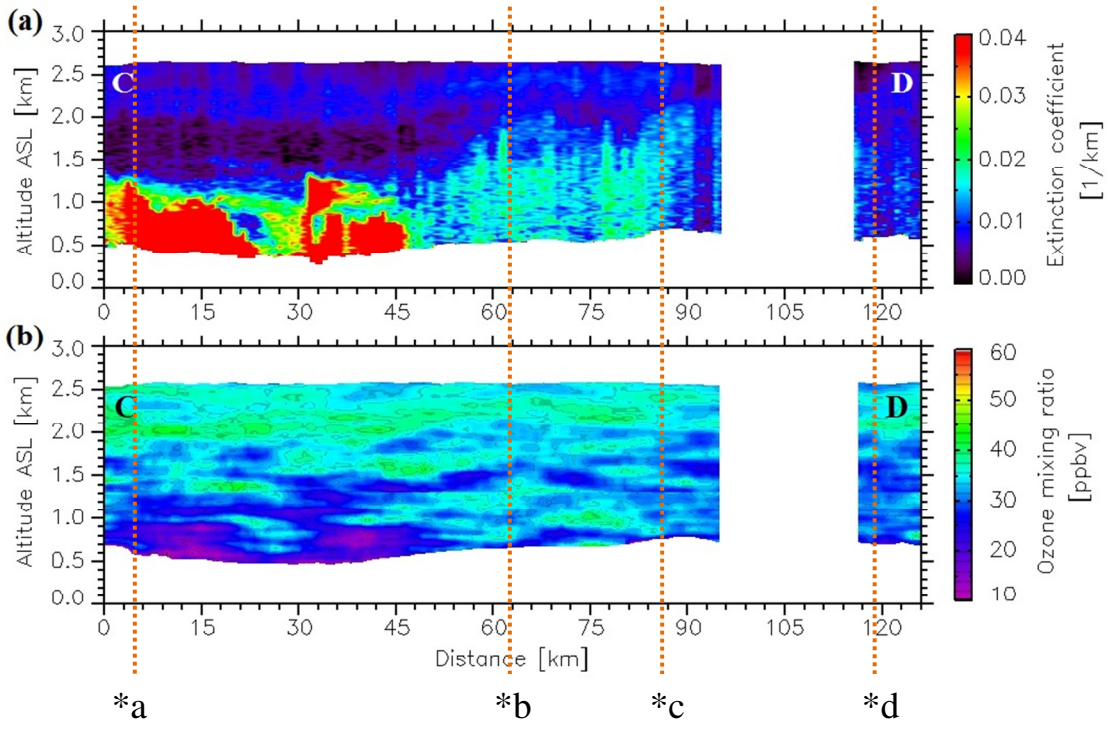

Figure 5.15: (a) The aerosol extinction coefficient measured at a wavelength of 532 nm and **(b)** the ozone mixing ratio derived from the lidar measurements for the flight segment C-D on August 23, 2013. Backward air trajectories were initiated along the measurement path and are represented by points *a to *d. These points are also marked along the flight segment in Fig. 5.14. The vertical white-section represents cloudy regions and lidar measurements collected within clouds were not used in the analysis.

The depth of the surface boundary layer over the industry (for distances between 0 and 45 km along the flight leg) is seen in Fig. 5.15(a) and has a value of approximately 1.3 km ASL (or 1 km above ground). The surface boundary layer height gradually increased from 1.3 km to 2.0 km ASL (or 1 km to 1.5 km above ground) downwind of the industry, or for distances greater than 45 km in Fig. 5.15(a). Downwind of the industry O_3 mixing ratios between 28 and 37 ppbv were measured within the boundary layer.

The measured values of O_3 mixing ratio over the industry are different within the boundary layer and above the boundary layer. An example of this is observed in Fig. 5.15(b) for distances between 6 and 45 km along the flight leg. In order to understand the difference in the O_3 mixing ratio above and within the surface boundary layer, lidar measurements taken between the first 9 km of this flight segment (location of lidar measurements is indicated in Fig. 5.14 by a pink box along the C-D flight segment) were compared to a Convair spiral ascent taken around the same time as the lidar measurement and over the oil sands industry. The location of the Convair spiral ascent is indicated in Fig. 5.14 by a star-shaped symbol. An area of significant amounts of pollution as observed from the lidar measurements (along the flight segment C-D) was chosen to compare with the in situ spiral ascent above the oil sands industry. The comparison of O_3 measurements in polluted air is shown in Fig. 5.16(a). Good agreement between the O_3 measurements from the in situ instrument and the lidar occur below 1.0 km ASL.

The uncertainty in the aerosol correction method was discussed in section 3.8.2. It was shown that the variation in the equivalent area radius of oil sands particles accounted for an uncertainty of approximately ±5 ppbv in the calculated O_3 value. This uncertainty does not have a significant impact on the calculated O_3 value as there is good agreement in Fig. 5.16(a) between the in situ O_3 measurements and the aerosol corrected O_3 from lidar measurements. The O_3 profile as derived from lidar measurements without applying the aerosol correction is also shown in Fig. 5.16(a) as a dashed line. The difference in the uncorrected O_3 and the aerosol corrected O_3

values (between altitudes of 0.5 and 1.3 km in Fig. 5.16(a)) are almost 15 ppbv and this is greater than the uncertainty due to the variation in the equivalent area radius of the particle. Thus, the uncertainty in the aerosol correction method doesn't have an impact on the results.

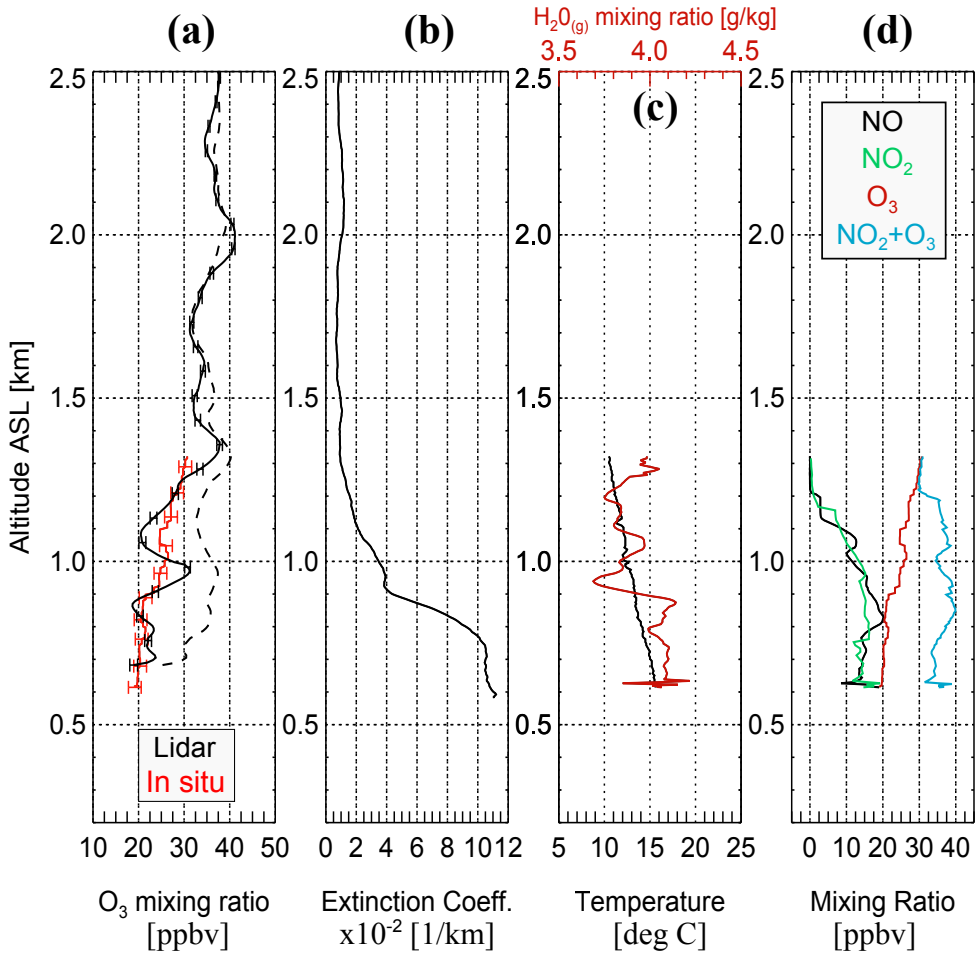

Figure 5.16: (a) A comparison between the in situ O_3 and lidar O_3 measurements. The dashed line represents the O_3 retrieval from lidar measurements without applying the aerosol correction technique and the solid black line represents the O_3 retrieval with aerosol correction. **(b)** Aerosol extinction coefficient derived from the lidar measurements at a wavelength of 532 nm (location of lidar measurements is shown in Fig. 5.14). **(c)** In situ temperature and water vapour mixing ratio, **(d)** in situ NO_x and O_3 measurements collected during a Convair ascent over a polluted region (location of ascent shown in Fig. 5.14). The measurements shown here were collected on August 23, 2013.

The depth of the surface boundary layer can be inferred from the aerosol extinction profile and from the water vapour mixing ratio profile. A change in the water vapour mixing ratio is observed at an altitude of 900 m ASL in Fig. 5.16(c) and this altitude coincides with a sharp change in the aerosol extinction coefficient in Fig. 5.16(b). In Fig. 5.16(d), a change in the NO and O_3 mixing ratios occurs at an altitude of approximately 900 m ASL. Below 900 m or within the surface boundary layer, the in situ O_3 mixing ratios remain at 20 ppbv. Above the boundary layer, the O_3 gradually increases to 30 ppbv, while the amount of NO gradually decreases. The reduction in O_3 within the boundary layer and in industrial pollution is consistent with NO titration: $NO + O_3 \rightarrow NO_2 + O_2$. This means that one NO_2 molecule is produced for every O_3 molecule that is lost in reaction with NO. If NO titration is the only chemistry responsible for the reduced O_3 values, then the plot of NO_2+O_3 as a function of height should be constant. In Fig. 5.16(d), the NO_2+O_3 mixing ratio is relatively constant with variations between 30 and 40 ppbv above and within the boundary layer. Hence, the reason for the difference in the O_3 mixing ratio above and within the boundary is due to the reaction with NO.

The flight segment E-F for the flight on August 23, 2013 is shown in Fig. 5.17. The Twin Otter started at point E and travelled west along a constant latitude of N57°06' to point F. Lidar measurements taken along this flight segment are shown in Fig. 5.18.

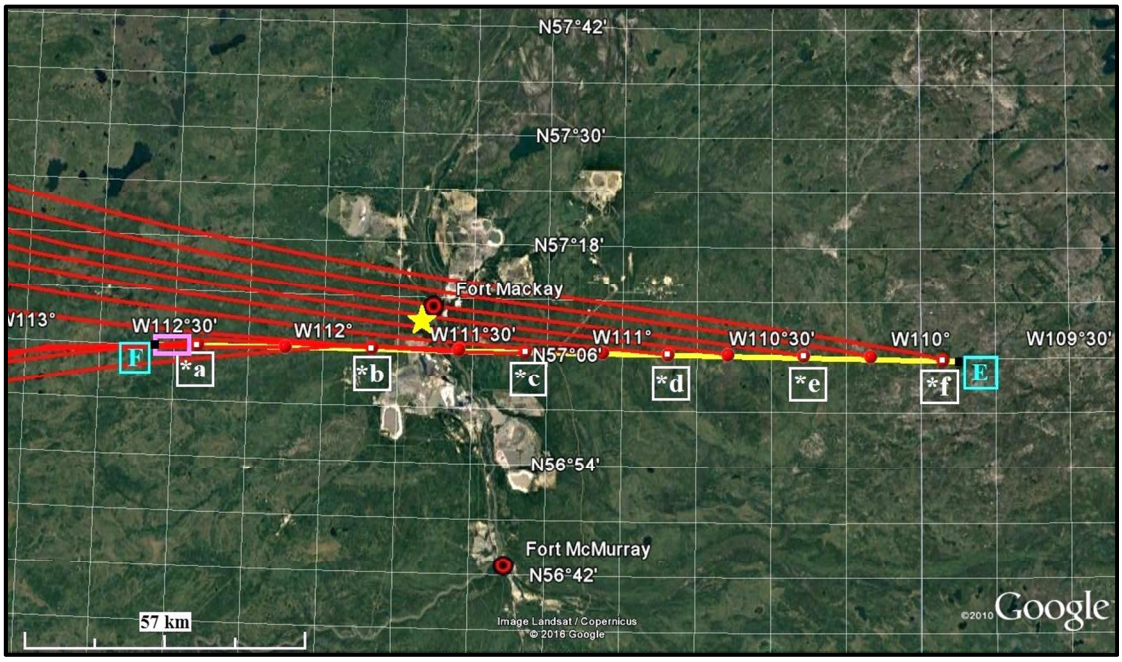

Figure 5.17: The flight segment E-F on August 23, 2013 is represented by the yellow line. Point E represents the starting position of the flight leg and point F, the ending position. Backward air trajectories initiated from an altitude of 800 m above sea level on August 23, 2013 at 18:30 UTC are shown in red and marked by the points *a to *f. The star shaped symbol represents the location of Convair's spiral ascent and the pink box along the flight segment E-F represents the location of lidar measurements for comparison with in situ.

Significant amounts of aerosol were observed over the industry (distance between 39 and 60 km along the flight segment) in Fig. 5.18(a). The depth of the boundary layer in this region was approximately 1.4 km ASL (or 1.0 km above

ground). The O_3 mixing ratio over the industry in Fig. 5.18(b) was observed to be in the range of 25-34 ppbv and mixing ratios greater than 45 ppbv were not observed in the industrial pollution.

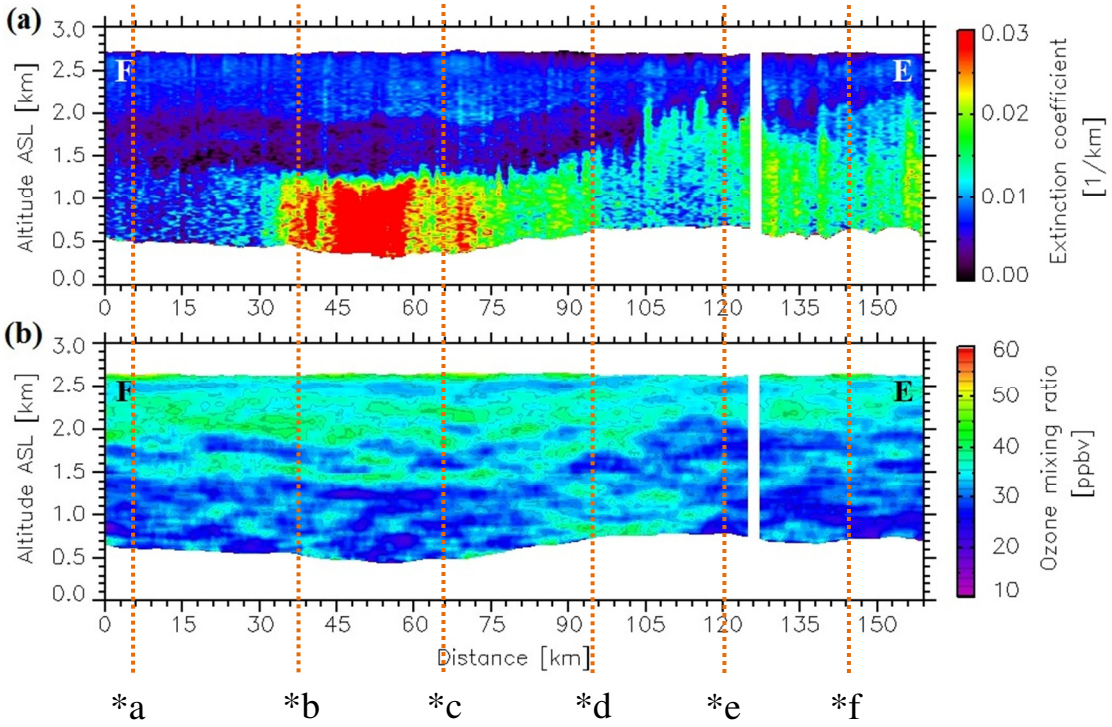

Figure 5.18: (a) The aerosol extinction coefficient measured at a wavelength of 532 nm and **(b)** the ozone mixing ratio derived from the lidar measurements for the flight segment E-F on August 23, 2013. Points *a to *f represent the location of backward trajectories along the measurement path and are marked on the flight segment in Fig. 5.17. The vertical white-section represents a cloudy region and lidar measurements collected in this region were not used in the analysis.

The dispersion of aerosol in regions downwind of the industry is seen in Fig. 5.18(a) for distances greater than 75 km along the flight segment and O_3 mixing ratios between 24 and 35 ppbv are observed in the industrial pollution that was transported downwind. Although the depth of the surface aerosol layer was 1.4 km ASL (or 1 km

above ground) over the industry and in the immediate vicinity of the industry (distance of 60 to 75 km along the flight segment), the depth of the aerosol layer gradually increased from 1.4 km to 2.2 km ASL (or 1 km to 1.5 km above ground) further downwind or for distances greater than 105 km in Fig. 5.18(a). This is evidence for dispersion and mixing with background air. The O_3 mixing ratio further downwind, where the depth of the surface aerosol layer increased to 2.2 km ASL (or 1.5 km above ground), varies between 20 to 36 ppbv. Again, O_3 mixing ratios greater than 45 ppbv were not observed further downwind of the oil sands industry.

However, the O_3 mixing ratios are different within the boundary layer and above the boundary layer. An example of this is observed in Fig. 5.18(b) for distances between 0 and 30 km along the flight leg, where insignificant amounts of aerosol were observed. In order to understand the difference in O_3 mixing ratios above and within the surface boundary layer, lidar measurements between distances of 0 to 7 km in Fig. 5.18 were compared to in situ measurements collected during an ascent of the Convair-580 aircraft on August 23, 2013. The location of the Convair spiral ascent and the lidar measurements for comparison are shown in Fig. 5.17. Both the lidar and in situ measurements were taken in a region that was not significantly affected by pollution from the oil sands industry. The measurements for comparison were about two hours apart. An area where relatively small amounts of aerosol were observed from the lidar measurements (along the flight segment E-F) were chosen to compare with the in situ spiral ascent in a region not affected significantly by pollution.

The comparison of O_3 measurements in air that was not affected by the oil sands pollution is shown in Fig. 5.19(a). Good agreement between O_3 measurements from the in situ instrument and the lidar occur between altitudes of 0.7 and 1.3 km ASL where O_3 mixing ratios within the range of 28-32 ppbv were observed. A change in the temperature value (and water vapour mixing ratio) at an altitude of 1.4 km ASL was observed in Fig. 5.19(c). This is a temperature inversion. A prominent increase in the temperature profile is typically used to indicate the top height of the boundary layer. A decrease in the aerosol extinction profile and water vapour mixing ratio profile in Fig. 5.19(b) and Fig. 5.19(c) respectively can also be used to determine the top height of the surface boundary layer. The height of the boundary layer from the vertical profiles of temperature, water vapour mixing ratio (measurements collected independently from lidar), and the aerosol extinction coefficient is approximately 1.4 km ASL. Although the location of the Convair ascent and the lidar measurements for comparison were collected in different regions, the height of the boundary layer as derived from the in situ measurements in Fig. 5.19(c) agrees with the boundary layer depth from the aerosol extinction height profile.

Lower water vapour mixing ratios and very little NO (almost zero) are associated with O_3 mixing ratios between 30 and 40 ppbv above the boundary layer (for altitudes greater than 1.4 km ASL). In Fig. 5.19, O_3 mixing ratios between 28 and 32 ppbv were observed within the boundary layer and are associated with high water vapour mixing ratios and with small amounts of NO (5 ppbv). The plot of NO_2+O_3 as a function of altitude in Fig. 5.19(d) is constant within the boundary layer. This means

that the reaction of an O_3 molecule with a NO molecule is the significant chemistry that is responsible for the reduced O_3 mixing ratio observed within the surface boundary layer. Hence, the difference in the O_3 mixing ratio above and within the boundary layer is due to larger quantities of NO molecules present within the boundary which reduce the concentration of ozone by NO titration.

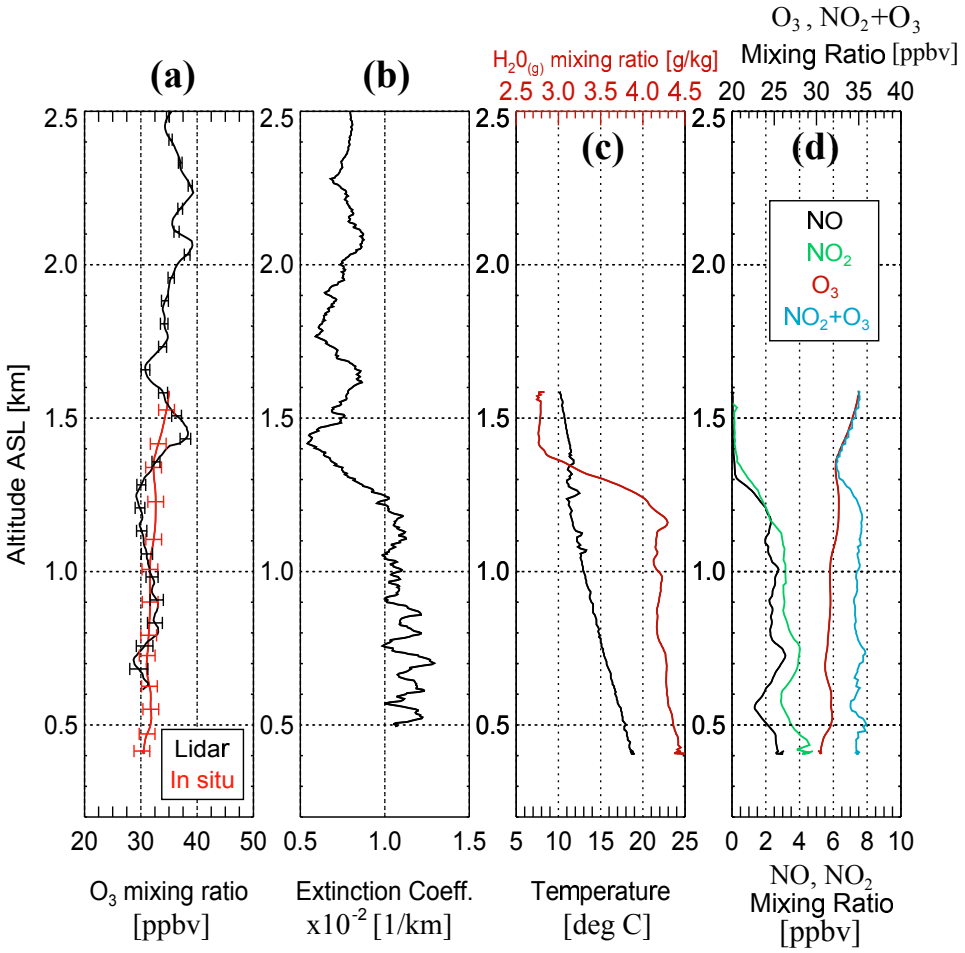

Figure 5.19: **(a)** A comparison between the in situ O_3 and lidar O_3 measurements. **(b)** Aerosol extinction coefficient derived from the lidar measurements at a wavelength of 532 nm (location of lidar measurements is shown in Fig. 5.17). **(c)** In situ temperature and water vapour mixing ratio, **(d)** in situ NO_x and O_3 measurements collected during a Convair ascent over an area not affected by pollution from the oil sands industry (location of spiral ascent is shown in Fig. 5.17). The measurements shown here were collected on August 23, 2013.

The flight segment J-K for the first flight on August 23, 2013 is shown in Fig. 5.20. This is another example of an east-west flight segment along constant latitude of N57°12'. The starting position was at point J in Fig. 5.20 and the Twin Otter aircraft traversed across the oil sands to point K. The lidar measurements collected along the flight segment J-K are shown in Fig. 5.21.

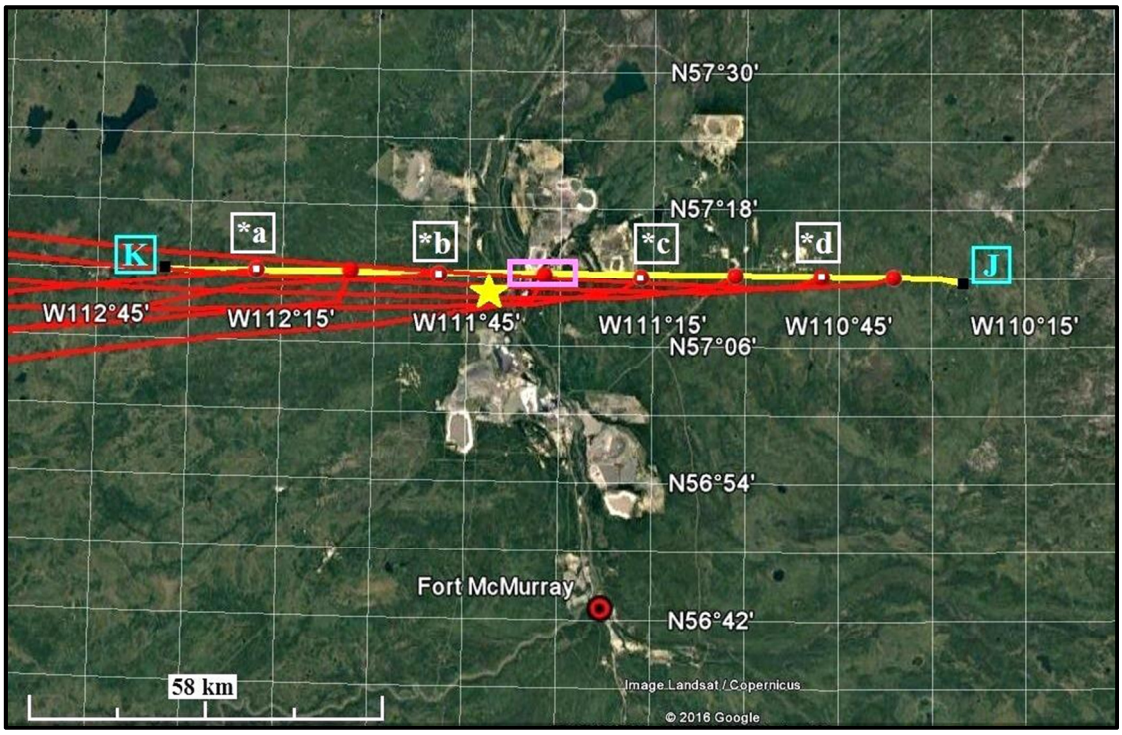

Figure 5.20: The flight segment J-K on August 23, 2013 is represented by the yellow line. Point J represents the starting position of the flight leg and point K, the ending position. Backward air trajectories initiated from an altitude of 1000 m above sea level on August 23, 2013 at 19:30 UTC are shown in red and marked by the points *a to *d. The star shaped symbol represents the location of the Convair's spiral ascent and the pink box along the flight segment J-K represents the location of lidar measurements for comparison with in situ.

In the upwind region (from 0 to 15 km along the flight segment in Fig. 5.21(a)), relatively small amounts of aerosol were present and the depth of the surface boundary layer was approximately 1.7 km ASL (or 1.2 km above ground). Upwind of the industry the O_3 mixing ratios have values between 22 and 34 ppbv within the surface boundary layer.

Significant amounts of aerosol were observed over the industry (at distances between 45 and 69 km along the flight segment in Fig. 5.21(a)) and aerosol were mixed up to an altitude of 1.3 km ASL (or 1 km above ground), which corresponds to the top of the boundary layer. Ozone mixing ratios between 22 and 34 ppbv were measured within the boundary layer and in the pollution from the oil sands industry. However, O_3 mixing ratios in Fig. 5.21(b) between 35 and 42 ppbv were observed above the boundary layer and are higher than the values within the boundary layer. A change in the O_3 mixing ratio at an altitude of 1.3 km ASL is seen in Fig. 5.21(b) and this occurs at the top of the surface boundary layer.

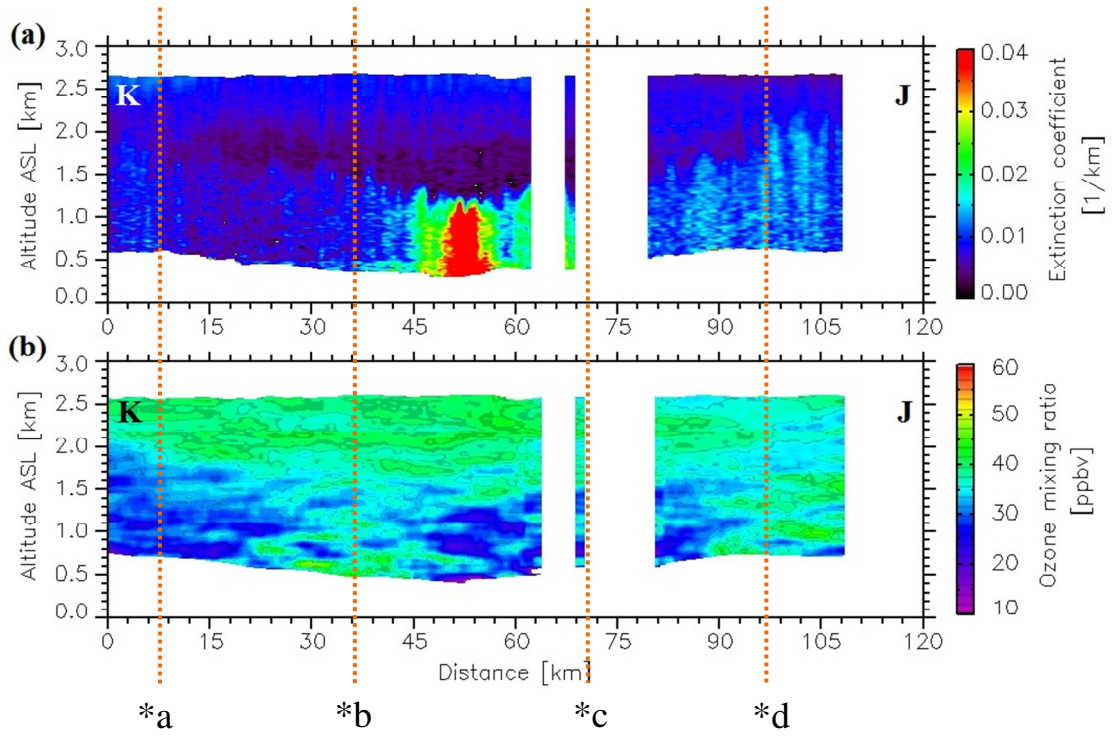

Figure 5.21: (a) The aerosol extinction coefficient measured at a wavelength of 532 nm and **(b)** the ozone mixing ratio derived from the lidar measurements for the flight segment J-K on August 23, 2013. Points *a to *d represent the location of backward trajectories along the measurement path and are marked on the flight segment in Fig. 5.20. The vertical white-sections represent cloudy regions and lidar measurements collected in these regions were not used in the analysis.

In order to understand the difference in the O_3 mixing ratio above and within the surface boundary layer, lidar measurements taken between distances of 55 and 62 km of this flight segment (location of lidar measurements is indicated in Fig. 5.20 by a pink box along the J-K flight segment) were compared to in situ measurements collected during an ascent of the Convair-580 aircraft on August 23, 2013. The location of the Convair spiral ascent is shown in Fig. 5.20 and the in situ measurements collected in this region were taken in close proximity to the Twin Otter

flight segment. The lidar and in situ measurements for comparison were taken two hours apart.

The comparison of O_3 measurements in air that was affected by the oil sands pollution is shown in Fig. 5.22(a). Lidar measurements of O_3 mixing ratio between 28 and 32 ppbv were measured within the surface boundary layer and in situ measurements of O_3 mixing ratios between 25 and 30 ppbv were observed in the same region. The height of the boundary layer inferred from the aerosol extinction coefficient profile is 1.3 km ASL and is different from the boundary layer depth as determined from the in situ measurements, which is approximately 900 m ASL. The difference in the boundary layer heights was likely a result of comparing measurements that were collected at two different times on the same day. The lidar measurements and in situ measurements in Fig. 5.22 were taken approximately two hours apart. Nevertheless, the in situ measurements of NO_2 and O_3 in Fig. 5.22(d) show that large quantities of NO molecules present within the boundary reduce the concentration of ozone by NO titration. The evidence of NO_2+O_3 being constant (between 28 and 30 ppbv in Fig. 5.22(d)) throughout the ascent period of the Convair aircraft supports that NO titration is the only chemistry responsible for the reduced O_3 mixing ratio observed within the surface boundary layer.

Downwind of the industry, or for distances greater than 90 km along the flight segment, the aerosol in Fig. 5.21(a) dispersed out and mixed to an altitude of 2.0 km ASL (or 1.5 km above ground). The depth of the surface aerosol layer gradually

increased downwind of the industry and the O_3 mixing ratios between 30 and 40 ppbv were measured within and above the boundary layer.

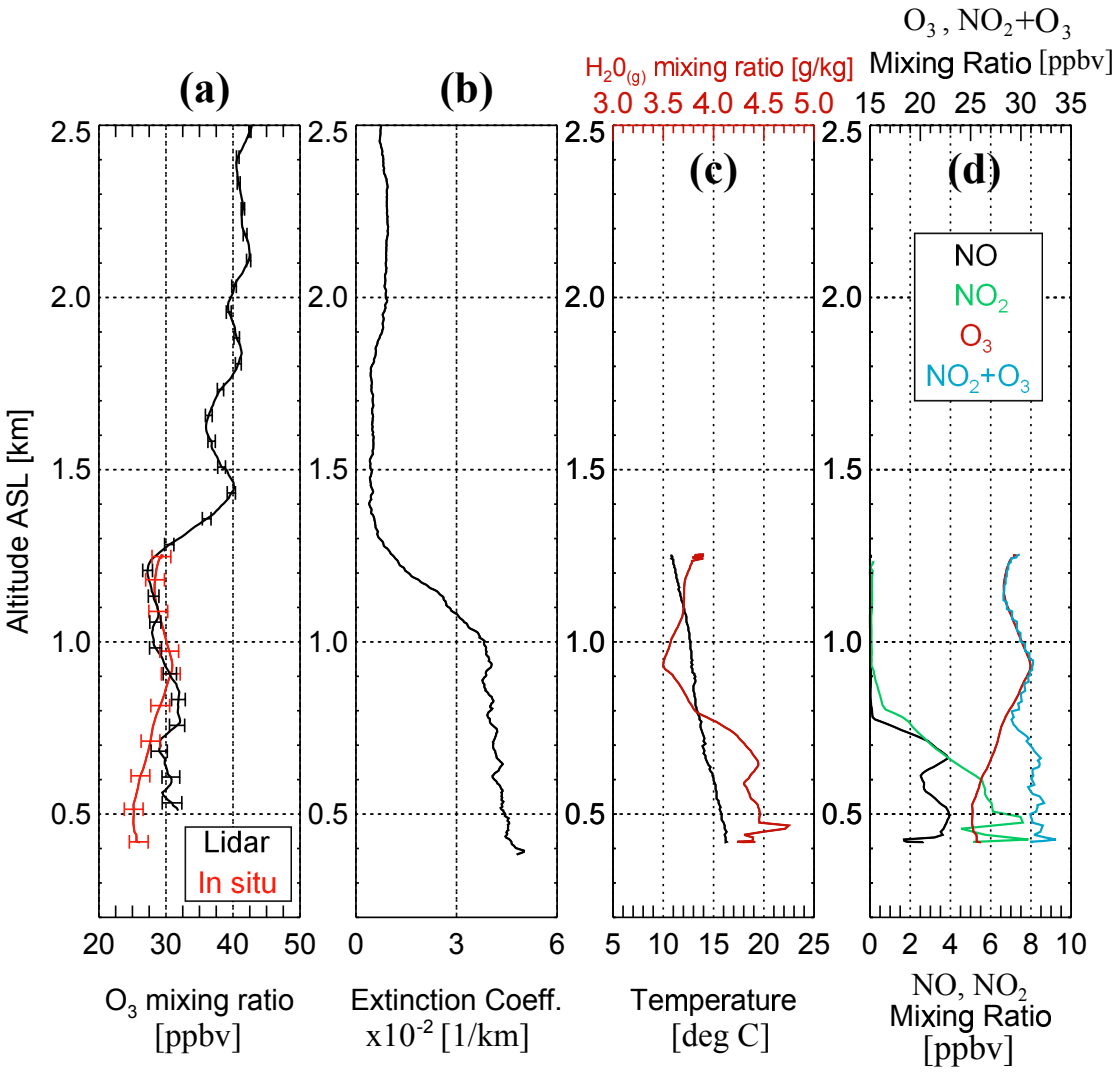

Figure 5.22: **(a)** A comparison between the in situ O_3 and lidar O_3 measurements. **(b)** Aerosol extinction coefficient derived from the lidar measurements at a wavelength of 532 nm (location of lidar measurements is shown in Fig. 5.20). **(c)** In situ temperature and water vapour mixing ratio, **(d)** in situ NO_x and O_3 measurements collected during a Convair ascent over an area affected by pollution from the oil sands industry (location of spiral ascent is shown in Fig. 5.20). The measurements shown here were collected on August 23, 2013.

There were two separate flights on August 23, 2013. The path of the first flight on August 23, 2013 is shown in Fig. 5.2. The Twin Otter aircraft landed for refuelling and took off again. The second flight path on August 23, 2013 is shown in Fig. 5.3. Measurements were collected along the east-west direction for the second flight on August 23, 2016 and the flight segment C-D is shown in Fig. 5.23. The Twin Otter started at point C and travelled across the oil sands industry to point D. The lidar measurements collected along this flight segment are shown in Fig. 5.24.

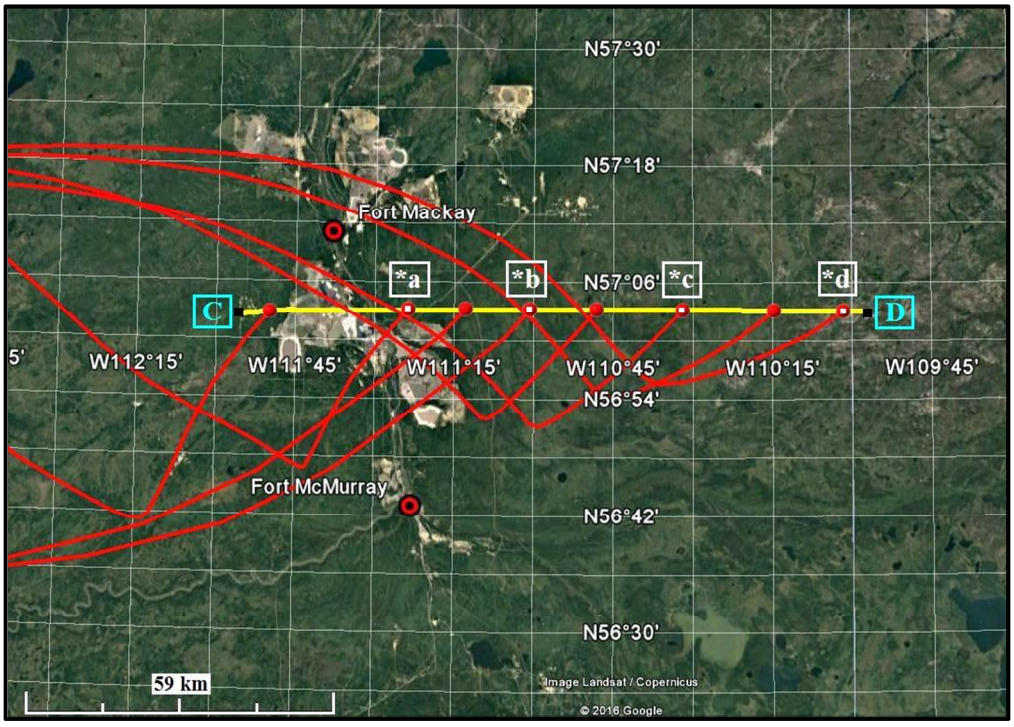

Figure 5.23: The segment C-D for the second flight on August 23, 2013 is represented by the yellow line. Point C represents the starting position of the flight leg and point D, the ending position. Backward air trajectories initiated from an altitude of 800 m above sea level on August 23, 2013 at 23:30 UTC are shown in red and marked by the points *a to *d.

In Fig. 5.24(a), aerosol pollution is observed directly over the oil sands industry (from a distance of 0 to 40 km along the flight segment) and in Fig. 5.24(b), the measured O_3 mixing ratio was between 25 and 40 ppbv in this region. Ozone mixing ratios up to 46 ppbv were observed downwind of the oil sands industry, for distances greater than 50 km along the flight segment.

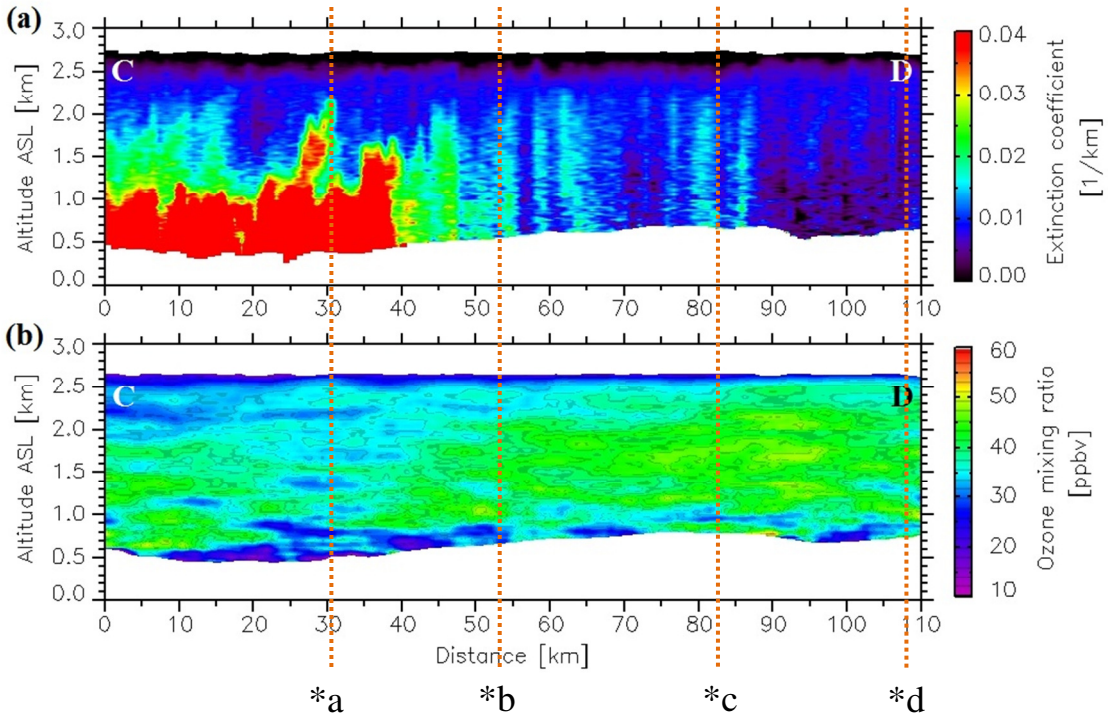

Figure 5.24: (a) The aerosol extinction coefficient measured at a wavelength of 532 nm and **(b)** the ozone mixing ratio derived from the lidar measurements for the flight segment C-D on August 23, 2013. Points *a to *d represent the location of backward trajectories along the measurement path and are marked on the flight segment in Fig. 5.23.

5.1.1.3 Measurements Downwind of the Oil Sands Industry

Multiple cases of the Twin Otter transect across the oil sands industry were shown in the previous section and lidar measurements illustrate that significant amounts of aerosol were observed over the oil sands industry and the O_3 mixing ratio in the industrial pollution ranged between 15 and 35 ppbv, which was less than the background level. The next few examples show lidar observations of industrial pollution within the range of 30 km to 100 km downwind of the oil and gas development facilities.

The segment M-N for the flight on August 22, 2013 is shown in Fig. 5.25. The Twin Otter aircraft started at position M and travelled along constant longitude of W111˚ to position N. Lidar measurements were taken approximately 30 km downwind of the oil sands industry along the north-south flight segment. Measurements of aerosol and O_3 for the flight segment M-N are shown in Fig. 5.26.

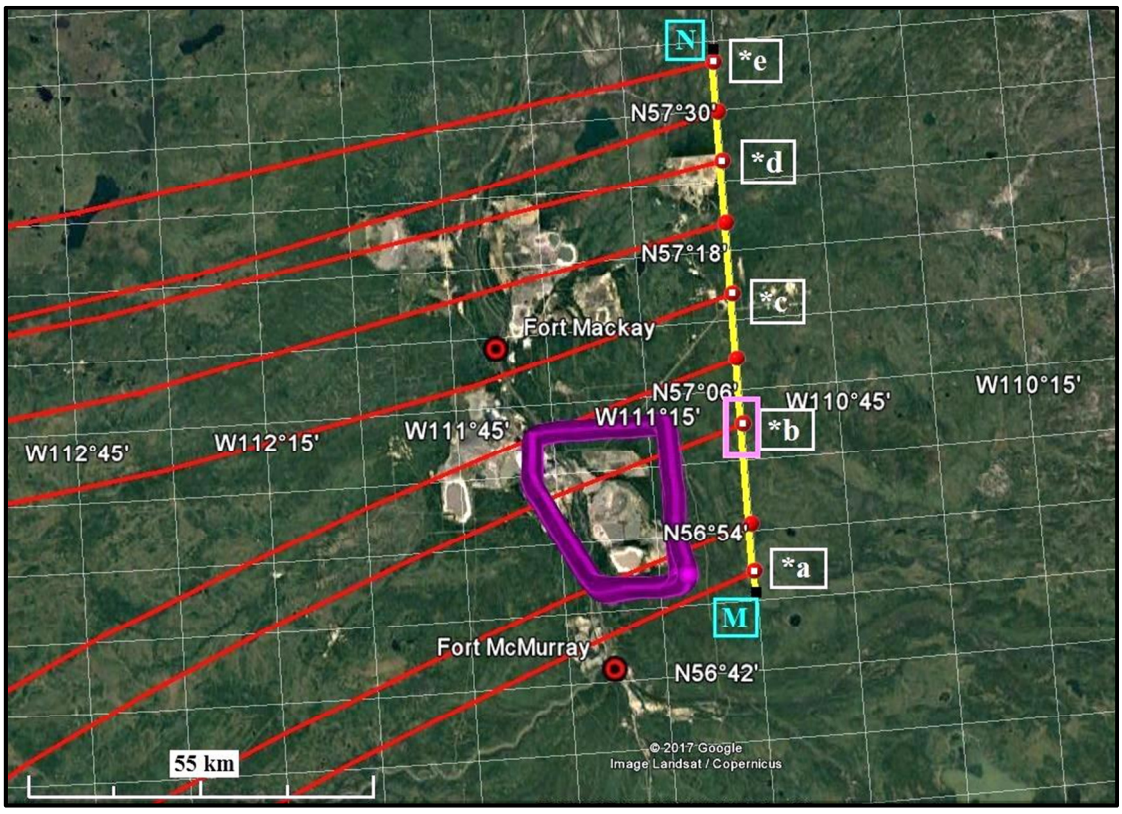

Figure 5.25: The flight segment M-N on August 22, 2013 is represented by the yellow line. Point M represents the starting position of the flight leg and point N, the ending position. Backward air trajectories initiated from an altitude of 850 m above sea level on August 22, 2013 at 21:00 UTC are shown in red and marked by points *a to *e. The purple box designates the location of Convair's spiral ascent in a box-like pattern and the pink box along the flight segment M-N represents the location of lidar measurements for comparison with in situ.

In Fig. 5.26(a), the layer of aerosol over the ground and up to a distance of 50 km along the flight segment indicated that the boundary layer had a depth of 2 km ASL (or 1.5 km above ground). The measured O_3 mixing ratio in Fig. 5.26(b) ranged between 25 and 34 ppbv within the boundary for distances of up to 50 km along the flight segment.

For distances greater than 50 km in Fig. 5.26(a), the depth of the surface aerosol layer gradually increased to 2.5 km ASL (or 2 km above ground). A change in the O_3 mixing ratio value (from approximately 25 to 40 ppbv) between an altitude of 2.0 and 2.5 km in Fig. 5.26(b) and Fig. 5.27(a) was observed and this change corresponds to the top of the boundary layer.

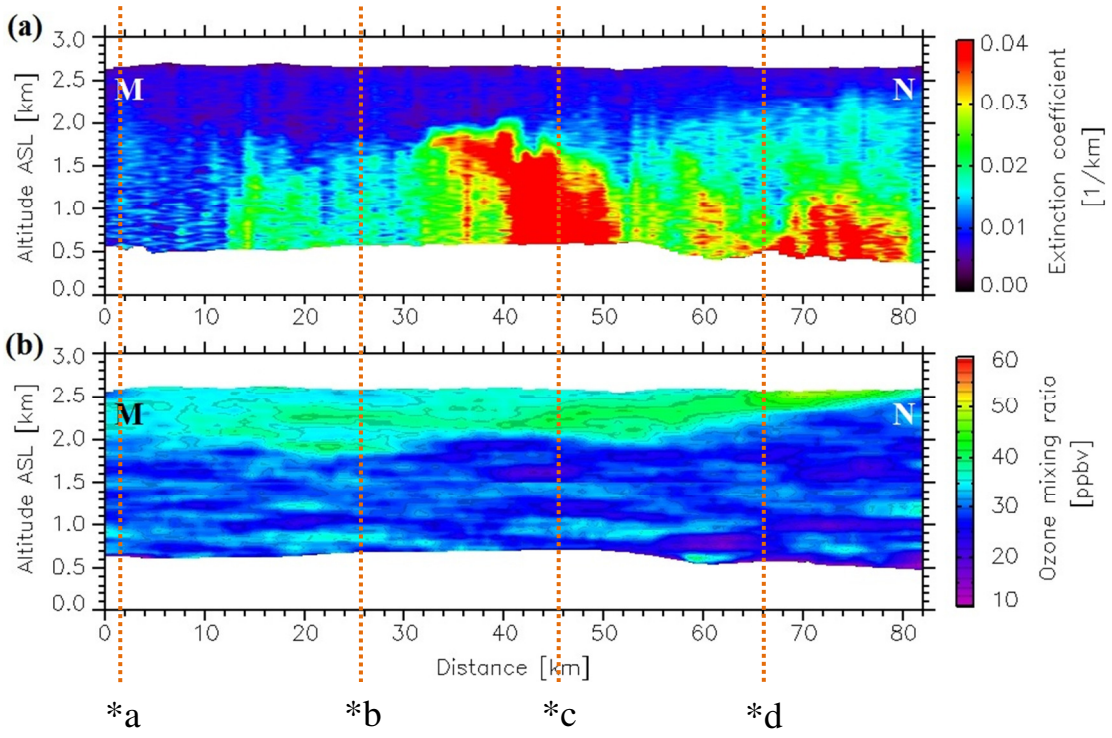

Figure 5.26: (a) The aerosol extinction coefficient measured at a wavelength of 532 nm and **(b)** the ozone mixing ratio derived from the lidar measurements for the flight segment M-N on August 22, 2013. Points *a to *d represent the location of backward trajectories along the measurement path and are marked on the flight segment in Fig. 5.25.

In order to understand the difference in the O_3 mixing ratio above and within the surface boundary layer, a region downwind of the oil sands (point *b along the flight

segment M-N) was chosen to compare with the in situ ascent. Lidar measurements between distances of 23 and 28 km in Fig. 5.26 were affected by pollution from the oil sands industry and the selected measurements were compared to in situ measurements collected during an ascent of the Convair-580 aircraft on August 22, 2013. The location of lidar and in situ measurements for comparison are indicated in Fig. 5.25. The in situ measurements collected along the Convair's ascent were also affected by pollution from the oil sands industry. The Convair gradually ascended in a box-like pattern around the industry and the ascent is not the same as the spiral ascents shown in the previous case studies. The Convair started at an altitude of 800 m ASL and ascended to an altitude of 1 km ASL. The Convair remained at 1.0 km ASL for some time and then ascended to 1.3 km ASL. The gradual ascent of the Convair consisted of short flight legs along a constant altitude then followed by an ascent of a few hundred meters.

The comparison of O_3 measurements in air that was affected by the oil sands pollution is shown in Fig. 5.27(a). Lidar measurements of O_3 mixing ratio between 25 and 35 ppbv were measured within the surface boundary layer. The lidar and in situ measurements show a significant change in the O_3 mixing ratio at an altitude of 1.8 km and 2.0 km ASL respectively. The height of the boundary layer inferred from the aerosol extinction coefficient profile in Fig. 5.27(b) is approximately 1.9 km ASL and is in agreement to the boundary layer depth as determined from the in situ measurements. In Fig. 5.27(c), sharp changes in the temperature and water vapour mixing ratio profiles are observed below an altitude of 2.0 km. Within the boundary

layer, Fig. 5.27 illustrates that values of O_3 between 25 and 35 ppbv are associated with larger water vapour mixing ratios and O_3 values between 35 and 40 ppbv above the boundary layer are associated with smaller water vapour mixing ratios.

The corresponding in situ measurements of NO and NO_2 during the Convair ascent were not shown in Fig. 5.27 as the instrument had problems. Based on previous case studies presented in this section (Figs. 5.14 and 5.19), it was observed that O_3 mixing ratio within the surface boundary layer were lower as compared to above the surface boundary layer. The reaction of O_3 molecules with NO molecules in the surface boundary layer was the likely reason for the difference between the O_3 mixing ratio values observed above and within the surface boundary layer in Fig. 5.26(b).

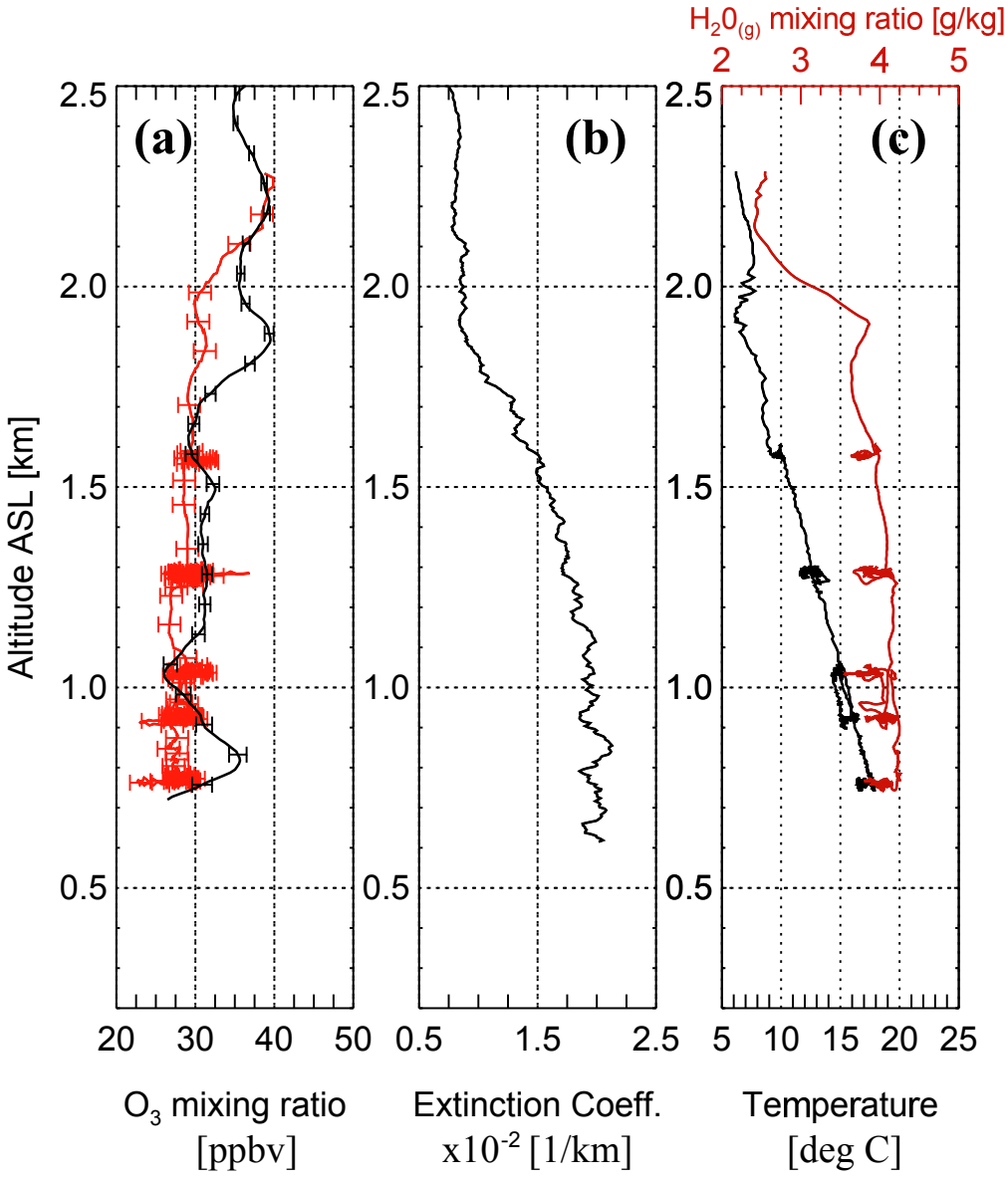

Figure 5.27: (a) A comparison between the in situ O_3 and lidar O_3 measurements. **(b)** Aerosol extinction coefficient derived from the lidar measurements at a wavelength of 532 nm (location of lidar measurements is shown in Fig. 5.25). **(c)** In situ temperature and water vapour mixing ratio measurements collected during a Convair ascent over an area affected by pollution from the oil sands industry (location of ascent is shown in Fig. 5.25). The measurements shown here were collected on August 22, 2013.

The segment I-J for the flight on August 22, 2013 is shown in Fig. 5.28. The Twin Otter aircraft started at position "I" and travelled south along a constant longitude of W109˚30' to position "J". Lidar measurements were taken approximately 100 km downwind of the oil sands industry along the north-south flight segment. The lidar measurements for the flight segment I-J are shown in Fig. 5.29.

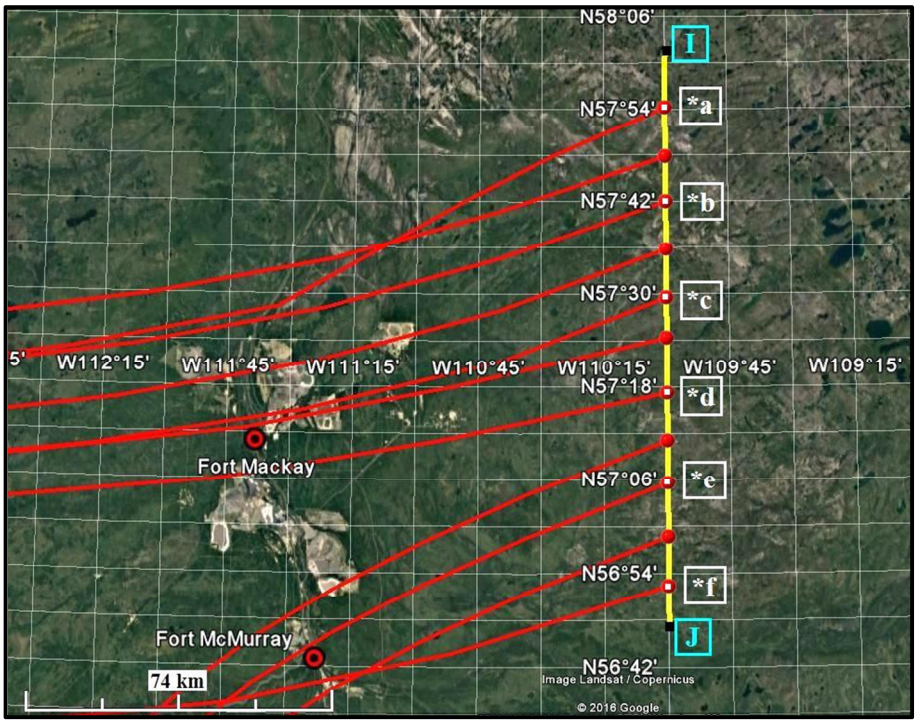

Figure 5.28: The flight segment I-J on August 22, 2013 is represented by the yellow line. Point "I" represents the starting position of the flight leg and point "J", the ending position. Backward air trajectories initiated from an altitude of 1000 m above sea level on August 22, 2013 at 20:00 UTC are shown in red and marked by the points *a to *f.

Aerosol was observed to be mixed from the ground to a height of 2.0 km ASL as shown in Fig. 5.29(a) and values of the O_3 mixing ratio within the boundary layer

varied between 27 and 38 ppbv throughout the flight segment. Ozone mixing ratios greater than 50 ppbv were not observed within the boundary layer at distances of 100 km downwind of the industry.

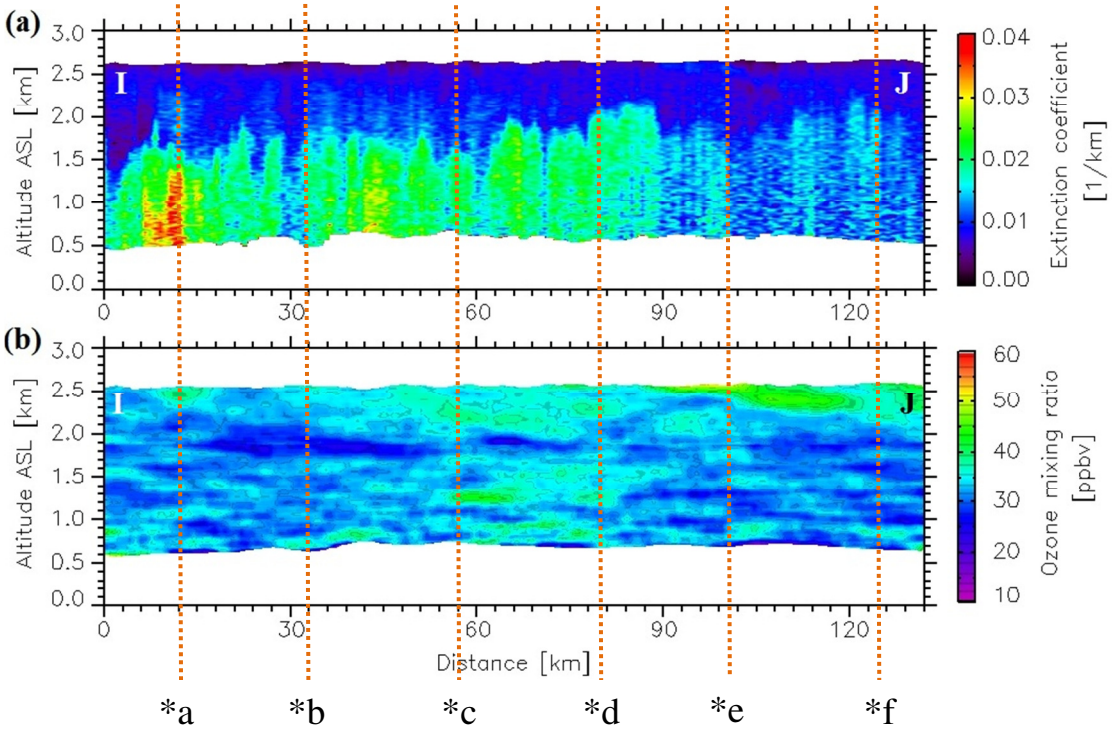

Figure 5.29: (a) The aerosol extinction coefficient measured at a wavelength of 532 nm and **(b)** the ozone mixing ratio derived from the lidar measurements for the flight segment I-J on August 22, 2013. Points *a to *f represent the location of backward trajectories along the measurement path and are marked on the flight segment in Fig. 5.28.

The segment G-H for the flight on August 22, 2013 is shown in Fig. 5.30. The Twin Otter aircraft started at position G and travelled to position H. Lidar measurements were taken approximately 140 km downwind to the north east of the oil sands industry. The lidar measurements for the flight segment G-H are shown in Fig. 5.31.

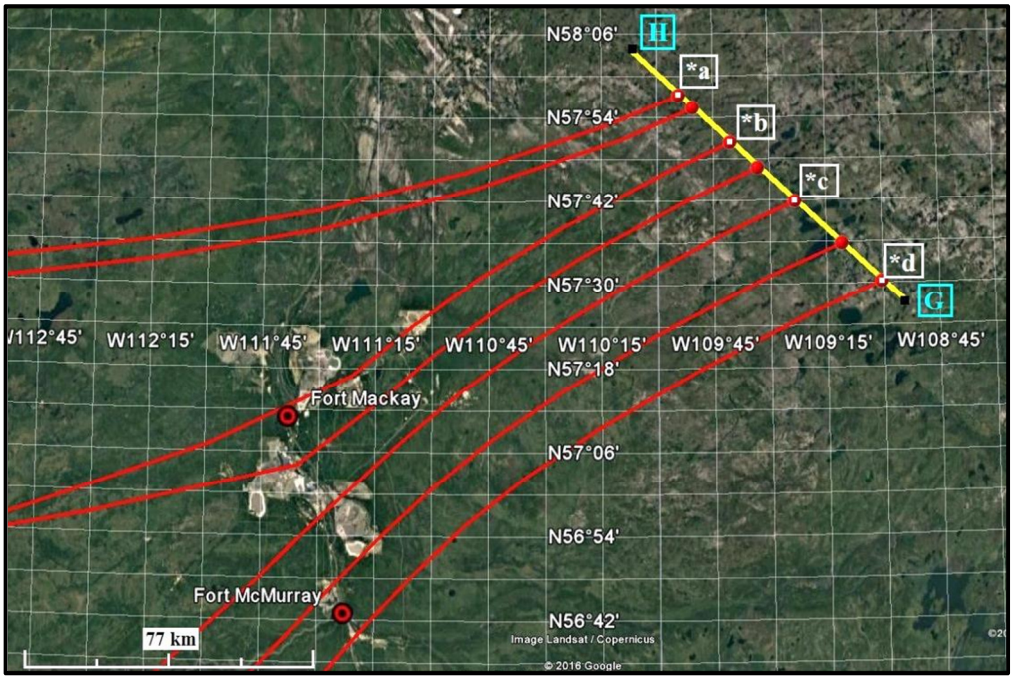

Figure 5.30: The flight segment G-H on August 22, 2013 is represented by the yellow line. Point G represents the starting position of the flight leg and point H, the ending position. Backward air trajectories initiated from an altitude of 900 m above sea level on August 22, 2013 at 19:30 UTC are shown in red and marked by the points *a to *d.

For distances up to 30 km along the flight segment, aerosol was observed in Fig. 5.31(a) to be mixed to a height of 2.0 km ASL (or 1.5 km above ground). The O_3 mixing ratio up to a distance of 30 km along the flight segment remained between 27

and 41 ppbv within the boundary layer. Above the boundary layer, O_3 mixing ratios between 26 and 39 ppbv were observed.

During the course of this flight leg, the alignment of the lidar system required optimization. As a result, lidar measurements between distances of 30 and 75 km along the flight segment were not recorded.

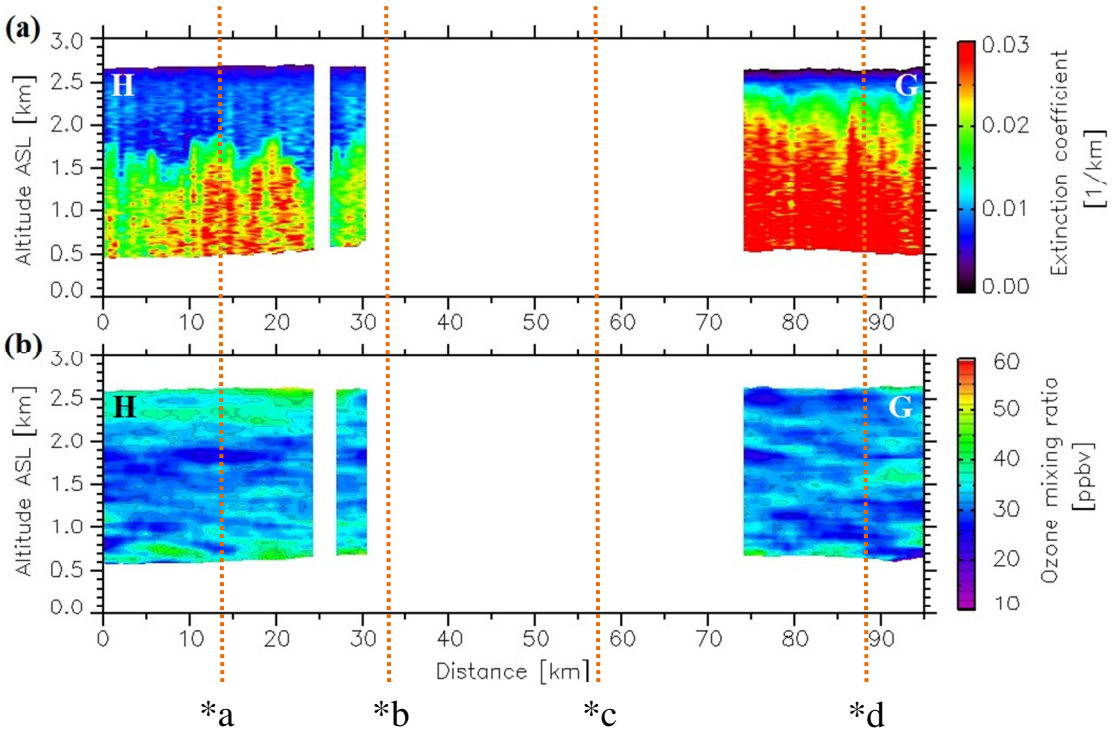

Figure 5.31: (a) The aerosol extinction coefficient measured at a wavelength of 532 nm and **(b)** the ozone mixing ratio derived from the lidar measurements for the flight segment G-H on August 22, 2013. Points *a to *d represent the location of backward trajectories along the measurement path and are marked on the flight segment in Fig. 5.30. The vertical white-sections represent the regions where lidar measurements were not recorded due to alignment checks.

For distances greater than 75 km along the flight segment, the aerosol in Fig. 5.31(a) was mixed to a height of 2.5 km ASL (or 2 km above ground). The O_3 mixing

ratio (in Fig. 5.31(b)) in this region was observed to be in between 27 and 35 ppbv throughout the mixed layer.

Measurements were collected in a north-south fashion for the second flight on August 23, 2016. The segment H-I for the second flight on August 23, 2013 is shown in Fig. 5.32. The Twin Otter started at position "H" and travelled to position "I". Lidar measurements were collected along this flight segment at approximately 100 km downwind of the oil sands industry. Air trajectories along the measurement path from position H to *b in Fig. 5.32 demonstrate that the air came from the oil sands extraction area.

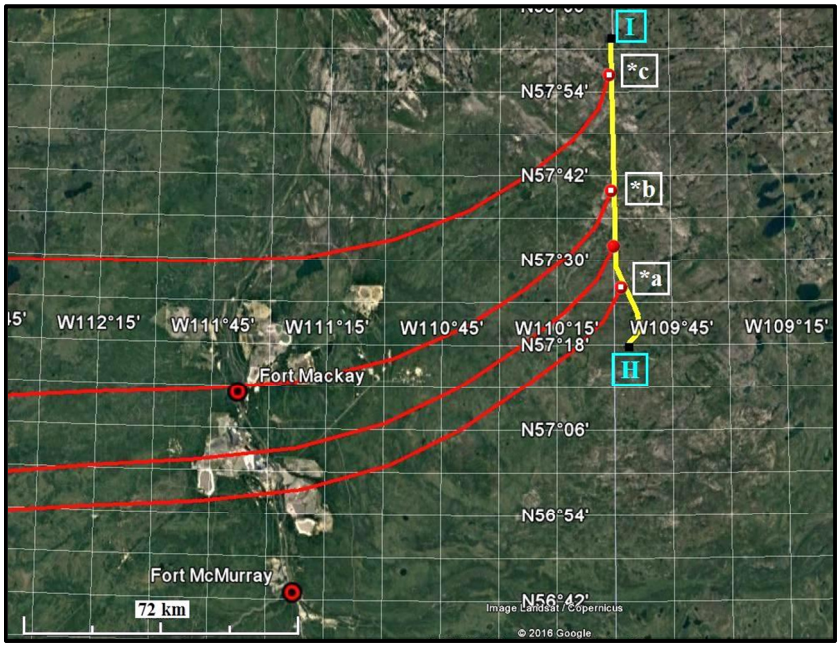

Figure 5.32: The flight segment H-I on August 23, 2013 is represented by the yellow line. Point "H" represents the starting position of the flight leg and point "I", the ending position. Backward air trajectories initiated from an altitude of 800 m above sea level on August 24, 2013 at 01:00 UTC are shown in red and marked by the points *a to *c.

Measurements of aerosol and O_3 mixing ratio along the H-I flight segment are shown in Fig. 5.33. The aerosol in Fig. 5.33(a) was observed to be mixed up to an altitude of 2.5 km ASL (or 2 km above ground), the top of the surface boundary layer. Significant amounts of aerosol from the oil sands industry was observed between a distance of 40 and 60 km along the flight segment and the O_3 mixing ratios varied between 25 and 38 ppbv in the polluted air. Ozone mixing ratio values greater than 50 ppbv were not observed in Fig. 5.33(b) within the boundary layer.

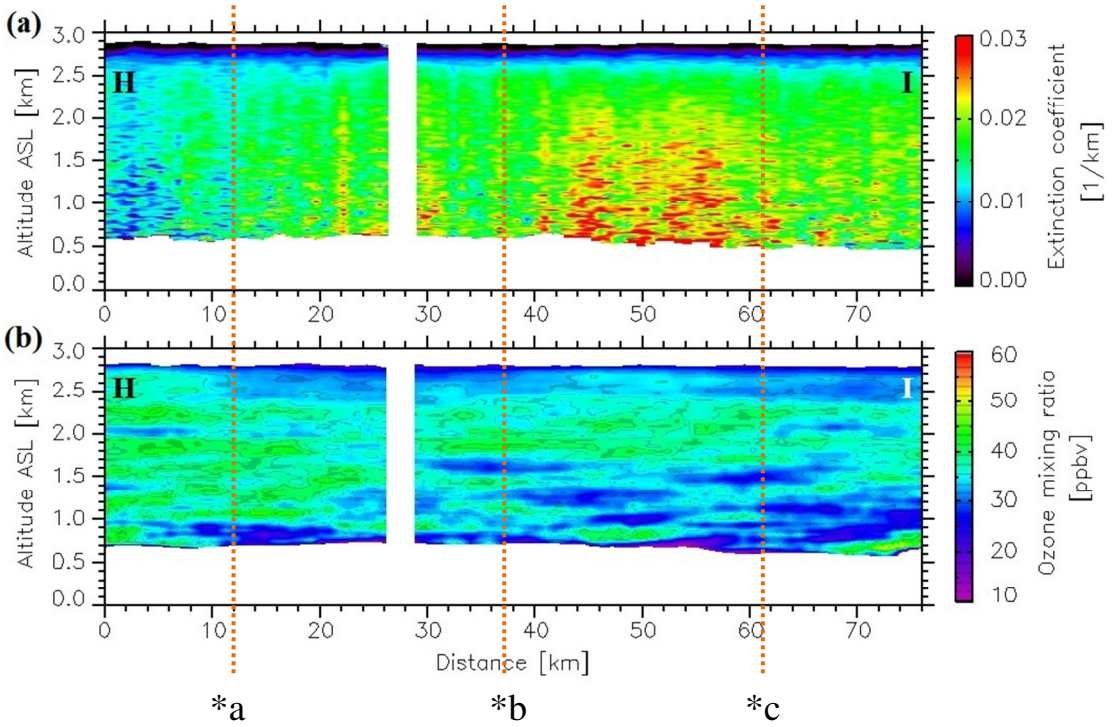

Figure 5.33: (a) The aerosol extinction coefficient measured at a wavelength of 532 nm and **(b)** the ozone mixing ratio derived from the lidar measurements for the flight segment H-I on August 23, 2013. Points *a to *c represent the location of backward trajectories along the measurement path and are marked on the flight segment in Fig. 5.32. The vertical white-section represents a cloudy region and lidar measurements collected in this region were not used in the analysis.

The flight segment J-K for the flight on August 26, 2013 is shown in Fig. 5.34. The Twin Otter started at position J and travelled to position K. Air trajectories along the flight segment in Fig. 5.34 show that the measurements were collected in air that originated from the oil sands extraction area. Lidar measurements collected along the J-K flight segment are shown in Fig. 5.35.

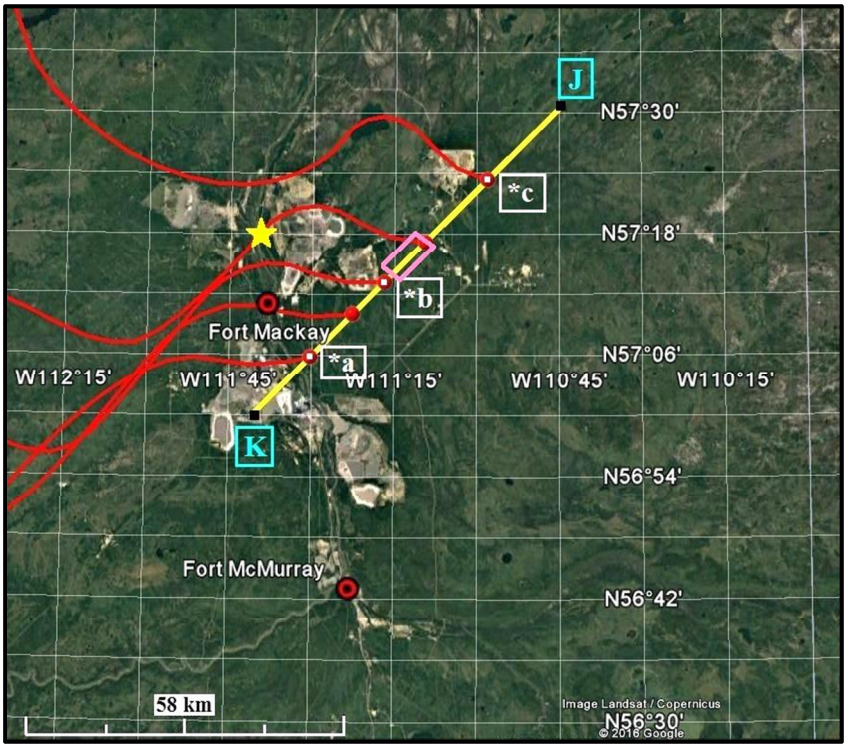

Figure 5.34: The flight segment J-K on August 26, 2013 is represented by the yellow line. Point J represents the starting position of the flight leg and point K, the ending position. Backward air trajectories initiated from an altitude of 600 m above sea level on August 26, 2013 at 23:00 UTC are shown in red and marked by the points *a to *c. The star shaped symbol represents the location of Convair's spiral ascent and the pink box along the flight segment J-K represents the location of lidar measurements for comparison with in situ.

This is an interesting case of air pollution because a layer of pollution in Fig. 5.35(a) was observed close to the surface along the entire flight leg. The depth of the aerosol layer increased along the flight track and extended to a height of 800 m above ground at distances greater than 70 km downwind of the industry. The increase in the surface boundary layer depth downwind of the oil sands industry is evidence for mixing with background air. Ozone mixing ratios in Fig. 5.35(b) ranged from 13 to 33 ppbv within the pollution layer from the oil sands industry.

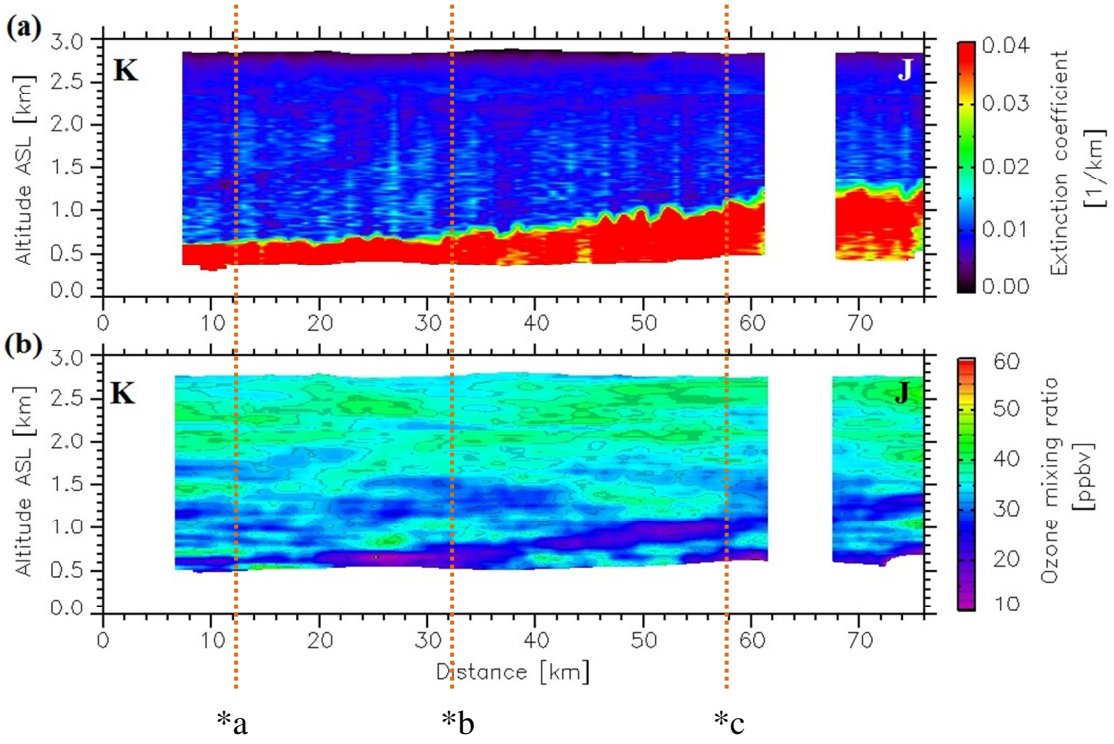

Figure 5.35: (a) The aerosol extinction coefficient measured at a wavelength of 532 nm and **(b)** the ozone mixing ratio derived from the lidar measurements for the flight segment J-K on August 26, 2013. Points *a to *c represent the location of backward trajectories along the measurement path and are marked on the flight segment in Fig. 5.34. The vertical white-sections represent a cloudy region and lidar measurements collected in these regions were not used in the analysis.

Lidar measurements between distances of 32 and 40 km in Fig. 5.35 (location of lidar measurements is indicated in Fig. 5.34 by a pink box along the J-K flight segment) were compared to in situ measurements collected during an ascent of the Convair-580 aircraft on August 26, 2013. The lidar measurements for comparison were chosen along the air trajectory that intersected the location of the Convair spiral ascent and these measurements were affected by pollution from the oil sands industry. The lidar and situ measurements were taken two hours apart, but on the same day. The location of the Convair spiral ascent is shown in Fig. 5.34 and the in situ measurements collected in this region were affected by pollution.

The depth of the surface boundary layer as determined from the lidar and in situ measurements is approximately 800 m ASL (or 500 m above ground) as shown in Fig. 5.36. The comparison of O_3 measurements in air that was affected by the oil sands pollution is shown in Fig. 5.36(a) and O_3 mixing ratios varied between 25 and 30 ppbv within the boundary layer and values from 30 to 40 ppbv were observed above the surface boundary layer.

Above the surface boundary layer in Fig. 5.36(d), the O_3 gradually increased to 30 ppbv, while the amount of NO gradually decreased to zero. The reduction in O_3 within the boundary layer and in industrial pollution can be explained by the NO titration reaction. The plot of NO_2+O_3 as a function of height in Fig. 5.36(d) is relatively constant with altitude with variations between 25 and 32 ppbv. The difference between the O_3 mixing ratio above and within the surface boundary layer can be explained by reaction with NO.

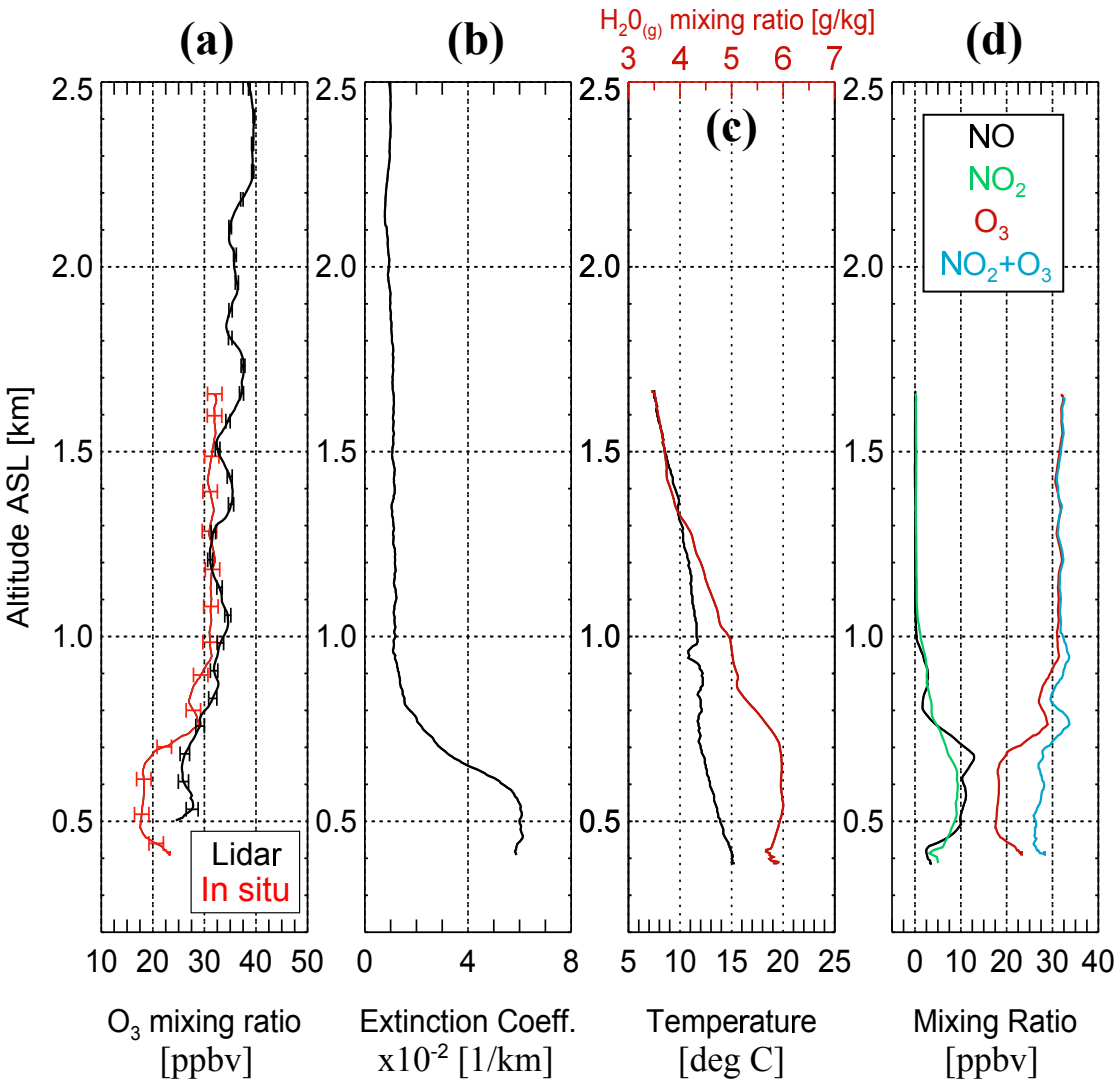

Figure 5.36: (a) A comparison between the in situ O_3 and lidar O_3 measurements. **(b)** Aerosol extinction coefficient derived from the lidar measurements at a wavelength of 532 nm (location of lidar measurements is shown in Fig. 5.34). **(c)** In situ temperature and water vapour mixing ratio, **(d)** in situ NO_x and O_3 measurements collected during a Convair ascent over an area affected by pollution from the oil sands industry (location of spiral ascent is shown in Fig. 5.34). The measurements shown here were collected on August 26, 2013.

5.1.1.4 Comparison between Lidar and In Situ Measurements

Backward trajectories were computed along all the Twin Otter and Convair flights during the August 22 to August 26 time period. The trajectories were separated into two categories. The air trajectories that did not pass over the oil sands industry were considered as "unpolluted air" and the trajectories that passed over the industry were categorized as polluted air. In situ measurements of O_3 were taken at a single altitude and compared with the vertical averaged lidar measurements of O_3 within the boundary layer for the measurements collected in unpolluted and polluted air.

Figure 5.37(a) shows a histogram of the O_3 measurements in unpolluted air for both the lidar and in situ measurements collected within the surface boundary layer. The peak of both distributions occurred at 30 ppbv in unpolluted air. However, in polluted air, Fig. 5.37(b) shows that both the O_3 distributions peak at 25 ppbv. The in situ and lidar O_3 mixing ratios in unpolluted air are consistent with background values of O_3.

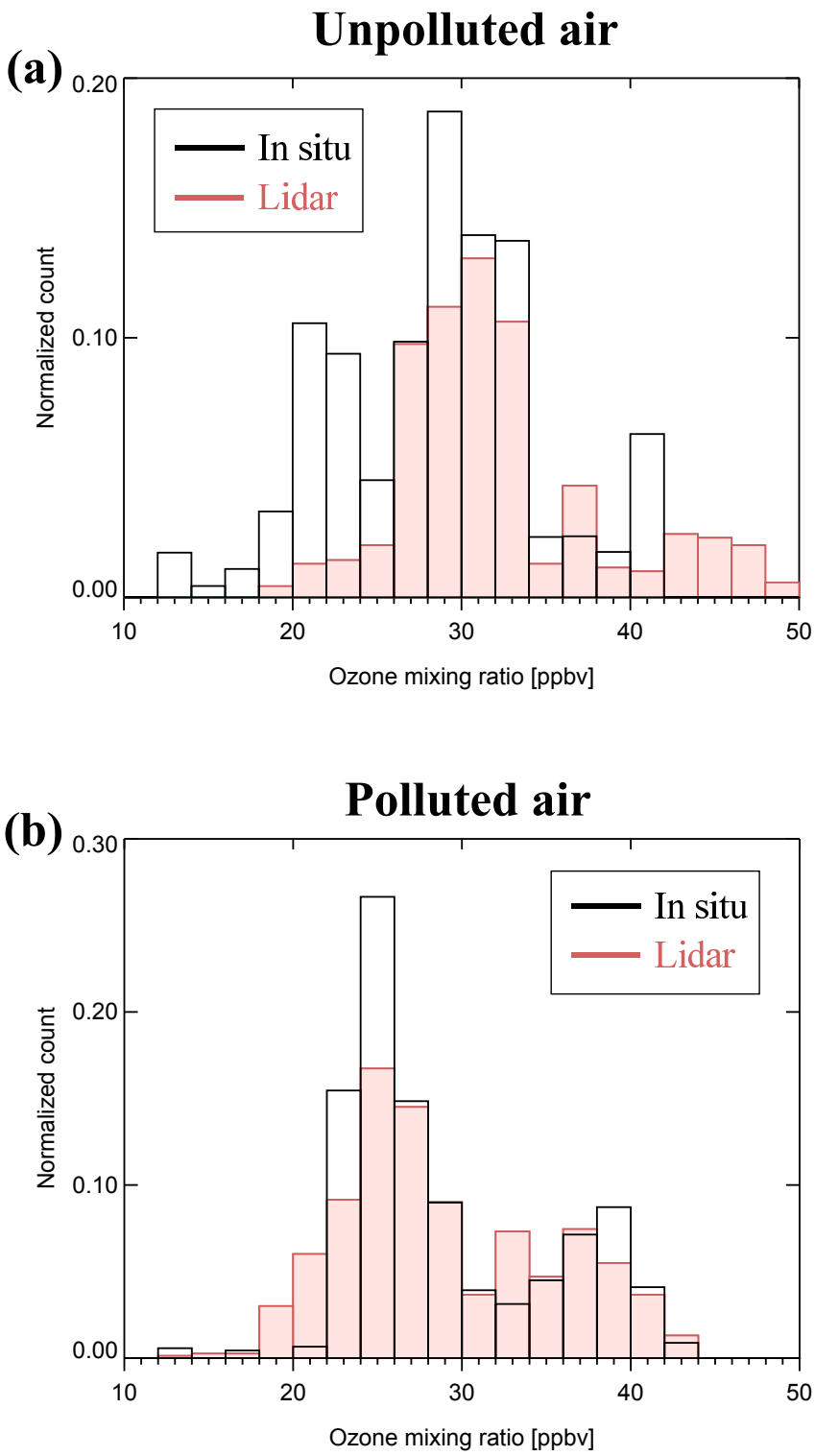

Figure 5.37: A histogram of the comparison between in situ and lidar derived O_3 for the measurements taken within the boundary layer in **(a)** unpolluted air and **(b)** polluted air.

5.1.1.5 Transport Distance of Air in the Oil Sands Region

Several cases of lidar measurements that were collected over the industry and up to 140 km downwind were presented in sections 5.1.1.2 and 5.1.1.3. It was observed that O_3 mixing ratios over the industry were as low as 13 ppbv and mixing ratios typically ranged from 25 to 45 ppbv in regions upwind and downwind of the industry.

In this section, air trajectories (executed from locations along the Twin Otter flight track) were analyzed to determine the transport time of a polluted air mass to reach the measurement point. This is useful for evaluating the production of O_3 in cases where the polluted air mass spent a lot of time in the oil sands region.

Backward trajectories were computed along the flight track for all of the five Twin Otter flights. The flight tracks are shown in Figs. 5.1 to 5.5. The trajectories that passed over the oil sands industry were selected for the analysis. The analysis consisted of determining the amount of time (along the trajectory) for the polluted air from the oil sands industry to travel downwind until it intercepted the Twin Otter flight track (or the measurement point). The HYSPLIT trajectory model outputs a text file with latitude, longitude, and time values every one hour along the trajectory. The amount of time a polluted air mass took to reach the measurement point was determined by subtracting the time interval when the trajectory intercepted the oil sands industry from the time value at the measurement point.

Not all of the HYSPLIT backward trajectories computed along the Twin Otter flight paths passed over the oil sands industry. Only the lidar measurements

corresponding to the trajectories that passed over the industry were used in the analysis. Figure 5.38 shows lidar measurements of the aerosol extinction coefficient and the O_3 mixing ratio for the trajectories that had passed over the oil sands extraction industry as a function of time taken by the air mass to reach the measurement point. These measurements in Fig. 5.38 were averaged within the surface boundary layer (from 500 to 800 m ASL).

It was observed in Fig. 5.38(a) that larger values of aerosol extinction coefficient occur closer to the source area and decrease further away from the source. The observed O_3 mixing ratio in Fig. 5.38(b) showed no significant enhancement with distance from the industry. There is no evidence for increasing O_3 even when the time since passing over the industry was as large as 10 hours. There were a few instances of O_3 mixing ratio below 20 ppbv in Fig. 5.38(b) at the longest times, and this is likely due to mixing.

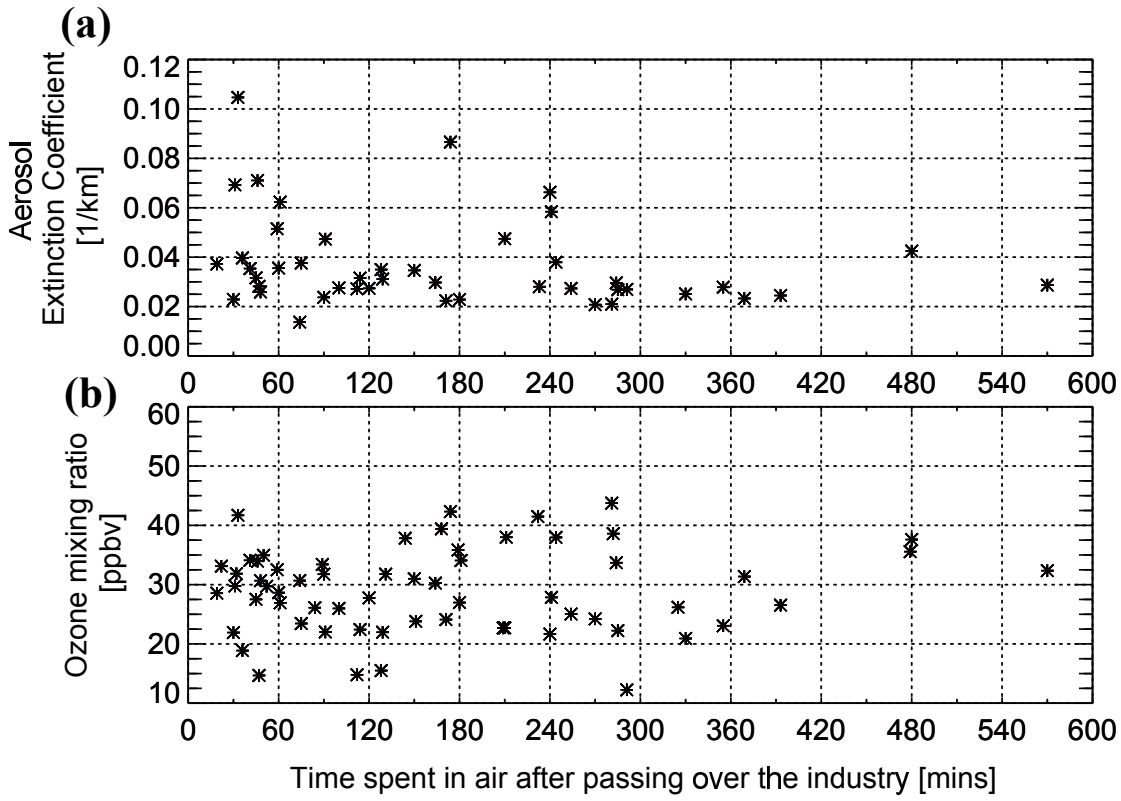

Figure 5.38: (a) The aerosol extinction coefficient and **(b)** the O_3 mixing ratio as a function of time the air had passed over the industry to reach the measurement point along all five flight tracks. The Twin Otter tracks of the flights that were carried out during the field campaign are shown in Figs. 5.1 - 5.5. The measurements shown here were collected between August 22 and 26, 2013.

Figure 5.39 shows backward trajectories initiated from a location that is central to the Fort McMurray oil sands and at a fixed time of 19:00 UTC on August 22 to August 26, 2013. The trajectories illustrate the past motion of air parcels over a 24 hour period. The straight path distance from the starting position to the end position of each trajectory was used to calculate the transport distance of air. An example of how the transport distance was calculated for a trajectory on August 22, 2013 is shown in

Fig. 5.39 by the white dashed line. Transport distances between 200 and 520 km were obtained for the air trajectories initiated between August 22 and August 26, 2013.

The effect of transport distance on O_3 is significant for distances of up to 800 km. Camalier et al. (2007) have reported that changes in the O_3 mixing ratio are negatively correlated with transport distances up to 800 km. Larger transport distances can be linked to normal concentrations of O_3 as higher wind speeds are associated with mixing and dilution of the polluted boundary layer. Thus, stagnant conditions were not present during the time of the field campaign as the transport distance of air in the oil sands region was determined to be approximately 500 km.

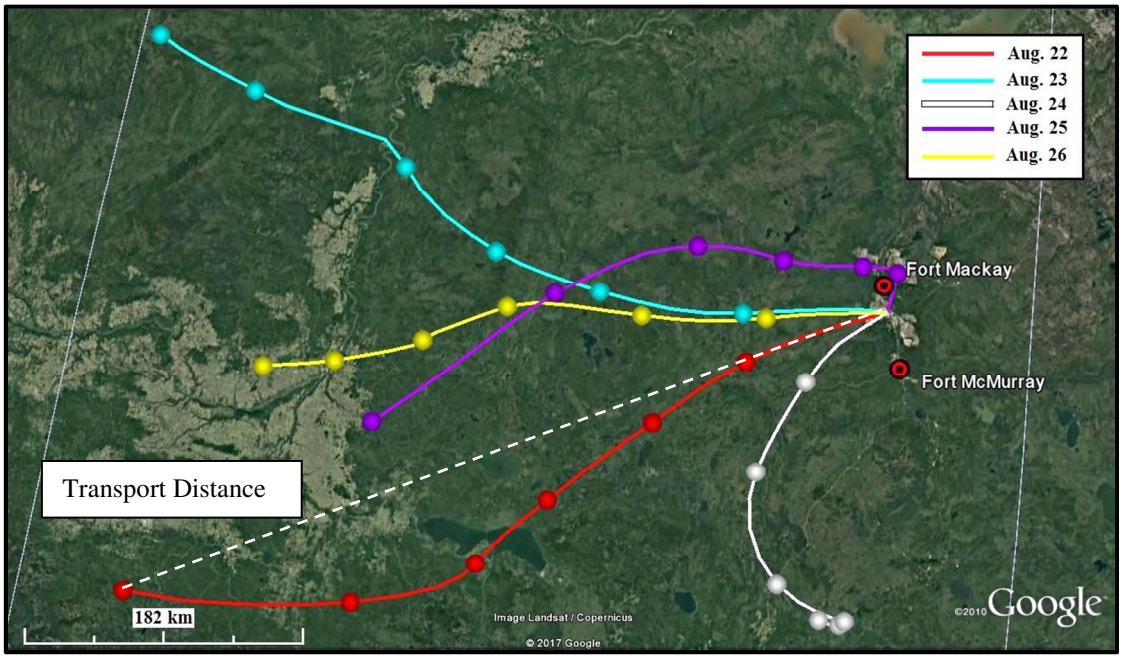

Figure 5.39: Backward air trajectories initiated from an altitude of 700 m above sea level on August 22 to August 26, 2013 at 19:00 UTC. The round mark along each trajectory represents a time interval of 4 hours. The white dashed line illustrates the transport distance for an air trajectory on August 22, 2013.

5.1.1.6 Ground Based Air Monitoring Stations

Air pollutants such as SO_2, NO, NO_2, O_3, and $PM_{2.5}$ were monitored in the Athabasca oil sands region by Wood Buffalo Environmental Association (WBEA). There were 15 air monitoring stations (AMS) situated in background areas and within the oil sands mining and extraction facilities. Not all pollutants were monitored equally at each station, only the air monitoring stations that collected measurements of ozone are shown in Fig. 5.40. Quality controlled measurements of O_3 mixing ratio can be found on WBEA's website (http://www.wbea.org/network-and-data/historical-monitoring-data).

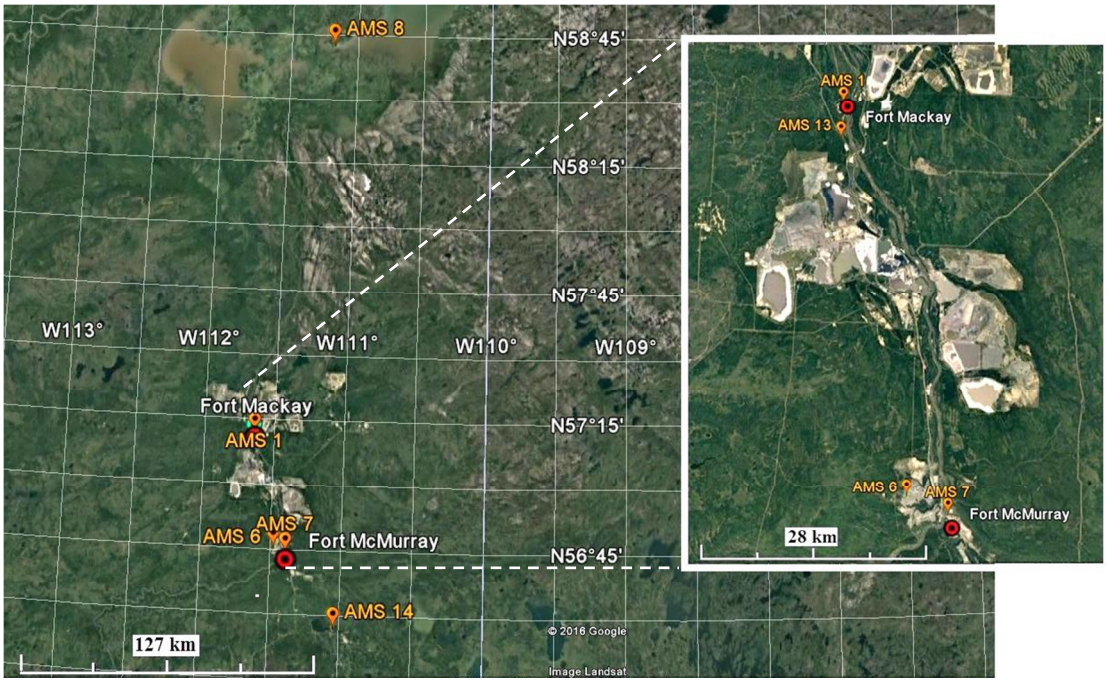

Figure 5.40: Location of a few selected WBEA's air monitoring station in the Athabasca oil sands region.

Ground level O_3 mixing ratios from air monitoring stations are plotted in Fig. 5.41 over the five day campaign period. The air monitoring stations 01, 06, 07, and 13 were located within the oil sands operation region and two monitoring stations, AMS 08 and AMS 14 were situated away from the industry. The diurnal variation of ground level O_3 was observed in Fig. 5.41 at all of the air monitoring stations. Ozone mixing ratios in Fig. 5.41 were observed to increase after sunrise, reach peak values in the afternoon and decrease after sunset.

Surface O_3 mixing ratios in Fig. 5.41 typically ranged between 20 and 40 ppbv on most days during the afternoon and are consistent with the O_3 mixing ratios derived from lidar measurements (within the surface boundary layer) at the same time of day. Figure 5.41 also shows that O_3 mixing ratios greater than 55 ppbv were not measured within the oil sands region at the air monitoring stations.

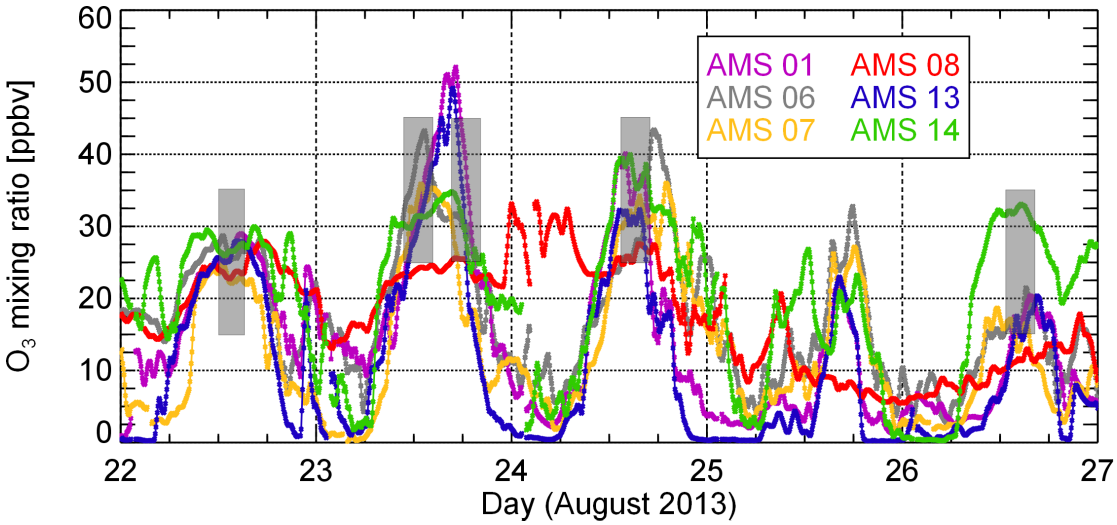

Figure 5.41: Ground level measurements of O_3 collected at six air monitoring stations (AMS) in the Athabasca oil sands region as a function of local time. The grey shaded regions represent the range of lidar O_3 values during the campaign measurement period. The location of the monitoring stations is shown in Fig. 5.40.

In Fig. 5.41, surface O_3 mixing ratios dropped to a low of almost zero at night. In order to explain the low O_3 values observed at night, measurements of NO and NO_2 collected at AMS 07 were analyzed. Figure 5.42 shows a plot of surface NO and NO_2 measurements in the early morning hours (before sunrise) on August 23, 2013. In Fig. 5.42, small amounts of O_3 were observed to be correlated with large amounts of NO_2. Hence, the reduction in O_3 can be explained by the NO titration reaction. The plot of NO_2+O_3 as a function of time is relatively constant with variations between 8 and 10 ppbv.

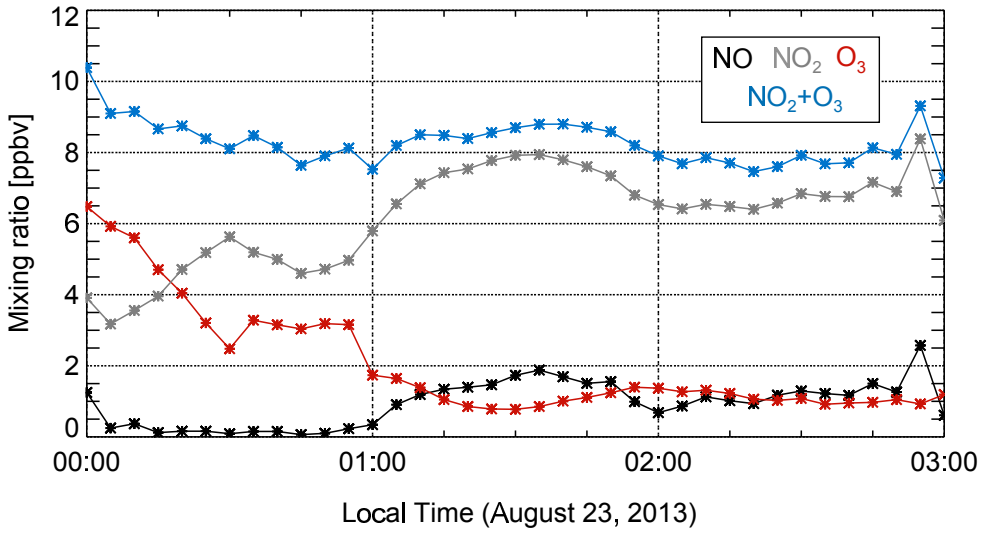

Figure 5.42: Ground level measurements of NO, NO_2, and O_3 collected at air monitoring station 07 on August 23, 2013. The location of the air monitoring station is shown in Fig. 5.40.

Continuous NO emissions from the oil sands industry provides a source of NO at night. An additional source of NO in a forest area is linked to microbiological activity in soil that has the potential to release NO emissions into the surface

boundary layer (Dorsey et al., 2004). Zhang et al. (2004) modelled the spatial distribution of O_3 in the Houston metropolitan region (large area impacted by petrochemical industries) and attributed O_3 mixing ratios <10 ppbv at night due to NO titration. The reduction of O_3 by dry deposition did not contribute substantially to the low O_3 values at night in the Houston area.

5.1.2 Forest Fire Smoke

A more interesting case of air pollution is shown in this section. Airborne lidar measurements to the north of Fort McMurray were made on August 24, 2013 and the corresponding flight segment is shown in Fig. 5.43. In this flight segment, the Twin Otter started at point A, a distance of ~90 km to the east of the oil sands industry and travelled westbound to point B along constant latitude of N57°06'.

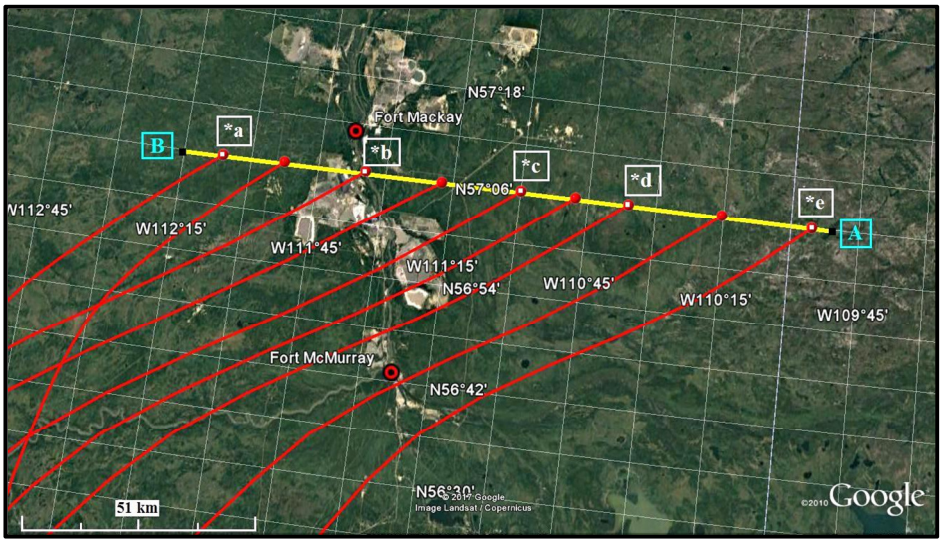

Figure 5.43: The flight segment A-B on August 24, 2013 is represented by the yellow line. Point A represents the starting position of the flight leg and point B, the ending position. Backward air trajectories initiated from an altitude of 1000 m above sea level on August 24, 2013 at 21:00 UTC are shown in red and marked by the points *a to *e along the flight segment.

Lidar measurements of the aerosol extinction coefficient and the O_3 mixing ratio are shown in Fig. 5.44. In Fig. 5.44(a), the lidar observed a layer of aerosol at an altitude of 2.0 km which was separated from the surface boundary layer. There was pollution from the oil sands industry within the boundary layer as usual below a height of 1.2 km ASL (between the distance of 15 and 50 km along the flight leg). Visual observation from the Twin Otter aircraft indicated that the aerosol layer separated above the boundary layer was advected from a region of forest fires burning to the west of Fort McMurray during the afternoon of August 24, 2013.

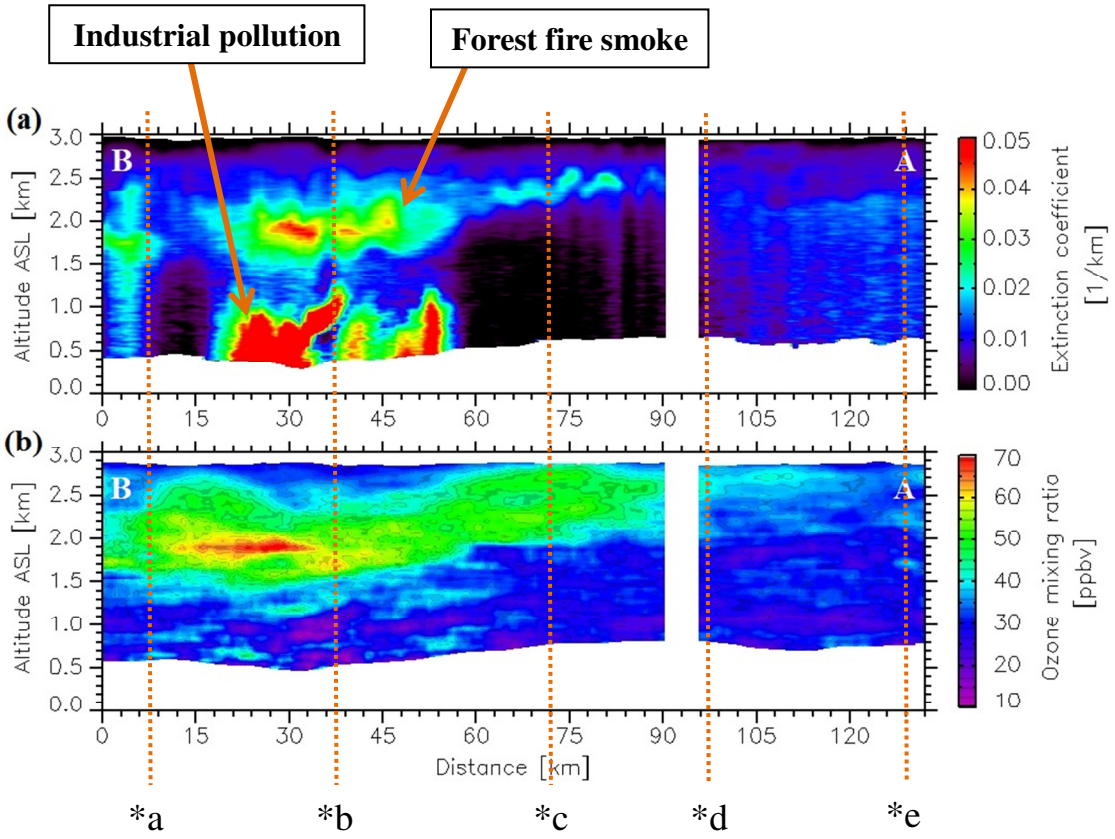

Figure 5.44: (a) The aerosol extinction coefficient measured at a wavelength of 532 nm and **(b)** the ozone mixing ratio derived from the lidar measurements for the flight segment A-B on August 24, 2013. The height is above sea level (ASL). Distance is along the flight segment in Fig. 5.43. The vertical white-section represents a cloudy region and lidar measurements collected in this region were not used in the analysis.

Alberta's wildfire management branch provided the location of the forest fires surrounding Fort McMurray. A backward trajectory was initiated from an altitude of 2.0 km ASL at a time and location the lidar observed the aerosol layer. Figure 5.45 shows that the air mass originated from an area of forest fires (southwest of the flight track).

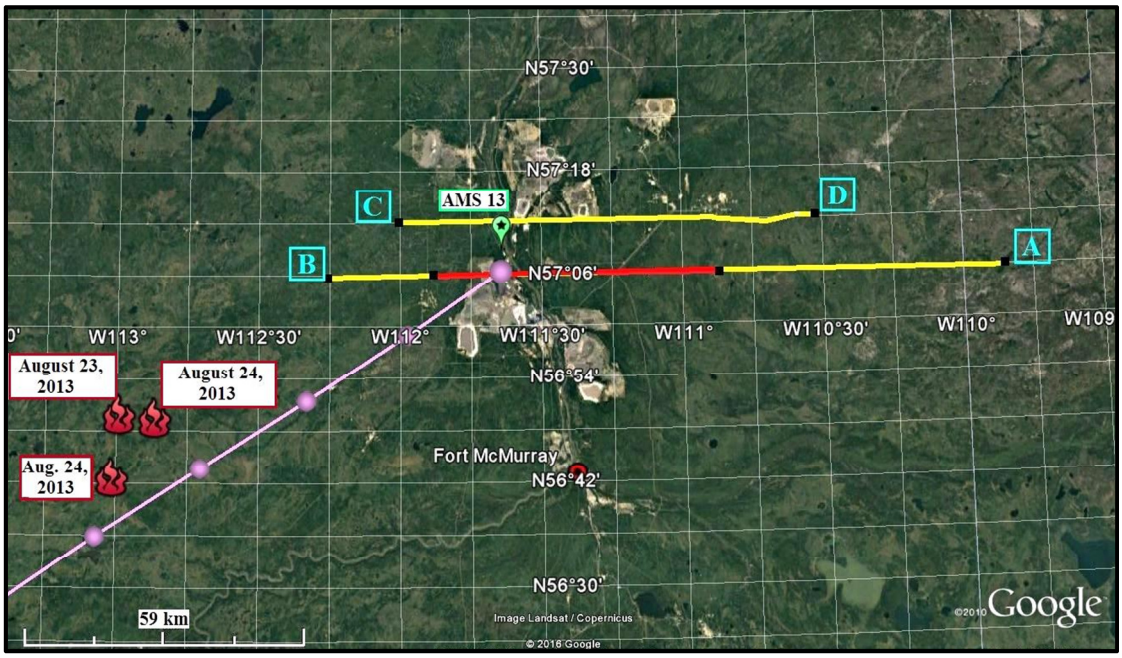

Figure 5.45: The flight segments A-B and C-D on August 24, 2013. The red section along the A-B flight segment represents the region where forest fire smoke was observed. The forest fires are depicted by red fire symbols with the estimated start day beside each fire. A backward air trajectory was initiated from an altitude of 2.0 km ASL at a time of 21:00 UTC on August 24, 2013. The round marks along the trajectory represent a time interval of 1 hour. The green flag indicates the location of Environment and Climate Change Canada's ground based lidar system.

The O_3 mixing ratio along this flight segment is shown in Fig. 5.44(b). The O_3 mixing ratio measured in forest fire smoke reaches a maximum value of 70 ppbv. This

enhancement in O_3 mixing ratio is consistent with previous in situ O_3 measurements in North American forest fires (Val Martin et al., 2006; Aggarwal, 2011). In the pollution from the oil sands industry (below the forest fire smoke layer), significant amounts of aerosol were observed in which the O_3 mixing ratio varies between 15 and 33 ppbv. In the eastern half of the flight leg, not much aerosol was observed and the O_3 mixing ratios consistent with background values (25-36 ppbv) were observed within the surface boundary layer.

The correction in the O_3 retrieval due to the interference of forest fire aerosol was carried out in a similar manner to that described in section 3.3.1. In situ particle size distribution measurements in a layer of forest fire smoke were made by the Convair aircraft during an ascent above the boundary layer approximately an hour before the time that the lidar observed the layer of smoke at the same height. The complex refractive index of forest fire aerosol that was used in this correction method was taken from Wandinger et al. (2002) and the value is listed in Table 5.1. The lidar ratio at a wavelength of 532 nm was found to be 65 sr from Mie scattering calculations with the in situ particle size distribution and refractive index for smoke particles. It was found that the correction due to the interference of forest fire aerosol decreased the O_3 measurement by a maximum of 7 ppbv.

There was some uncertainty since the in situ measurements used in the correction method were taken one hour before the time the lidar observed the layer of forest fire smoke. Additional lognormal parameters of biomass aerosol (Chakrabarty et al., 2006; Pirjola et al., 2015) were used to validate the amount of correction in the

O_3 retrieval due to the forest fire smoke. The amount of correction in the O_3 measurement by using the size distribution of forest fire smoke found in literature was 5 ppbv (for an average equivalent area radius of 0.09 μm) and it is slightly smaller than the calculated correction value of 7 ppbv by using the in situ size distribution measurements collected on August 24, 2013.

Table 5.1: Input parameters used in Mie calculations for the aerosol correction. The equivalent area radius and lidar ratio of particles were derived from in situ size distribution measurements in forest fire smoke. The refractive index for forest fire aerosol was taken from literature (Wandinger et al., 2002).

Quantity	Forest fire aerosol
Equivalent area radius of the particle, R_a	0.071 μm
Aerosol lidar ratio, S_A (532 nm)	65 sr
Particle refractive index, m	$1.61 + 0.06i$

The amount of correction in the O_3 retrieval due to interference of forest fire aerosol was smaller than the amount of correction due to the interference of oil sands aerosol. The absence of large gradients in the amount of forest fire aerosol (as compared to the aerosol backscatter profile over the oil sands industry) contributed to a smaller correction term $N_b(z)$ in equation (15) and this led to a smaller amount of correction due to the interference of forest fire aerosol.

It would have been interesting to continue the flight leg further west (past point B) to collect more measurement of forest fire smoke, but this could not be

accomplished because convective thunderstorm clouds were in the way of the flight path. Instead, the Twin Otter aircraft diverted northeast at point B to avoid the convective clouds and collected measurements along the flight segment C-D as shown in Fig. 5.45. The Twin Otter aircraft started at position C and travelled eastbound to position D. Lidar measurements of aerosol extinction coefficient and O_3 mixing ratio taken along the flight segment C-D are shown in Fig. 5.46.

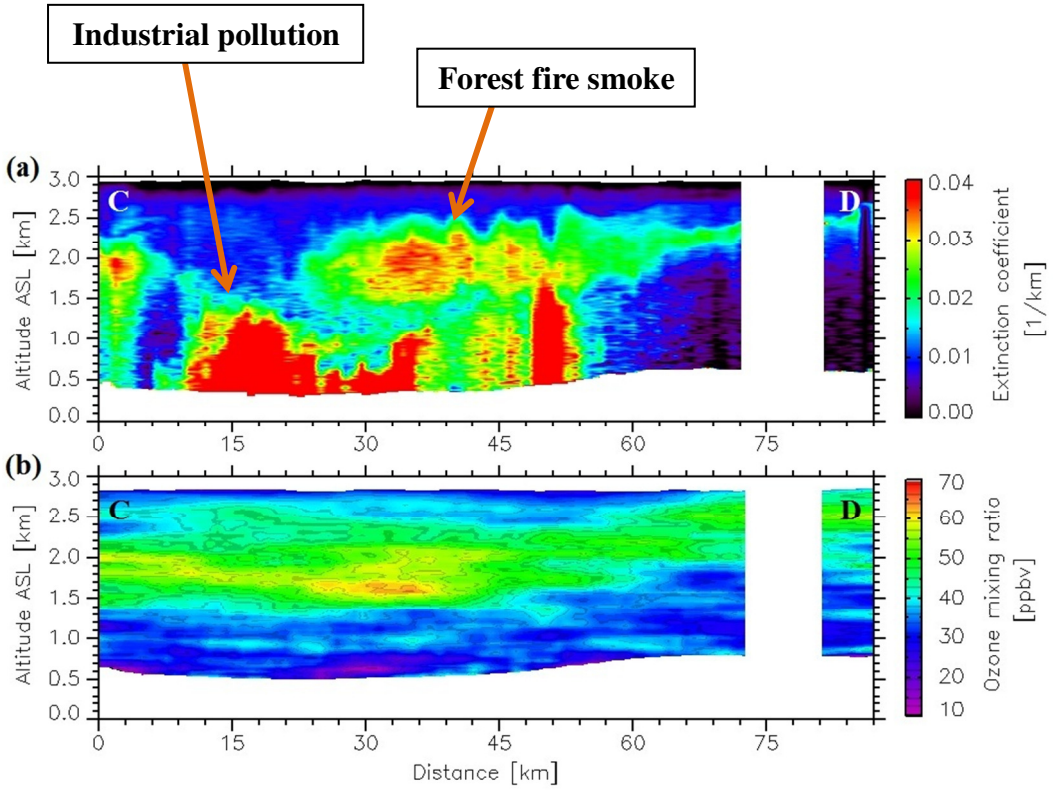

Figure 5.46: (a) The aerosol extinction coefficient measured at a wavelength of 532 nm and **(b)** the ozone mixing ratio derived from the lidar measurements for the flight segment C-D on August 24, 2013. The height is above sea level (ASL). Distance is along the flight segment C-D in Fig. 5.45. The vertical white-section represents a cloudy region and lidar measurements collected in this region were not used in the analysis.

Forest fire smoke was also observed above the surface boundary layer in Fig. 5.46(a) at an altitude range of 1.5 to 2.5 km ASL along a distance between 24 and 87 km of the C-D flight segment and O_3 mixing ratios between 50 and 65 ppbv were measured in the forest fire smoke layer. Aerosol from the oil sands industry was observed at heights below 1.5 km ASL between distances of 10 and 50 km along the flight, in which the O_3 mixing ratio in Fig. 5.46(b) was not greater than 40 ppbv in the industrial pollution.

5.1.2.1 More Evidence of Forest Fire Smoke

A comparison of measurements between the ECCC ground based lidar at AMS 13 and the York University airborne lidar is presented in this section. Environment and Climate Change Canada's ground based lidar system observed the same layer of forest fire smoke at an altitude of approximately 1.8 km ASL. As seen in Fig. 5.45, ECCC's ground based lidar system was approximately 5 km from the York University airborne lidar for the flight segment A-B and C-D.

The depolarization ratio is a useful tool for discriminating particles of different shapes. Environment and Climate Change Canada provided a data product in which linear volume depolarization ratios were derived from the lidar measurements collected with a ground based lidar system that was operating at AMS 13 in Fig. 5.45. The ratio of the perpendicular to the parallel component of linear polarization at a wavelength of 532 nm (of the backscattered radiation) was used to calculate the volume depolarization ratio. In this section, linear volume depolarization ratios within the forest fire smoke layer and in industrial pollution will be presented.

A difference in the volume depolarization ratio between the industrial pollution and forest fire smoke is seen in Fig. 5.47(c). The volume depolarization ratio throughout the forest fire smoke layer was measured to be 5-6% and this value is consistent with the linear volume depolarization ratios measured in North American forest fires in previous aircraft lidar studies (Aggarwal, 2011). The small values of volume depolarization ratio measured in the smoke layer reveal the spherical nature of forest fire particles. The volume depolarization ratio in the pollution from the oil and gas extraction facilities at altitudes below 1.5 km ASL in Fig. 5.47(c) had a larger depolarization ratio with values between 7% and 10%. The larger depolarization ratio observed in industrial pollution suggests that the particles are less spherical in nature or of larger size (Sassen, 1991). This provides further evidence that the layer with enhanced O_3 mixing ratio had originated from forest fires rather than industrial pollution.

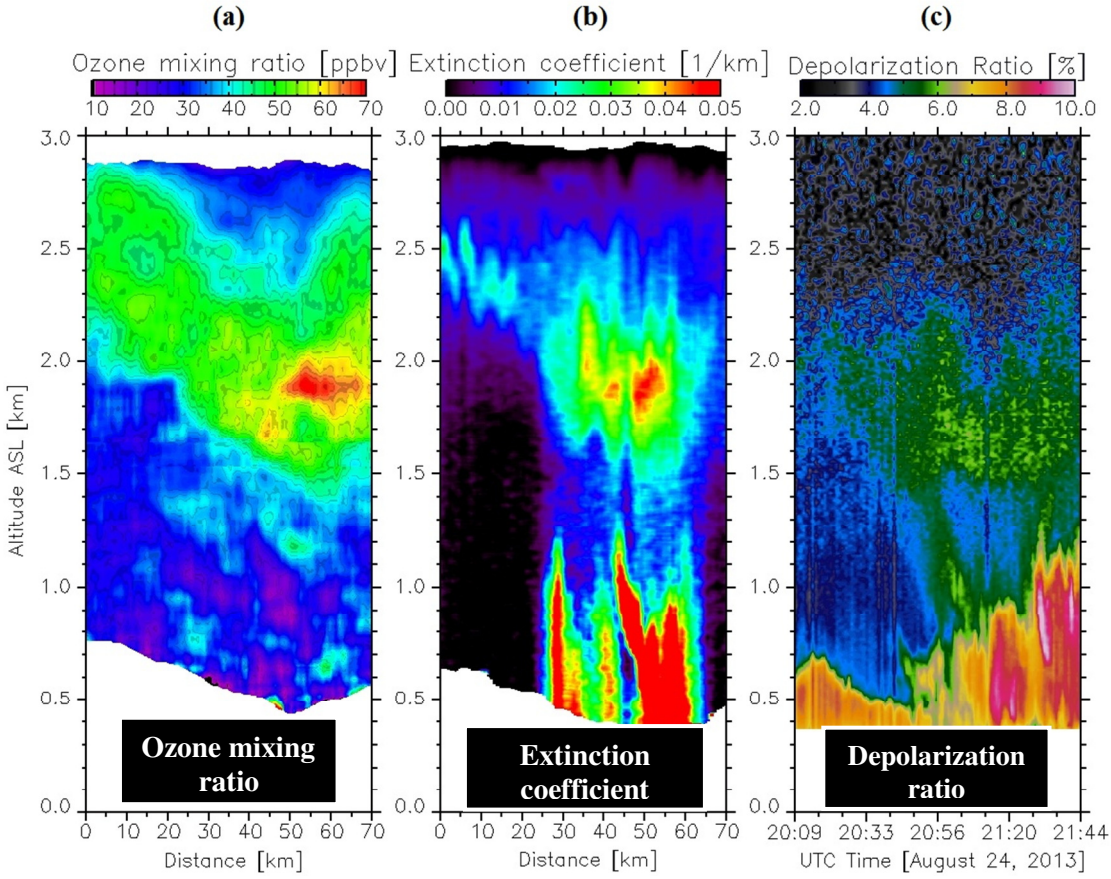

Figure 5.47: (a) The ozone mixing ratio and **(b)** aerosol extinction coefficient derived from airborne lidar measurements along a section of the flight segment A-B (as shown in Fig. 5.45) where forest fire smoke was observed. Distance is along the red section of the flight in Fig. 5.45. **(c)** Ground-based depolarization ratio measurements taken by Environment and Climate Change Canada's lidar system located at 57.14° N, 111.6° W. This site is indicated as AMS 13 in Fig. 5.45.

5.2 Discussion

5.2.1 Industrial Pollution

Natural and anthropogenic sources of pollution were encountered in the Fort McMurray oil sands region. Significant amounts of aerosol were observed directly

over the oil sands industry and within the surface boundary layer, up to an altitude of 1.5 km ASL (or 1 km above ground). The O_3 mixing ratio measured within the polluted air ranged between 15 and 35 ppbv.

There was a difference in the O_3 mixing ratio values above and within the surface boundary layer. In the industrial pollution, in situ measurements of NO+O_3 were relatively constant throughout the mixed layer and above, as shown in Fig. 5.16 and Fig. 5.36. Large amounts of NO emissions were observed directly over the industry and reduced values of O_3 (as low as 13 ppbv) are interpreted as being a result of the chemical reaction of O_3 with NO. Above the surface boundary layer where the concentrations of NO are approximately zero, O_3 mixing ratios range between 35 to 45 ppbv and are consistent with background values. In some cases it was observed that a difference in the O_3 mixing ratio above and within the boundary still exists in regions that are not influenced strongly by the oil sands pollution. For example, Fig. 5.19 illustrates that small amounts of NO (less than 5 ppbv) were observed within the mixed layer in a region upwind of the oil sands industry and the presence of small amounts of NO resulted in lower O_3 mixing ratios within the boundary layer as compared to above the surface boundary layer.

It was expected that the pollution from the oil sands industry would produce values of O_3 up to 100 ppbv, as in the urban pollution over Toronto (chapter 4) and as seen in previous studies of air pollution surrounding petrochemical plants in Houston, Texas (Banta et al., 2005; Senff et al., 2010; Langford et al., 2011).

Air pollution in the Athabasca oil sands region has been studied from both an aircraft (Rudolph, 2004; Simpson et al., 2010), from the ground (Bari and Kindzierski, 2015), and in this campaign (Gordon et al., 2015; Shephard et al., 2015; Liggio et al., 2016). Airborne measurements of trace gases collected within the boundary layer near the Athabasca mining facilities in July 2008 were reported by Simpson et al. (2010). Although the focus of their study was more towards the atmospheric composition of the Arctic troposphere and forest fire emissions in Western Canada, a systematic campaign to study the air pollution in the Athabasca oil sands region was not planned and an opportunity was taken by Simpson et al. (2010) to collect measurements in the oil sands region. Nonetheless, Simpson et al. (2010) have reported a maximum O_3 mixing ratio of 31 ppbv and no observed enhancement in O_3 as compared to the background value. They also reported that large NO_x (NO_x = NO + NO_2) mixing ratios (approximately 20 ppbv) were correlated with small O_3 mixing ratios (20 ppbv) directly over the oil sands industry. The O_3 mixing ratios presented in this section are consistent with the O_3 measurements collected by Simpson et al. (2010) in unpolluted and polluted air and also with Fig. 5.9, in which higher concentrations of NO_x and related to lower concentrations of O_3.

In another study, aircraft based O_3 measurements were carried out by Rudolph (2004) in the summer of 2001 and 2002 and within the Athabasca oil sands region to assess the chemical formation of O_3. Rudolph (2004) observed that ambient temperatures of 18-20°C and light to moderate wind speeds close to the surface were not favourable for O_3 production. Large concentrations of O_3 are usually associated

with hot and stagnant conditions (Jacob et al., 1993; Chu, 1995; Camalier et al., 2007; Haman et al., 2014). Temperatures greater than 25°C (Chu, 1995; Camalier et al., 2007) are linked to high values of O_3 mixing ratio. However, Figs. 5.16, 5.19, 5.22, 5.27, and 5.36 show that temperatures ranged between 10 and 20°C within the boundary layer (400 – 600 m ASL) and temperatures greater than 20°C were not observed in the oil sands region during the campaign. Furthermore, transport distances calculated during August 22 to 26, 2013 show that the air moved between 200 and 520 km in previous 24 hours. This means that stagnant conditions were not present during the measurement time; higher winds are associated with more vertical mixing and ventilation of the polluted boundary layer.

The amount of time taken to generate O_3 in a polluted environment is an important factor and it should be considered in the formation process. The O_3 chemistry in plumes from a power plant was simulated by Karamchandani et al. (1998) using an air quality model. The model predicts that a minimum of five hours is required to generate O_3 from the time the air mass left the plume stack during the afternoon hours of summer. In addition, Chu (1995) observed that pollutants released from emission sources typically require four to six hours to generate large quantities of O_3 during the afternoon. Lidar measurements in Fig. 5.38 show that there was not a significant increase in O_3 mixing ratio downwind, even when the time since passing over the oil sands industry was as large as 10 hours.

The emissions released from Alberta's oil and gas industry are similar to emissions from petrochemical industries in the U.S. (Jobson et al., 2004; Buzcu and

Fraser, 2006; Washenfelder et al., 2010). Aircraft lidar studies of air pollution surrounding petrochemical plants in Houston, Texas have observed O_3 mixing ratios to be as high as 85 ppbv in regions downwind of the industry and under daytime maximum temperatures between 30°C and 42°C and (Senff et al., 2010). In this study, it was found that air temperatures between 10°C and 20°C (within the 400 – 600 m ASL region of the boundary layer) are associated with O_3 mixing ratios of 20 to 30 ppbv in the oil sands region (see Figs. 5.16, 5.19, 5.22, 5.27, and 5.36). Lower air temperatures are not effective in stimulating biogenic VOCs into the atmosphere from plants and trees (Calfapietra et al., 2013) and smaller concentrations of these VOCs contribute to the lack of O_3 formation. Hence, air temperatures of less than 20°C in the oil sands region partly contributed to the lack of O_3 formation downwind of the industry.

Ozone mixing ratios as low as 13 ppbv observed directly over the Athabasca oil sands industry are interpreted as being a result of NO titration. Chemical reactions involved with NO emissions reduce the concentration of O_3 by the formation NO_2: $NO + O_3 \rightarrow NO_2 + O_2$ (Sillman, 1999; Monks, 2005). The reduction of O_3 in industrial pollution is seen in Figs. 5.16, 5.22, 5.36, and 5.9. In situ measurements of $NO + O_3$ were relatively constant throughout the mixed layer and above in Figs. 5.16, 5.22, 5.36, and 5.9.

Lidar measurements of aerosol in Figs. 5.15, 5.18, 5.21, 5.26, and 5.31 show that aerosols were transported downwind of the industry and the depth of the aerosol layer increased by 500 m (on average) for the measurements collected further

downwind. An increase in the aerosol layer depth above the surface with distance downwind is evidence for vertical mixing. As the pollutants mixed with the clean background air, O_3 mixing ratios further downwind of the industry gradually increased to between 30 and 45 ppbv and are consistent with background levels. Downwind of the industry, vertical mixing of pollutants with clean air and temperatures of less than 20°C provided meteorological conditions that were not favourable for the generation of O_3.

Isoprene emissions are the dominant source of biogenic VOCs that are released from plants and trees (Guenther et al., 1995). Greater concentrations of isoprene in the atmosphere result in the production of O_3 by the conversion of NO to NO_2 (reaction (C5) in chapter 1). It is well known that large amounts of biogenic isoprene are released under conditions of high air temperatures (Calfapietra et al., 2013). Volatile organic compounds were measured in Taiwan by Wang et al. (2013) and a temperature dependant simulation study of isoprene emissions by Coates et al. (2016) showed that significant amounts of biogenic isoprene were released for air temperatures close to 30°C. The studies linked higher O_3 concentrations to large amounts of isoprene emissions that were observed in the summer months and under a significant amount of NO_x. The surface air temperatures in the Alberta oil sands region during the measurement period was less than 20°C and it was not high enough to produce substantial amounts of isoprene for the generation of O_3.

Ground based measurements of VOCs across Canada are available on the National Air Pollution Surveillance (NAPS) network. Concentrations of VOC

compounds such as benzene, toluene, and ethlybenzene were obtained from the NAPS website for a station in Toronto during July 2010 and these measurements were compared to the VOC concentrations collected by the Convair in the Alberta oil sands region. NAPS data revealed that higher concentrations of benzene, toluene, and ethylbenzene were present in Toronto (on a day with high levels of O_3 pollution) as compared the Alberta oil sands region. This strongly suggests that benzene, toluene, and ethlybenzene were involved in the generation of O_3 and higher concentrations of those compounds can be linked to O_3 pollution events that were observed in Toronto during July 6 – 8, 2010. Thus, smaller concentrations of VOCs partly contributed to the lack of O_3 formation in the oil sands region.

At distances of 30, 100, and 140 km downwind of the industry, the absence of enhanced O_3 in pollution is interpreted as being a result of 1) the polluted air mass mixing with clean background air, 2) no regional stagnation of air (Camalier et al., 2007), and 3) ambient temperatures not greater than 20°C (which led to insufficient amount of biogenic VOCs) (Jacob et al., 1993; Calfapietra et al., 2013; Coates et al., 2016) resulted in conditions that were not favourable for the generation of O_3.

5.2.2 Forest Fire Smoke

Above the surface boundary layer, forest fire smoke was observed from local forest fires located south-west of Fort McMurray. The O_3 mixing ratio in the forest fire smoke layer was measured to be up to 70 ppbv, which was significantly greater than the background value. Other studies have also reported the generation of ozone in forest fire smoke (Jost et al., 2003; Trentmann et al., 2003). Forest fires are a major

source of air pollution and air pollutants such as NO_x, CO, and CH_4 are produced by incomplete combustion of the burning fires. The production of O_3 in forest fire smoke is a result of photochemical reactions between CO and CH_4 that take place in sufficient amounts of NO (Crutzen and Birks, 1982):

$$CO + OH \rightarrow H + CO_2 \quad \text{(C7)}$$
$$H + O_2 + M \rightarrow HO_2 + M \quad \text{(C8)}$$
$$HO_2 + NO \rightarrow OH + NO_2 \quad \text{(C9)}$$
$$NO_2 + h\nu \rightarrow NO + O \quad \text{(C10)}$$
$$O + O_2 + M \rightarrow O_3 + M \quad \text{(C11)}$$

Net reaction: $CO + 2O_2 \rightarrow CO_2 + O_3$

And

$$CH_4 + OH \rightarrow CH_3 + H_2O \quad \text{(C12)}$$
$$CH_3 + O_2 + M \rightarrow CH_3O_2 + M \quad \text{(C13)}$$
$$CH_3O_2 + NO \rightarrow CH_3O + NO_2 \quad \text{(C14)}$$
$$CH_3O + O_2 \rightarrow CH_2O + HO_2 \quad \text{(C15)}$$
$$HO_2 + NO \rightarrow OH + NO_2 \quad \text{(C16)}$$
$$2NO_2 + 2h\nu \rightarrow 2NO + 2O \quad \text{(C17)}$$
$$2O + 2O_2 + 2M \rightarrow 2O_3 + 2M \quad \text{(C18)}$$
$$CH_2O + h\nu \rightarrow CO + H_2 \quad \text{(C19)}$$

Net reaction: $CH_4 + 4O_2 \rightarrow CO + H_2 + 2O_3 + H_2O$

The molecule, *M* in above chemical reactions represents any inert molecule that removes energy and balances the equation.

The value of O_3 measured in forest fire smoke is in contrast to measurements of O_3 in industrial pollution. This is an interesting result because the two different

pollution sources were exposed to the same environment, and O_3 was produced only in the forest fire emissions. This difference may provide a test case for the models.

6 Conclusion

In August 2013, airborne lidar measurements were carried out to assess the regional air quality in the Athabasca oil sands region. Significant amounts of aerosol were observed directly over the industry, up to an altitude of 1.5 km ASL. Ozone mixing ratios varied between 15 and 35 ppbv in the polluted air from the oil sands industry. Large emissions of NO were observed over the industry and the titration reaction of NO with O_3 can explain why the observed O_3 values were reduced to as low as 12 ppbv.

In regions upwind of the oil sands industry, insignificant amounts of aerosol were present and downwind of the industry the aerosols had dispersed by mixing. Ozone mixing ratios in regions upwind and downwind of the pollution source were comparable to local background levels (25 – 45 ppbv). Downwind of the industry, an increase in the aerosol layer depth provided evidence for vertical mixing. The mixing of polluted air with clean background air, temperatures of less than 20°C, and small concentrations of VOCs provided conditions that were not favourable for the generation of O_3 further downwind of the oil sands industry.

An innovative approach to correct the interference of aerosol in the lidar O_3 retrieval using in situ aerosol measurements was developed in this study. Appropriate

correction of the aerosol interference in the ozone lidar retrieval is important because of the elevated levels of aerosol that were observed in the oil sands region and are usually present in large quantities within the surface boundary layer. Assumptions such as aerosol optical properties being constant within the boundary layer and the value for the particle refractive index were made in this correction technique. The amount of correction in the O_3 mixing ratio was as large as -15 ppbv at the top of the boundary layer, due to large gradients in the aerosol backscatter profile. The aerosol correction was found to be insignificant in regions where background amounts of aerosol were observed and where there are no substantial gradients in the aerosol backscatter profile. The O_3 mixing ratios derived from the lidar measurements agreed with the in situ O_3 measurements collected within the oil sands region on the Convair aircraft.

On one of the Twin Otter flights, smoke from nearby forest fires was observed in a layer above the surface boundary layer. The mixing ratio of O_3 in the pollution from forest fires was measured to be up to 70 ppbv. This is significantly greater than the O_3 mixing ratio measured in industrial pollution. One unique aspect that the airborne O_3 lidar has brought to this study is the demonstration of ozone chemistry in industrial emissions being different than forest fire smoke even though both pollution sources are exposed to the same environment.

There is a significant difference in O_3 pollution during the summer in the city of Toronto and in the Athabasca oil sands region. The O_3 produced by pollution in Toronto is greater than the O_3 pollution in the Athabasca oil sands region. The air

mass transported to the city of Toronto was previously polluted from the oil and petroleum refineries in Toledo, coal powered plants in Detroit, Chicago, the Ohio Valley, and local emissions from the Hamilton industry. Ambient daytime temperatures of 34°C close to the surface, substantial VOC concentrations, and a stable boundary layer that limited the vertical mixing of pollutants (due to a temperature inversion) accommodated the production of O_3 in Toronto. These conditions were not present over the Athabasca oil sands region.

Environment and Climate Change Canada developed an air quality model, the Global Environmental Multiscale model - Modelling Air Quality and Chemistry (GEM-MACH), to forecast the concentrations of O_3 and $PM_{2.5}$ on a regional scale. The atmospheric chemistry and meteorology are coupled together in the GEM-MACH model. This model requires input parameters from the emissions inventory to evaluate emission levels of ozone precursors. The results of the airborne lidar measurements during the JOSM campaign will inform the further development of the GEM-MACH model.

Appendix 1: Retrieval of Aerosol Extinction Coefficient

Extinction height profiles shown in this dissertation were derived from the lidar measurements by using the method of Fernald (Fernald, 1984). The derivation of Fernald's extinction coefficient algorithm (Fernald et al., 1972) is shown in this section.

The first step is to write the lidar equation (Eq. (11)) with the backscatter and extinction coefficients separated in terms of their aerosol and molecular components:

$$P(z) = \frac{C}{z^2} \left(\beta_A(z) + \beta_M(z)\right) exp\left[-2 \int_0^z \left(\alpha_A(z) + \alpha_M(z)\right) dz\right] \tag{28}$$

For simplicity, the wavelength dependence of the lidar equation is not included in the derivation and in this study Fernald's extinction coefficient algorithm was applied to the lidar measurements collected at a wavelength of 532 nm.

The following variables in Eq. (28) represent:

$P(z)$ – The backscattered lidar signal as a function of range z.
C – The lidar constant. This includes factors such as the detector efficiency, pulse energy, optical throughput, and the area of the receiver.
$\beta_A(z)$ – The backscatter coefficient of aerosol particles as a function of range.
$\beta_M(z)$ – The backscatter coefficient of air molecules as a function of range.
$\alpha_A(z)$ – The extinction coefficient of aerosol particles as a function of range.
$\alpha_M(z)$ – The extinction coefficient of air molecules as a function of range.

The molecular component of the backscatter and extinction coefficient can be calculated from atmospheric measurements of temperature, T, and pressure, P, by using radiosonde (weather balloons) data.

The round trip transmittance of the laser pulse between the lidar transmitter and range z for aerosol and air molecules is

$$T^2{}_A(z) = exp\left[-2\int_0^z \alpha_A(z)\, dz\right] \tag{29a}$$

$$T^2{}_M(z) = exp\left[-2\int_0^z \alpha_M(z)\, dz\right] \tag{29b}$$

The lidar equation (Eq. (28)) contains two unknown parameters: the extinction coefficient ($\alpha_A(z)$) and backscatter coefficient ($\beta_A(z)$) of aerosol particles. One of the unknown parameters can be eliminated by assuming a simple relationship between the backscatter and extinction coefficients. This is called the lidar ratio and in Fernald's algorithm the lidar ratio does not vary with range. The lidar ratio for air molecules is well defined and has a value of $S_M = \alpha_M/\beta_M = 8\pi/3$. For aerosol particles, the value of

the lidar ratio $S_A = \alpha_A/\beta_A$ (Eq. (19)) can be estimated from literature or it can be calculated by using Eqs. (17) - (18), if the particle size distribution is known.

The lidar ratios, S_A and S_M, are substituted into Eqs. (29a) and (29b) to eliminate one unknown parameter:

$$T^2{}_A(z) = exp\left[-2S_A \int_0^z \beta_A(z)\, dz\right] \tag{30a}$$

$$T^2{}_M(z) = exp\left[-2S_M \int_0^z \beta_M(z)\, dz\right] \tag{30b}$$

The next step is to isolate for the aerosol backscatter coefficient in Eq. (30a). This can be accomplished by differentiating both sides of Eq. (30a) with respect to range:

$$\beta_A(z) = \frac{-1}{2\, S_A\ T^2{}_A(z)} \frac{d}{dz} T^2{}_A(z) \tag{31}$$

Substituting the aerosol backscatter coefficient in Eq. (31) into Eq. (28), the lidar equation can be expressed as

$$P(z) = \frac{C}{z^2}\left(\beta_M(z) - \frac{1}{2\, S_A\ T^2{}_A(z)} \frac{d}{dz} T^2{}_A(z)\right) T^2{}_A(z)\, T^2{}_M(z) \tag{32}$$

Equation (32) can be expanded and simplified to obtain the lidar equation as a first order linear differential equation:

$$\frac{d}{dz}T^2{}_A(z) - 2S_A\beta_M(z)\,T^2{}_A(z) = -\frac{2\,S_A}{C}\,\frac{1}{T^2{}_M(z)}\,P(z)z^2 \tag{33}$$

For a first order linear differential equation in the form of $dy/_{dz} + M(z)\,y = N(z)$, a standard solution for *y* is:

$$y(z) = \frac{1}{exp[\int M(z)\,dz]}\left\{\int\left(N(z)\,exp\left[\int M(z)\,dz\right]\right)dz + C_1\right\} \tag{34}$$

Where C_1 in Eq. (34) represents the integration constant.

By using the standard solution in Eq. (34), $T^2{}_A(z)$ in Eq. (33) can be solved as

$$\begin{aligned} T^2{}_A(z) = exp\left[2S_A\int_0^z \beta_M(z)\,dz\right]\Bigg\{1 \\ -\frac{2\,S_A}{C}\int_0^z\left(\frac{P(z)z^2}{T^2{}_M(z)}\times exp\left[-2S_A\int_0^z\beta_M(z)\,dz\right]\right)dz\Bigg\} \end{aligned} \tag{35}$$

Equation (35) can be simplified further by substituting Eq. (29b) into Eq. (35) to eliminate the molecular transmittance term ($T^2{}_M(z)$):

$$\begin{aligned} T^2{}_A(z) = exp\left[2S_A\int_0^z \beta_M(z)\,dz\right]\Bigg\{1 \\ -\frac{2\,S_A}{C}\int_0^z\left(P(z)z^2\times exp\left[-2(S_A-S_M)\int_0^z\beta_M(z)\,dz\right]\right)dz\Bigg\} \end{aligned} \tag{36}$$

Next, the total backscatter coefficient (sum of the molecular and aerosol component) in the lidar equation will be solved for by substituting Eq. (36) into Eq. (28):

$$\beta_A(z) + \beta_M(z) = \frac{P(z)z^2 \times exp\left[-2(S_A - S_M)\int_0^z \beta_M(z)\, dz\right]}{\left[C - 2\,S_A \int_0^z \left(P(z)z^2 \times exp\left[-2(S_A - S_M)\int_0^z \beta_M(z)\, dz\right]\right)dz\right]} \quad (37)$$

Equation (37) is mostly expressed in terms of known parameters (if the aerosol lidar ratio is known). The only variable that needs to be solved for is the lidar constant, *C*, in Eq. (37). This can be achieved by using a known value of the backscatter coefficient at a chosen reference range, z_c, and defining the range normalized lidar signal as $X(z) = P(z)z^2$:

$$\beta_A(z) + \beta_M(z) = \frac{X(z) \times exp\left[-2(S_A - S_M)\int_{z_c}^z \beta_M(z)\, dz\right]}{\left[\frac{X(z_c)}{\beta_A(z_c) + \beta_M(z_c)} - 2\,S_A \int_{z_c}^z \left(X(z) \times exp\left[-2(S_A - S_M)\int_{z_c}^z \beta_M(z)\, dz\right]\right) dz\right]} \quad (38)$$

Fernald's algorithm adopts a simple numerical integration method between adjacent lidar data points located Δz apart. This is done by replacing the exponential terms in Eq. (38) by the following expression:

$$A(i, i+1) = (S_A - S_M)[\beta_M(i) + \beta_M(i+1)]\,\Delta z \quad (39)$$

The following algorithm was used to calculate the total backscatter coefficient (for ranges above the chosen reference point) by numerical integration:

$$\beta_A(i+1) + \beta_M(i+1) = \frac{X(i+1) \times exp[-A(i,i+1)]}{\left[\frac{X(i)}{\beta_A(i) + \beta_M(i)} - S_A\{[X(i) + X(i+1)]\, exp[-A(i,i+1)]\}\Delta z\right]} \quad (40)$$

The final algorithm used to derive the aerosol extinction coefficient is presented in equations (41a) and (41b). Equations (41a) and (41b) were obtained by substituting $S_A = \alpha_A/\beta_A$ and $S_M = \alpha_M/\beta_M$ in Eq. (40) to retrieve the height profile in terms of extinction coefficient instead of backscatter coefficient. Lidar measurements at a wavelength of 532 nm were evaluated in equations (41a) and (41b) in successive steps (according to range) above and below a chosen reference point to retrieve the height profile.

$$\alpha_A(i+1) = \frac{X(i+1)\exp\left(-A(i,i+1)\right)}{\frac{X(i)}{\alpha_A(i) + \left(S_A/S_M\right)\alpha_M(i)} - \left(X(i) + X(i+1)\exp(-A(i,i+1)\right)\Delta z} - \frac{S_A}{S_M}\alpha_M(i+1) \quad (41a)$$

$$\alpha_A(i-1) = \frac{X(i-1)\exp(+A(i-1,i))}{\frac{X(i)}{\alpha_A(i) + \left(S_A/S_M\right)\alpha_M(i)} + \left(X(i) + X(i+1)\exp(+A(i-1,i)\right)\Delta z} - \frac{S_A}{S_M}\alpha_M(i-1) \quad (41b)$$

where

$$A(i,i+1) = (S_A - S_M)[\beta_M(i) + \beta_M(i+1)]\,\Delta z$$

$$A(i-1,i) = (S_A - S_M)[\beta_M(i-1) + \beta_M(i)]\,\Delta z$$

Bibliography

Abbatt, J., Aherne, J., Austin, C., Banic, C., Blanchard, P., Charland, J. P., Kelly, E., Li, S. M., Makar, P., Martin, R., McCullum, K., McDonald, K., McLinden, C., Mihele, C., Percy, K., Rideout, G., Rudolph, J., Savard, M., Spink, D., Vet, R., and Watson, J. (2011), Integrated Monitoring Plan for the Oil Sands: Air Quality Component, Retrieved from http://publications.gc.ca/site/eng/394253/publication.html (date accessed: June 01, 2017)

Aggarwal, M. (2011), *Lidar measurements of forest fire smoke and stratospheric aerosol*, Thesis, York University.

Alvarez II, R. J., Senff, C. J., Hardesty, R. M., Parrish, D. D., Luke, W. T., Watson, T. B., Daum, P. H., and Gillani, N. (1998), Comparisons of airborne lidar measurements of ozone with airborne in situ measurements during the 1995 Southern Oxidants Study, *J. Geophys. Res.*, **103**, 31,155-31,171.

Ancellet, G., Papayannis, A., Pelon, J., and Mégie, G. (1989), DIAL tropospheric ozone measurement using a Nd:YAG laser and the Raman shifting technique, *Journal of Atmospheric and Oceanic Technology*, **6**, 832 – 839.

Angle, R. P., and Sandhu, H. S. (1986), Rural ozone concentrations in Alberta, Canada, *Atmos. Environ.*, **20**(6), 1221–1228.

Arakawa, E. T., Tuminello, P. S., Khare, B. N., Milham, M. E., Authier, S., and Pierce, J. (1997), Measurement of optical properties of small particles, In *1997 Scientific Conference on Obscuration and Aerosol Research* (pp. 1–30), Maryland. Document ID: ORNL/CP-95872.

Banta, R. M., Senff, C. J., Nielsen-Gammon, J., Darby, L. S., Ryerson, T. B., Alvarez, R. J., Sandberg, S. P., Williams, E. J., and Trainer, M. (2005), A bad air day in Houston, *Am. Met. Soc.*, 657 – 669, doi:10.1175/BAMS-86-5-657.

Bari, M., and Kindzierski, W. B. (2015), Fifteen-year trends in criteria air pollutants in oil sands communities of Alberta, Canada, *Environment International*, **74**, 200–208, doi:10.1016/j.envint.2014.10.009.

Barshad, I. (1955), Adsorptive and swelling properties of clay-water system, *Clays and Clay Technology*, **169**, 70-77.

Baumgardner, D., Dye, J. E., Gandrud, B. W., and Knollenberg, R. G. (1992), Interpretation of measurements made by the Forward Scattering Spectrometer Probe (FSSP-300) during the airborne stratospheric expedition, *J. Geophys. Res.*, **97**(D8), 8035 – 8046.

Baumann, K., and Stohl, A. (1997), Validation of a long-range trajectory model using gas balloon tracks from the Gordon Bennett Cup 95, *J. Appl. Met.*, **36**, 711–720.

Bogumil, K., Orphal, J., Homann, T., Voigt, S., Spietz, P., Fleischmann, O. C., Vogel, A., Hartmann, M., Kromminga, H., Bovensmann, H., Frerick, J., and Burrows, J. P. (2003), Measurements of molecular absorption spectra with the SCIAMACHY pre-flight model: Instrument characterization and reference data for atmospheric remote-sensing in the 230-2380 nm region, *Journal of Photochemistry and Photobiology A: Chemistry*, **157**, 167–184, doi:10.1016/S1010-6030(03)00062-5.

Bohren, C. F. and Huffman, D. R.: Absorption and Scattering of light by small particles, John Wiley & Sons, Inc., New York, 1983.

Browell, E. V., Ismail, S., and Shipley, S. T. (1985), Ultraviolet DIAL measurements of O_3 profiles in regions of spatially inhomogeneous aerosols, Appl. Opt., **24**(17), 2827 – 2836.

Buzcu, B., and Fraser, M. P. (2006), Source identification and apportionment of volatile organic compounds in Houston, TX, *Atmos. Environ.*, **40**, 2385–2400, doi:10.1016/j.atmosenv.2005.12.020.

Calfapietra, C., Fares, S., Manes, F., Morani, A., Sgrigna, G., and Loreto, F. (2013), Role of biogenic volatile organic compounds (BVOC) emitted by urban trees on ozone concentration in cities: A review, *Environmental Pollution*, **183**, 71 – 80, doi:10.1016/j.envpol.2013.03.012.

Camalier, L., Cox, W., Dolwick, P. (2007), The effects of meteorology on ozone in urban areas and their use in assessing ozone trends, *Atmos. Environ.*, **41**, 7127 – 7137, doi:10.1016/j.atmosenv.2007.04.061.

Chakrabarty, R. K., Moosmuller, H., Garro, M. A., Arnott, W. P., Walker, J., Susott, R. A., Babbitt, R. E., Wold, C. E., Lincoln, E. N., and Hao, W. M. (2006), Emissions from the laboratory combustion of wildland fuels: Particle morphology and size, *J. Geophys. Res.,* **111**, 1 – 16, doi:10.1029/2005JD006659.

Chu, S.-H. (1995), Meteorological considerations in siting photochemical pollutant monitors, *Atmos. Environ.*, **29**(21), 2905–2913.

Cloutis, E. A., Gaffey, M. J., and Moslow, T. F. (1995), Characterization of minerals in oil sands by reflectance spectroscopy, *Fuel*, **74**(6), 874–879.

Coates, J., Mar, K. A., Ojha, N., and Butler, T. M. (2016), The influence of temperature on ozone production under varying NO_x conditions – a modelling study, *Atmos. Chem. Phys.*, **16**, 11601 – 11615, doi:10.5194/acp-16-11601-2016.

Crutzen, P. J. (1979), The role of NO and NO_2 in the chemisty of the troposphere and stratosphere, *Ann. Rev. Earth Planet. Sci.*, **7**, 443–472.

Crutzen, P. J., Heidt, L. E., Krasnec, J. P., Pollock, W. H., and Seiler, W. (1979), Biomass burning as a source of atmospheric gases CO, H_2, N_2O, NO, CH_3Cl and COS, *Nature*, **282**, 253–256.

Crutzen, P. J., and Birks, J. W. (1982), The atmosphere after a nuclear war: Twilight at noon, *Ambio*, **11**(2/3), 114–125.

Davies, M. J. E. (2012), Air quality modeling in the Athabasca Oil Sands Region, In K. E. Percy (Ed.), *Alberta Oil Sands: Energy, Industry and the Environment* (1st ed., pp. 267–309), Oxford: Elsevier Ltd.

Donovan, D. P., Whiteway, J. A., and Carswell, A. I. (1993), Correction for nonlinear photon-counting effects in lidar systems, *Appl. Opt.*, **32**(33), 6742–6753.

Dorsey, J. R., Duyzer, J. H., Gallagher, M. W., Coe, H., Pilegaard, K., Weststrate, J. H., Jensen, N. O., and Walton, S. (2004), Oxidized nitrogen and ozone interaction with forests. I: Experimental observations and analysis of exchange with Douglas fir, *Q. J. R. Met. Soc.*, **130**, 1941 – 1955, doi: 10.1256/qj.03.124.

Draxler, R. R., and Hess, G. D. (1998), An overview of the HYSPLIT_4 modeling system of trajectories, dispersion, and deposition, *Aust. Met. Mag.*, **47**, 295–308.

Droplet Measurement Technologies Incorporated. (2013), Ultra High Sensitivity Aerosol Spectrometer (UHSAS) Operator Manual, Retrieved from http://www.dropletmeasurement.com/sites/default/files/ManualsGuides/Hardware%20Manuals/UHSAS.pdf (date accessed: October 17, 2016).

Eisele, H., and Trickl, T. (2005), Improvements of the aerosol algorithm in ozone lidar data processing by use of evolutionary strategies, *Appl. Opt.*, **44**(13), 2638–2651.

Elliott, C. T., and Copes, R. (2011), Burden of Mortality Due to Ambient Fine Particulate Air Pollution ($PM_{2.5}$) in Interior and northern BC, *Canadian Journal Of Public Health*, **102**(5), 390–393.

Evans, R. D. (1955), Applications of Poisson statistics to some instruments used in nuclear physics. In *The atomic nucleus* (1st ed., pp. 785–794), New York: McGraw-Hill, Inc.

Fernald, F. G., Herman, B. M., and Reagan, J. A. (1972), Determination of aerosol height distributions by lidar, *J. Appl. Met.*, **11**, 482 – 489.

Fernald, F. G. (1984), Analysis of atmospheric lidar observations: some comments, *Appl. Opt.*, **23**(5), 652–653.

Franklin, M., Zeka, A., and Schwartz, J. (2007), Association between $PM_{2.5}$ and all-cause and specific-cause mortality in 27 US communities, *Journal of Exposure Science & Environmental Epidemiology*, **17**, 279–287, doi:10.1038/sj.jes.7500530.

Fukuchi, T., Nayuki, T., Cao, N., Fujii, T., and Nemoto, K. (2003), Differential absorption lidar system for simultaneous measurement of O_3 and NO_2: system development and measurement error estimation, *Opt. Eng.*, **42**(1), 98 – 104, doi:10.1117/1.1525274.

Gao, L., Lemarchand, R., and Lequime, M. (2013), Refractive index determination of SiO_2 layer in the UV/Vis/NIR range: Spectrophotometric reverse engineering on single and bi-layer designs, *J. Europ. Opt. Soc. Rap. Public.*, **8**, doi:10.2971/jeos.2013.13010.

Geddes, J. A., Murphy, J. G., and Wang, D. K. (2009), Long term changes in nitrogen oxides and volatile organic compunds in Toronto and the challenges facing local ozone control, *Atmos. Environ.*, **43**, 3407 – 3415, doi:10.1016/j.atmosenv.2009.03.053.

Gordon, M., Li, S.-M., Staebler, R., Darlington, A., Hayden, K., O'Brien, J., and Wolde, M. (2015), Determining air pollutant emission rates based on mass balance using airborne measurement data over the Alberta oil sands operations, *Atmo. Meas. Tech.*, **8**, 3745–3765, doi:10.5194/amt-8-3745-2015.

Guenther, A., Hewitt, C. N., Erickson, D., Fall, H., Geron, C., Graedel, T., Harley, P., Klinger, L., Lerdau, M., McKay, W. A., Pierce, T., Scholes, B., Steinbrecher, R., Tallamraju, R., Taylor, J., and Zimmerman, P. (1995), A global model of natural volatile organic compound emissions, *J. Geophys. Res.*, **100**, 8873 – 8892.

Haagen-Smit, A. J. (1952), Chemistry and physiology of Los Angeles Smog, *Industrial and Engineering Chemistry*, **44**(6), 1342–1346.

Hamamatsu Photonics K. K. (2007), Hamamatsu Photonics Technical Publication (Chapter 6: Photon Counting), Retrieved from https://www.hamamatsu.com/resources/pdf/etd/PMT_handbook_v3aE-Chapter6.pdf (date accessed: April 14, 2015).

Haman, C. L., Couzo, E., Flynn, J. H., Vizuete, W., Heffron, B., and Lefer, B. L. (2014), Relationship between boundary layer heights and growth rates with ground-level ozone in Houston, Texas, *J. Geophys. Res. Atmos.*, **119**, 6230–6245, doi:10.1002/2013JD020473.

Heese, B., Flentje, H., Althausen, D., Ansmann, A, and Frey, S. (2010), Ceilometer lidar comparison: backscatter coefficient retrieval and signal-to-noise ratio determination, *Atmos. Meas. Tech.*, **3**, 1763 – 1770, doi:10.5194/amt-3-1763-2010.

Hellwarth, R. W. (1963), Theory of stimulated Raman scattering, *Physical Review*, **130**(5), 1850 – 1852.

Howell, S. G., Clarke, A. D., Freitag, S., McNaughton, C. S., Kapustin, V., Brekovskikh, V., Jimenez, J.-L., and Cubison, M. J. (2014), An airborne assessment of atmospheric particulate emissions from the processing of Athabasca oil sands, *Atmo. Chem. Phys.*, **14**, 5073–5087, doi:10.5194/acp-14-5073-2014.

Ismail, O. S., and Umukoro, G. E. (2016), Modelling combustion reactions for gas flaring and its resulting emissions, *Journal of King Saud University (Engineering Sciences)*, 28, 130 – 140, doi:10.1016/j.jksues.2014.02.003.

Jacob, D. J., Logan, J. A., Gardner, G. M., Yevich, R. M., Spivakovsky, C. M., and Wofsy, S. C. (1993), Factors regulating ozone over the United States and its export to the global atmosphere, *J. Geophys. Res.*, **98**, 14,817 – 14,826.

Jobson, B. T., Berkowitz, C. M., Kuster, W. C., Goldan, P. D., Williams, E. J., Fesenfeld, F. C., Apel, E. C., Karl, T., Lonneman, W. A., and Riemer, D. (2004), Hydrocarbon source signatures in Houston, Texas: Influence of the petrochemical industry, *J. Geophys. Res.*, **109**, doi:10.1029/2004JD004887.

Jost, C., Trentmann, J., Sprung, D., Andreae, M. O., McQuaid, J. B., and Barjat, H. (2003), Trace gas chemistry in a young biomass burning plume over Namibia: Observations and model simulations, *J. Geophys. Res.*, **108**, doi:10.1029/2002JD002431.

Karamchandani, P., Koo, A., and Seigneur, C. (1998), Reduced gas-phase kinetic mechanism for atmospheric plume chemistry, *Environ. Sci. Tech.*, **32**(11), 1709–1720.

Kirk, J. L., Muir, D. C. G., Gleason, A., Wang, X., Lawson, G., Frank, R. A., Lehnherr, I., and Wrona, F. (2014), Atmospheric deposition of mercury and methylmercury to landscapes and waterbodies of the Athabasca oil sands region, *Environ. Sci. Tech.*, **48**, 7374–7383, doi:10.1021/es500986r.

Kozma, I. Z., Krok, P., and Riedle, E. (2005), Direct measurement of the group-velocity mismatch and derivation of the refractive-index dispersion for a variety of solvents in the ultraviolet, *J. Opt. Soc. Am. B*, **22**(7), 1479–1485.

Kuang, S., Newchurch, M. J., Burris, J., Wang, L., Buckley, P. I., Johnson, S., Knupp, K., Huang, G., Phillips, D., and Cantrell, W. (2011), Nocturnal ozone enhancement in the lower troposphere observed by lidar, *Atmos. Environ.*, **45**, 6078–6084, doi:10.1016/j.atmosenv.2011.07.038.

Kuhn, H., and Forsterling, H.-D. (2000), *Principles of Physical chemistry: Understanding molecules, molecular assemblies, supramolecular machines*, West Sussex: John Wiley & Sons Ltd.

Langford, A. O., Tucker, S. C., Senff, C. J., Banta, W. A., Brewer, W. A., Alvarez II, R. J., Hardesty, R. M., Lerner, B. M., and Williams, E. J. (2010), Convective venting and surface ozone in Houston during TexAQS 2006, *J. Geophys. Res.*, **115**, doi:10.1029/2009JD013301.

Langford, A. O., Senff, C. J., Alvarez II, R. J., Banta, R. M., Hardesty, R. M., Parrish, D. D., and Ryerson, T. B. (2011), Comparison between the TOPAZ airborne ozone ldiar and in situ measurements during TexAQS 2006, *Journal of Atmospheric and Oceanic Technology*, **28**, 1243 – 1257, doi: 10.1175/JTECH-D-10-05043.1.

Leiva G, M. A., Santibañez, D. A., Ibarra E, S., Matus C, P., and Seguel, R. (2013), A five-year study of particulate matter ($PM_{2.5}$) and cerebrovascular diseases, *Environmental Pollution*, **181**, 1–6, doi:10.1016/j.envpol.2013.05.057.

Liggio, J., Li, S.-M., Hayden, K., Taha, Y. M., Stroud, C., Darlington, A., Drollette, B. D., Gordon, M., Lee, P., Liu, P., Leithead, A., Moussa, S. G., Wang, D., O'Brien, J., Mittermeier, R. L., Brook, J. R., Lu, G., Staebler, R. M., Han, Y., Tokarek, T. W., Osthoff, H. D., Makar, P. A., Zhang, J., Plata, D. L., and Gentner, D. R. (2016), Oil sands operations as a large source of secondary organic aerosols, *Nature*, **534**, 91–94, doi:10.1038/nature17646.

Mégie, G., Allain, J. Y., Chanin, M. L., and Blamont, J. E. (1977), Vertical profile of stratospheric ozone by lidar sounding from the ground, *Nature*, **270**, 329 – 331.

Menyuk, N., Killinger, D. K., and DeFeo, W. E. (1980), Remote sensing of NO using a differential absorption lidar, *Appl. Opt.*, **19**(19), 3282 – 3286.

Menzies, R. T. and Shumate, M. S. (1978), Tropospheric ozone distributions measured with an airborne laser absorption spectrometer, *J. Geophys. Res.*, **83**, 4039 – 4043.

Mercier, P. H. J., Le Page, Y., Tu, Y., and Kotlyar, L. (2008), Powder X-ray Diffraction Determination of Phyllosilicate Mass and Area versus Particle Thickness Distributions for Clays from the Athabasca Oil Sands, *Petroleum Science and Technology*, **26**, 307–321, doi:10.1080/10916460600806069.

Metha, M., Chen, L.-C., Gordon, T., Rom, W., and Tang, M.-S. (2008), Particulate matter inhibits DNA repair and enhances mutagenesis, *Mutat. Res.*, **657**(2), 116–121, doi:10.1016/j.mrgentox.2008.08.015.

Michel Flores, J., Bar-Or, R. Z., Bluvshtein, N., Abo-Riziq, A., Kostinski, A., Borrmann, S., Koren, I., Koren, I., and Rudich, Y. (2012), Absorbing aerosols at high relative humidity: Linking hygroscopic growth to optical properties, *Atmo. Chem. Phys.*, **12**, 5511–5521, doi:10.5194/acp-12-5511-2012.

Monks, P. S. (2005), Gas-phase radical chemistry in the troposphere, *Chemical Society Reviews*, **34**, 376–395, doi:10.1039/b307982c.

Morgan, P. B., Ainsworth, E. A., and Long, S. P. (2003), How does elevated ozone impact soybean? A meta-analysis of photosynthesis, growth and yield, *Plant, Cell and Environment*, **26**, 1317–1328.

Nakazato, M., Nagai, T., Sakai, T., and Hirose, Y. (2007), Tropospheric ozone differential-absorption lidar using stimulated Raman scattering in carbon dioxide, *Appl. Opt.*, **46**(12), 2269–2279.

Omotoso, O. E., and Mikula, R. J. (2004), High surface areas caused by smectitic interstratification of kaolinite and illite in Athabasca oil sands, *Applied Clay Science*, **25**, 37–47, doi:10.1016/j.clay.2003.08.002.

Papayannis, A., Ancellet, G., Pelon, J., and Mégie, G. (1990), Multiwavelength lidar for ozone measurements in the troposphere and the lower stratosphere, *Appl. Opt.*, **29**(4), 467–76.

Permadi, D. A., and Oanh, N. T. (2008), Episodic ozone air quality in Jakarta in relation to meteorological conditions, *Atmospheric Environment*, **42**, 6806–6815, doi:10.1016/j.atmosenv.2008.05.014.

Pirjola, L., Virkkula, A., Petäjä, T., Levula, J., Kukkonen, J., and Kulmala, M. (2015), Mobile ground-based measurements of aerosol and trace gases during a prescribed burning experiment in boreal forest in Finland, *Boreal Environment Research*, **20**, 105 – 119, ISSN:1239-6095.

Portelli, R. V. (1977), *Mixing heights, wind speeds and ventilation coefficients for Canada*, pp. 1 – 87, Fisheries and Environment Canada, Downsview, ON, ISBN: 0-660-10010-X.

Rothman, L. S., Gordon, I. E., Babikov, Y., Barbe, A., Chris Benner, D., Bernath, P. F., Birk, M., Bizzocchi, L., Boudon, V., Brown, L. R., Campargue, A., Chance, K., Cohen, E. A., Coudert, L. H., Devi, V. M., Drouin, B. J., Fayt, A., Flaud, J.-M., Gamache, R. R., Harrison, J. J., Hartmann, J.-M., Hill, C., Hodges, J. T., Jacquemart, D., Jolly, A., Lamouroux, J., Le Roy, R. J., Li, G., Long, D. A., Lyulin, O. M., Mackie, C. J., Massie, S. T., Mikhailenko, S., Müller, H. S. P., Naumenko, O. V., Nikitin, A. V., Orphal, J., Perevalov, V., Perrin, A., Polovtseva, E. R., Richard, C., Smith, M. A. H., Starikova, E, Sung, K., Tashkun, S., Tennyson, J., Toon, G. C. Tyuterev, V. G., and Wagner, G. (2013), The HITRAN2012 molecular spectroscopic database, *Journal of Quantitative Spectroscopy and Radiative Transfer*, **130**, 4 –50, doi:10.1016/j.jqsrt.2013.07.002.

Rudolph, R. (2004), *Analysis of airborne ozone and ozone precursor measurements in the oil sands summer 2001 and 2002*, *Cumulative Environmental Management Association*, pp. 1 – 536. Document ID: 1023971.

Sassen, K. (1991), The polarization lidar technique for cloud research: A review and current assessment, *B. Am. Meteorol. Soc.*, **72**, 1848 – 1866.

Schotland, R. M. (1964), The determination of the vertical profile of atmospheric gases by means of a ground based optical radar, In *Proceedings of the 3rd Symposium on Remote Sensing of the Environment*, Ann Arbor, University of

Michigan, 215 – 224.

Schuttlefield, J. D., Cox, D., and Grassian, V. H. (2007), An investigation of water uptake on clay minerals using ATR-FTIR spectroscopy coupled with quartz crystal microbalance measurements, *J. Geophys. Res.*, **112**, doi:10.1029/2007JD008973.

Seabrook, J. A., Whiteway, J. A., Gray, L. H., Staebler, R., and Herber, A. (2013), Airborne lidar measurements of surface ozone depletion over Arctic sea ice, *Atmo. Chem. Phys.*, **13**, 6023–6029, doi:10.5194/acp-13-6023-2013.

Senff, C. J., Alvarez II, R. J., Hardesty, R. M., Banta, R. M., and Langford, A. O. (2010), Airborne lidar measurements of ozone flux downwind of Houston and Dallas, *J. Geophys. Res.*, **115**, doi:10.1029/2009JD013689.

Sharkey, T. D., Wiberley, A. E., and Donohue, A. R. (2008), Isoprene emission from plants: Why and how, *Annals of Botany*, **101**, 5–18, doi:10.1093/aob/mcm240.

Shephard, M. W., McLinden, C. A., Cady-Pereira, K. E., Luo, M., Moussa, S. G., Leithead, A., Liggio, J., Staebler, R. M., Akingunola, A., Makar, P., Lehr, P., Zhang, J., Henze, D. K., Millet, D. B., Bash, J. O., Zhu, L., Wells, K. C., Capps, S. L., Chaliyakunnel, S., Gordon, M., Hayden, K., Brook, J. R., Wolde, M., and Li, S. M. (2015), Tropospheric Emission Spectrometer (TES) satellite observations of ammonia, methanol, formic acid, and carbon monoxide over the Canadian oil sands: Validation and model evaluation, *Atmo. Meas. Tech.*, **8**, 5189–5211, doi:10.5194/amt-8-5189-2015.

Sillman, S. (1999), The relation between ozone, NO_x and hydrocarbons in urban and polluted rural environments, *Atmos. Environ.*, **33**, 1821–1845.

Simpson, I. J., Akagi, S. K., Barletta, B., Blake, N. J., Choi, Y., Diskin, G. S., Fried, A., Fuelberg, H. E., Meinardi, S., Rowland, F. S., Vay, S. A., Weinheimer, A. J., Wennberg, P. O., Wiebring, P., Wisthaler, A., Yang, M., Yokelson, R. J., and Blake, D. R. (2011), Boreal forest fire emissions in fresh Canadian smoke plumes: C_1-C_{10} volatile organic compounds (VOCs), CO_2, CO, NO_2, NO, HCN and CH_3CN, *Atmo. Chem. Phys.*, **11**, 6445–6463, doi:10.5194/acp-11-6445-2011.

Simpson, I. J., Blake, N. J., Barletta, B., Diskin, G. S., Fuelberg, H. E., Gorham, K., Huey, L. G., Meinardi, S., Rowland, F. S., Vay, S. A., Weinheimer, A. J., Yang, M., and Blake, D. R. (2010), Characterization of trace gases measured over Alberta oil sands mining operations: 76 speciated C_2-C_{10} volatile organic compounds (VOCs), CO_2, CH_4, CO, NO, NO_2, NO_y, O_3 and SO_2, *Atmo. Chem. Phys.*, **10**, 11931–11954, doi:10.5194/acp-10-11931-2010.

Strausz, O. P. (1989), Bitumen and heavy oil chemistry. In L. G. Hepler and C. Hsi (Eds.), *AOSTRA Technical Handbook on Oil Sands, Bitumen and Heavy Oils* (6th ed., pp. 35–73), Edmonton: Alberta Oil Sands Technology and Research Authority.

Sullivan, J. T., McGee, T. J., Sumnicht, G. K., Twigg, L. W., and Hoff, R. M. (2014), A mobile differential absorption lidar to measure sub-hourly fluctuation of tropospheric ozone profiles in the Baltimore-Washington, D.C. region, *Atmo. Meas. Tech.*, **7**, 3529–3548, doi:10.5194/amt-7-3529-2014.

Sunesson, J. A, Apituley, A., and Swart, D. P. (1994), Differential absorption lidar system for routine monitoring of tropospheric ozone, *Appl. Opt.*, **33**(30), 7045–7058.

Thermo Fisher Scientific Incorporated. (2007), Chemiluminescence NO-NO_2-NO_x Analyzer (Model 42*i*) Instruction Manual, Retrieved from https://tools.thermofisher.com/content/sfs/manuals/EPM-manual-Model%2042i.pdf (date accessed: May 25, 2017).

Thermo Fisher Scientific Incorporated. (2007), UV Photometric O_3 Analyzer (Model 49*i*) Instruction Manual, Retrieved from https://tools.thermofisher.com/content/sfs/manuals/EPM-manual-Model%2049i.pdf (date accessed: October 05, 2016).

Trentmann, J., Andreae, M. O., and Graf, H.-F. (2003), Chemical processes in a young biomass-burning plume, *J. Geophys. Res.*, **108**, doi:10.1029/2003JD003732.

Val Martin, M., Honrath, R. E., Owen, R. C., Pfister, G., Fialho, P., and Barata F. (2006), Significiant enhancements of nitrogen oxides, black carbon, and ozone in the North American lower free troposphere resulting from North American boreal wildfires, *J. Geophys. Res.*, **111**, 1 – 17, doi:10.1029/2006JD007530.

Wallace, J., Corr, D., Deluca, P., Kanaroglou, P., and McCarry, B. (2009), Mobile monitoring of air pollution in cities: the case of Hamilton, Ontario, Canada, *Journal of Environmental Monitoring*, **11**, 998 – 1003, doi:10.1039/b818477a.

Wandinger, U., Müller, D., Böckmann, C., Althausen, D., Matthias, V., Bösenberg, J., Weib, V., Fiebig, M., Wendisch, M., Stohl, A., and Ansmann, A. (2002), Optical and microphysical characterization of biomass-burning and industrial-pollution aerosols from multiwavelength lidar and aircraft measurements, *J. Geophys. Res.*, **107,** doi:10.1029/2000JD000202.

Wang, J.-L., Chew, C., Chang, C.-Y., Liao, W.-C., Lung, S.-C., Chen, W.-N., Lee, P.-J., Lin, P.-H., and Chang, C.-C. (2013), Biogenic isoprene in subtropical urban settings and implications for air quality, *Atmos. Environ.*, **79**, 369 – 379, doi:10.1016/j.atmosenv.2013.06.055.

Wang, G., Zhao, J., Jiang, R., and Song, W. (2013), Rat Lung Response to Ozone and Fine Particulate Matter ($PM_{2.5}$) Exposures, *Environmental Toxicology*, **30**, 343–356, doi:10.1002/tox.21912.

Washenfelder, R. A., Trainer, M., Frost, G. J., Ryerson, T. B., Atlas, E. L., de Gouw, J. A., Flocke, F. M., Fried, A., Holloway, J. S., Parrish, D. D., Peischl, J., Richter, D., Schauffler, S. M., Walega, J. G., Warneke, C., Weibring, P., and Zheng, W. (2010), Characterization of NO_x, SO_2, ethene, and propene from industrial emission sources in Houston, Texas, *J. Geophys. Res.*, **115**, doi:10.1029/2009JD013645.

Wightman, D., Rottenfusser, B., Kramers, J., and Harrison, R. (1989), Geology of the Alberta oil sands deposits. In L. G. Hepler and C. Hsi (Eds.), *AOSTRA Technical Handbook on Oil Sands, Bitumen and Heavy Oils* (6th ed., pp. 3–9), Edmonton: Alberta Oil Sands Technology and Research Authority, ISBN: 0-7732-0189-0.

Xiaoqin, L., Yinchao, Z., Huanling, H., Kun, T., Zongming, T., Shisheng, S., Kaifa, C., Xin, F., and Shihua, Y. (2005), Mobile lidar for measurements of SO_2 and O_3 in the low troposphere, In *Proceedings of SPIE:Optical Technologies for Atmospheric, Ocean, and Environmental Studies*, **5832**, 156 – 163, doi:10.1117/12.619553.

Yap, D., Ning, D. T., and Dong, W. (1988), An assessment of source contributions to the ozone concentrations in southern Ontario, 1979-1985, *Atmos. Environ.*, **22**(6), 1161–1168.

Zhang, R., Lei, W., Tie, X., and Hess, P. (2004), Industrial emissions cause extreme urban ozone diurnal variability, In *Proceedings of the National Academy of Sciences*, **101**(17), 6346 – 6350, doi: 10.1073/pnas.0401484101.

Zhao, Y. (1999), Signal-induced flourescence in photomultipliers in differential absorption lidar systems, *Appl. Opt.*, **38**(21), 4639 – 4648.